ORIGIN AND STRUCTURE OF THE CEDUNA DELTA SYSTEM, OFFSHORE SOUTH AUSTRALIA

Justin Dedric MacDonald, B.Sc. (Hons), M.Sc.

The Australian School of Petroleum

The University of Adelaide

This thesis is submitted in fulfilment of the

requirements for the degree of Doctor of Philosophy

in the Faculty of Science, The University of Adelaide

April 15, 2013

Abstract

This thesis consists of five papers, each of which complements the regional understanding of the Ceduna Delta System, offshore South Australia. Deltas commonly form linked systems of extension, on the delta top, and compression, in the delta toe. This link is promoted by the presence of a detachment layer of more ductile sediments at the base of the delta, which mechanically decouples deltaic sediments from those beneath it. These systems are often explained using Critical Taper Wedge mechanics, which is commonly applied to understand the rock strength properties and the role of pore fluid pressure at the base of the wedge (within the detachment layer) and within the wedge, in these linked systems of extension and compression.

To better understand the effect of basal pore fluid pressure on delta—deepwater fold thrust belt systems, I present an in-depth application of Critical Taper Wedge mechanics to the data-rich deepwater Niger Delta Toe in West Africa, a modern day analogue for the ancient Ceduna Sub-basin (Paper 1). This application involved developing a new technique to measure key variables from seismic reflection data in the Niger Delta Toe and input them into a script to calculate the basal pore fluid pressure required to form the observed present-day geometries. With this new approach and increased understanding of the role of basal pore fluid pressure on delta wedge geometry it was possible to better understand how detachment variables control distribution of the lobes that comprise the Cretaceous-age Ceduna Delta. Regional structural mapping of the Ceduna Delta resulted in separation of the delta lobes based on tectonic style and also examining the linkages between the systems, explaining the unique stacking of the delta tops while each system maintained independent deepwater fold-thrust belts (Paper 2).

Furthermore, detailed 3D seismic reflection data is interpreted to investigate inversion structures and potential for fault reactivation in the basin (Paper 3). The boundary element method geomechanical code Poly3D© was used to investigate delta-top fault reactivation potential from a 3D seismic derived fault network along with the present day stress determined from petroleum wells. Results demonstrate a moderate to high probability for contemporary reactivation of faults under a strike-slip to strike-slip-normal fault stress regime (Paper 3).

In addition, detrital zircon analysis, apatite fission track analysis and zircon fission track analysis were undertaken to investigate the potential source(s) for the deltaic sediment input in the Ceduna Delta system (Paper 4). Over 1500 detrital zircon and apatite grains were analysed from petroleum wells and outcrop samples located onshore and offshore South Australia. The results indicate approximately 1-2 km of Late Cretaceous uplift/exhumation of the proximal arcuate shaped South Australian southern margin provided the source for the Santonian-Maastrichtian delta lobe, mainly from erosion of existing Permian-Cenomanian sedimentary cover. Finally, the last paper presented in this thesis (Paper 5) ties in new 2D reflection seismic data that was not available when Paper 2 was written, to further examine the geometry of the deepwater fold-thrust belts and the hydrocarbon potential of the Ceduna Sub-basin.

Table of Contents

Papers

Paper 1: MacDonald, J.D., Healy, D., King, R., and Backé, G., (*in review*): Mapping basal pore fluid pressure variations in the Niger Delta toe with a critical taper wedge model. *Marine and Petroleum Geology.*

Paper 2: MacDonald, J.D., King, R., Hillis, R.R., and Backé, G., (2010): Structural style of the White Pointer and Hammerhead Delta—Deepwater Fold-Thrust Belts, Bight Basin, Australia. *The Australian Association of Petroleum Production and Exploration Journal,* v 50, 487-510.

Paper 3: MacDonald, J.D., Backé, G., King, R., Holford, S., and Hillis, R.R., (2012): Geomechanical modelling of fault reactivation in the Ceduna Sub-basin, Bight Basin, Australia, *in*: Healy, D., Butler, R. W. H., Shipton, Z. K. & Sibson, R. H. (eds) 2012. Faulting, Fracturing and Igneous Intrusion in the Earth's Crust. *Geological Society, London, Special Publications*, 367, 71–89.

Paper 4: MacDonald, J.D., Holford, S., Green, P.F., Duddy, I., King, R., and Backé, G., (2013): Detrital Zircon Data Reveal the Origin of Australia's Largest Delta System. *Journal of the Geological Society, London*.

Paper 5: MacDonald, J.D., Holford, S., and King, R., (*in press*): Structure and Prospectivity of the Ceduna Delta—Deepwater Fold-Thrust Belt Systems, Bight Basin, Australia, *in*: Rosen, N.C., (ed) 2012. New understanding of the petroleum systems of the continental margins of the world. *GCSSEPM Foundation Bob F. Perkins Research Conference, v 32*.

Declaration

I certify that this work contains no material which has been accepted for the award of any other degree or diploma in any university or other tertiary institution and, to the best of my knowledge and belief, contains no material previously published or written by another person, except where due reference has been made in the text. In addition, I certify that no part of this work will, in the future, be used in a submission for any other degree or diploma in any university or other tertiary institution without the prior approval of the University of Adelaide and where applicable, any partner institution responsible for the joint-award of this degree.

I give consent to this copy of my thesis when deposited in the University Library, being made available for loan and photocopying, subject to the provisions of the Copyright Act 1968.

The author acknowledges that copyright of published works contained within this thesis resides with the copyright holder(s) of those works.

I also give permission for the digital version of my thesis to be made available on the web, via the University's digital research repository, the Library catalogue and also through web search engines, unless permission has been granted by the University to restrict access for a period of time.

4/4/2013

Justin Dedric MacDonald — Date

Statement of Authors' Contributions

The research summarized in the papers that constitute this thesis was undertaken within the 'S^3' research group (Stress, Seismic and Structure; formally the stress group) at the Australian School of Petroleum (ASP), with industry collaborators (Geotrack International Pty Ltd; Paul Green & Ian Duddy) and with an external co-supervisor at the University of Aberdeen (Dave Healy). The ASP 'S^3'group comprises several PhD students, research staff and lecturers who collaborate across a broad range of stress, tectonic, thermochronological, geochronological and structural/geomechanical related issues. Hence, all the papers presented are co-authored and detailed statements of relative contribution are summarised below and endorsed by the co-authors.

Acknowledgements

This thesis and the work undertaken within it could not have been completed without the support and encouragement of many people.

- **My supervisory committee: Rosalind King, Guillaume Backé, Simon Holford and Richard Hillis.** You are all outstanding researchers in your respective fields. You encouraged me to challenge myself, explore interesting problems as they arose and provided advice when sought. Most importantly you let me make my own mistakes, which in hindsight is how you really learn. Rosalind, thanks for taking me on as your PhD student and being an incredibly punctual, supportive and enthusiastic supervisor. Guillaume, for all those questions I had over the last few years that I felt could not wait 5 minutes – your door was *always* open. Simon, you somehow taught me to condense 10,000 words into 2000; your passion for geology is contagious. Richard, although you only directly supervised me for a short time, your style is deeply engrained into Rosalind, Simon and Guillaume, so I never missed out.
- **My external and unofficial supervisors**: **Dave Healy, Paul Green and Ian Duddy**. Dave, thanks for all the technical help while in Aberdeen and for the spectacular field trip to the Outer Hebrides and Skye, it was great to work with you. Paul and Ian, thanks for passing on some of your knowledge on Australian Geology.
- **The sponsors**: Thanks to the Australian Government for my IPRS scholarship, the Australian Research Council for research funding (ARC Discovery Grants DP0878258 and DP0897612) and Geoscience Australia and Ion Geophysical for access to seismic data. I would also like to especially thank PESA, Midland Valley and the AAPG Grants-in-aid Foundation for scholarships and grants that assisted my funding.

- **The S^3 research group (formally the stress group) at ASP:** Thanks to the members of our research group (especially Mark Tingay), for all the excellent discussions and support over the last three years.

- **My Friends:** I have met too many good friends to list here, but special thanks to the few fellow PhD students who have stuck it out with me: Dave, Abbas, Ernest and Ali. Also a special thanks to Maureen and Andy for all you're help and to Ian for help with all of my computer problems.

- **My Family:** Thanks to my parents, Denise and Terry, for the continual support over my 10 year academic career. To my in-laws, Kim and Peter, thank you kindly for all your support and encouragement over the last few years. Also thanks to my siblings, Jon, Joanne & Ingo, Jessica, Neal and T.C. for your support and visiting us in Australia. Finally, thanks to my wife Kelsey and baby Jack; this PhD is dedicated to you guys.

1. Contextual Statement

Large offshore delta—deepwater fold-thrust belts such as the Niger Delta and Baram Delta often exhibit gravitationally-driven extension on the delta top linked to compression in the delta toe (Yassir & Zerwer, 1997; Morley, 2003a; Corredor et al, 2005; King et al., 2009), where the system detaches above a ductile medium such as overpressured mud. In order for the system to slide basinward, primary overpressure from rapid burial of water logged marine mud (by a process known as disequilibrium compaction) must be created at the base of the detachment; this is often referred to as basal pore fluid pressure (Hubbert and Rubey, 1959; Davis, 1983; Swarbrick). Secondary overpressure generation mechanisms are also possible, and can account for significant changes in basal pore fluid pressure (Osborne and Swarbrick, 1998; Cobbold et al., 2009). Together, the basal pore fluid pressure, detachment medium, detachment thickness and the thickness and geometry of the overlying deltaic wedge all influence the structural style of the deltaic system, and can have significant influence on hydrocarbon trap formation, geometry and charge history, as well as subsequent fault reactivation and possible trap breach (Rowan et al., 2004; Morley et al., 2011). Understanding the detachment system and its influence on the structural style of associated deltas is essential for study of these systems, especially in relatively data poor areas such as the Ceduna Sub-basin, which hosts two juxtaposed, shale-rich, delta—deepwater fold-thrust belts.

The Ceduna Sub-basin delta—deepwater fold-thrust belts were first recognized and described following the acquisition of offshore 2D seismic reflection data in the 1970's (Bouef and Doust, 1975; Fraser and Tilbury, 1979). Over a decade later, several authors had focused on the geodynamic setting and stratigraphic nomenclature of the Ceduna Sub-basin and larger Bight Basin but little hydrocarbon exploration in the basin followed this work (Veevers and Eittreim,

1988; Willcox and Stagg, 1990; Hill, 1991). An initiative by Geoscience Australia to study the basin in detail in the late 1990's resulted in some ten years of continuous publications (starting with Totterdell et al., 2000) examining all facets of the hydrocarbon potential of the sub-basin. To date, only two wells have actually penetrated the Ceduna Sub-basin and the delta systems that are responsible for the geometry of the Ceduna Terrace, leaving many unanswered questions regarding the geometry of the delta, and how the two delta lobes influenced one another in terms of initial structural geometry and subsequent fault reactivation from loading.

Although an in-depth fault reactivation study had already been completed for the basin (Reynolds et al., 2003), due to limited data this was based solely on 2D maps of fault traces rather than actual fault geometry. Finally, the largest question that remained unanswered up to this point was the origin of these two delta systems. With limited to no data from offshore this has remained perhaps the most enigmatic part of the Ceduna Delta systems to date. This thesis applies a variety of techniques, such as seismic interpretation, geomechanical fault reactivation modelling, geochronology and thermochronology to examine:

- How the Critical Taper Wedge model may be used to aid in the understanding and prediction of basal pore fluid pressure distribution in present-day, active, delta detachments (paper 1);
- The Ceduna Delta systems, their structural interaction and how their detachment surfaces control their overall geometries (paper 2);
- The potential for fault reactivation in the Ceduna Sub-basin, and interaction of the two delta systems affects fault reactivation (paper 3);
- The sedimentary provenance of the Ceduna Delta systems (paper 4); and,

- A review of the regional structural controls on hydrocarbon prospectivity in the Ceduna Sub-basin (paper 5).

These five aims are discussed below with respect to the five papers presented herein, in order to give an account of the research progress achieved with each paper, and the linking of the papers. Further discussion of the thesis aims with respect to previous work, and an account of the previous work, is given in the literature review and the papers themselves.

1.1 New methodology for predicting basal pore fluid pressure in active delta—deepwater fold-thrust belt systems: a case study using the deepwater Niger Delta toe (Paper 1)

We apply the Critical Taper Wedge model to predict both the magnitude and spatial variation of basal pore fluid pressure along the detachment of the Niger Delta toe. Previous studies have used either a single or multiple widespread measurements of bathymetric slope dip angle and detachment dip angle for an entire wedge profile (Davis et al., 1983; Bilotti and Shaw, 2005; Suppe, 2007). In contrast, we have developed a workflow to measure the kilometer scale variation in these key parameters. Using the standard Critical Taper Wedge equation (Dahlen, 1990) we solve for basal pore fluid pressure using three variables: the bathymetric slope angle, the basal detachment angle and the vertical thickness between these measurements (i.e. wedge height) for different positions along the wedge (Fig. 1).

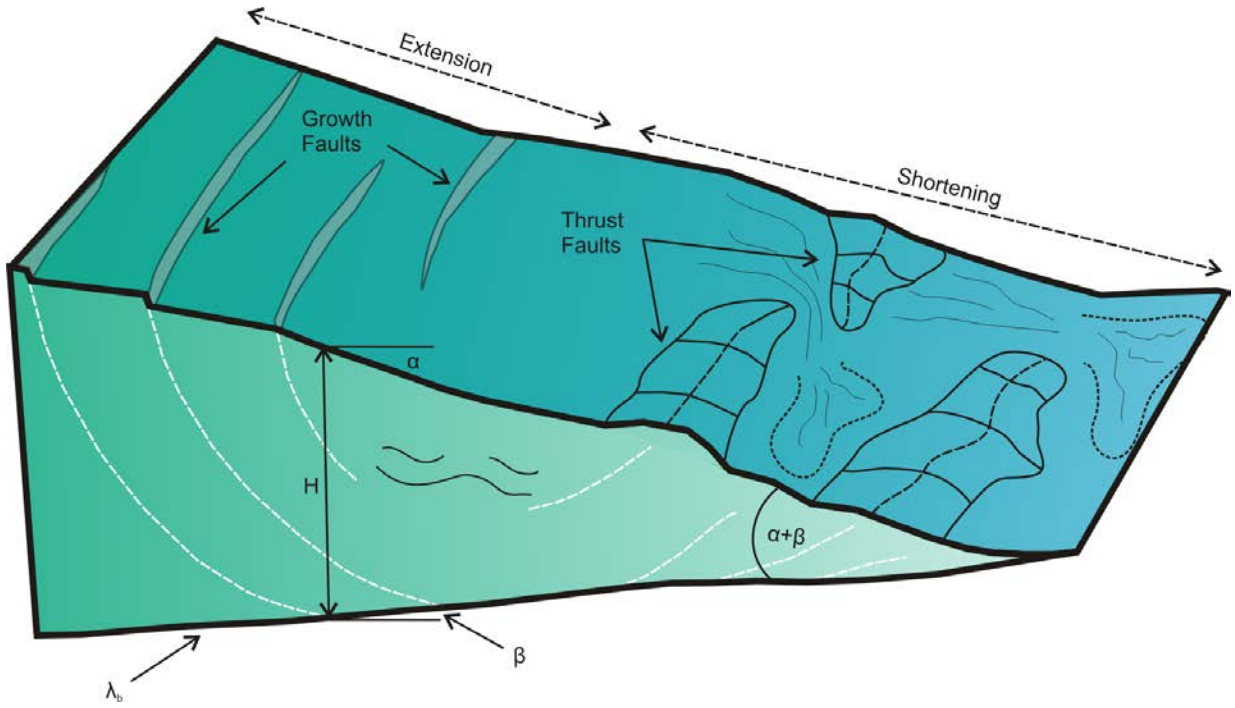

Figure 1*: A schematic of a critically tapered wedge (MacDonald et al., in review) showing positions of α, β and H.*

We present graphs of basal pore fluid pressure versus distance showing the predicted change along a measured seismic section, mapping the variation across a 560 km^2 area of the delta toe. Our model predictions show variations in basal pore fluid pressure (lambda b) along strike with magnitudes that range from ≈ 0.80 (sublithostatic) to 1.20 (supralithostatic). We also demonstrate that the Critical Taper Wedge equation is applicable to seaward-dipping detachments, or negative beta, which have not previously been considered. Variation in beta is a first order control on the magnitude of the basal pore fluid pressure, whereby negative beta lowers the wedge taper angle resulting in a thinner, stronger wedge that in turn requires a higher basal pore fluid pressure in order to slide. Our approach allows us to predict the magnitude of the basal pore fluid pressure and correlate this to the present-day structural geometry of the Niger

Delta Toe, at a much smaller scale than previously possible and thus has implications for structural style and pore pressure prediction.

Paper 1 sets the stage for and is fundamentally linked to paper 2 and 3 based on the similarity in these systems such as detachment medium, thickness of detachment and overpressure generating mechanisms required for gravity sliding of the deltaic wedge. Although the systems are not entirely similar, the Niger Delta forms the best modern-day analogue for the Cretaceous Ceduna Delta system, and in particularly the Cenomanian-age White Pointer delta.

1.2 Structural style of the Ceduna Sub-basin delta—deepwater fold-thrust belt systems offshore South Australia (Paper 2)

The White Pointer and Hammerhead delta—deepwater fold-thrust belt systems (DDWFTB) are structurally independent deltaic wedges of late Albian-Santonian and late Santonian-Maastrichtian age, respectively (Totterdell et al., 2000; Krassay and Totterdell, 2003). The White Pointer and Hammerhead DDWFTBs detach above Santonian-Albian marine shales of the Blue Whale and Tiger supersequences, respectively (Totterdell et al., 2000; Totterdell and Bradshaw, 2004). The DDWFTBs are constrained by the position of the delta lobes, with the Santonian-Maastrichtian lobe in the east and the Cenomanian lobe in the west, each of which is defined by the position of their associated (down-dip) fold-thrust belt. The geometry of the structures in the DDWFTBs are dependent on the interaction of numerous variables including sediment input, amount of progradation, shape and depth of the detachment, thickness and lithology of the detachment substrate, overpressure development and presence of basement rift-related structures. However, geometric differences between the two DDWFTBs are exist,

particularly in the two deepwater fold-thrust belts; resulting in different styles of deformation and differing geometries of potential hydrocarbon traps.

The White Pointer DDWFTB contains up to three levels of detachment, while the Hammerhead DDWFTB changes from a single level of detachment in the west to two in the east. Both DDWFTBs are composed of extensional, transitional and compressional provinces, whereby the extensional province is consistent with the delta top and the compressional province with the deepwater fold-thrust belt. The extensional provinces are characterised by regional listric, normal, growth faults and, rarely, counter-regional faults. The transitional provinces comprise large-scale (wavelength <15 km) detachment folds, minor thrust faults and chaotic folding of deltaic sediments where imaged. The compressional provinces are defined by imbricate thrust faults and associated folds of various geometries, spacing and scale. All structures in the DDWFTBs sole out or are rooted at or above the level of the basal detachment. Thus, deformation is constrained to within the deltaic wedges.

Deformation observed in these DDWFTBs has produced potential hydrocarbon traps that could form viable exploration targets in the future. The DDWFTBs from the Ceduna Sub-basin provide a good example of the style of tectonism associated with distal parts of marine deltas and is useful for the development of structural models that could be applied elsewhere.Paper 2 is the first regional interpretation of the Ceduna Sub-basin with a purely structural focus; aspects of this paper are closely related to each of papers 1, 3 and 4. The regional interpretation of the detachment surfaces, listric extensional faults, detachment fold provinces and toe thrust structures are stemmed from knowledge gained by studying the Niger Delta system through background research done for preparation of paper 1. The regional interpretation and delta model proposed in this paper was a strong starting foundation for the more detailed investigation of the

extensional faults, and their interaction and reactivation, between the two delta systems in paper 3. Finally, this paper sparked the interest to investigate if there was a change in depositional mechanisms in the Late Cretaceous to produce the strikingly different delta lobe geometries we observe today. With these criteria for a model in mind, it was possible to unravel the origin of the sediments forming the younger delta lobe, and speculate on the origin of sediments forming the older Cenomanian delta lobe in paper 4.

1.3 Geomechanical modelling of fault reactivation in the Ceduna Sub-basin, Bight Basin, Australia (Paper 3)

The present-day normal fault stress regime identified in the Bight Basin indicates that the maximum horizontal stress (S_{Hmax}) is oriented margin parallel (Reynolds et al., 2003); Therefore, Andersonian faulting theory implies that the margin-parallel striking delta-top extensional faults are oriented favourably for reactivation. A breached hydrocarbon trap encountered in the Jerboa-1 well is an example of this recent fault reactivation. Two pulses of inversion are identified in the Ceduna Sub-basin and correlate with the onset of rifting and fault reactivation in the Santonian. We propose a ridge-push driving force for this compressional stress, which selectively reactivates extensional faults on the delta top, forming inversion anticlines that are prospective for hydrocarbon exploration.

With the acquisition of the first 3D seismic reflection dataset in 2005 by Woodside, construction of a 3D model of the delta top extensional faults was allowed. This model was then used in a newly developed geomechanical boundary element code Poly3D©, allowing for the previously calculated in-situ stress tensor (from Reynolds et al., 2003) to be applied to the code for use with the new 3D fault model. This new approach to investigating the fault reactivation

potential in the Ceduna Sub-basin not only confirmed the predictions made by Reynolds et al. (2003), but also allowed for an increased understanding of which segments of the extensional faults were at risk of reactivation. A major result of this paper was that fault plane roughness, or rugosity, played a significant role in the susceptibility to reactivation under present day stress conditions. The study demonstrates that both synthetic and antithetic faults dipping between 40-70° show increased risk (medium to high) of reactivation. In addition, several examples of offset seabed topography are identified, supporting the fault reactivation predictions and indicating that faults are indeed active at present day. This will pose a risk to exploration initiatives in the Ceduna Sub-basin, and understanding fault geometry and reactivation potential should be a key component of any exploration program in this area. This paper includes new seismic reflection data that was not available when paper 2 was written, and allows for further subdivision of the delta systems, examining the role of existing extensional faults in the geometry of the younger Campanian-Maastrichtian (Hammerhead) delta.

1.4 A geochronological and thermochronological analysis of the Ceduna Sub-basin to constrain the origin and basin fill history of the Late Cretaceous Ceduna Delta System (Paper 4)

The Late Cretaceous Ceduna delta system offshore South Australia consists of two spatially and temporally separated deltaic lobes of Cenomanian and Santonian-Maastrichtian age. Together, they constitute the largest preserved deltaic system on the Australian continent, yet their source has never been identified, and the cause of the abrupt termination in the Maastrichtian is unknown. To determine the source of the younger delta lobe we analysed >780 detrital zircon grains from Late Cretaceous sedimentary rocks in Gnarlyknots-1A well. In the

Late Cretaceous, a major tectonic event occurred across southern Australia that triggered widespread exhumation and erosion (Gibson and Stuwe, 2000; Tingate et al., 2007; Tingate and Duddy, 2002). Detrital zircon and apatite fission track evidence show that the younger Santonian-Maastrichtian delta system was sourced largely from recycled Permian to Early Cretaceous cover and underlying basement eroded from an uplifted, arcuate shaped region of the South Australian margin, proximal to the basin. The system was eventually terminated by the latest Cretaceous due to diminishing sediment supply following erosional degradation of the uplifted landmass. This result challenges the widely accepted model that the delta is a product of a far-travelled river system originating from erosion of the Australian Eastern Highlands.

This paper relates to paper 2 and 3 as it steps back to examine the overall geometry of the basin fill, from the mid Cretaceous onward to the Cenozoic. With the two-delta model in mind, it was possible to suggest a model, supported by considerable data, which could explain the two different sources needed to produce the strikingly different delta lobes observed in the Ceduna Sub-basin. This paper also relates to paper 3 as it helps explain why the younger delta is so sand rich, being sourced from recycled sedimentary rocks onshore. This can affect fault gouge as high net-to-gross is unfavorable for fault seal and thus further increases the potential for breaching of fault-dependent traps.

1.5 Structure and Prospectivity of the Ceduna Delta—Deepwater Fold-Thrust Belt Systems, Bight Basin, Australia (Paper 5)

The change in structural style described in paper 2 and 3 is further described in paper 5, with the addition of the new BightSPAN© 2D seismic reflection data covering the DDWFTB systems. This new data set was used to further define the differences between the White Pointer

and Hammerhead DDWFTB systems, and to investigate the hydrocarbon prospectivity of the region. The seismic data images abundant volcanic intrusions in the western White Pointer DDWFTB which has significant effects on the prospectivity of this deepwater fold-thrust belt and further complicates the structure of this region. New delta-top targets are interpreted from 3D seismic reflection data, which is the first evidence of four-way closure on listric growth faults, inferring significant trapping potential in the Hammerhead supersequence. Finally, the prospectivity is largely dependent on Cretaceous generation of hydrocarbons as a significant Cenozoic burial is largely absent from the basin, thus Cenozoic generation is unlikely. This model is successfully demonstrated to produce hydrocarbons in the Gippsland and Otway basins, and possibly in the Duntroon and far eastern Ceduna Sub-basin where up to two kilometers of Cenozoic burial is suggested to drive recent generation and migration of hydrocarbons. This paper is a review of papers 2, 3 and 4 and was an invited paper for the upcoming Gulf Coast Section Society for Sedimentary Geology (GCSSEPM) Bob F. Perkins Research Conference in December 2012 on hydrocarbon potential of frontier continental margins of the world. This paper also integrates the results of paper 4 with the structural geometry and hydrocarbon prospectivity in the Ceduna Sub-basin.

2. Literature Review

The following literature review provides an overview of the regional geology of the Bight Basin, which is located along the southern margin of Australia. The first part of this literature review is focused on the Ceduna Sub-basin, located within the larger Bight Basin, directly offshore South Australia where the study area is located. The Ceduna Sub-basin contains two DDWFTBs, is Late Cretaceous in age and assumed relatively tectonically inactive at present day. Therefore, we must first place these systems into context with respect to other modern-day analogues, which are data rich and widely studied (e.g. Niger, GoM, etc).

The second part of this literature review examines several DDWFTB systems from around the world that are tectonically active at present day, and which are referred to in the individual publications in this thesis. This essential background will provide the reader with the global context needed to understand the 'grassroots' nature of the Ceduna Sub-basin, which is essentially unexplored and poorly constrained. This literature review will set the stage for the thesis, which examines both regional-scale issues such as the delta sources and tectonic styles, and local-scale issues such as fault reactivation potential.

a. Regional Geology of the Bight Basin, Australia with emphasis on the Ceduna Sub-basin Delta—Deepwater Fold-Thrust Belts

Introduction

The Bight Basin is located in the centre of the southern margin of Australia and is host to a number of sub-basins, the largest of which is the Ceduna Sub-basin, a significantly

underexplored prospective hydrocarbon province (Fig. 2). The Ceduna Sub-basin covers an area of approximately 90,000 km^2 and is composed of Middle Jurassic to Cenozoic sedimentary rocks that exceed 12 km in thickness in places (Fig. 3), and are located in water depths ranging from 200 to >4000 m (Struckmeyer et al., 2001; Krassay and Totterdell, 2003). The southern margin of Australia, between Kangaroo Island and Cape Leeuwin (Western Australia), exceeds 3000 km in length but hosts only twelve exploration wells. Two of these wells have been drilled in the Ceduna Sub-basin and indications of past hydrocarbon accumulation were observed in Jerboa-1 well (Totterdell et al., 2000; Struckmeyer et al., 2001; Somerville, 2001).

Figure 2*: Location map showing the position of the Ceduna Sub-basin within the Bight Basin on the southern Australian margin and locations of the Jerboa-1, Potoroo-1 and Gnarlyknots-1A wells (from Totterdell and Bradshaw, 2004).*

Previous work completed by Geoscience Australia in 1999-2008 and Woodside Energy Limited in 2000-2005 resulted in an improved understanding of the hydrocarbon prospectivity of

the Bight Basin, particularly the Ceduna Sub-basin. This work focused on the sequence stratigraphy, tectonics and petroleum systems of the sub-basin and aimed to identify probable organic-rich supersequences, understand the regional maturity of these rocks and identify suitable traps and seals for hydrocarbon accumulation (Blevin et al., 2000; Totterdell et al., 2000; Somerville, 2001; Ruble et al., 2001; Struckmeyer et al., 2001; Sayers et al., 2001; Struckmeyer et al., 2002; Krassay and Totterdell, 2003; Totterdell and Krassay, 2003; Totterdell and Bradshaw, 2004; King and Mee, 2004; Tapley et al., 2005; Totterdell et al., 2008).

***Figure 3**: Litho vs. Chrono-stratigraphic framework of the Bight Basin showing age, lithostratigraphic formation names, chronostratigraphic supersequence names, basin phases and sea level curve (after Totterdell et al., 2000).*

The Ceduna Sub-basin contains two spatially and temporally separate Late Cretaceous delta—deepwater fold-thrust belt (DDWFTB) systems; the late Albian-Cenomanian White Pointer DDWFTB and the late Santonian-Maastrichtian Hammerhead DDWFTB. These systems detach above the mud-rich Albian Blue Whale and Turonian-Santonian Tiger supersequences, respectively. These DDWFTBs vary in both size and geometry, but both contain a number of prospective hydrocarbon traps whose geometries are controlled by the lithology and thickness of the underlying detachments. These two Cretaceous DDWFTBs are the focal point for the following literature review, particularly their structural geometries and the nature of their associated detachments.

Regional Tectonics

The southern margin of Australia was originally considered to be a simple passive margin system that formed during the breakup of Gondwana (Willcox and Stagg, 1990). A detachment model has been proposed for the separation of Antarctica and Australia, whereby the lower Australian plate was pulled out from beneath the upper Antarctic plate along a NW-SE direction (Fig. 4; Espurt et al., 2009; Totterdell and Bradshaw, 2004; Brown et al., 2001; Willcox and Stagg, 1990). Early models for the lithospheric extension suggested an azimuth orthogonal to the regional trend of the rift (Mutter et al., 1985; Willcox et al., 1987; Veevers and Eittreim, 1988); although this is now widely accepted as being oblique to the trend of the rift with a sinistral transtensional couple (Fig. 5; Norvick and Smith, 2001; Stagg et al., 1990).

The breakup of eastern Gondwana resulted in a triple junction between India, Australia and Antarctica, with the Australian-Antarctic rift stalling soon after commencement in the Middle-Late Jurassic (Totterdell and Bradshaw, 2004). This stalled rift was later followed by an

onset of spreading in the late Santonian (Tikku and Cande, 1999) or early Campanian at ~83 Ma (Sayers et al., 2001). These rifting events resulted in the formation of a series of extensional basins from the Cretaceous onward, namely the Eyre Sub-basin, Great Australian Bight Basin, Duntroon Basin and the Otway Basin. These basins were considered to be underlain by Early Cretaceous intra-rift sediments, overlying the basement complexes of the Precambrian Albany-Fraser Province and Gawler Block in the Great Australian Bight, and Paleozoic metasediments of the Tasman Orogen in the Tasmanian region (Willcox and Stagg, 1990).

Figure 4*: Possible conceptual scenario for the Australian-Antarctic continental passive margins evolution based on paleo-Alps margin geometries. (a): Oceanic present-day state with strongly asymmetrical shape of the Australian and Antarctic conjugate margins.COT: Continent-Ocean Transition zone. (b): Before the Late Santonian breakup event, a simple shear mechanism results in the development of a low-angle detachment fault (D0 modelled). The top-to-the-south sense of displacement accommodates exhumation of the continental mantle ahead the southern Australian*

margin. The continental crust is highly stretched with formation of a crustal klippe (after Espurt et al., 2009).

***Figure 5**: Plate tectonic reconstructions for the Australian-Antarctic conjugate margin; red polygon indicates position of Ceduna Delta system (after Norvick and Smith, 2001).*

Tectono-stratigraphic Framework of the Bight Basin

The Mesozoic Bight Basin is located in the Great Australian Bight and underlies a broad bathymetric terrace (Ceduna Terrace) forming the continental slope and rise in southern Australia (Totterdell et al., 2000). The basin formed during a period of extension and passive margin evolution and is bound to the north by basement composed of Proterozoic and older

terranes and to the east the basin overlaps the Proterozoic basement rocks of the Gawler Craton (Krassay and Toterdell, 2003). The Eyre Sub-basin defines the western limit while the Duntroon Basin forms the southeast boundary and to the south it tapers out onto the thin oceanic crust of the South Australian Abyssal Plain (Fraser and Tilbury, 1979; Bein and Taylor, 1981; Willcox and Stagg, 1990; Hill, 1995; Norvick and Smith, 2001; Totterdell and Krassay, 2003). Late Cretaceous break-up resulted in the separation of the Bight Basin into three structurally controlled sub-basins; the Eyre, Ceduna and Recherche, of which the Ceduna Sub-basin is the largest depocentre (Totterdell et al., 2000; Krassay and Toterdell, 2003; Fig.2). The sub-basins are separated by northwest striking accommodation zones, which were formed by rifting and crustal thinning of the Australian Plate; thus, creating a series of depocentres (Stagg et al, 1990; Wilcox and Stagg, 1990; Totterdell et al, 2000).

The Ceduna Sub-basin stratigraphy is divided into ten supersequences which relate to four distinct basin phases first identified by Totterdell et al. (2000) (Fig. 3). Basin Phase 1 marks the onset of sedimentation in the basin during the Middle-Late Jurassic extension with the contemporaneous formation of a series of extensional and transtensional half-graben structures. Pre-existing basement trends appear to have focused the deformation during this phase (Totterdell et al., 2000). Basin Phase 2 records the slow thermal subsidence during the Early Cretaceous, which ended abruptly with the onset of rapid subsidence during the late Albian (Basin Phase 3) (Totterdell et al., 2000). Basin Phase 3 ended with the start of sea-floor spreading, which caused the breakup of Australia and Antarctica in the late Santonian (Fig. 5). This continental breakup was followed by Basin Phase 4; a period of thermal subsidence, which marked the initiation of the late Santonian south Australian passive margin (Totterdell and Krassay, 2003).

The ten supersequences are constrained by the four Basin Phases and are systematically defined in Totterdell et al. (2000), where the new nomenclature for the Bight Basin sequence stratigraphy is first presented (Fig. 3). The supersequences that are of particular importance to this study are the stratigraphic units with known potential for hydrocarbon generation (Blevin et al., 2000; Totterdell et al., 2008). At the margin of the Bight Basin these include the Late Jurassic to Early Cretaceous Sea Lion and Minke supersequences, the Early Cretaceous Southern Right, Bronze Whaler and Blue Whale supersequences, and the Late Cretaceous White Pointer, Tiger and Hammerhead supersequences (Blevin et al, 2000). These supersequences have also been conceptually modelled for the distal parts of the Sub-basin with the uppermost Bronze Whaler, Blue Whale, White Pointer and Tiger supersequences containing the most prospective source rocks (Blevin et al., 2000). Dredging by Geoscience Australia in 2007 in the Bight Basin found that late Cenomanian–early Turonian rocks (White Pointer and Tiger supersequences) have high organic carbon content (2.1–6.2% total organic carbon [TOC]), and the potential to generate liquid hydrocarbons (hydrocarbon index (HI) values ranging from 274 to 479 mg hydrocarbons/gTOC) (Totterdell et al., 2008).

The relevant supersequence lithology descriptions below are based on the work of Totterdell et al. (2000), who used well data from the Bight and Duntroon basins. Early stratigraphic work was established prior to this using a lithostratigraphic (formation-based) focus rather than chronostratigraphic (e.g. Fraser and Tilbury, 1979; Stagg et al., 1990; Hill, 1991; Smith and Donaldson, 1995; Fig. 3). This did not allow for major basin fill events to be extrapolated across the sub-basins (Totterdell et al., 2000). The oldest unit of relevance to this study is the Valanginian to middle Albian Bronze Whaler supersequence. This is largely composed of an aggradational succession of fluvial and lacustrine sandstone and mudstone with

intermittent marine influence. Above this, the middle Albian-Cenomanian Blue Whale supersequence records the first major marine flooding event with the deposition of restricted marine siltstones nearest the palaeo-shelf and a thick package of marine mudstones in the basin. This package of marine mudstone forms the detachment for the above Cenomanian White Pointer DDWFTB, which is composed of the White Pointer supersequence. Deposition of the aggradational White Pointer supersequence led to overpressure in the underlying ductile marine mudstone enabling gravity-driven deformation, which resulted in the formation of the DDWFTB; where growth faults and toe thrusts sole out or are rooted in the Blue Whale mudstone (Fig. 6A, B). The White Pointer supersequence is composed primarily of fluvial to lagoonal siltstone and mudstone intercalated with minor sandstone and coal units. An angular unconformity within the White Pointer supersequence is thought to be related to cessation of growth fault activity, whereby a package of reflections that diverge towards the bounding faults from an overlying flat-lying unit suggest cessation of movement on growth faults (Totterdell et al., 2000). Cessation of faulting was likely due to dewatering of the underlying shale resulting in a loss of overpressure (Totterdell et al., 2000; Totterdell and Krassay, 2003). Subsequently, all gravity-driven deformation ceased.

A)

B)

C)

D)

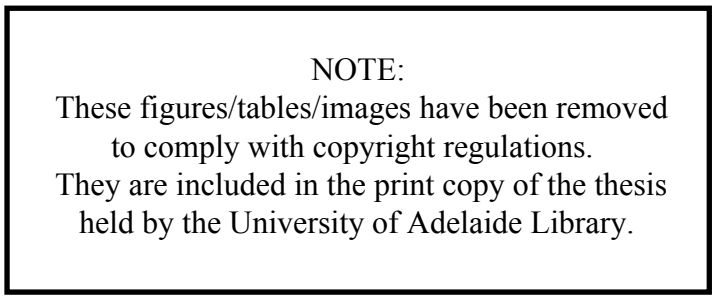

***Figure 6**: Regional basin map (A) with three regional seismic profiles (B, C, D) showing geometry of White Pointer DDWFTB system (blue-orange) and Hammerhead DDWFTB system (green) with extensional province to north and compressional province to south. White Pointer system displays up-dip extension in the western part of the basin (B) with linked down-dip compression while Hammerhead system displays up-dip extension in central and eastern part of basin (C) with down-dip compression. On the far eastern side of the basin neither system has preserved down-dip compressional province (D). Basal detachment surfaces are located at the*

base of the Blue Whale supersequence (Blue) for the White Pointer system and at the base of the Tiger supersequence (purple) for the Hammerhead system (after Totterdell and Bradshaw, 2004).

Overlying the White Pointer DDWFTB is the Turonian-Santonian Tiger supersequence, which consists of an aggradational package of what is suggested to be marine shale based on seismic stratigraphy and extrapolation of well data from Potoroo-1 well in the northern Ceduna Sub-basin (Totterdell et al, 2000). The unit is heavily faulted in the Ceduna Sub-basin, which is a result of reactivation of older faults (Mulgara Fault Family) controlled by the underlying ductile shale system of the Blue Whale supersequence. The timing of this fault reactivation is well constrained to the late Santonian because this faulting had ceased before deposition of the overlying Hammerhead supersequence which detaches at the base of and within the Tiger supersequence (Fig. 6C, D).

The 110,000 km^2 Santonian-Maastrichtian Hammerhead supersequence has an overall progradational to aggradational character and is composed almost entirely of sandstone nearest the present-day shelf in the Ceduna Sub-basin. Three major successions have been deduced from seismic imagery, with the lowermost and middle identified as progradational and the uppermost as aggradational. The lowermost two sequences of the Hammerhead supersequence display evidence on seismic profiles for a basinward change to a more shale-rich system (e.g. lack of strong stratal geometries observed on the shelf, more homogeneous seismic character). The 19 My progradation of the Hammerhead DDWFTB across the palaeo-shelf resulted in the initiation of gravity-driven deformation with the top of the Tiger supersequence forming the detachment surface (Figs. 6C, 7). The palaeo-shelf margin is where gravitational tectonics initiated because the Hammerhead supersequence is thickest (~ 5000 m at this location; Totterdell and Krassay, 2003; Fig. 6). The Hammerhead supersequence is overlain by the Paleocene-early Eocene Wobbegong supersequence, which consists of marginal marine-to-deltaic sandstone and

siltstone, which was deposited on a hiatus that is believed to represent 5-7 million years. Above this, the Middle Eocene to Pleistocene Dugong supersequence is present consisting of a basal coarse sandstone and thick uniform carbonate succession. These supersequences represent the development of a stable carbonate shelf.

Figure 7*: Seismic profile 199-07 of Hammerhead DDWFTB with well-developed extensional, transitional and compressional provinces. Basal detachment within the Tiger supersequence (green) has a seaward dip in the western extent of the deepwater fold-thrust belt (after Totterdell and Bradshaw, 2004).*

Structural Framework of the Ceduna Sub-basin

The Ceduna Sub-basin contains two Cretaceous DDWFTBs, the late Albian-Cenomanian White Pointer and the late Santonian-Maastrichtian Hammerhead (Fig. 6A-D). The geometry of the Ceduna DDWFTBs was first recognized by Boeuf and Doust (1975) and Fraser and Tilbury (1979) and have since been investigated by several authors including Totterdell and Krassay

(2003), Totterdell and Bradshaw (2004), Espurt et al. (2009) and King and Becké (2010). The Ceduna Sub-basin provides a unique opportunity to study two separate DDWFTB systems that are independent in size, shape and structural geometry. Both DDWFTBs exhibit well-developed gravity-driven deformation structures making them analogous to other delta systems around the world. Of particular interest to this study are the deepwater fold-thrust belts that form the down-dip compressional provinces of the White Pointer and Hammerhead DDWFTBs. This structural interpretation of the White Pointer and Hammerhead DDWFTBs is based on time-migrated 2D seismic reflection data made available by Geoscience Australia. The White Pointer and Hammerhead deepwater fold-thrust belts are discontinuous along strike; the White Pointer is located to the northwest while the Hammerhead is located to the southeast (Figs. 6, 8).

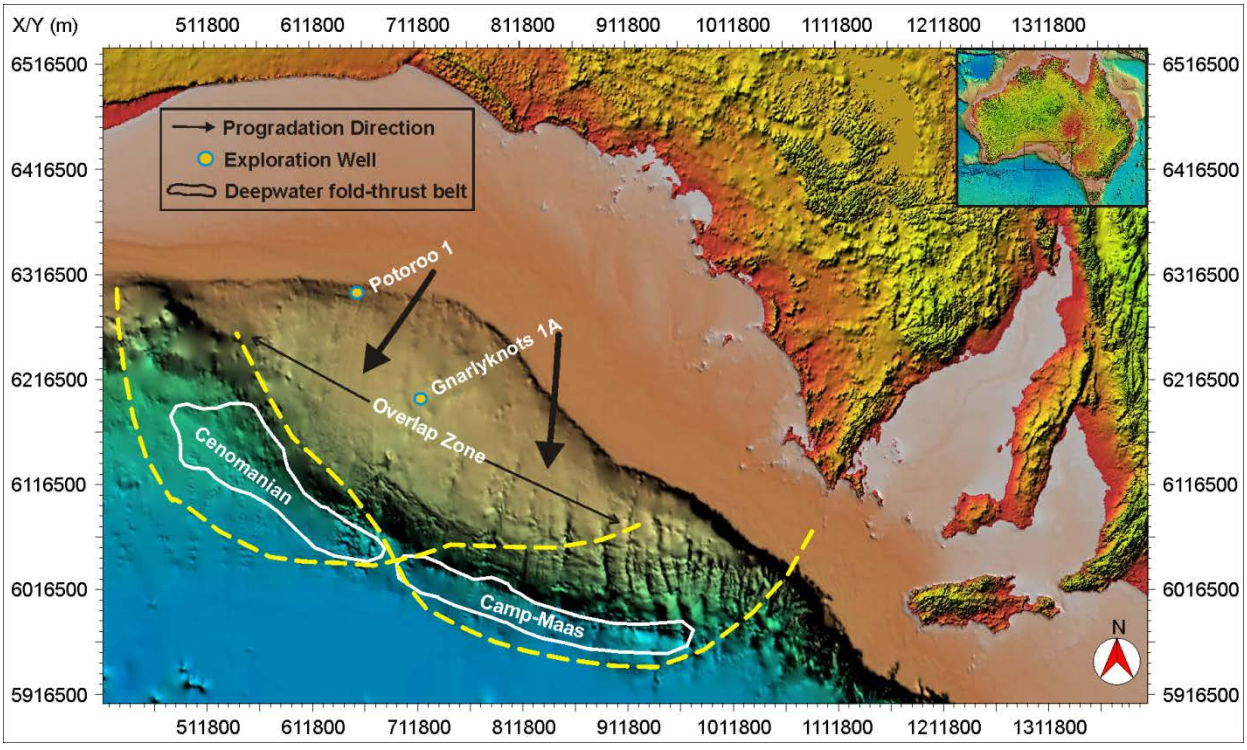

***Figure 8**: Digital elevation model of Ceduna Sub-basin showing the locations of the White Pointer (Cenomanian) deepwater fold-thrust belt to the west from the Hammerhead (Campanian-Maastrichtian) deepwater fold-thrust belt to the east; yellow lines represent*

approximate delta lobe positions and white lines outline each delta-toe (after MacDonald et al., 2012).

Fault Reactivation Potential in the Ceduna Delta

The in-situ stress field for the Bight Basin has been evaluated by Reynolds et al. (2003) and the following description of techniques is derived from this work. Determination of the in-situ stress field was completed by analysing drilling and log data from nine petroleum wells in the Bight Basin, and the interpolation of data from the wider Australian Stress Map database (Reynolds et al., 2003). The FAST (Fault Analysis Seal Technology) technique was applied to determine the fault reactivation risk using the stress tensor (3D Mohr circle) and fault-rock strength (failure envelope). A composite Griffith-Coulomb failure envelope was assumed in the study; and, because no fault rock failure envelopes were available for the area, a cohesive strength of 5 MPa and a friction angle of 0.6 were also assumed (Reynolds et al., 2003). Brittle failure is predicted by the FAST technique if the Mohr circle touches the failure envelope. All fault orientations plot within the Mohr circle and those closest to the failure envelope are at the highest risk of reactivation (Reynolds et al., 2003). The horizontal distance between the fault orientations on the Mohr circle and the failure envelope indicate the required pore pressure increase (ΔP) needed to induce failure. The smaller the ΔP value the higher the risk of reactivation. The ΔP values are observed for all fault planes that are plotted on the stereonets as poles to planes and reactivation risk can be assessed using these diagrams.

A total of three scenarios were identified based on different stress regimes; where case 1 is a strike-slip fault stress regime, case 2 is a borderline strike-slip fault to normal fault stress regime and case 3 is a normal fault stress regime (Reynolds et al., 2003). Case 1 displayed the most variation in ΔP values ranging from 2.0-20.0 MPa required for reactivation (low to high

reactivation potential), while case 2 and 3 displayed a range of 5.8-10.0 MPa (moderate reactivation potential). In-situ stress magnitudes calculated for the Bight Basin indicate the area is currently under a borderline strike-slip fault to normal fault stress regime (case 1; Reynolds et al., 2003).

The in-situ stress field analyses of Reynolds et al. (2003) demonstrated that faults striking 040 (± 15°) with any dip value are least likely to be reactivated, while vertical faults striking 100 and 160 are most likely to be reactivated. Thrust faults strike 308° and 290° in the White Pointer and Hammerhead deepwater fold-thrust belts, while listric, normal, growth faults strike 128° and 110°, respectively. Assuming all faults in the deepwater fold-thrust belts have the typical geometry of a thrust fault, with dips ranging between 0-35°, and that there are no lateral or oblique ramps, the ΔP values (~6-10 MPa) infer that all the NW-SE striking faults in the deepwater fold-thrust belt are at moderate to low reactivation potential. The NW-SE striking listric, normal, growth faults located in the extensional provinces of both the White Pointer and Hammerhead DDWFTBs have high reactivation potential (~2-4 MPa) based on a minimum 40° dip value.

In terms of regional seals for hydrocarbon traps, a number of candidate stratigraphic units have been considered. For the White Pointer supersequence, the overlying Tiger supersequence is a possible regional seal, while the deltaic sediments themselves are composed of interbedded sands and shales allowing for intra-stratal shales to form seals as they become more common in the distal basin. This is supported by the multiple detachment horizons, which develop in the more distal parts of the basin; as well as sequence stratigraphic work by Totterdell et al. (2000). The Hammerhead DDWFTB is likely restricted to intra-formational sealing units, particularly as

the supersequence becomes more shale-prone toward the basin (Blevin et al., 2000; Totterdell et al., 2000).

Understanding fault reactivation potential in the Bight Basin is a critical tool for predicting seal breach. While there are numerous potential sealing mechanisms in the Ceduna Sub-basin studies of fault reactivation (i.e. Reynolds et al., 2003) demonstrate that seals in the extensional provinces of the White Pointer and Hammerhead DDWFTBs are at high risk of breach, whereas seals in the compressional provinces of the White Pointer and Hammerhead DDWFTBs are at low risk of breach. Potential fault reactivation and seal breach in the Ceduna Sub-basin has also been suggested based on results from airborne laser fluorescence detection and the presence of asphaltite strandings on the coast (Sommerville, 2001).

Part 2

2.2 Structural Geometry of Analogue Delta—Deepwater Fold-Thrust Belts

Introduction

The structural geometry of DDWFTBs has been widely studied where they form prolific hydrocarbon provinces such as the Niger (e.g. Doust and Omatsola, 1990; Morley and Guerin, 1996; Cohen and McClay, 1996) and Baram DDWFTBs (e.g. James, 1984; Koopman et al., 1996; Sandal, 1996; Schreurs, 1997; Van Rensbergen et al., 1999). Delta—deepwater fold-thrust belts typically form at continental margins where rapid progradation of deltaic sediments over salt or water-prone mud results in overpressure development (in water-prone mud) and deformation under gravitational forces (Morley, 2003a). The result is a broad segregation of the delta into extensional and compressional provinces, whereby margin-parallel gravitational extensional stresses on the delta top drive down-dip, margin-normal, compressional stresses in the deepwater fold-thrust belt (Yassir & Zerwer, 1997; Corredor et al, 2005; King et al., 2009). The delta-top is typically characterised by regional and counter-regional listric, normal, growth faults that sole out at the level of the underlying pro-delta sediments (salt or shale) (Morley and Guerin, 1996). These extensional structures are balanced by the deepwater fold-thrust belt, which is composed of imbricate thrust sheets and associated fault propagation folds rooted at the basal detachment (Morley and Guerin, 1996; McClay et al., 2003; King et al., 2009). The extensional and compressional provinces are commonly separated by a transitional province that is characterised by detachment folds and reactive, active and passive diapirs of shale or salt (Morley and Guerin, 1996).

The detachment horizons are dependent on the development and maintenance of overpressure, with rapid progradation of delta sediments over the water-prone mud or salt

contributing the initial overpressure due to disequilibrium compaction of the muds (Morley & Guerin, 1996; Cobbold et al., 2009; Morley et al., 2011). Overpressure is not required for salt as it is naturally weak and mobile; whereas shale requires overpressure to induce weakness and mobility (Morley & Guerin, 1996; Osborne and Swarbrick, 1997; Rowan et al., 2004; Morley et al., 2011). Subsequent inflationary overpressures can also develop, most often by dewatering during the smectite-illite transition and volume increase due to hydrocarbon generation; these serve to maintain overpressure (Morley and Guerin, 1996; Osborne and Swarbrick, 1997; Morley et al., 2011).Variations in sediment supply, detachment parameters such as lithology and thickness of the detachment horizon(s) and development of overpressure are some of the key factors that contribute to the varied structural styles observed in DDWFTBs worldwide.

Delta—deepwater fold-thrust belts often form excellent hydrocarbon provinces due to the generation of hydrocarbons from marine sediments and an abundance of trapping mechanisms in the deltaic sediments as a result of the gravity-driven deformation. There are numerous structures formed in these settings, many of which have excellent hydrocarbon trapping potential (Cobbold et al., 2009). For example, rollover anticlines and tilted fault blocks develop in the extensional province (Finkbeiner et al., 2001). Hangingwall and footwall folds developed due to thrust fault propagation in a deepwater fold-thrust belt also form excellent fault-independent and dependent traps (Cobbold et al., 2009). The imbricate thrusts can provide fluid pathways from the often hydrocarbon generating, detachment horizon into the overlying traps (Cobbold et al., 2009). Deepwater fold-thrust belts are proven hydrocarbon provinces worldwide, such as deepwater Nigeria (Briggs et al., 2006), deepwater NW Borneo (Tingay et al., 2009) and deepwater Gulf of Mexico (Rowan, 1997).

Niger Delta-Deepwater Fold-Thrust Belt System

The Niger Delta-deepwater fold-thrust belt (DDWFTB), located offshore Nigeria, is one of the world's most structurally complex DDWFTB systems (e.g. Doust and Omatsola, 1990; Morley and Guerin, 1996; Cohen and McClay, 1996; Bilotti and Shaw, 2005; Corredor et al., 2005; Briggs et al., 2006). The Niger DDWFTB is divided into two western and southern delta lobes, separated by the Charcot Fracture Zone, a basement high that is absent of diapir structures (Cobbold et al., 2009; Fig. 9). The unique system is characterized by an extensional province (which can be divided based on regional and counter-regional growth faults), an intermediate detachment fold/diapir province, a thrusted diapir province and an outer fold-thrust belt province (Morley and Guerin, 1996). Many of the unique structures observed in this DDWFTB can be attributed to the thick, overpressured pro-delta mud over which the deltaic sediments prograded (Morley and Guerin, 1996).

***Figure 9**: Sediment lobes and their outer thrust belts, offshore Niger Delta. Thickness (key at top right) is for total sediment cover. High oceanic basement of Charcot fracture zone separates southern and western lobes. Each has an outer thrust belt, consisting of between 10 and 25 anticlinal fold hinges (thin black lines). In the western lobe, transfer zones (dashed lines), parallel to oceanic fracture zones, separate domains in which structures are continuous along strike. Deep-water discovery wells (white circles) are mainly in the southern lobe, and only three are in outer thrust belts and all sites pertain to original article (after Cobbold et al., 2009).*

Stratigraphy of the Niger DDWFTB

The Niger DDWFTB is characterized by a thick (up to 6km) package of Eocene-Pliocene pro-delta mud, known as the Akata Formation, over which the Eocene-Quaternary Agbada Opuana and Benin Formations prograded forming the thick (~2.5km) package of deltaic sediments (Corredor et al., 2005; Fig. 10). Primary overpressure development in the Akata Formation, caused by gravitational loading, and secondary overpressure derived from hydrocarbon generation resulted in deformation of the overlying deltaic wedge with ongoing progradation (Morley and Guerin, 1996). The overlying deltaic sediments of the Agbada, Opuana and Benin Formations provide the reservoir units for the system while the interstratal clays, namely the Agbada, Buguma, Soku and Afam provide the seal mechanisms (Corredor et al., 2005). Hydrocarbon traps are typically controlled by the gravity-driven deformation which characterizes these systems (Morley and Guerin, 1996).

***Figure 10**: Schematic diagram of the regional stratigraphy of the Niger Delta and variable density seismic display of the main stratigraphic units in the outer fold and thrust belt and main reflectors, including (1) top of the Agbada Formation, (2) top of the Akata Formation, (3) mid-Akata reflection, (4) speculated top of the synrift clastic deposits, and (5) top of the oceanic crust. Main detachment levels are highlighted with red arrows (after Corredor et al., 2005).*

Structure of the Niger DDWFTB

The structural geometry of the Niger DDWFTB is influenced by a number of factors including the lithology and thickness of the substrate, geometry of detachment(s), angle and dip-direction of the base of the deltaic wedge (β), amount of overpressure, thickness of the deltaic

wedge, and local stress regime (Morley and Guerin, 1996; Stewart, 1996; McClay et al., 1998; Morley, 2003; McClay et al., 2003; Bilotti and Shaw, 2005). Due to the limited extent of this review, the author would like to note that the mechanism most likely responsible for the structural geometry of the Niger DDWFTB is the thick, overpressured, mobile Akata Formation (Morely and Guerin, 1996; McClay et al., 2003). The structural geometry can be divided into five provinces, which are characteristically different and all structures in the Niger DDWFTB can be classified into one of these structural provinces (Fig. 11).

Figure 11*: Uninterpreted and interpreted regional seismic profile across the Niger Delta showing the link between the extensional province on the shelf and the contraction in the toe-thrust systems in the deep water, as well as the main structural domains. Both regional and counter-regional normal faults are present in the extensional province. Slip on these faults soles onto one or a series of basal detachments and extends across a diapiric zone into the deep-water fold and thrust belts. The inner and outer fold and thrust belts are separated by a zone of little or*

no deformation. Along strike, this transitional zone is characterized by detachment folds. Seismic section is poststack migrated and depth converted (after Corredor et al., 2005).

The extensional province in the Niger DDWFTB can be subdivided into a regional and counter-regional regime, whereby margin parallel stresses result in formation of extensional faults that dip both landward and seaward and detach above a thick (~4-6km) detachment (Corredor et al., 2005). McClay et al. (1998) have indicated that in analogue models the formation of the first regional extensional fault with ongoing progradation is succeeded by a counter-regional fault, forming an active graben system. With ongoing extension, the margin parallel gravitational extensional stresses on the delta top drive down-dip margin normal compressional stresses in the transitional and compressional provinces when the substrate is mobile and overpressured (Morley and Guerin, 1996; McClay et al., 2003; King et al., 2009). On the seaward flank of the extensional province is the diapiric belt/province, characterized by active shale mobilization forming diapirs that are represented on seismic profiles by chaotic masses with down-building along the flanks and eventual ponded mini-basin formation between adjacent diapirs (Doust and Omastola, 1990; Cohen and McClay, 1996; Morley and Guerin, 1996; McClay et al., 1998; Morley, 2003; McClay et al., 2003; Corredor et al., 2005). Farther seaward, the formation of an inner fold-thrust belt province, characterized by steep thrust faults and accompanying shale diapirs in the footwall, is related to a change in dip of the basement at this location (Corredor et al., 2005).

The fourth major province in the Niger DDWFTB is the transitional province, which is represented by either detachment folds or minor deformation along strike of the DDWFTB (Morley and Guerin, 1996; Corredor et al., 2005). The last province is the outer fold-thrust belt

or compressional province, which is characterized by a series of hanging-wall anticlines and imbricate thrust faults that detach above thinner (~2km) Akata Formation.

The Baram Delta-Deepwater Fold-Thrust Belt System

The Baram DDWFTB is located offshore NW Borneo and consists of three Eocene to Recent delta systems that were deposited on an active margin (Sandal, 1996; Lambiase et al., 2002). The deltas were sourced and built out from the Crocker-Rajang Ranges, inland Borneo, onto the Setap Shale prodelta sediments (Hutchison, 2005; Fig. 12). The convergence of the South China Sea plate beneath NW Borneo resulted in the formation of an accretionary prism in the Crocker-Rajang Ranges, which was followed by subsequent uplift and reworking of the proximal Baram DDWFTB with continued pulses of subduction during the Miocene and Pliocene (Sandal 1996; Morley et al., 2003; Tingay et al., 2005; King et al., 2010a; 2010b). The extent of the present day gravitationally driven deformation observed in the Baram DDWFTB is an artifact of the thick, mobile Setap Shale over which the system is prograding (Morley et al., 2008; King et al., 2010a).

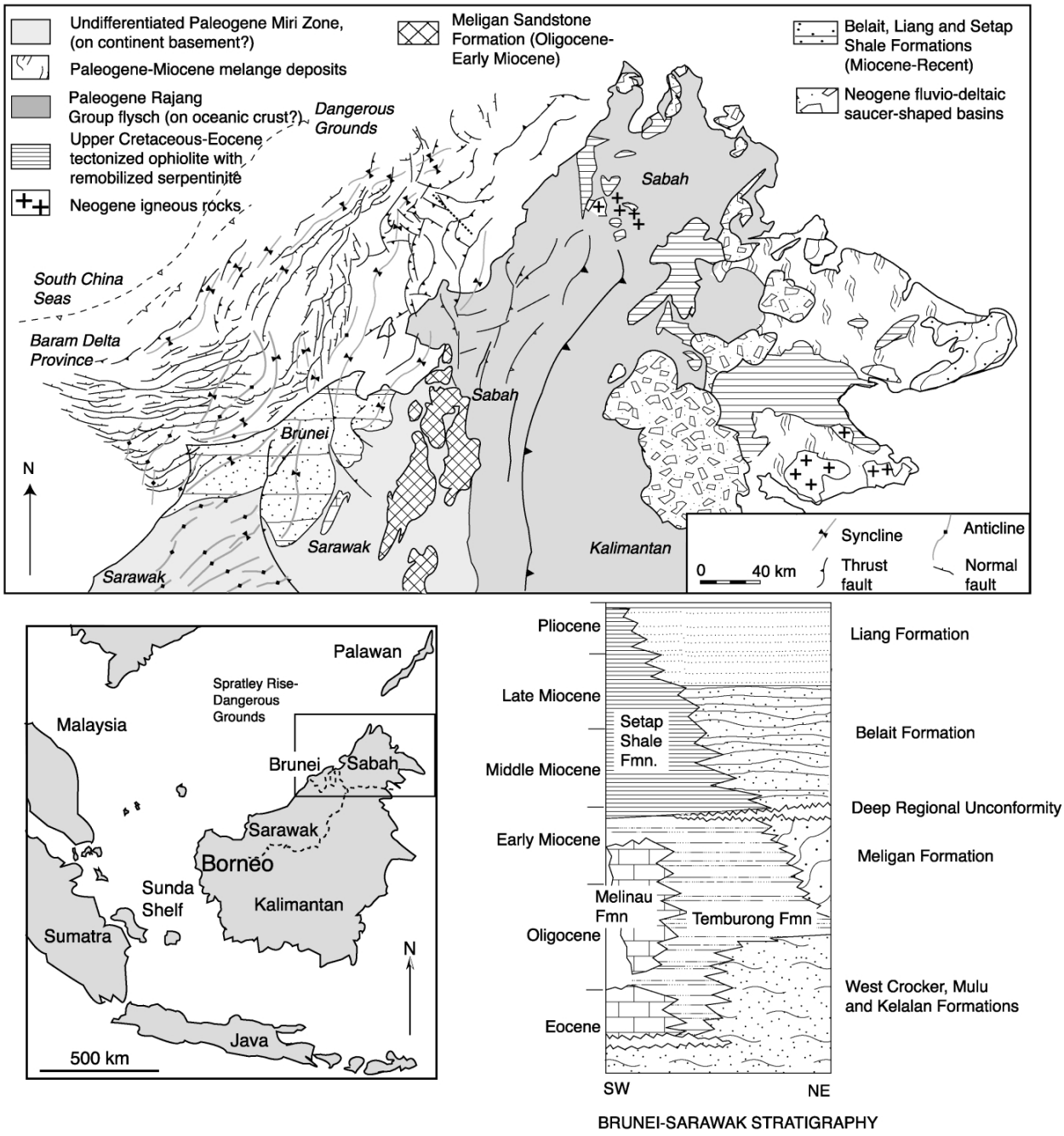

***Figure 12**: Regional geological map of Northern Borneo including stratigraphy (after Morley et al., 2003).*

Stratigraphy of the Baram DDWFTB

The Baram DDWFTB consists of a thick (10-12km) package of ~17 Ma to Recent clastic rocks and sediments derived from the Crocker-Rajang Ranges (Sandal, 1996). The Crocker-Rajang Rages are predominately Cretaceous-Paleogene deep marine shelfal deposits deformed in an accretionary prism setting (Morley et al., 2008; Fig. 12). This ~17 Ma to Recent sedimentary section is a first order prograding sequence comprised of shelfal deposits that overlie the shale-prone outer shelf-deepwater sequence, the Setap Shale Formation (Lambiase et al., 2002; Fig. 12). The main stratigraphic units in the DDWFTB are the cyclic sand-shale sequences of the Belait and Miri Formations (Mid-Late Miocene) and the Liang Formation (latest Miocene-Pliocene) (James, 1984; Sandal, 1996; Morley et al., 2008). As with many shale-prone DDWFTB systems, the Setap Shale is demonstrated to be overpressured (Tingay et al., 2009) thus resulting in shale diapirs and development of a deepwater fold-thrust belt at the delta-toe (Morley et al., 1998).

Structure of the Baram DDWFTB

During the Miocene and Pliocene pulses of contraction, the proximal part of the Baram Delta was uplifted and reworked (Morley et al., 2003, Tingay et al., 2003; Tingay et al., 2005). With this uplift event the original gravity-driven extensional growth faults nearest the present-day margin were inverted, resulting in a change in the stress configuration from margin parallel (palaeo-stress) to margin normal (Morley et al., 2003; Tingay et al., 2005; Morley et al., 2008; King et al., 2010b). Inversion in the proximal part of the Baram delta resulted in the formation of numerous anticlinal folds that form the most productive hydrocarbon play in the Baram Delta Province (Morley et al., 2008; Morley et al., 2011). However, at present-day the onshore and

inner shelf region demonstrates normal fault stress magnitudes, inferring that the inversion structures are no longer active, and thus, are potentially sealing fault systems (Tingay et al., 2009; King et al., 2010b; Morley et al., 2011). Figure 13 displays a seismic profile through the Baram Delta Province, with the inverted province represented by the Ampa Anticline, as well as the presence of the mobile Setap Shale Formation forming diapirs and pipes.

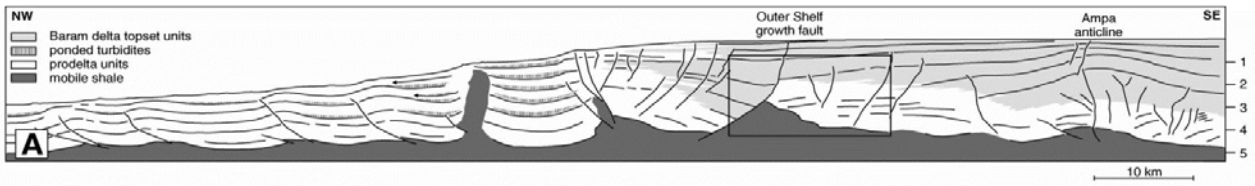

Figure 13*: Seismic profile across the Baram Delta Province showing the inverted province to the SE and the delta-toe to the NW (after Van Rensbergen and Morley, 2000).*

The Baram Delta Province is composed of several zones or provinces from onshore to offshore, each with different structural geometries. Zone 1 is composed of N-S trending folds and thrusts and is not affected by gravitational related normal faults or diapirs (Morley et al., 2008; Fig. 14). Zone 2 is the inverted province, which is composed of mixed anticlines striking N-S and NE-SW and growth faults striking NE-SW. Zone 3 is the current extensional province, which is dominated by regional growth faults and some minor shale mobilization (Morley et al., 2008; Fig. 13). Zone 4 represents the seaward extent of the system and is represented by a deepwater fold-thrust belt that is thought to have developed during the Miocene-Recent age (Ingram et al., 2004; Morley et al., 2008; King et al., 2010c). Majority of the structures listed above are all developed above a basal detachment zone within the overpressured Setap Shale Formation with the exception of the N-S inversion structures (Van Rensbergen and Morley, 2000; Morley et al., 2008).

***Figure 14**: Structural trends in offshore and onshore Brunei Darussalam. Offshore area is underlain by a time slice section through 3-D seismic at 1 s depth, two way travel time. Linear trends of reflections indicate the strike of bedding (after Morley et al., 2008).*

The Gulf of Mexico DDWFTB Systems

The Gulf of Mexico is located in the south-western United States and Eastern Mexico, bound on the east by Florida and the Caribbean Sea. In the west and north it is composed of several fold belts, namely the Mexican Ridges Fold Belt in the southwest, the Perdido Fold Belt in the northwest and the Mississippi Fan Fold Belt in the northeast, all of which are known hydrocarbon provinces (Trudgill et al., 1999; Fig. 15). The Gulf of Mexico is unique in that there

is an abundance of Jurassic salt above the rifted basement rocks, resulting in very complex structures throughout the northern fold belts (Rowan, 1997; Trudgill et al., 1999; Rowan et al., 2004). Unlike shale-prone systems, where overpressure is needed to trigger diapirism, salt is a viscous material with essentially no strength so only a thin overburden is required to initiate migration (Davis and Engelder, 1985; Rowan et al., 2004). This stratigraphic scenario is conducive to the formation of large scale (>100 km) fold and fold-thrust belts that are generated by gravitationally driven margin parallel forces on the shelf (Yassir and Zerwer, 1997; Rowan, 1997; Trudgill et al., 1999; Rowan et al., 2004; Trevino and Vendeville, 2008; King et al., 2009).

***Figure 15**: Regional map of northern Gulf of Mexico showing the three Cenozoic fold belts and extent of allochthonous salt. The location of the closest released deep borehole (Exxon "Diana" well) to the Perdido fold belt is shown, as are the DSDP holes 90 and 91 that provide well information for the shallow section in the deep Gulf of Mexico (after Trudgill et al., 1999).*

Stratigraphy of the Gulf of Mexico DDWFTB Systems

The stratigraphy varies from the western part to north-eastern parts of the Gulf of Mexico, which spans some >1000 km. However, a generalized stratigraphic column is presented in Figure 16 (after ref). Above the transitional crust of the basement lies the Mid-Jurassic Louann Salt, this is the main detachment level for gravitationally driven deformation that affects the

basin (Rowan, 1997; Trudgill et al., 1999). The Louann Salt is overlain by the Challenger and Campeche sequences, which are Late Jurassic and composed of carbonates, shales and chalks. This is overlain by the Tertiary Lower, Middle and Upper Mexican Ridges sequences, and eventually the ~5.5Ma to present-day Mississippi Fan sequence. The Lower and Middle Mexican Ridges sequences are composed of marls, chalk and shale while the Upper Mexican Ridges and Mississippi Fan sequences are dominantly deep-water turbidites (Rowan, 1997; Trudgill et al., 1999).

***Figure 16**: Stratigraphic column showing sequence names, known or inferred lithologies and interpreted seismic horizons with ages (after Trudgill et al., 1999).*

Structure of the Gulf of Mexico DDWFTB Systems

The northern Gulf of Mexico fold belts, the Perdido and Mississippi Fan, are controlled primarily by the presence of the autochthonous Louann Salt above the basement while the Mexican Ridges Fold Belt in the southwest is absent of salt and detaches above Cenozoic shale (Trudgill et al., 1999; Fig 17). The Perdido and Mississippi Fan fold belts are controlled by sediment loading above a highly mobile salt unit, which results in folding being the dominant deformation mechanism in the compressional province. Figure 18 is a cross section through the north-western Gulf of Mexico that shows the gravitationally-driven margin parallel extensional faulting on the shelf, which is linked to the down-slope margin normal compressional deformation in the Port Isabel Fold Belt (Yassir and Zerwer, 1997; Trudgill et al., 1999). Seaward of the Port Isabel Fold Belt, in the Perdido Fold Belt, the folds are typically detachment anticlines that are bound by steep reverse faults, typically cored with salt. These have been interpreted as accommodation structures rather than fault bend folds, driven by gravitational loading of the overburden on the mobile Louann Salt (Rowan, 1997; Trudgill et al., 1999). This system is unique in that a basement fault block separates the fold-thrust belt at the delta toe from the fold belt to the south. Thus, the structures observed in the Perdido fold belt are not a result of up-dip extension but solely gravitational loading on the mobile salt. This is one of the major differences between this system and the classic gravitationally-driven Baram and Niger Delta systems.

***Figure 17**: Schematic cross sections across the fold belts based on regional seismic data. The Mississippi Fan and Perdido fold belts are interpreted to detach on autochthonous salt, whereas the Mexican Ridges fold belt lies above a higher level shale detachment (after Trudgill et al., 1999).*

***Figure 18**: Regional cross section across the north-western Gulf of Mexico. This section shows the Perdido fold belt at the downdip limit of a complex, multilayered linked system comprised of extensional fault systems, salt canopies and welds, and contractional folds (after Trudgill et al., 1999).*

Conclusions

The three systems presented in this literature review are all delta—deepwater fold-thrust belts that exhibit different structural geometries, are deposited on active and passive continental margins, and are all prolific hydrocarbon provinces. In the broadest sense, all three systems detach above a mobile substrate and exhibit a shelf that is defined by a gravitationally-driven margin parallel stress regime, which is linked down-dip to a margin normal stress regime within the fold-thrust belt. Major differences include the thick mobile shale in the Niger, with two distinct fold-thrust belts and a shale diapir province, the inverted shelf of the Baram Delta with development on a once active margin, and the presence of a thick salt above the basement in the Gulf of Mexico (and abundant diapirs) which is responsible for the Perdido Fold Belt and Mississippi Fold Belt, and the associated complex salt structures within them. By studying these well-known data-rich systems worldwide, we can apply knowledge to data-poor regions, such as the Bight Basin, where these systems are relatively unexplored and yet have excellent hydrocarbon potential.

3. References

BEIN, J. AND TAYLOR, M.L., 1981—The Eyre Sub-basin: recent exploration results. The APEA Journal, 21, 91–98.

BLEVIN, J.E., TOTTERDELL, J.M., LOGAN, G.A., KENNARD, J.M., STRUCKMEYER, H.I.M. AND COLWELL, J.B., 2000— Hydrocarbon prospectivity of the Bight Basin—petroleum systems analysis in a frontier basin, In: 2nd Sprigg Symposium – Frontier Basins, Frontier Ideas, Adelaide, June 29-30th, 2000. Geological Society of Australia, Abstracts 60, 24–29.

BILOTTI, F. AND SHAW, J.H. 2005—Deep-water Niger Delta fold and thrust belt modelled as a critical-taper wedge: The influence of elevated basal fluid pressure on structural styles. American Association of Petroleum Geologists Bulletin, 89, 1475–1491.

BOUEF, M.G., AND DOUST, H., 1975—Structure and development of the southern margin of Australia. APEA Journal, 15, 33-43.

BRIGGS, S.E., DAVIES, R.J., CARTWRIGHT, J.A. AND MORGAN, R. 2006—Multiple detachment levels and their control on fold styles in the compressional domain of the deepwater west Niger Delta. Basin Research, 18, 435–450 DOI:10.1111/j.1365-2117.2006.00300.x.

BROWN, B.J., MÜLLER, R.D., AND STRUCKMEYER, H.I.M., 2001— Anomalous Tectonic Subsidence of the Southern Australian Passive Margin: Response to Cretaceous Dynamic Topography or Differential Lithospheric Stretching? PESA Eastern Australasian Basins Symposium, 563-569

BRUCE D. TRUDGILL, MARK G. ROWAN, J. CARL FIDUK, PAUL WEIMER, PETER E. GALE, BRYANT E. KORN, RONALD L. PHAIR, WILLIAM T. GAFFORD, GENEVA R. ROBERTS, AND STEVEN W. D, 1999—The Perdido Fold Belt, North-western Deep Gulf of Mexico, Part 1: Structural Geometry, Evolution and Regional Implications1 AAPG Bulletin, V. 83, No. 1, P. 88–113.

COBBOLD, P.R., CLARKE, B.J. AND LØSETH, H., 2009—Structural consequences of fluid overpressure and seepage forces in the outer thrust belt of the Niger Delta. Petroleum Geoscience, 15, 3–15 DOI 10.1144/1354-079309-784

COHEN, H.A. AND MCCLAY, K., 1996—Sedimentation and shale tectonics of the northwestern Niger Delta front. Marine and Petroleum Geology, 13, 313-328.

CORREDOR, F., SHAW, J. H., AND BILOTTI, F., 2005—Structural styles in the deep-water fold and thrust belts of the Niger Delta, American Association of Petroleum Geologists Bulletin, 89, 753–780.

DAVIS, D.M. & ENGELDER, T. 1985—The role of salt in fold-and-thrust belts. In: N.L. Carter and S. Uyeda (Eds.), Collision Tectonics: Deformation of Continental Lithosphere. Tectonophysics, 100:67-88.

DOUST, H. AND OMATSOLA, E., 1990—Niger Delta. In: Edwards, J.D. and Santogrossi, P.A. (Eds), Divergent/passive margin basins. American Association of Petroleum Geologists Memoir 48, 201–238.

ESPURT, N., CALLOT, J.-P., TOTTERDELL, J., STRUCKMEYER, H., AND VIALLY, R., 2009—Interactions between continental breakup dynamics and large-scale delta system evolution: Insights from the Cretaceous Ceduna delta system, Bight basin, Southern Australia margin. Tectonics, 28, TC6002, doi:10.1029/2009TC002447, 2009.

FINKBEINER, T., ZOBACK, M., FLEMINGS, P., AND STUMP, B., 2001—Stress, pore pressure, and dynamically constrained hydrocarbon columns in the South Eugene Island 330 field, northern Gulf of Mexico. American Association of Petroleum Geologists Bulletin, 85 (6), 1007–1031

FRASER, A.R. AND TILBURY, L.A., 1979—Structure and stratigraphy of the Ceduna Terrace region, Great Australian Bight. The APEA Journal, 19, 53–65.

HUTCHISON, C.S., 2005—Geology of North-West Borneo, Sarawak, Brunei and Sabah. Elsevier, London

INGRAM, G.M., CHISHOLM, T.J., GRANT, C.J., HEDLUND, C.A., STUART-SMITH, P., TEASDALE, J., 2004—Deepwater North West Borneo: hydrocarbon accumulation in an active fold and thrust belt. Mar. Pet. Geol. 21, 879–887

JAMES, 1984—The geology and hydrocarbon resources of Negara Brueni Dalussalam, Muzium Bmnei and Brunei Shell Petroleum Company Berhad Special Publication, 8, 2–21.

HILL, A.J., 1991—Revisions to the Cretaceous stratigraphic nomenclature of the Bight and Duntroon Basins, South Australia. Geological Survey of South Australia, Quarterly Notes, 120, 2–20.

HILL, A.J., 1995—Bight Basin. In: Drexel, J.F. and Preiss, W.V. (Eds), The geology of South Australia. Vol. 2, The Phanerozoic. South Australia, Geological Survey, Bulletin 54, 133–149.

KING, R.C. AND BACKÉ, G., 2011—A balanced 2D structural model of Hammerhead Delta—Deepwater Fold-Thrust Belt, Bight Basin, Australia. Australian Journal of Earth Sciences.

KING, R.C., TINGAY, M.R.P., HILLIS, R.R., MORLEY, C.K. & CLARK, J., 2010c—Present-day stress orientations and tectonic provinces of the NW Borneo Collisional Margin. Journal of Geophysical Research **115**, B10415.

KING, R.C.**,** HILLIS, R.R., TINGAY, M.R.P. & DAMIT, A.-R., 2010b—Present-day stresses in Brunei, NW Borneo: superposition of deltaic and active margin tectonics. Basin Research **22**, 236-247.

KING, R.C.**,** BACKÉ, G., MORLEY, C.K., HILLIS, R.R. & TINGAY, M.R.P., 2010a—Balancing deformation in NW Borneo: Quantifying plate-scale vs gravitational tectonics in a Delta and Deepwater Fold-Thrust Belt System. Marine and Petroleum Geology **27**, 238-246.

KING, R. C., HILLIS, R. R. AND TINGAY, M. R. P., 2009—Present-day stress and neotectonic provinces of the Baram Delta and deepwater fold-thrust belt. Journal of the Geological Society, London 166, 197-200.

KING, S.J. AND MEE, B.C., 2004—The seismic stratigraphy and petroleum potential of the Late Cretaceous Ceduna Delta, Ceduna Sub-basin, Great Australian Bight. *In*: Boult, P.J., Johns, D.R. and Lang, S.C. (Eds), Eastern Australasian Basins Symposium II. Petroleum Exploration Society of Australia, Special Publication, 63–73.

KOOPMAN, A., J. SCHREURS, AND D. W. ELLENOR., 1996—The oil and gas resources of Brunei Darussalam—the coastal and offshore oil and gas fields, In: S.T. Sandal, Editor, Geology and Hydrocarbon Resources of Negara Brunei Darussalam, Bandar Seri Begawan, Syabas, Chapter 5, 155–192.
KRASSAY, A.A. AND TOTTERDELL, J.M., 2003—Seismic stratigraphy of a large, Cretaceous shelf-margin delta complex, offshore southern Australia. American Association of Petroleum Geologists Bulletin, 87(6), 935–963.

LAMBIASE, J.J., RAHIM, A.A.A. &PENG, C.Y., 2002—Facies distribution and sedimentary processes on the modern Baram Delta: implications for the reservoir sandstones of NW Borneo. Mar. Petrol. Geol., 19, 69-78

MACDONALD, J., BACKÉ, G., KING, R., HOLFORD, S., AND HILLIS, R. 2012. Geomechanical modelling of fault reactivation in the Ceduna Sub-basin, Bight Basin, Australia, in Healy, D., Butler, R.W.H., Shipton, Z.K. and Sibson, R.H. eds., Faulting, Fracturing and Igneous Intrusion in the Earth's Crust. Geological Society, London, Special Publications, v. 367, p. 71-89.

MACDONALD, J.D., KING, R., HILLIS, R.R., AND BACKÉ, G., (2010): Structural style of the White Pointer and Hammerhead delta—deepwater fold-thrust belts, Bight Basin, Australia: Implications for hydrocarbon migration and accumulation. The APPEA Journal, v 50, xxx-xxx.

MCCLAY K. R., T. DOOLEY AND G. LEWIS, 2008—Analog modelling of progradational delta systems. Geology; September 1998; v. 26; no. 9; p. 771–774

MCCLAY, K., T. DOOLEY, AND G. ZAMORA., 2003—Analogue models of delta systems above ductile substrates, In: Van Rensbergen, P., Hillis, R.R.., Maltman, A.J. and Morley, C.K. (Eds), Subsurface sediment mobilization, Geological Society, London, Special Publications, 216, 411–428.

MORLEY, C.K., TINGAY, M., HILLIS, R., KING, R., 2008—Relationship between structural style, overpressures and modern tress, Baram Delta Province, NW Borneo.
J. Geophys. Res. 113, B09410. doi:10.1029/2007JB005324

MORLEY, C.K., 2003—Mobile shale related deformation in large deltas developed on passive and active margins. In: van Rensbergen, P., Hillis, R.R., Maltman, A.J. & Morley, C.K. (eds) Subsurface Sediment Mobilization. Geological Society, London, Special Publications, 216, 335–357.

MORLEY, C.K., BACK, S.,VAN RENSBERGEN, P., CREVELLO, P. & LAMBIASE, J.J., 2003—Characteristics of repeated, detached, Miocene^Pliocene tectonic inversion events, in a large delta province on an active margin, Brunei Darussalam, Borneo. J. Struct. Geol., 25, 1147-1169

MORLEY, C.K. AND GUERIN, G., 1996—Comparison of gravity-driven deformation styles and behaviour associated with mobile shales and salt. Tectonics, 15, 1154-1170.

MUTTER, J.C., HEGARTY, K.A., CANDE, SC. AND WEISSEL, J.K., 1985—Breakup between Australia and Antarctica: a brief review in light of new data. In: ES. Husebye, G.L. Johnson and Y. Kristoffersen (Editors), Geophysics of the Polar Regions. Tectonophysics, 114, 255-280.

NORVICK, M.S. AND SMITH, M.A., 2001—Mapping the plate tectonic reconstruction of southern and southeastern Australia and implications for petroleum systems. The APPEA Journal, 41, 15–35.

OSBORNE, M.J., AND SWARBRICK, R.E., 1998—Mechanisms for Generating Overpressure in Sedimentary Basins: A Reevaluation. American Association of Petroleum Geologists Bulletin, 81, (6), 1023–1041.

RAMO´ N H. TREVIN˜ O AND BRUNO C. VENDEVILLE, 2008—Origin of coast-perpendicular extensional faults, western Gulf of Mexico: The relationship between an early-stage ridge and a late-stage fault AAPG Bulletin, v. 92, no. 7 pp. 951–964

REYNOLDS, S., HILLIS, R., AND PARASCHIVOIU, E., 2003—In situ stress field, fault reactivation and seal integrity in the Bight Basin, South Australia. Exploration Geophysics, 34, 174-81.

ROWAN, M. G., 1997—Three-dimensional geometry andevolution of a segmented detachment fold, Mississippi Fan fold belt, Gulf of Mexico: Journal of Structural Geology, v. 19, p. 463-480.

ROWAN, M.G, PEEL, F.J., AND VENDEVILLE, B.C., 2004—Gravity-driven fold belts on passive margins. In: K.R. McClay, ed., Thrust tectonics and hydrocarbons systems: American Association of Petroleum Geologists Memoir, 82, 157-182.

RUBLE, T.E., LOGAN, G.A., BLEVIN, J.E., STRUCKMEYER, H.I.M., LIU, K., AHMED, M., EADINGTON, P.J. AND QUEZADA, R.A., 2001—Geochemistry and charge history of a

palaeo-oil column: Jerboa-1, Eyre Sub-basin, Great Australian Bight. In: Hill, K.C. and Bernecker, T. (eds), Eastern Australasian Basins Symposium. A Refocused Energy Perspective for the Future. Petroleum Exploration Society of Australia, Special Publication, 521-530.

SANDAL, S.T. 1996—The Geology and Hydrocarbon Resources of Negara Brunei Darussalam. Brunei Shell Petroleum Company Sendirian Berhad and BruneiMuseum, Syabas, Brunei

SANDAL, S.T., 1996—The Geology and Hydrocarbon Resources of Negara Brunei Darussalam. Brunei Shell Petroleum Company/Brunei Museum, Syabas Bandar Seri Begawan, Brunei Darussalam.

SAYERS, J., SYMONDS, P., DIREEN, N.G., AND BERNARDEL, G., 2001—Nature of the continent-ocean transition on the non-volcanic rifted margin of the central Great Australian Bight, in R. C. L. Wilson, R. B. Whitmarsh, B. Taylor, and N. Froitzheim, eds., Non-volcanic rifting of continental margins: a comparison of evidence from land and sea: Geological Society (London) Special Publication, 187, p. 51–76.

SCHREURS, G., 1997—The petroleum geology of Negara Brunei Darussalem; an update. In: Howes, J.V.C. and Noble, R. A. (eds) Proceedings of the IPA Petroleum Systems of SE Asia and Australasia Conference, Jakarta, Indonesia, May, 1997, Indonesian Petroleum Association, Jakarta, 751–766.

SMITH, M.A., AND DONALDSON, I.F., 1995—The hydrocarbon potential of the Duntroon Basin. The APEA Journal, 35, 203–219.

SOMERVILLE, R., 2001—The Ceduna Sub-basin – a snapshot of prospectivity. The APPEA Journal, 41, 321–346.

STAGG, H.M.V., COCKSHELL, C.D., WILLCOX, J.B., HILL, A.J., NEEDHAM, D.V.L., THOMAS, B., O'BRIEN, G.W. AND HOUGH, L.P., 1990—Basins of the Great Australian Bight region: geology and petroleum potential. Bureau of Mineral Resources, Australia, Continental Margins Program, Folio 5.

STEWART, S.A., 1996— Influence of detachment layer thickness on style of thin-skinned shortening. Journal of Structural Geology, 18 (10), 1271-74.

STRUCKMEYER, H.I.M., TOTTERDELL, J.M., BLEVIN, J.E., LOGAN, G.A., BOREHAM, C.J., DEIGHTON, I., KRASSAY, A.A. AND BRADSHAW, M.T., 2001—Character, maturity and distribution of potential Cretaceous oil source rocks in the Ceduna Sub-basin, Bight Basin, Great Australian Bight. In: Hill, K.C. and Bernecker, T. (Eds), Eastern Australasian Basin Symposium, a refocused energy perspective for the future. Petroleum Exploration Society of Australia, Special Publication, 543–552.

STRUCKMEYER, H.I.M., WILLIAMS, A.K., COWLEY, R., TOTTERDELL, J.M., LAWRENCE, G. AND O'BRIEN, G.W., 2002—Evaluation of hydrocarbon seepage in the Great Australian Bight. The APPEA Journal , 42, 371-385.

TAPLEY, D., MEE, B.C., KING, S.J., DAVIS, R.C. AND LEISCHNER, K.R., 2005—Petroleum potential of the Ceduna Sub-basin: impact of Gnarlyknots-1A. The APPEA Journal, 45, 365–380.

TIKKU, A.A. AND CANDE, S.C., 1999—The oldest magnetic anomalies in the Australian–Antarctic Basin: are they isochrons? Journal of Geophysical Research, B1, v. 104, 661–677.

TINGAY, M., HILLIS, R., MORLEY, C., KING, R., SWARBRICK, R., AND DAMIT, A., 2009—Present-day stress and neotectonics of Brunei: implications for petroleum exploration and production. American Association of Petroleum Geologists Bulletin, 93 (1), 75–100.

TINGAY, M.R.P., HILLIS, R.R., MORLEY, C.K., SWARBRICK, R.E. & DRAKE, S.J. 2005—Present-day stress orientation in Brunei:a snapshot of prograding tectonics in a Tertiary delta. J. Geol. Soc. Lond., 162, 39-49

TINGAY, M., HILLIS, R., MORLEY, C., SWARBRICK, R. & OKPERE, E. 2003a—Pore pressure-stress coupling in Brunei Darussalam— Implications for shale injection, in P. Van Rensbergen, R. Hillis, A. Maltman, and C. Morley, eds., Subsurface sediment mobilization: Geological Society (London) Special Publication 216, p. 369–379.

TOTTERDELL, J.M., BLEVIN, J.E., STRUCKMEYER, H.I.M., BRADSHAW, B.E., COLWELL, J.B. AND KENNARD, J.M., 2000—A new sequence framework for the Great Australian Bight: starting with a clean slate. The APPEA Journal, 40, 95–117.

TOTTERDELL, J.M. AND KRASSAY, A.A., 2003—The role of shale deformation and growth faulting in the Late Cretaceous evolution of the Bight Basin, offshore southern Australia. In: Van Rensbergen, P., Hillis, R.R.., Maltman, A.J. and Morley, C.K. (Eds), Subsurface sediment mobilisation. Geological Society of London, Special Publications 216, 429–442.

TOTTERDELL, J.M. AND BRADSHAW, B.E., 2004—The structural framework and tectonic evolution of the Bight Basin. In: Boult, P.J., Johns, D.R. & Lang, S.C. (Eds), Eastern Australasian Basins Symposium II. Petroleum Exploration Society of Australia, Special Publication, 41-61.

TOTTERDELL, J.M., STRUCKMEYER, H.I.M., BOREHAM, C.J., MITCHELL, C.H., MONTEIL, E., AND BRADSHAW, B.E., 2008—Mid–Late Cretaceous organic-rich rocks from the eastern Bight Basin: implications for prospectivity. PESA Eastern Australasian Basins Symposium III, 137-158.

VAN RENSBERGEN, P., AND C. K. MORLEY, 2000—3D seismic study of a shale 1231
expulsion syncline at the base of the Champion Delta, offshore Brunei and 1232
its implications for the early structural evolution of large delta systems, 1233
Mar. Pet. Geol., 17, 861– 872, doi:10.1016/S0264-8172(00)00026-X

VAN RENSBERGEN, P., MORLEY, C. K., ANG, D.W., HOAN, T.Q., AND LAM N.T., 1999—Structural evolution of shale diapirs from reactive rise to mud volcanism: 3D seismic data from the Baram delta, offshore Brunei Darussalam, Journal of the Geological Society London, 156, 633–650.

VEEVERS. J.J. AND EITTREIM, S.L., 1988—Reconstruction of Antarctica and Australia at breakup (95 + 5 Ma) and before rifting (160 Ma). Australian Journal of Earth Sciences, 35, 325-362.

WILLCOX, J.B. AND STAGG, H.M.J., 1990—Australia's southern margin: a product of oblique extension. Tectonophysics, 173, 269–281.

WILLCOX, J.B., SYMONDS, P.A. and STAGG, H.M.J., 1987—Tectonic evolution of the central southern margin of Australia. In: Extended Abstracts-Applied Extension Tectonics. Bur. Miner. Resour. Aust. Rec., 51, 150-161.

YASSIR, N.A. AND ZERWER, A. 1997—Stress regimes in the Gulf Coast, offshore Louisiana: data from well-bore breakout analysis. AAPG Bulletin, 81, 293–307. Rowan, M.G., Peel, F.J. & Vendeville, B.C. 2004. Gravity-driven fold belts on passive margins. In: McClay, K.R. (ed.) Thrust Tectonics and Hydrocarbon Systems. American Association of Petroleum Geologists Memoirs, 82, 157–182.

4.1 Paper 1

MacDonald, J.D., Healy, D., King, R., and Backé, G., (*in review*): Mapping basal pore fluid pressure variations in the Niger Delta toe with a critical taper wedge model. *Marine and Petroleum Geology*.

Mapping Basal Pore Fluid Pressure Variations in the Niger Delta Toe with a Critical Taper Wedge Model

MacDonald, J.,[a] Healy, D.,[b] King, R.[c] and Backé, G.[a]

[a] TRaX Australian School of Petroleum, Santos Petroleum Engineering Building, University of Adelaide, Adelaide, SA, 5005, Australia

[b] School of Geosciences, King's College, University of Aberdeen, Aberdeen, AB24 3UE, United Kingdom

[c] TRaX, School of Earth and Environmental Sciences, University of Adelaide, Adelaide, SA, 5005, Australia

Justin MacDonald: jmacdonald@asp.adelaide.edu.au

Dave Healy: d.healy@abdn.ac.uk

Rosalind King: rosalind.king@adelaide.edu.au

Guillaume Backé: guillaume.backe@adelaide.edu.au

Corresponding Author: Justin MacDonald

Australian School of Petroleum

Santos Petroleum Engineering Building

University of Adelaide

Adelaide, SA, 5005, Australia

Phone: 61 (0)8 8303 4302

Fax: 61 (0)8 8303 4345

Abstract

We apply the Critical Taper Wedge model to predict both the magnitude and spatial variation of basal pore fluid pressure along the detachment of the Niger Delta toe. Previous studies have used either a single or multiple widespread measurements of bathymetric slope dip angle and detachment dip angle for an entire wedge profile. In contrast, we have developed a workflow to measure the kilometre scale variation in these key parameters.

Using the standard Critical Taper Wedge equation, we solve for basal pore fluid pressure using three variables: the bathymetric slope angle, the basal detachment angle and the vertical thickness between these measurements (i.e. wedge height) for different positions along the wedge.

We present graphs of basal pore fluid pressure versus distance showing the predicted change along a measured seismic section, mapping the variation across a 560 km^2 area of the delta toe. Our model predictions show variations in basal pore fluid pressure along strike with magnitudes that range from ≈ 0.80 (sublithostatic) to 1.20 (supralithostatic). We also demonstrate that the Critical Taper Wedge equation is applicable to seaward-dipping detachments, or negative beta. Variation in beta is a first order control on the magnitude of the basal pore fluid pressure, whereby negative beta lowers the wedge taper angle resulting in a thinner, stronger wedge that in turn requires a higher basal pore fluid pressure in order to slide. Our approach allows us to predict the magnitude of the basal pore fluid pressure and correlate this to the present-day structural geometry of the Niger Delta Toe, at a much smaller scale than previously possible.

Keywords

Critical Taper Wedge, Niger Delta, Supralithostatic, Lamda_b, Overpressure

1 Introduction

The Niger Delta is located in the Gulf of Guinea on the West African passive margin (Fig. 1). The delta contains significant reserves of hydrocarbons generated from rapid burial of the pro-delta mud that was deposited between the Paleocene and the Pliocene (Cobbold et al. 2009). Extensive study of this system due to its endowment of hydrocarbons has made it an excellent analogue for shale or mud based delta systems around the globe. The age of the delta and continuous progradation of the system due to ongoing sediment supply from the Niger River means the system is actively deforming, which enables study of the structural

geometry in real time rather than looking at outcrop analogues of shale deltas that have experienced burial, lithification and uplift.

The Niger Delta can be divided into four main provinces based on significant changes in structural style from extension on the delta top to shortening at the delta toe. With the ongoing input of sediment the delta top eventually undergoes gravitational collapse resulting in extensional faulting that is linked at depth to a detachment zone. The increase in pore fluid pressure at the basal detachment level allows for the gravitational gliding of the system offshore.

The conventional method of predicting the basal pore fluid pressure (λ_b) in a sedimentary wedge is based on taking single 'averaged' measurements of the bathymetric slope angle (α) and the basal detachment angle (β) for an entire wedge. Here we introduce a new technique for measuring these values at fixed intervals to examine variations in λ_b along the wedge, in an attempt to link λ_b to changes in structural style. We use the Critical Taper Wedge (CTW) model to predict the magnitude of λ_b for any portion of the submarine wedge based on its bathymetric slope angle (α), basal detachment angle (β) and the wedge height (H).

Our model predictions suggest that parts of the detachment of the Niger Delta toe exhibit basal pore fluid pressures varying from sublithostatic to supralithostatic. We correlate these variations to the kilometre scale structural observations from selected 2D seismic lines across the Niger Delta. We explore the nature of supralithostatic overpressure using examples of measured overpressure in submarine wedges and observations made in outcrop examples.

2 Critical Taper Wedge model

The CTW model has been widely used to explain the mechanical and kinematic evolution of accretionary wedges, orogenic fold-thrust belts and, most recently, submarine wedges (Bilotti and Shaw, 2005; Dahlen, 1990; Dahlen et al. 1984; Davis et al. 1983;

Simpson, 2010; Suppe, 2007; Morley, 2007). The model seeks to explain the observed geometry of fold-thrust belts based on the internal wedge strength and the fault strength at the base of the wedge (detachment). A corollary of the CTW model is that different wedge and detachment materials (e.g. a shale or a salt detachment) result in different wedge geometries (Rowan et al., 2004). The common analogy for this system is a snow-plough or bulldozer, where a plough blade pushes a pile of snow until a wedge forms in front of it. As the wedge deforms internally, more material is added at the front of the wedge (shortening) and lost at the back of the wedge (extension; Fig. 2) until equilibrium is reached within the wedge and it begins to slide along a basal detachment (Fig. 2). Such a wedge would have two distinct stress regimes: a blade normal S_{Hmax} at the toe of the wedge (analogous to a fold-thrust belt) and a blade parallel S_{Hmax} at the top of the wedge nearest the blade (analogous to an extensional regime at a delta-top; King et al., 2009a). The wedge is predicted to start sliding only when the internal strength of the wedge exceeds the strength of the detachment, and this state is referred to as critical taper (Davis et al., 1983). During the phase of critical taper, the wedge deforms internally and is free to slide or propagate forward until the sediment supply is exhausted (for a deltaic wedge) or the regional stress conditions change (i.e. cessation of subduction in an accretionary wedge; Bilotti and Shaw, 2005).

The application of the CTW model to gravity-driven submarine fold-thrust belts has been used to explain the observed geometry of linked systems of extension (delta-top) and shortening (delta-toe) in the Niger and Baram Deltas (Fig. 1; Bilotti and Shaw, 2005; Morley, 2007). In particular, Bilotti and Shaw (2005) demonstrated that the toe of the deepwater Niger Delta is at critical taper, resulting in the system “gliding” or propagating basinward and increasing in width. In their study, the authors show that unlike orogenic wedges and accretionary prisms, the Niger Delta receives sediment input on the delta top from the Niger River, while at the same time adding material at the delta toe from the forward propagation of

the fold-thrust belt. This net material influx is a first-order influence on wedge taper (α+β) and increases the gravitational drive within the system, resulting in modification of the wedge (Bilotti and Shaw, 2005).

2.1 The Critical Taper Wedge Equation

The equations in the CTW model were first derived by Davis et al. (1983) and later modified to include the effect of cohesion (after Dahlen, 1990). Our analysis uses the Dahlen (1990) equation, which is derived for the wedge taper (α+β) by force-balancing a wedge at critical taper (Bilotti and Shaw, 2005; Dahlen, 1990; Davis, 1983). In the CTW equation, the Hubbert and Rubey (1959) pore fluid pressure ratio (λ) is the ratio of pore fluid pressure to lithostatic pressure. The default value for λ with hydrostatic pore fluid pressure would be 0.43. For the Niger Delta, the regional value for λ is calculated to be 0.54 based on pressure data from 13 deepwater wells indicating a slight overpressure (Bilotti and Shaw, 2005).

The pore fluid pressure ration (λ) is calculated using equation 1 below:

(1) $$\lambda = \left(P_f - \frac{\rho_w g D}{\rho g h} \right)$$

where, P_f is the pore fluid pressure measured from deepwater wells, ρ_w is the density of seawater, h is the depth of the measurement below the seabed (Dahlen et al. 1984), D is the water depth, g is the gravitational constant and ρ is the bulk rock density from well-density logs (Bilotti and Shaw, 2005). This removes the effect of the water as hydrostatic and lithostatic pressure curves are identical in the water column. If $\lambda < 1$ the term sublithostatic is used and infers that the pore fluid pressure is less than the lithostatic pressure. When $\lambda = 1$ the pore fluid pressure is equal to the lithostatic pressure and if $\lambda > 1$, the pore fluid pressure exceeds the lithostatic pressure and this is termed supralithostatic (Sibson, 1995). In compressional settings supralithostatic pore fluid pressure is required to induce hydraulic fracturing, whereas in extensional settings a slightly elevated (above hydrostatic) pore fluid

pressure can result in formation of extensional fractures (Sibson, 1995). The CTW equation (Equation 2) allows for us to fix the pore fluid pressure factor within the wedge ($\lambda = 0.54$) to solve for the pore fluid pressure factor at the base of the wedge (λ_b):

$$\alpha + \beta = \frac{\beta\left(1-\left(\frac{\rho_f}{\rho}\right)\right) + \mu_b\left(1-\lambda_b\right) + \left(\frac{S_b}{\rho g h}\right)}{\left(1-\left(\frac{\rho_f}{\rho}\right)\right) + 2\left(1-\lambda\right)\left(\frac{\sin\varphi}{1-\sin\varphi}\right) + \left(\frac{C}{\rho g h}\right)} \quad (2)$$

where, ρ is the density of sediment or rock in the wedge, ρ_f is the density of the overlying water column, g is the gravitational constant, C is the uniaxial compressive stress, S_b is the basal step-up angle, H is the height of the wedge between any α-β pair (Fig. 2) and φ is the angle of internal friction (after Dahlen, 1990). The wedge taper, $\alpha+\beta$, reflects the strength of the detachment and wedge material. A weak detachment and strong wedge material result in a long, thin wedge with low taper (Suppe, 2007). The α and β angles are used to determine μ and μ_b (Fig. 2).

The values for α, β and H constitute our observations from a selection of 2D seismic profiles across the deepwater Niger Delta toe (Fig. 3). In order to solve for λ_b, we select values for the remaining parameters. Due to the scarcity of public domain data for the Niger Delta, we have chosen to use the same values for these parameters as Bilotti and Shaw (2005), which were based on depth-converted seismic data, pressure data from deepwater wells, density logs and several assumptions (Table 1).

3 Modelling Workflow

Previous workers who have applied the CTW model to orogenic and submarine wedges have taken a larger-scale approach, solving the equation for an entire wedge profile (Bilotti and Shaw, 2005; Dahlen, 1990; Davis et al. 1983; Morley, 2007; Suppe, 2007). These applications are based on a single or multiple large scale measurements of α and β from an averaged profile of the bathymetry (or digital elevation in a subaerial wedge) and basal

detachment along a 2D seismic line or cross section. This approach provides a result for λ_b that is assumed as homogeneous across the whole 2D section, which could be much greater than 100 km in length. Given the observed changes in wedge morphology and internal structure along 2D profiles in many wedges, a single or even several measurements for alpha and beta probably cannot account for variability along a wedge. A series of closely spaced α and β measurements along a single 2D profile provides insight into changes in wedge properties and wedge behaviour.

The CTW equation formulated by Dahlen (1990) is one dimensional in that it requires only a single measurement of α and β along a given vertical slice through the wedge profile. We have devised a simple workflow that allows us to define the sample point spacing, or vertical slice spacing (i.e. 1250 m) along a 2D seismic profile, to measure multiple values of α, β and H (Fig. 2) in order to investigate spatial variability in the wedge along a 2D profile.

3.1 Interpretation of 2D Seismic Data

A total of 15 crosslines (parallel to tectonic transport direction) were extracted from a pre-stack time migrated (PSTM) 3D seismic survey covering 560 km^2 in the Niger Delta toe (Fig. 4). The selected lines were extracted at 1250 m spacing, in order to capture kilometre-scale changes in α, β and H (Fig. 3). Following interpretation of the horizons, including the seabed, base Agbada Formation, mid Akata Formation reflection (basal detachment) and the base Akata Formation (approximately basement contact), the picked stratigraphic boundaries were compared to published examples (Bilotti and Shaw, 2005; Cobbold et al. 2009; Maloney et al. 2010; Figs. 4, 5). Thrust faults and back thrusts were mapped throughout the section. This dataset was then imported into GOCAD® for a simple depth conversion and to construct 3D surfaces of the horizons and faults, to investigate regional changes in structural style along strike (e.g. the welds in Figs. 3, 4).

3.2 Measurement Workflow

The depth-converted surfaces were imported into 3D MOVE© and a total of 15 α – β profiles were extracted from the 3D model, along the original 2D seismic profiles (Fig. 3). This ensures the measurements were taken from the interpreted parts of the 3D model, rather than the interpolated volumes between the 1250 m spaced 2D lines. These 15 profiles were then re-sampled at 1250 m spacing along each line such that any node along the α line would have a corresponding node along the β line below, thus the two nodes would be in the same vertical plane. Once this was completed, the lines are converted to wells, resulting in one α well and one β well for all 15 2D profiles. The attributes for each well are easily displayed including a deviation from vertical, UTM coordinates and a depth/elevation measurement for each node; this is then copied to Microsoft Excel. For each α – β well pair, we make a series of simple corrections in order to prepare the data for our analysis of λ_b. For each pair of vertically stacked nodes (top node is α, bottom node is β; Fig. 3) we have UTM coordinates and we subtract the elevation of the top node from the bottom node to derive H. Next we must correct α and β separately because they are measured as deviation from vertical rather than from horizontal. This will give us UTM coordinates and measurements of α, β and H for each 1250 m spaced node along a single 2D profile, repeated 15 times across the 3D model.

3.3 Solving the Critical Taper Wedge Equation for λ_b

Equation 1 can easily be rearranged to solve for λ_b using the large number of measurements collected using our method herein. The parameters used in this code to solve the equation are based on those defined in Bilotti and Shaw (2005), which they derived from well data and seismic observations across the entire Niger deepwater fold-thrust belt (Table 1). As is well documented in previous work (Bilotti and Shaw, 2005; Dahlen, 1990; Davis et al. 1983; Suppe, 2007), all that is required to solve the equation is α and β. We measure the H parameter as we are performing numerous iterations along the wedge, where the thickness changes between each α and β pair. This parameter is not explained in Bilotti and Shaw's

(2005) study, as it is not possible to measure accurately with a regional approach of averaging α and β, even though there is a change in thickness between the landward and seaward sides of the wedge. We wrote a simple script to solve for the pore fluid pressure at the base of the wedge, i.e. λ_b. We choose to solve for this parameter to explore the possibility of a link between observed structural style and predicted λ_b at the detachment level (here, the mid Akata Formation reflection; Fig. 4). The basal detachment in the Niger Delta toe, typically located within the mid Akata Formation, has been interpreted as a significantly overpressured interval that behaves in a ductile fashion (Bilotti and Shaw, 2005; Cobbold et al. 2009; Morley and Guerin, 1996), although more recent studies indicate that it behaves as mechanically competent stratigraphy rather than being remobilized along the detachment like low density evaporites (Maloney et al. 2010).

Our workflow produces graph(s) of λ_b versus distance for each profile (Figs. 6-9). In addition, because the node spacing and the spacing of the individual 2D seismic lines are both set to 1250m (Fig. 3), we were able to produce a contour map of λ_b for basal detachment within the study area (Fig. 10). This map can be then compared to the 3D geometry of the detachment surface (Fig. 3), and particularly the 3D geometry of the thrust faults as they develop along strike.

4 Results of Basal Pore Fluid Pressure (λ_b) Modelling in the Niger Delta Toe

The parameters used for modelling basal pore fluid pressure in this study are based on those published by Bilotti and Shaw, (2005). Due to the limited availability of well data for the Niger Delta, we have not modified these parameters. Table 1 lists the parameters used for the modelling and the values and corresponding method(s) of determination. For detailed explanation of the derivation of each parameter we refer the reader to Bilotti and Shaw, (2005).

4.1 Regional Geology

4.1.1 Seismic Stratigraphy of the Deepwater Niger Delta

The dataset for this study is comprised of a 560 km^2 3D seismic cube from which a series of 2D seismic lines have been extracted at 1250 m spacing. Of these lines, we have selected four examples from across the volume to track any changes in geometry along the strike length of the deepwater fold-thrust belt. Figure 4 is a 3D block diagram composed of four evenly spaced interpretations of 2D seismic lines (lines A, B, C and D, Figs. 6-9). We have subdivided the Niger Delta into its respective stratigraphic packages based on those identified by Corredor et al. (2005) (Fig. 5). The pink unit in Figures 6-9 represents both the oceanic crust and fragmented continental crust formed during the Early Cretaceous rifting of the south Atlantic Margin (Corredor et al. 2005). Below the Niger Delta the basement is overlain by Late Cretaceous sedimentary rocks, which have never been penetrated by drilling, but are inferred based on exposure in the Anambra basin to the northeast (Corredor et al. 2005). These Late Cretaceous strata are recognized as synrift clastic sediments formed during the Albian-Maastrichtian. Overlying the Cretaceous strata is the Akata shale, a Paleocene transgressive sequence that forms the major detachment for the Niger Delta (Fig. 5). An important amplitude reflection is recognized within this otherwise transparent package, the mid-Akata reflection (Figs. 4, 6-9). The thickness of the Akata Formation varies significantly from 7000 m near the continental shelf to 2000 m at the most distal part of the delta (Doust and Omatsola, 1990), while in the deepwater fold-thrust belts the thickness is up to 5000 m due to structural repetition (Corredor et al. 2005). The Akata Formation is thought to be the main hydrocarbon source rock for the Niger Delta and the low P-wave velocities of approximately 2000 m/s may reflect regional fluid overpressures (Bilotti and Shaw, 2001; Corredor et al. 2005). The Akata Formation has been subdivided into the Lower Akata Formation and Upper Akata Formation in order to separate the strata below and above the mid-Akata reflection (Figs. 4, 6-9).

The overlying Agbada Formation is Eocene-Present in age and is the major hydrocarbon bearing stratigraphic unit in the Niger Delta (Fig. 5). The Agbada Formation is > 3500 m thick in places, is siliciclastic in composition, and represents the deltaic portion of the sequence (Corredor et al. 2005). This unit is represented, herein, as prekinematic Agbada Formation, or the flat lying strata that was deposited prior to initiation of thrusting (after Maloney et al. 2010; Fig. 4). Finally, above the prekinematic Agbada Formation are the thrust-related synkinematic strata (growth strata formed in response to ongoing deformation), which are represented by synkinematic Agbada Formation in the block diagram (Fig. 4). As the Niger Delta's deepwater fold thrust belt is considered active at present-day (Bilotti and Shaw, 2005), we choose to subdivide the pre- and synkinematic Agbada Formation for display purposes only. For the purpose of this analysis, the strata between the mid-Akata reflector and the seabed are treated as an actively deforming homogeneous deltaic wedge.

4.1.2 Local Variability in Structural Geometry

The volume imaged shows a slight thickening in stratigraphy (approximately 500 m across 19 km) from northwest to southeast, with the basal detachment dipping gently towards the southeast (Fig. 3). The structural geometry of the Niger delta toe in the area covered by the 3D seismic survey changes along strike of the fold-thrust belt, whereby more complex structure is observed in the southeast (Fig. 6) and becomes progressively simpler toward the northwest (Fig. 9). In the southeast (Fig. 6), numerous fore-thrusts and back-thrusts (at least 6 have been interpreted) are observed and the basal detachment has a variable dip along the 2D profile from seaward to landward. On the seaward side of the detachment there is a weld between the overlying Agbada Formation and the mid Akata Formation reflection, which forms the basal detachment in this area (Fig. 6). This weld is located under the footwall ramp of an overlying fore-thrust/back-thrust structure that thins the upper Akata Formation above the mid Akata Formation reflection (Fig. 6). Along strike there is evidence for significant

back-thrust development and reversal of thrust propagation direction from forward-verging to backward-verging and combinations, thereof, within a single thrust sheet (Fig. 4). This has been documented in detail in the deepwater Niger Delta by previous authors (i.e. Higgins et al. 2007). The weld observed throughout Figures 6-8 is the same weld occurring along strike, where a fore-thrust and back-thrust are working simultaneously to accommodate deformation; a phenomenon which is not observed in the northwestern most area (Fig. 9). In this NW area (Fig. 9), we observe only two fore-thrusts and a relatively flat detachment with a slight seaward dip. Thus, the structural complexity increases in the southwest, where the detachment is slightly deeper, the stratigraphy is slightly thicker and the contact between the Akata Formation and the oceanic crust appears to be more irregular.

4.1.3 Detachment Geometry

Picking the detachment in the Niger Delta is challenging due to the poor resolution of the Akata Formation in seismic data (Corredor et al. 2005; Maloney et al. 2010), and the observation that deepwater fold-thrust belt systems often deform above a series of detachments rather than a single master detachment (Briggs et al. 2006). In order to apply the CTW model, we must choose a single detachment for the β angle measurement at the base of the wedge profile (i.e. Fig. 6). For the purpose of this exercise, we have decided to use the prominent mid-Akata Formation reflector as the basal detachment surface. This reflection is of sufficient resolution in our seismic data to map it accurately and thrust faults are interpreted to root or detach at this level in all four seismic lines presented above (Figs. 6-9). In the data we present, we do not observe displacement or offset of this reflector. However, there is displacement observed above this reflector, notably at the contact between the Akata Formation and the overlying Agbada Formation (Fig. 4). This contact appears to act as an upper level of detachment in our data, and has been identified by previous authors as the accepted detachment level (Corredor et al. 2005; Maloney et al. 2010). Maloney et al. (2010)

also demonstrate that the mid-Akata Formation reflector acts as the basal detachment surface and is a mechanically acceptable detachment level for the structures observed above it (Fig. 11).

The basal detachment in this part of the Niger Delta toe is illustrated on 2D seismic profiles to have an irregular dip along the profile, oriented perpendicular to the strike of the fold-thrust belt (Fig. 4). On a pre-stack time migrated seismic line from the deepwater fold thrust belt (Fig. 12), we can see the detachment dips are variable and frequently change dip direction from seaward to landward across a single 2D seismic profile. Because the fold-thrust belt is inferred to be at critical taper and actively deforming at present-day (Bilotti and Shaw, 2005), we can make the assumption that the geometry of the basal detachment at present-day is the active geometry which is required to form the structures currently "growing" or deforming above the detachment. Thus, we can now use this basal detachment geometry for our β measurements and solve the CTW equation for basal pore fluid pressure.

4.2 Modelling Results

4.2.1 Basal Pore Fluid Pressure (λ_b) Plots

Of the 15 measured profile lines, we have chosen four representative lines at equal spacing across the volume (Figures 6-9). These four lines display the uninterpreted 2D seismic profiles in two-way-time as well as an interpreted line drawing showing the stratigraphy, basal and upper detachment surfaces, both thrust geometries and the geometry of the seabed (Fig. 4). Plotted between the uninterpreted and interpreted seismic data are the corresponding λ_b plots, which are scaled to the accompanying seismic line. The variability of the λ_b plot corresponds to the variability of the parameters from which it is calculated in the above seismic line at any given vertical line through the wedge, namely α, β and H (Figs. 6-9). What is observed in the λ_b plot is the significant variability in basal pore fluid pressure

factor (at the detachment). By examining each of the four seismic sections in turn we highlight some observations that help to explain the λ_b results.

4.2.2 Line A

This line is located in the southeastern extent of the 3D seismic cube (Line A - Fig. 6). In this area we observe a highly deformed section of the deepwater fold-thrust belt. Both fore-thrusts and back-thrusts are observed and irregular fault-propagation anticlines, some displaying kink-style folding on select fold limbs, indicating increased displacement (Fig. 6; Dewey, 1965; Suppe, 1983). There is evidence in this seismic profile for back-thrust development and welding of the base Agbada Formation with the mid-Akata Formation reflector indicating a structural thinning of the Upper Akata Formation above the basal detachment (Fig. 6). This welding above the detachment may be due to shale mobility (Morley and Guerin, 1996) or structural thinning driven by sub-seismic scale imbricate thrusting within the cores of anticlines (Fig. 6 - SW most anticline; Maloney et al. 2010). Whatever the cause, this has a drastic effect on the geometry of the detachment, resulting in a switch of dip direction from landward to seaward which in turn causes an increase in λ_b to supralithostatic ($\lambda_b > 1$). The corresponding λ_b curve shown on Figure 6 indicates a generally highly overpressured λ_b ranging from 0.85 to 1.2. In the centre of the curve, the λ_b value averages approximately 0.95. This is a result of the detachment angle, β, dipping gently landward ($1\text{-}5^0$), resulting in a more positive β angle (Fig. 6). On the areas of the λ_b curve that average $\lambda_b > 1$ (far right and far left, respectively), we can attribute this to a change in the basal detachment dip to seaward ($1\text{-}6^0$), or a negative β angle, where α and β are approaching parallelism requiring a higher basal pore fluid pressure to achieve critical taper based on equation 2.

4.2.3 Line B

The next seismic line is located some 5 kilometres to the northwest of Line A and slightly up dip on the basal detachment (Fig. 7). In this section we observe slightly less deformation with fault-propagation folds having gentler limb dips and an absence of kink folds. Back-thrusts are still present, even imbricate back-thrusts on the leading fore-thrust (Fig. 7). Most notably, the weld between the Lower Agbada Formation and mid-Akata Formation reflector is still present, although the geometry of the detachment at this location is less acute compared to the same position of the above thrust fault along strike to the southeast (i.e. Fig. 6). The basal detachment in this section is better imaged on the uninterpreted seismic profile (Fig. 7 – bottom) and displays a less acute dip variation with dips ranging between 1-3^0, although reversal in dip-direction still occurs across the section. Some component of the basal detachment dip variation might be an inherited geometry from the basement contact below the Akata Formation, as observed elsewhere in the Niger Delta (Bilotti and Shaw, 2005). The λ_b curve indicates a value between 0.93-1.15 for the entire section, which is, on average, higher than in seismic line A to the southeast. Where the basal detachment is generally flat, we observe a λ_b value of ~1.0, or lithostatic. When the detachment dips >1^0 seaward (negative β), we observe an increase in the λ_b value to supralithostatic. In the area of the seismic section on the northeast side of the weld structure (Fig. 7), we observe a landward dipping detachment but the λ_b value still indicates a supralithostatic pore fluid pressure. In this area, the seabed is relatively flat, and α and β are approaching parallelism once again. In addition, the southwest portion of the section displays a slightly ($\approx$ 400 m) thinner stratigraphy, where the weld occurs, which also contributes to the rise in λ_b based on equation 2.

4.2.4 Line C

In line C we observe a slightly thinner stratigraphic package (≈ 3500 m vs. ≈ 3800 m in Line B) as we move up-dip along the basal detachment surface toward the northwest (Fig. 8). In this seismic profile, we observe the weld structure identified in lines A and B but here it is beginning to taper out as we move northwest. The deformation is attained by several fore-thrusts and back-thrusts, and fault-propagation folds display moderately dipping limbs with thrust faults detaching at both the base of the Agbada Formation and on the basal detachment at the level of the mid Akata Formation reflector. In the uninterpreted seismic profile (Fig. 8; bottom) we observe the well imaged mid Akata Formation reflector that shows no offset, only gentle variation in dip along the section. The basal detachment mimics the inherited geometry of the basement contact, as is observed on the southwest side of the section nearest the weld structure (Fig. 8), this is observed elsewhere in the Niger Delta as noted by previous authors (Bilotti and Shaw, 2005). The λ_b curve for this seismic profile shows an overall range between 0.95-1.2, similar to the curve for seismic line B to the southeast (Fig. 7). The curve can be divided into two broad regions for this section, where the southwest side demonstrates a supralithostatic value for λ_b due to variation in the basal detachment geometry that appears to be a result of inherited basement geometry and influence from the weld structure in this area. Fluctuation of β results in variation of detachment dip-direction on the southwest side of the seismic profile resulting in the acute changes in the λ_b curve and thus basal pore fluid pressure below this area (Fig. 8). On the northeast side of the λ_b curve we observe a lithostatic (λ_b =1) to supralithostatic value due to the relatively flat-to-negative β angle. In addition, as in seismic line B, the progressively thinning stratigraphic package contributes to the elevated λ_b value we observe in the accompanying curve for this section.

4.2.5 Line D

This seismic profile is located in the northwest of the study area and demonstrates the least amount of deformation within the 3D seismic dataset we use for this study (Fig. 9). The section here images just two fore-thrusts and displays no evidence for back-thrusting or welds. Although the uninterpreted seismic profile (Fig. 9; bottom) is of relatively poor resolution, it is still possible to identify the higher amplitude mid Akata Formation reflector to define the basal detachment surface. It is apparent that this portion of the deepwater fold-thrust belt is thinner than to the southeast of the area, by approximately 500 m. Similar to the above seismic profiles, the basal detachment displays a reversal in dip-direction across the profile, resulting in areas of negative β. The λ_b curve that corresponds to this seismic profile (Fig. 9) ranges in value from 0.85-1.14, with several dramatic spikes present. The λ_b average value for this profile is approximately 1.05 or supralithostatic due to the predominately seaward dip of the basal detachment (negative β). The acute changes in λ_b value are attributed to sharp changes in detachment dip due to loading of the detachment directly under footwall thrust ramps (Fig. 9). In addition, on the northwest side of the profile the seabed changes geometry from a gentle ($1\text{-}2^0$) seaward dip to flat, contributing to the increase observed on the λ_b curve. By examining this seismic profile, it becomes apparent that parts of the Niger Delta's deepwater fold-thrust belt have a seaward dipping basal detachment. Thus, the standard model of a purely positive β for this area is indeed questionable as it is clearly not the case everywhere.

4.3 Sensitivity Analysis

In order to gauge how sensitive equation 2 is to changes in input variable(s), we have performed a sensitivity analysis of λ_b by iterating through restricted ranges of parameter values. We designed the sensitivity analysis to test the response of $\lambda = \lambda_b$ values to variation of the three input variables: α, β and H.

4.3.1 Fixed wedge thickness H

The first test demonstrates what the range of λ_b values would be for a series of fixed wedge thicknesses at H = 1000, 2000, 4000 and 6000 m (Fig. 13a). Here, ranges for α and β from -10° to 10° are displayed on the y and x axis. The white dot (Fig. 13a) located at approximately α = 1°, β = 1° (for each fixed position of H) corresponds to a particular colour at that exact position. That colour then corresponds to a λ_b value in the adjacent colour bar, which indicates a range in λ_b values from dark blue (λ_b = 0.5) to red (λ_b =1.5): where $\lambda_b < 1$, it is sublithostatic; where $\lambda_b = 1$, it is lithostatic, and; where $\lambda_b > 1$, it is supralithostatic. The results of this sensitivity test indicate that for a wedge thickness of H = 1000 m the dot sits above the yellow position; and thus, would require a λ_b value of > 1 or supralithostatic based on equation 2 (after Dahlen, 1990) with the Bilotti and Shaw (2005) input variables. For a fixed wedge thickness of H = 2000 m and the same α and β angles as above we observe a green colour, corresponding to a λ_b value of < 1 or sublithostatic. For the final two tests with fixed wedge thicknesses of H = 4000 m and H = 6000 m we observe a similar result as for H = 2000 m. This indicates that a very thin wedge (H = 1000 m) requires a supralithostatic λ_b value to slide and once the threshold of approximately H = 2000 m is passed the wedge thickness does not significantly change the λ_b value required to slide, at least not for a wedge with a thickness between 2000 and 6000 m. For a fixed value of H, the sensitivity of λ_b to variations in α and β is uniform (contours of λ_b are evenly spaced).

4.3.2 Fixed detachment angle β

The second test (Fig. 13b) demonstrates the range of λ_b values for fixed β angles of +5°, +2°, -3° and -8° from horizontal with H ranging between 2000 and 8000 m and α ranging from -10° to 10° on the y and x axis. As is indicated above, the white dot (Fig. 13b) corresponds to a particular colour which is represented on the adjacent colour bar, indicating the λ_b values. The position of the dot(s) is fixed at H = 4000 m and β = 2° for the four scenarios in Figure 13b. In the first scenario where fixed β = 5°, α = 2° and a relatively thick

wedge (H = 4000 m) the corresponding λ_b value is < 1 or sublithostatic. The second scenario with a fixed β = 2° and the white dot in the same position the corresponding λ_b value is again < 1 or sublithostatic. In the third (fixed β = -3°) and fourth (fixed β = -8°) scenarios with the white dot in the same position we see a drastic change in the λ_b value required to initiate sliding of the wedge (Fig. 13b). In these scenarios, with fixed negative β values, a positive α angle and an H = 4000 m the corresponding λ_b value is >1 or supralithostatic. Thus once the system has a seaward dipping basal detachment (i.e. a negative β), equation 2 (after Dahlen, 1990) requires a higher λ_b to initiate sliding. Although, the fixed β = -8° scenario is rather extreme and unlikely, this sensitivity test demonstrates that the CTW equation (Equation 2) is very sensitive to change in β angle from +ve to –ve.

4.3.3 Fixed seabed angle α

The final test (Fig. 13c) demonstrates the range of λ_b values for fixed α angles of -5°, -2°, +3° and +8° from horizontal with H ranging between 2000 and 8000 m and β ranging from -10° to 10° on the y and x axis. As is indicated above, the white dot (Fig. 13c) corresponds to a particular colour, which is represented on the adjacent colour bar indicating the λ_b values. The position of the dot(s) is fixed at H = 4000 m and α = 2° for the four scenarios in Figure 13c. Although, there are demonstrated examples of minor fluctuations in seabed dip direction due to active shortening in deepwater fold-thrust belts (such as is observed in Figure 12), a fixed α angle of -5° is an extreme and only demonstrated here as an end-member for the sensitivity analysis. This first example demonstrates that with a fixed α angle of -5° (landward dipping seabed) the corresponding λ_b value would be > 1 or supralithostatic. The second scenario is commonly observed in the deepwater Niger delta (on the backlimbs of hangingwall anticlines) with a fixed α angle of -2° and the same H and β angle as the first scenario. Here, the required λ_b value is at the lithostatic – supralithostatic boundary. This demonstrates that a change in direction of the seabed from seaward dipping to

landward dipping will cause λ_b values to increase to >1 or supralithostatic. In the final two scenarios, where α is fixed at +3° and +8°, the corresponding λ_b values are well below 1 or sublithostatic. For most submarine wedges this would be the scenario where the seabed tends to dip seaward. As stated above it is only where we observe anticlines that you have reversal of seabed dip direction toward the land. This sensitivity analysis indicates that Equation 2 (after Dahlen, 1990) is very sensitive to both negative β angles and negative α angles for low values of H, resulting in a corresponding supralithostatic λ_b value for the wedge to slide.

One important observation here is that even with a slightly negative β or α angle, if the wedge is reasonably thick (say H = 4000 m) a corresponding positive value for α or β will offset the negative values, driving the λ_b value below lithostatic. For example, in Figure 13b scenario three (fixed β = -3°), where the white dot corresponds to a supralithostatic λ_b value, if we were to observe a steeper α angle (more positive, i.e. +5 degrees) then we would drive the λ_b value below lithostatic. Thus, there are ways to accommodate both negative α angles and negative β angles (landward dipping seabed or seaward dipping basal detachment, respectively) without driving the λ_b value into the supralithostatic range.

5 Discussion

5.1 Change in Lamda B Within a Submarine Wedge

Submarine wedges often have variable detachment geometries in 2D seismic data (Fig. 12; Bilotti and Shaw, 2005; Butler and Paton, 2010; Davis et al. 1983; Fort et al. 2004; MacDonald et al. 2010). In some instances, we observe a gentle variability of detachment dip-direction within submarine wedges from landward to seaward (i.e. McClay et al. 1998), especially below deepwater fold-thrust belt systems (Bilotti and Shaw, 2005; Fig. 12). Some systems show almost exclusively a negative or seaward dipping detachment (e.g. offshore Angola: Fort et al. 2004; offshore South Australia: MacDonald et al. 2010; offshore Namibia: Butler and Paton, 2010; Fig 12) but are still technically critical taper wedges with up-dip

extension linked to down-dip shortening. This variability in detachment dip-direction has been shown on 2D seismic profiles and cross-sections. However, when β angles are derived from sections they are always averaged for the entire wedge, or the part of the wedge in question (i.e. Bilotti and Shaw, 2005; Davis et al. 1983). The result is a single measurement for the β angle that is always a positive value for input into equation 2. We feel that this is an oversimplified approach to the calculation of the λ_b value, as it does not take into account any fluctuations in detachment dip-direction.

Our method to predict λ_b for each 2D seismic line shows a complex, laterally variable result. This is due to the variable geometry of α, β and H along strike. Taking these lateral fluctuations in dip-direction of both the detachment and seabed into account, we illustrate that, where the λ_b value is sublithostatic, both α and β values are commonly positive; a result that has also been demonstrated in past studies, albeit without the fluctuations (Bilotti and Shaw. 2005; Davis et al. 1983; Suppe, 2007). It is when we predict λ_b values > 1 or supralithostatic that we believe this result is directly related to the negative value(s) measured for β and/or α, or due to a very thin wedge (Fig. 13a; sensitivity analysis). We believe that the equation 2 can be used to show that a slightly negative β and/or α angle will result in a supralithostatic basal pore fluid pressure ratio (λ_b) below the Deepwater Niger Delta toe (Fig. 6). We provide evidence that seaward dipping detachments in both salt and overpressured shale exist both on a regional and kilometre scale. Thus, we can model negative β values using the conventional Dahlen (1990) CTW model (Equation 2; Fig. 12).

5.2 Modelling Negative Beta

There are numerous examples of submarine wedges (or parts thereof) displaying negative β angles, or seaward dips, such as in the Orange Delta (west africa), Camamu Basin (NE Brazil), Ceduna Delta (South Australia), Kwanza Basin (Angola) and the Niger Delta (west Africa) (Fig. 12; Bilotti and Shaw, 2005; Briggs et al. 2006; Butler and Paton, 2010;

Cobbold et al. 2010; Fort et al. 2004; MacDonald et al. 2010; McClay et al. 2003; McClay et al. 2000; Morley and Guerin, 1996; Mourgues and Cobbold, 2006). Each of these systems displays wedge geometry of up-dip extension linked to down-dip shortening, indicating gravity sliding or spreading into the basin (Schultz-Ela, 2001). From a mechanics standpoint, all the elements of the Mohr-Coulumb wedge are maintained in these examples, and therefore, we can justify the application of the CTW model (Equation 2) to these systems. In terms of equation 2, input of a negative β value does not hinder solving the equation for λ_b (Suppe, 2007). However, it results in a non-linear relationship between α and β (Fig. 14) and often an increase in λ_b. Figure 14 illustrates the corresponding α versus β plots for seismic lines A, B, C and D used in this study. The plots show some scatter, without a clear inverse relationship between α and β which is likely caused by noise at this small scale (i.e. a resolution effect). This differs from the results of previous studies where α and β profiles are averaged (Suppe, 2005; Bilotti and Shaw, 2005).

It has been shown that thinner wedges with low taper angles require higher values of λ_b to initiate sliding (Davis et al. 1983), and increased strain is observed near the front of the wedge, seaward of the leading thrust fault in finite element method modelling of thrust wedges (Simpson, 2011). Figure 15 illustrates the change in λ_b based on different α and β measurements in four hypothetical wedge geometries. The two end members in Figure 15 show a highly positive α and β pair with low values of λ_b and a highly negative β and positive α which, based on our modelling, would have a supralithostatic λ_b. This case is most akin to the Orange Delta, offshore Namibia, where the basal detachment is seaward dipping, sub-parallel to the seabed (Fig. 12; Butler and Paton, 2010). Interestingly, the intensity of thrust fault imbrications in the deepwater fold-thrust belt of the Orange Delta is quite unique when compared to other similar aged systems worldwide. We believe that this is may be a

consequence of the negative β angle which, according to our modelling, suggests a supralithostatic λ_b.

5.3 Sublithostatic versus Supralithostatic Basal Pore Fluid Pressure

The results presented above indicate that supralithostatic overpressure was required to produce the wedge geometry we observe in some areas of Niger Delta toe. While this is not interpreted to be the representative overpressure value at present day, there is evidence that at some point in time, overpressures at the detachment level in the mid-Akata Formation exceeded the overburden stress. In order to overcome the lithostatic stress resulting from the relatively thin overburden (2 km in study area), there must be a significant horizontal stress along the detachment. Evidence for extensional fractures that are sub-parallel to the basal detachment has been documented in fold-thrust belts, such as the Larra Thrust of the Spanish Pyrenees (Teixell et al. 2000). Here, detachment (and bedding) parallel extensional fractures open normal to the minimum principal stress (vertical stress), thus overcoming the lithostatic stress. This is attributed to high differential stress channelling in the hard limestone unit that forms the detachment lithology (Teixell et al. 2000). Teixell et al. (2000) also demonstrate that slip on the thrust was accommodated by slip on water sills formed by detachment parallel extensional fractures (Fig. 16a). This system is an excellent field example of the role that fluids can play in creating detachment parallel extensional fracture networks and in accommodating episodic displacement on active thrust sheets. The key to this model is generating lithostatic or supralithostatic overpressure to initiate detachment parallel extensional fracture networks. There are several ways to generate near lithostatic overpressure in submarine wedges; we briefly address those mechanisms thought to be actively occurring in the deepwater Niger Delta toe.

5.3.1 Mechanisms for Overpressure Generation

There are several overpressure generation mechanisms which could produce the near-lithostatic measured overpressures in the Niger Delta toe. For a detailed review of overpressure generation mechanisms, we refer the reader to Osborne and Swarbrick (1997) and Swarbrick et al. (2002). The primary overpressure generation mechanism in the Akata Formation of the Niger Delta is thought to be disequilibrium compaction due to rapid burial of low permeability marine muds by the prograding deltaic deposits of the overlying Agbada Formation (Morley and Guerin, 1996; Osborne and Swarbrick, 1997). Secondary overpressure generation is observed from a number of mechanisms, such as aquathermal expansion, smectite to illite transformation in shales, gypsum to anhydrite transformation in evaporites and finally maturation of hydrocarbons such as kerogen. The latter is thought to result in a volumetric expansion of up to 25% (Osborne and Swarbrick, 1997). Cobbold et al. (2009) have even suggested that generation and seepage of hydrocarbons in the deepwater Niger Delta Toe are responsible for the initiation of thrust propagation, driving the system seaward. Coupling one or more of these mechanisms while maintaining a “near perfect” seal is the only way to achieve lithostatic or supralithostatic overpressure, as a finite permeability in the seal would result in pressure bleed-off and disequilibrium compaction resulting in the overpressure failing to reach the lithostatic threshold (Osborne and Swarbrick, 1997).

5.4 Evidence for Lithostatic and Supralithostatic Basal Pore Fluid Pressure

To our knowledge, there are no existing means to measure supralithostatic overpressure while drilling. Fortunately, there are important field examples that indicate that this process must occur in numerous settings, from brittle fold-thrust belts (Cobbold and Rogrigues, 2007; Cosgrove, 2001; Teixell et al. 2000; Fig. 16a) to dehydrating subducting slabs in the ductile regime (Dobson et al. 2002; Healy, 2011; Healy et al. 2009; Fig. 16b). Sibson et al. (1988) show that high-angle reverse faults act as valves, allowing for fluctuation

in fluid pressure from supralithostatic to hydrostatic. This is determined by examining reactivated faults of unfavourable orientation to the prevailing stress field, thus, requiring a supralithostatic pore fluid pressure to initiate. Sibson et al. (1988) proposed that the seismogenic fault failure creates the fractures necessary to bleed off the overpressure rapidly, returning the stress state to hydrostatic. This example is well supported from observations in the Abitibi greenstone belt of 'flats' or extensional fluid filled veins opening parallel to the minimum principle stress orientation.

There are published data from both accretionary and submarine deltaic wedges demonstrating near lithostatic to lithostatic overpressure, such as is demonstrated in the Barbados Toe from Davis et al. (1983). Here, the Lesser Antilles wedge extending west of Barbados has an overall taper corresponding to a predicted fluid pressure ratio $\lambda = 0.92$ within the wedge. The Barbados Toe has a much narrower taper and a predicted pore fluid pressure of $\lambda = 0.97$ (Davis et al. 1983). This prediction was later confirmed and exceeded by direct measurement when Deep Sea Drilling Project (DSDP) hole 543 (leg 78A) was drilled 1.5 km inboard of the deformation front and recorded a $\lambda \approx 1$ or lithostatic at the base of the hole. This hole did not reach the basal detachment; however, we would expect to observe $\lambda > 1$ or supralithostatic at the basal detachment level in this scenario due to elevated pore fluid pressure at the detachment level compared to within the wedge. This is due to the nature of the CTW code used in this study where λ is fixed by the ρ_w/ρ_{wedge} (average density of wedge) and thus, λ_b is free to vary; possibly allowing for a higher value of pore fluid pressure at the detachment level at the base of the wedge. This result is perhaps the most significant measurement from a sedimentary wedge, and supports the relationship between a narrow taper and high pore fluid pressure as predicted by the CTW model (Equation 2; Fig. 13a; sensitivity analysis). Other published examples include an observed pore fluid pressure of $\lambda \approx 1$ in the Makran accretionary wedge, offshore Pakistan (Davis et al. 1983). To date, the Akata

Formation of the Niger Delta has not been penetrated by a well so we lack pressure data to confirm our predicted overpressures in the study area. Given the strong correlation presented in the Davis et al. (1983) study between predicted vs. measured pore fluid pressures in Barbados, we feel that our results are within the limits of both the measured examples and outcrop observations. The increase in predicted basal pore fluid pressure associated to observed negative β values in the corresponding seismic data suggests that a narrowing of the taper angle requires a lithostatic to supralithostatic overpressure state. As further pressure measurements become available from increasingly deeper parts of the Niger Delta Toe it may be possible to test this prediction. This would allow for better calibration of input parameters for equation 2, rather than relying on assumptions and basin-wide averaged values.

6 Conclusions

This study has explored the possibility of a link between predicted high values of basal pore fluid pressures and observed structural style in a submarine wedge (the Niger Delta toe). While previously published examples of basal pore fluid pressure calculations using the CTW model have provided reasonable results, they all contain one common assumption: the validity of averaging α and β angles for each modelled profile. This provides a single estimated value for the λ_b for each section, when realistically we might expect variations commensurate with observed variations in: structural style, detachment and bathymetric slope angles and direction, changes of lithology and changes in thickness. The new method presented in this study with repeated measurements of bathymetric slope, basal detachment angle and wedge thickness is a step forward from the existing tools and provides a more systematic, quantitative approach.

From any selected profile, our method predicts a λ_b value for all points using a predefined spacing. This enables us to map variations in predicted λ_b and to compare these predictions with changes in structural style and wedge thickness. In addition, we can plot λ_b

against distance at the same scale as the 2D seismic data, from which the input parameters were acquired, to allow detailed 2D comparisons of structural geometry, detachment dip fluctuations and thickness changes. An alternative and mechanically equivalent approach would be to fix λ_b as constant, and solve for μ or μ_b and explore predicted changes in coefficients of friction at the detachment level or within the wedge.

Our predictions show a variation in λ_b from sublithostatic to supralithostatic. Previous workers (i.e. Bilotti and Shaw, 2005) obtained a result of $\lambda \approx 0.90$ for the deepwater Niger Delta toe using averaged bathymetric slope and basal detachment angles for the whole profile. Our results for λ_b range from 0.8 to 1.2, but note that we have mapped this variation over the kilometre scale rather than the tens of kilometre scale, and we have made no attempts to average our input data.

We believe our predictions of supralithostatic λ_b presented above are significant and provide insight into the processes occurring in submarine fold-thrust belts, such as the Niger Delta. Although, there is limited published evidence for supralithostatic overpressures in well data, it has been demonstrated in outcrop examples from fold-thrust belts (Pyrenees), exhumed subducted slabs (Italy, Corsica) and greenschist facies gold deposits (Canada). Lithostatic values have been observed in drilling pressure data in the Barbados Toe within a relatively shallow section that did not reach the basal detachment, some 1.5 kilometres inboard of the leading toe thrust. These examples document the reality of supralithostatic λ_b in a variety of settings and likely due to a variety of different processes. Our analysis predicts extreme overpressures in the toe region of the Niger Delta, although testing this prediction remains extremely hazardous. Further work to pinpoint the exact detachment geometry would provide more accurate results, which may come from better quality 3D seismic data and careful kinematic reconstructions.

Acknowledgements

The authors thank CGG Veritas and the Virtual Seismic Atlas (http://www.seismicatlas.org) for access to seismic data and SMT and Midland Valley for access to software. The authors thank the AAPG Foundation Grants Society for financial support through the Gordon I. Atwater Memorial Grant and the Australian Research Council for additional funding support through Discovery Grant DP0878258. David Iacopini is thanked for discussions on the deepwater Niger Delta. This manuscript forms TRaX # xxx.

References

Bilotti, F., Shaw, J.H., 2005. Deep-water Niger Delta fold and thrust belt modeled as a critical taper wedge: The influence of elevated basal fluid pressure on structural styles. American Association of Petroleum Geologists Bulletin. 89(11), 1475-1491.

Briggs, S.E., Davies, R.J., Cartwright, J.A., Morgan, R. 2006. Multiple detachment levels and their control on fold styles in the compressional domain of the deepwater west Niger Delta. Basin Research. 18, 435-450.

Butler, R.W.H., Paton, D.A., 2010. Evaluating lateral compaction in deepwater fold and thrust belts: How much are we missing from “nature’s sandbox”? Geological Society of America Today. 20(3).

Byerlee, J., 1978. Friction of rocks: Pure and Applied Geophysics. 116, 615-626.

Cobbold, P.R., Clarke, B.J., Løseth, H., 2009. Structural consequences of fluid overpressure and seepage forces in the outer thrust belt of the Niger Delta. Petroleum Geoscience. 15, 3-15.

Cobbold, P.R., Gilchrist, G., Scotchman, I., Chiossi, D., Chaves, F.F., Gomes De Souza, F., Lilletveit, R., 2010. Large submarine slides on a steep continental margin (Camamu Basin, NE Brazil). Journal of the Geological Society, London. 167, 583-592.

Corredor, F., Shaw, J. H., Bilotti, F., 2005. Structural styles in the deep-water fold and thrust belts of the Niger Delta. American Association of Petroleum Geologists Bulletin. 89(6), 753-780.

Cosgrove, J.W., 2001. Hydraulic fracturing during the formation and deformation of a basin: A factor in the dewatering of low-permeability sediments. American Association of Petroleum Geologists Bulletin. 85(4), 737-748.

Dahlen, F. A., 1990. Critical taper model of fold-and-thrust belts and accretionary wedges. Annual Review of Earth and Planetary Sciences. 18, 55- 99.

Dahlen, F.A., Suppe, J., Davis, D.M., 1984. Mechanics' of fold-and-thrust belts and accretionary wedges: cohesive Coulomb theory. Journal of Geophysical Research. 89, 10087-10101.

Davis, D., Suppe, J., Dahlen, F.A., 1983. Mechanics of fold-and thrust belts and accretionary wedges. Journal of Geophysical Research. 88(B2), 1153-1172.

Dewey, J.F., 1965. Nature and Origin of Kink-Bands. Tectonophysics. 1(6), 459-494.

Dobson, D.P., Meredith, P.G., Boon, S.A., 2002. Simulation of subduction zone seismicity by dehydration of serpentine. Science. 298, 1407-1410.

Doust, H., Omatsola, E., 1990. Niger Delta, in: Edwards, J.D., Santogrossi, P.A. (Eds.), Divergent/passive margin basins. American Association of Petroleum Geologists Memoir 48, pp. 201-238.

Fort, X., Brun, J., Chauvel, F., 2004. Salt tectonics on the Angolan margin, synsedimentary deformation processes. American Association of Petroleum Geologists Bulletin. 88(11), 1523-1544.

Healy, D., 2011. Dehydration-induced brittle vein in a serpentinite mylonite: Photograph of the month. Journal of Structural Geology. 33, 757.

Healy, D., Reddy, S., Timms, N., Gray, E., Vitale Brovarone, A., 2009. Trench-parallel fast axes of seismic anisotropy due to fluid-filled cracks in subducting slabs. Earth and Planetary Science Letters. 283(1-4), 75-86.

Higgins, S., Davies, R.J., Clarke, B., 2007. Antithetic fault linkages in a deep water fold and thrust belt. Journal of Structural Geology. 29, 1900-1914.

Hoshino, K., Inami, K., Iwamura, S., Koide, H., Mitsui, S., 1972. Mechanical properties of Japanese Tertiary sedimentary rocks under high confining pressures. Japanese Geological Survey Report 244, pp. 0-200.

Hubbert, M.K., Rubey, W.M., 1959. Role of fluid pressure in mechanics of overthrust faulting. Geological Society of America Bulletin. 70, 115-166.

King, R.C., Hillis, R.R., Tingay, M.R.P., 2009. Present-day stress and neotectonic provinces of the Baram Delta and deepwater fold-thrust belt. Journal of the Geological Society, London. 166, 197-0200.

MacDonald, J.D., King, R., Hillis, R.R., Backé, G., 2010. Structural style of the White Pointer and Hammerhead delta—deepwater fold-thrust belts, Bight Basin, Australia. The Australian Petroleum Production and Exploration Association Journal. 50, 487-510.

Maloney, D., Davies, R., Imber, J., Higgins, S., King, S., 2010. New insights into deformation mechanisms in the gravitationally driven Niger Delta deep-water fold and thrust belt. American Association of Petroleum Geologists Bulletin. 94(9), 1401-1424.

McClay, K., Dooley, T., Zamora, G., 2003. Analogue models of delta systems above ductile substrates, in: Van Rensbergen, P., Hillis, R.R.., Maltman, A.J., Morley, C.K. (Eds.), Subsurface sediment mobilization. Geological Society, London, Special Publication 216, pp. 411-428.

McClay, K.R., Doole¥, T., Ferguson, A., Poblet J., 2000. Tectonic evolution of the Sanga Sanga block, Mahakam delta, Kalimantan, Indonesia. American Association of Petroleum Geologists Bulletin. 84(6), 765-786.

McClay, K.R., Dooley, T., Lewis, G. 1998. Analog modelling of progradational delta systems. Geology. 26(9), 771-774.

Moore, J.C., von Huene, R., 1980. Abnormal pore pressure and hold instability in forearc regions: A preliminary report. Ocean Margin Drilling Project report. 0-29.

Moore, J.C., 1982. Offscraping and underthrusting of sediment at the deformation front of the Barbados Ridge: Deep Sea Drilling Project leg 78A. Geological Society of America Bulletin. 93, 1065-1077.

Morley, C.K., 2007. Interaction between critical wedge geometry and sediment supply in a deepwater fold belt, NW Borneo. Geology. 35, 139-142.

Morley, C.K., Guerin, G., 1996. Comparison of gravity-driven deformation styles and behaviour associated with mobile shales and salt. Tectonics. 15, 1154-1170.

Mourgues, R., Cobbold, P.R. 2006. Sandbox experiments on gravitational spreading and gliding in the presence of fluid overpressures. Journal of Structural Geology. 28, 887-901.

Osborne, M.J., Swarbrick, R.E., 1997. Mechanisms for Generating Overpressure in Sedimentary Basins: A Reevaluation. American Association of Petroleum Geologists Bulletin. 81(6), 1023-1041.

Rowan, M.G, Peel, F.J., Vendeville, B.C., 2004. Gravity-driven fold belts on passive margins: in: McClay, K.R. (Ed.), Thrust tectonics and hydrocarbons systems. American Association of Petroleum Geologists Memoir 82, pp. 157-182.

Schult-Ela, D.D., 2001. Excursis on gravity gliding and gravity spreading. Journal of Structural Geology.23, 725-731.

Sibson, R.H., 1995. Selective fault reactivation during basin inversion: potential for fluid redistribution through fault-valve action: in Buchanan, J. G., Buchanan, P.G. (Eds.), Basin Inversion. Geological Society, London, Special Publication 88, pp. 3-19.

Sibson, R.H., Robert, F., Poulsen, K.H., 1988. High-angle reverse faults, fluid-pressure cycling, and mesothermal gold-quartz deposit. Geology.16, 551-555.

Simpson, G., 2011. Mechanics of non-critical fold-thrust belts based on finite element models. Tectonophysics. 499, 142-155.

Simpson, G., 2010. Formation of accretionary prisms influenced by sediment subduction and supplied by sediments from adjacent continents. Geology. 38, 131-134.

Smith, W.H.F., Sandwell, D. T., 1997. Global seafloor topography from satellite altimetry and ship depth soundings. Science. 277, 1957-1962.

Suppe, J., 2007. Absolute fault and crustal strength from wedge tapers. Geology. 35, 1127-1130.

Suppe, J., 1983. Geometry and kinematics of fault-bend folding. American Journal of Science. 283, 684-721.

Swarbrick, R.E., Osborne, M.J., Yardley, G.S., 2002. Comparison of overpressure magnitude resulting from the main generating mechanisms, in Huffman, A.R., Bowers, G.L., (Eds.), Pressure regimes in sedimentary basins and their prediction. American Association of Petroleum Geologists Memoir 76, pp. 1-12.

Teixell, A., Durney, D.W., Arboleya, M., 2000. Stress and fluid control on decollement within competent Limestone. Journal of Structural Geology. 22, 349-371.

Figure Captions

Figure 1: a) High resolution bathymetric image of the Niger Delta, West Africa interpreted from a dense two-dimensional seismic reflection database and the global bathymetric database (after Corredor et al. 2005; Smith and Sandwell, 1997) with b) an approximate outline of the five structural provinces including the extensional province, mud-diapir province, inner fold-thrust belt, detachment fold province and outer fold-thrust belt where the data for this study is located (modified after Corredor et al. 2005).

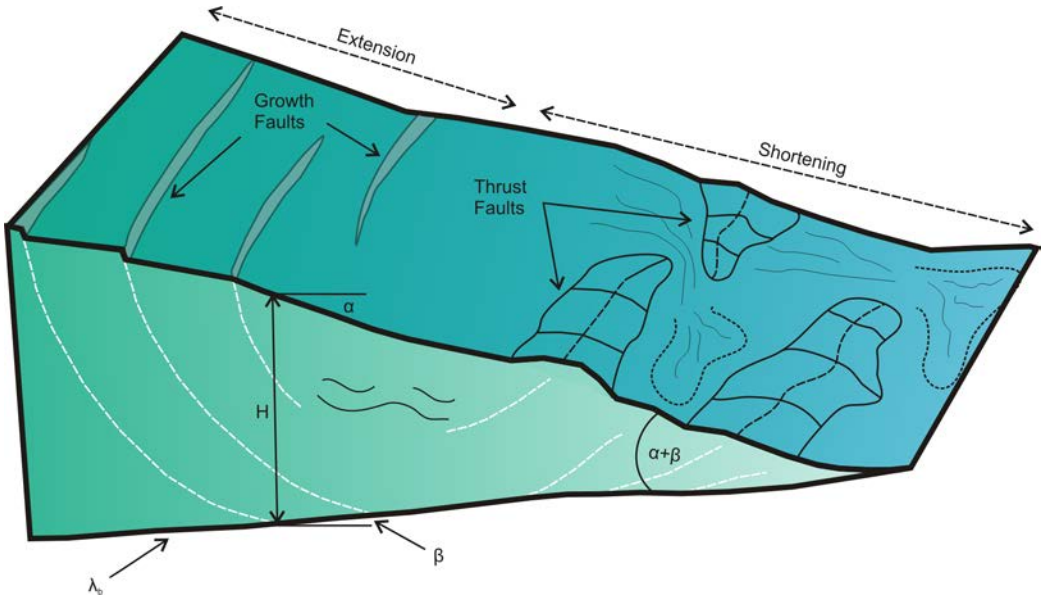

Figure 2: Simplified schematic of a critically tapered deltaic wedge (modified after Dahlen, 1990). Linkage between extension at the top and shortening at the toe result in the wedge shaped geometry. Note the basal detachment angle β (measured from horizontal, positive downward and negative upward) and seabed angle α (measured from horizontal; positive upward and negative downward). H is the thickness of the wedge between any pair of α-β points. The taper angle α+β is the angle between the seabed and basal detachment and is a first order control on the basal and wedge pore fluid pressure ratio.

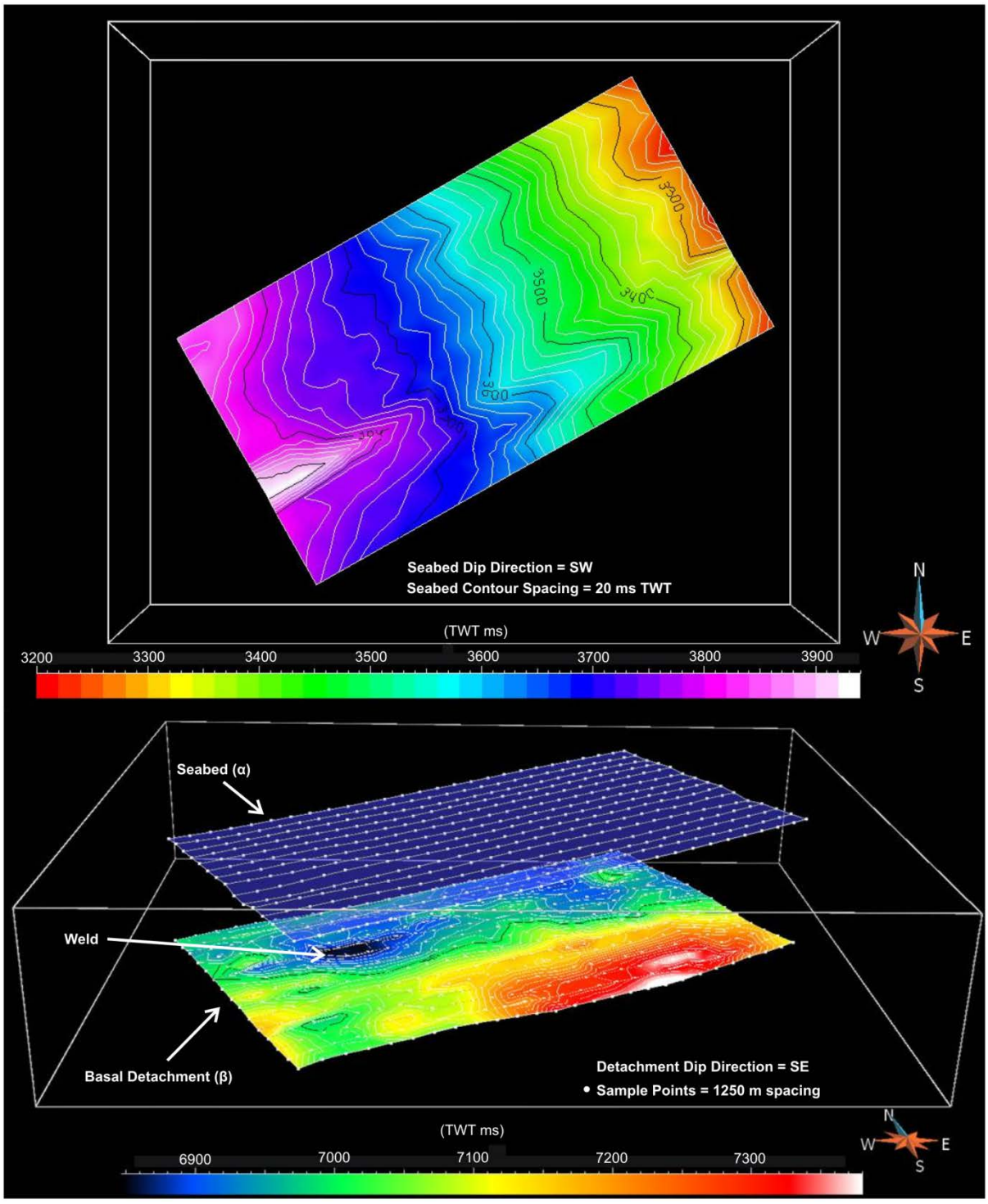

Figure 3: Interpreted horizon map for the seabed (α) and basal detachment (β) in the study area. The sample points for both α and β are represented by the white dots and are spaced at 1250 m throughout the study area. The lines connecting the sample points are the traces of the extracted 2D seismic data used in the study to map the seabed and basal detachment surfaces. Detachment dip is approximately to the southeast with blue representing shallower parts of the basal detachment and red representing the deepest parts. A weld has been identified in the seismic data and its position is indicated on the mapped basal detachment horizon.

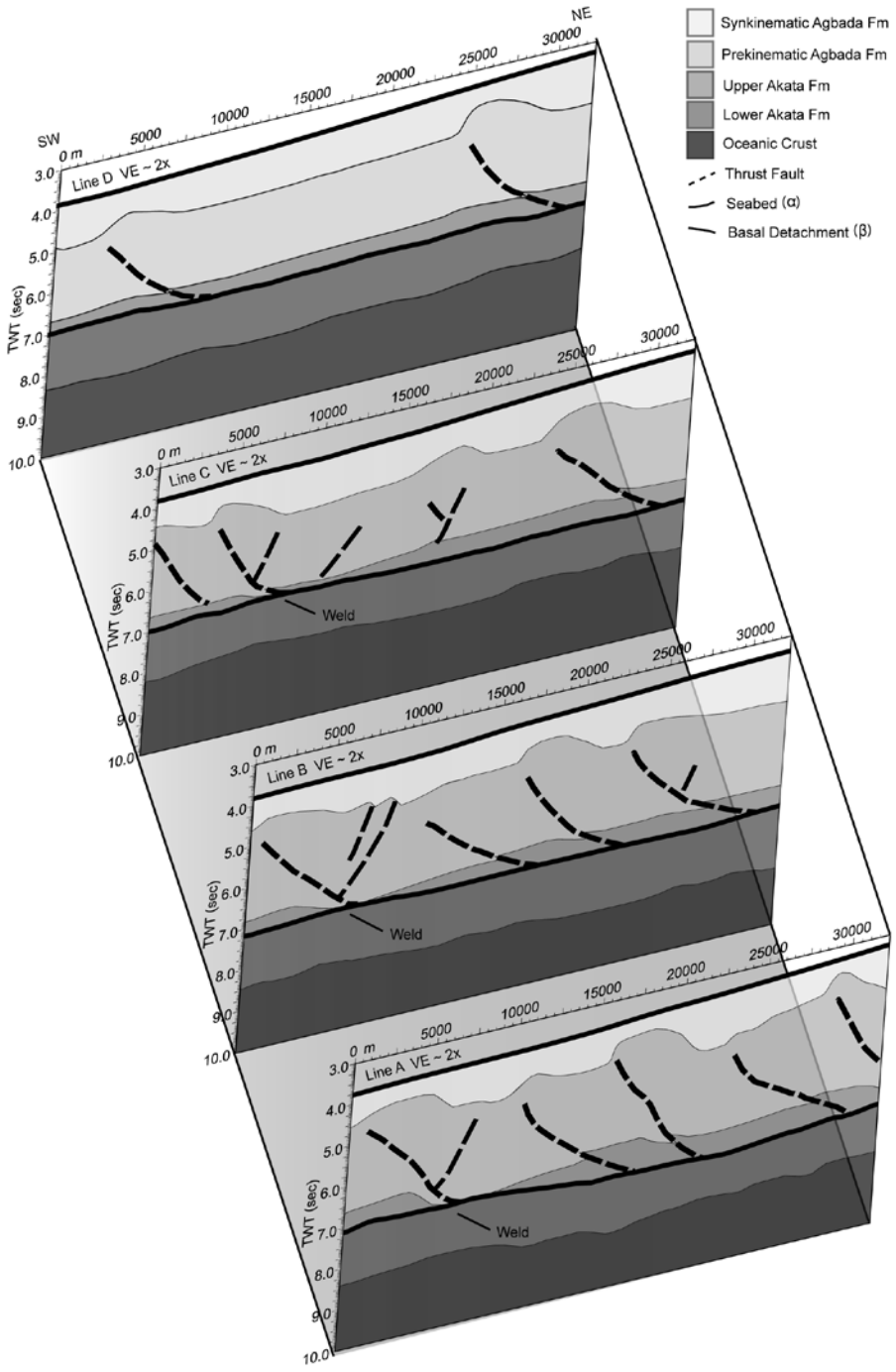

Figure 4: Box diagram of the study area with four interpreted 2D seismic lines (location bottom left) illustrating the change in geometry across the system. Solid black lines represent the basal detachment (bottom; β angle) and the seabed (top; α angle). Stratigraphy is divided based on Corredor et al. (2005) with prekinematic strata (green) representing Agbada Formation prior to thrusting and synkinematic strata (purple) representing ongoing deposition during active deformation. The Akata Formation (upper blue; lower yellow), particularly the mid Akata reflection, is interpreted to act as the basal detachment in this location. Interpreted thrust faults are represented by black dashed lines. A prominent weld is interpreted in seismic lines A, B and C whereby the Agbada Formation has detached directly above the Lower Akata Formation, at the base of the basal detachment. Frequency and complexity of thrust faulting is more prominent in the southeast where several fore-thrusts and back-thrusts occur and decreases in the northwest to two fore-thrusts.

Figure 5: Stratigraphy of the Niger Delta (after Corredor et al. 2005) demonstrating the basis for the interpreted “packages” in Figure 4. Most relevant to this study in the offshore deepwater fold-thrust belt are the Akata Formation (overpressured mud which forms the basal detachment zone) and the Agbada Formaton (deltaic deposits). Numbers 1-5 on the accompanying seismic section represent the following stratigraphic positions: 1) top of prekinematic reflection within the Agbada Formation, 2) base Agbada Formation and top level of detachment, 3) mid Akata Formation reflection and interpreted basal detachment level, 4) top Cretaceous carbonate rocks and 5) top oceanic crust (crystalline basement).

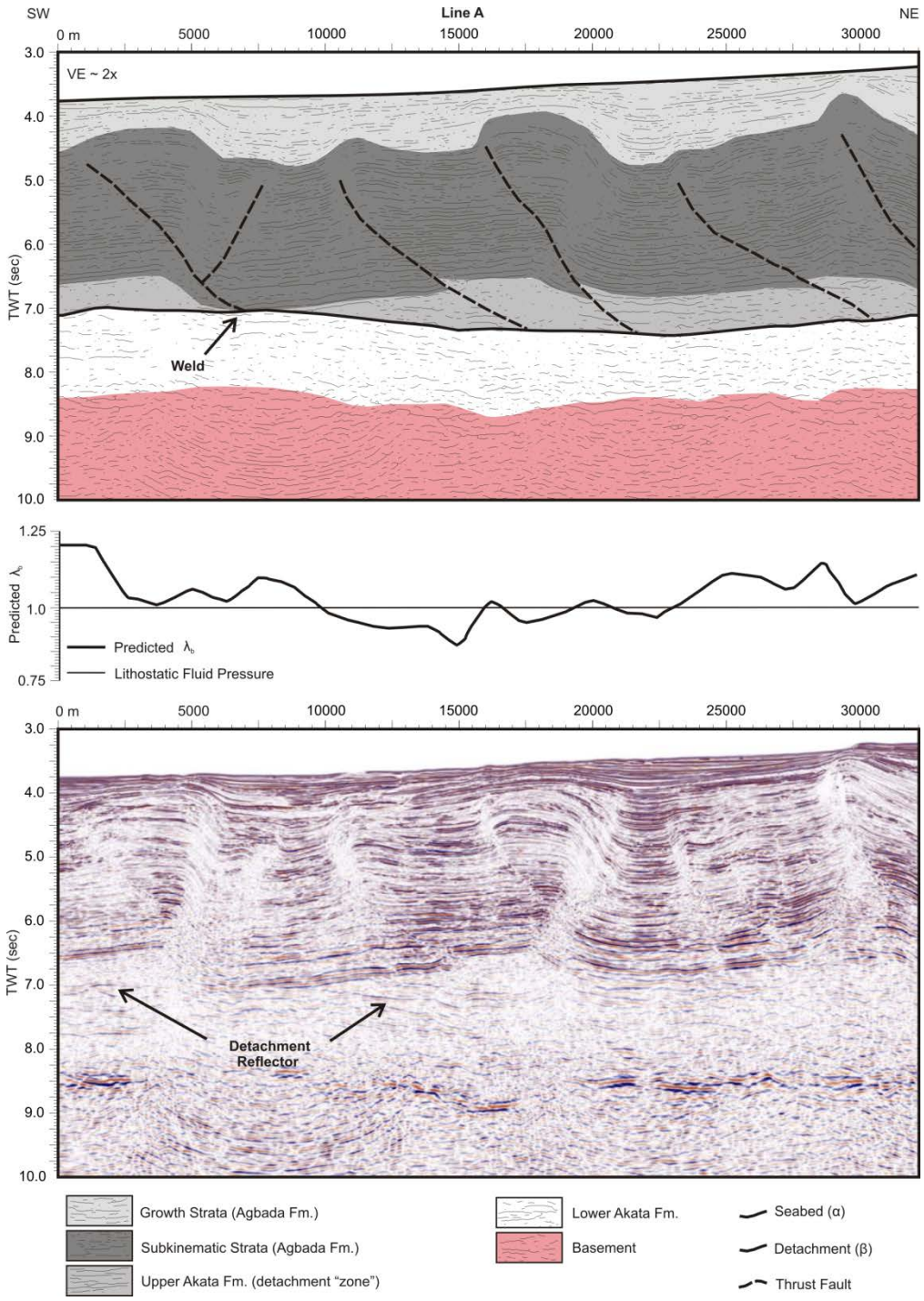

Figure 6: Line drawing of 2D seismic line A (top) with position of basal detachment and bathymetric slope represented by solid black lines. The black dashed lines represent thrust faults and a weld is observed in the southwest side of the section where the Agbada Formation is welded to the mid Akata Formation reflector following withdrawal of the upper Akata Formation. Uninterpreted 2D seismic line (bottom) shows position of prominent amplitude reflections used to pick basal detachment at the mid Akata Formaton reflection level. The predicted λ_b vs. distance plot for the corresponding 2D seismic section is shown (middle) and demonstrates areas of sublithostatic and supralithostatic basal pore fluid pressure.

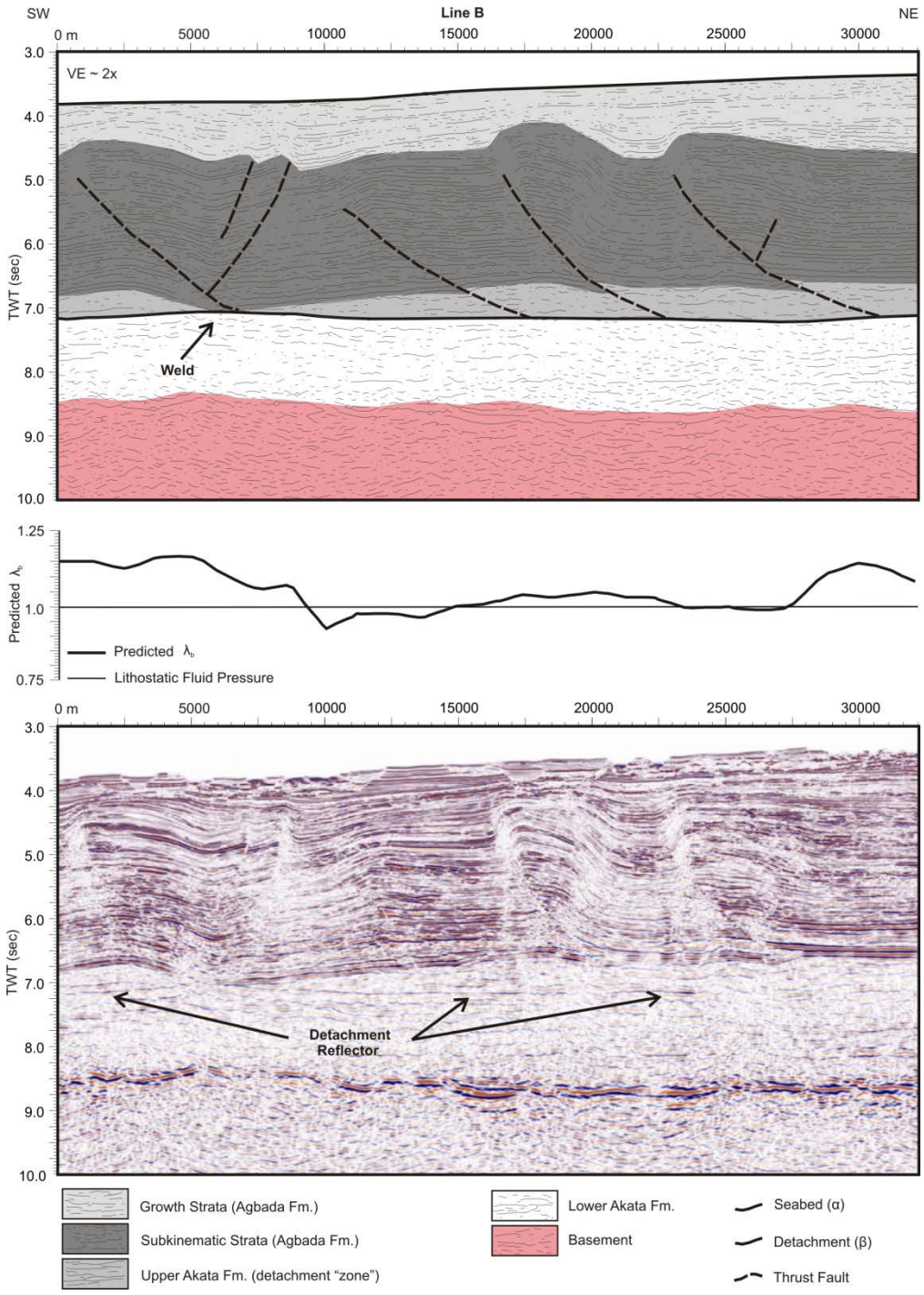

Figure 7: Line drawing of 2D seismic line B (top) with position of basal detachment and bathymetric slope represented by solid black lines. The black dashed lines represent thrust faults and a weld is observed in the southwest side of the section where the Agbada Formation is welded to the mid Akata Formation reflector following withdrawal of the upper Akata Formation. The dip of the basal detachment is much more uniform in this section relative to Figure 6. Uninterpreted 2D seismic line (bottom) shows position of prominent amplitude reflections used to pick basal detachment at the mid Akata Formaton reflection level. The predicted λ_b vs. distance plot for the corresponding 2D seismic section is shown (middle) and demonstrates areas of sub vs. supralithostatic basal pore fluid pressure with an overall lithostatic to supralithostatic response for the given 2D seismic line based on the Dahlen (1990) Critical Taper Wedge equation.

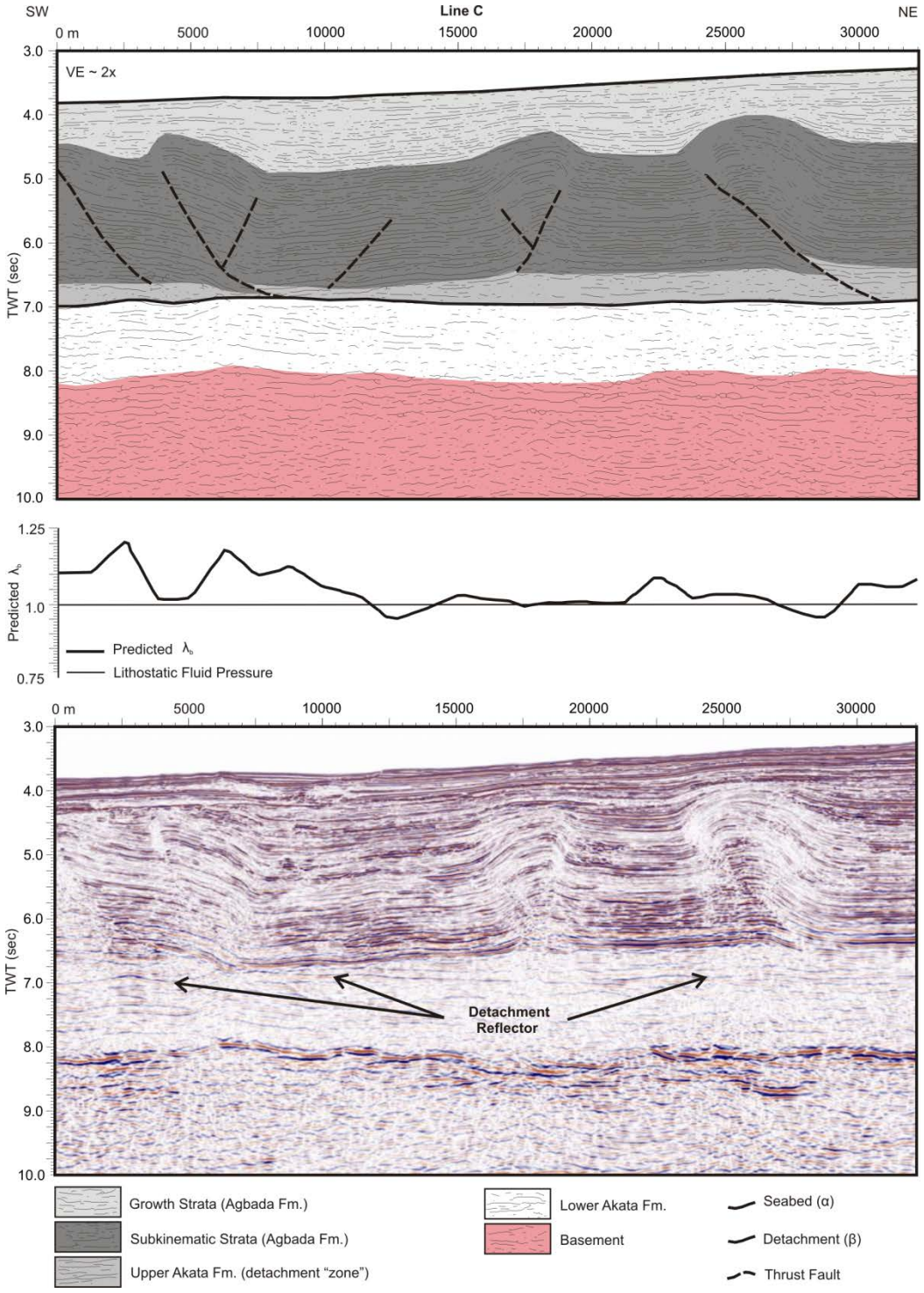

Figure 8: Line drawing of 2D seismic line C (top) with position of basal detachment and bathymetric slope represented by solid black lines. The black dashed lines represent thrust faults and the onset of a weld is observed in the southwest side of the section where the Agbada Formation is welded to the mid Akata Formation reflector following withdrawal of the upper Akata Formation. Uninterpreted 2D seismic line (bottom) shows position of prominent amplitude reflections used to pick basal detachment at the mid Akata Formaton reflection level. The predicted λ_b vs. distance plot for the corresponding 2D seismic section is shown (middle) and demonstrates areas of sub vs. supralithostatic basal pore fluid pressure based on the Dahlen (1990) Critical Taper Wedge equation.

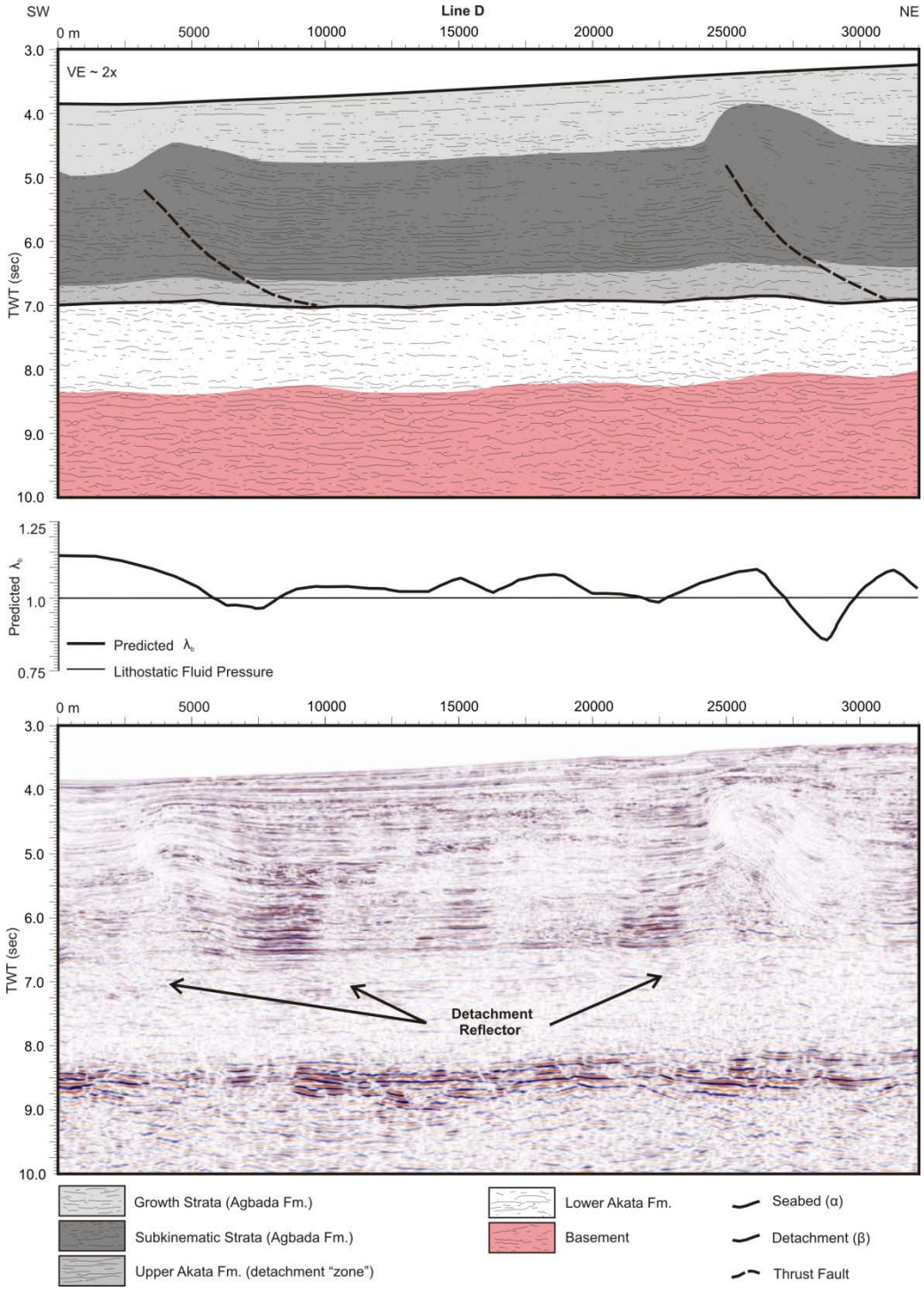

Figure 9: Line drawing of 2D seismic line D (top) with position of basal detachment and bathymetric slope represented by solid black lines. The black dashed lines represent thrust faults. The dip of the basal detachment is much more uniform in this section relative to Figures 6-8 while the structure is much less complex, with just two forward verging thrust faults in the section and an absence of back-thrust faulting. Uninterpreted 2D seismic line (bottom) shows position of prominent amplitude reflections used to pick basal detachment at the mid Akata Formation reflection level. The predicted λ_b vs. distance plot for the corresponding 2D seismic section is shown (middle) and demonstrates areas of sub vs. supralithostatic basal pore fluid pressure based on the Dahlen (1990) Critical Taper Wedge equation.

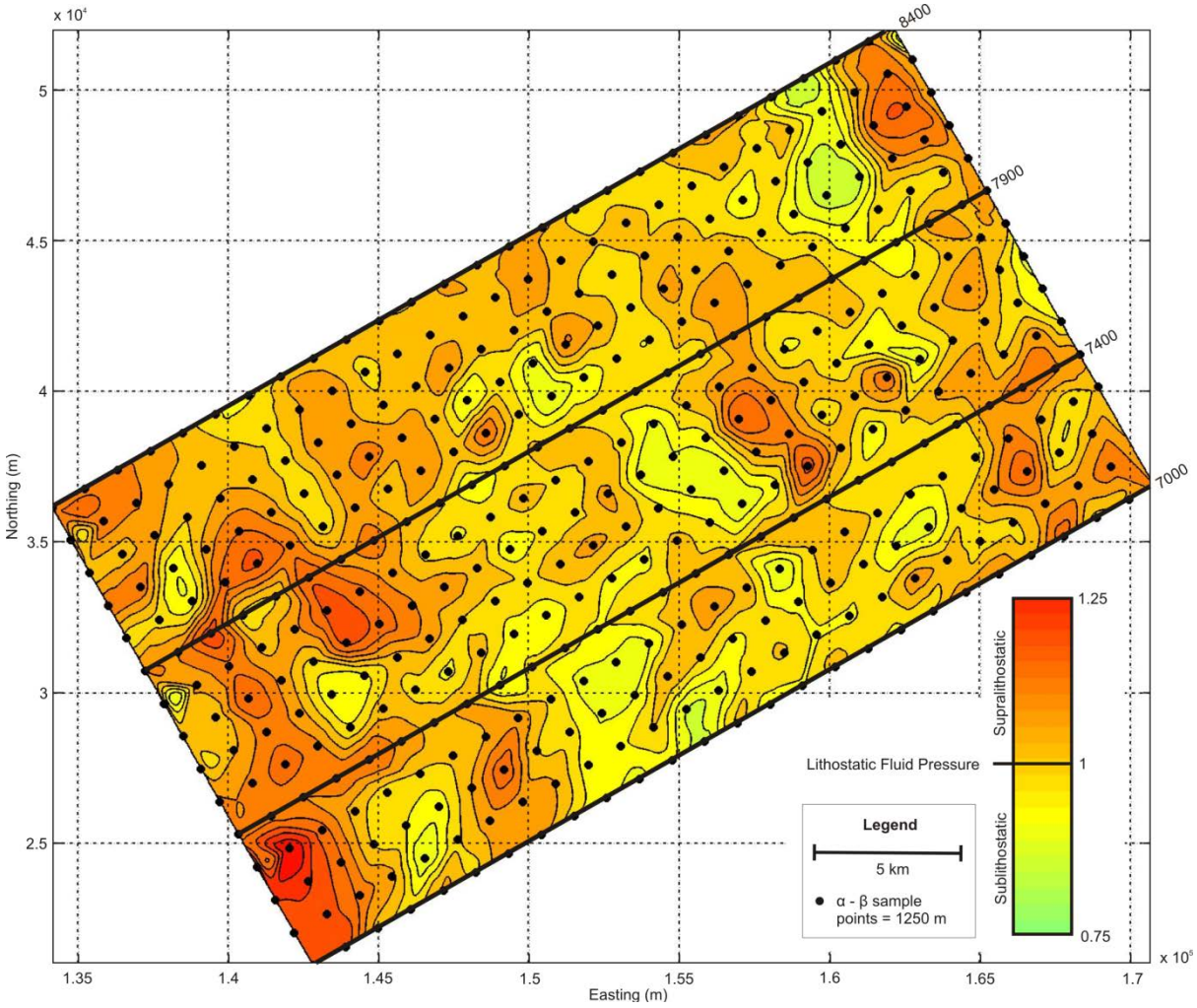

Figure 10: Basal lamda map showing the distribution of pore fluid pressure at the level of the basal detachment in the study area. Position of four 2D seismic lines presented in this work (Figs. 6-9) represented by black lines. Red areas indicate supralithostatic pore fluid pressure while light green to yellow areas represent sublithostatic pore fluid pressure.

Figure 11: Schematic of deepwater Niger Delta showing location of upper and lower detachment surfaces at the base of the Agbada Formation (e) and at the level of the mid Akata Formation reflection (f; after Maloney et al., 2010).

NOTE:
These figures/tables/images have been removed to comply with copyright regulations.
They are included in the print copy of the thesis held by the University of Adelaide Library.

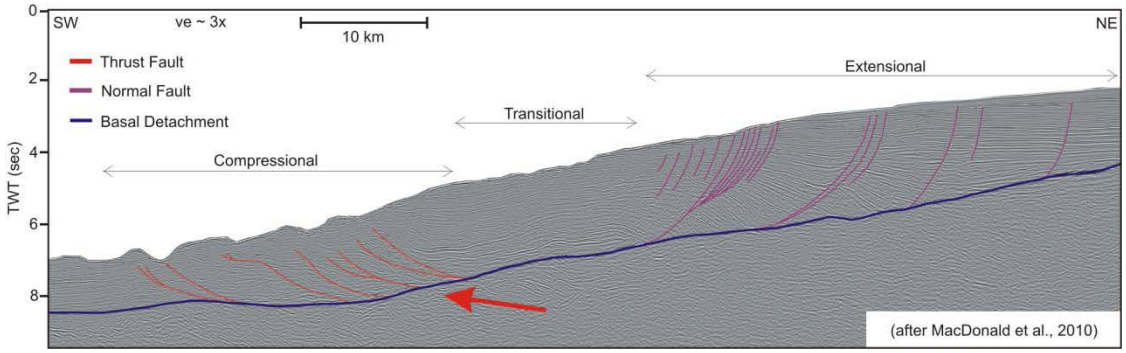

Figure 12: Compilation of 2D seismic lines from submarine wedges including: deepwater Niger Delta toe (a; Bilotti and Shaw, 2005), Orange Delta offshore Namibia (b; Butler and Paton, 2010), offshore Angola (c; Fort et al. 2004) and the Ceduna Delta offshore South Australia (d; MacDonald et al. 2010). Evidence for negative beta or seaward dipping basal detachment is present in each of these examples (red arrows) particularly the western side of the Niger Delta toe (a) where the detachment changes from landward dipping to seaward dipping beneath the deepwater fold-thrust belt. In the Orange Delta (b), the entire basal detachment is seaward dipping or negative, and the deepwater fold-thrust belt is expressed as tightly spaced imbricate thrust faults linked to up-dip extension. Although offshore Namibia

(c) involves a salt rather than an overpressured shale detachment the basal detachment is also negative and dips offshore thus lowering the taper angle of the wedge. Finally, the Ceduna Delta offshore South Australia (d) has a seaward dipping basal detachment that is clearly defined in 2D seismic data and exhibits a linked system of up-dip extension and down-dip shortening indicating it too is deforming as a critically tapered wedge with a low taper angle. Based on the Critical Taper Wedge equation (Dahlen, 1990; Equation 2), areas with negative beta imply a net decrease in the taper angle for the wedge(s), and a corresponding high level of basal pore fluid pressure for the wedge to slide.

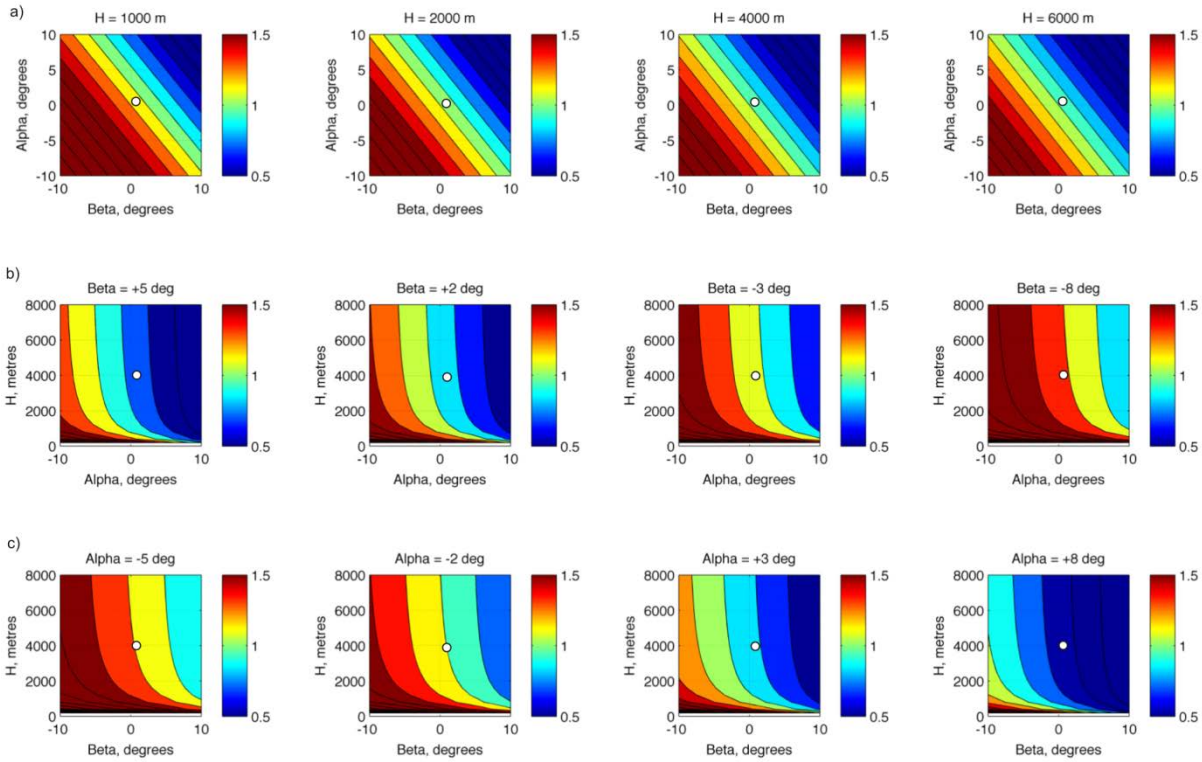

Figure 13: Sensitivity analysis for Dahlen (1990) Critical Taper Wedge equation using set input parameters from Bilotti and Shaw (2005). Colour bar on right of each plot represents range of λ_b values from sublithostatic (0.5) to supralithostatic (1.5). The objective of the sensitivity analysis is to demonstrate how sensitive the equation is to varying parameters of H (thickness) alpha (bathymetric slope) and beta (basal detachment angle). The top four analyses (a) are for a fixed wedge thickness of H=1000, 2000, 4000 and 6000 m with alpha and beta on the y and x axes. White dot represents position of alpha = 1 and beta = 1 with corresponding λ_b value displayed on scale to right of image. This shows λ_b is not very sensitive to variations in alpha and beta. The next analysis (b) is for fixed beta = +5, +2, -3 and -8 degrees. Here H is on the y axis and alpha on the x axis. White dot represents alpha = 1 and beta = 1 with corresponding λ_b value displayed on scale to right of image. This example shows that λ_b is very sensitive to low values of H (i.e. rapid variations in λ_b colour bars for small variations in H or alpha and beta at very low H). Final analysis (c) is for fixed alpha = +5, +2, -3 and -8 degrees. Again, H is on the y axis and beta on the x axis. White dot represents alpha = 1 and beta = 1 with corresponding λ_b value displayed on scale to right of image. This example also shows that λ_b is very sensitive to low values of H (i.e. rapid variations in λ_b colour bars for small variations in H or alpha and beta at very low H).

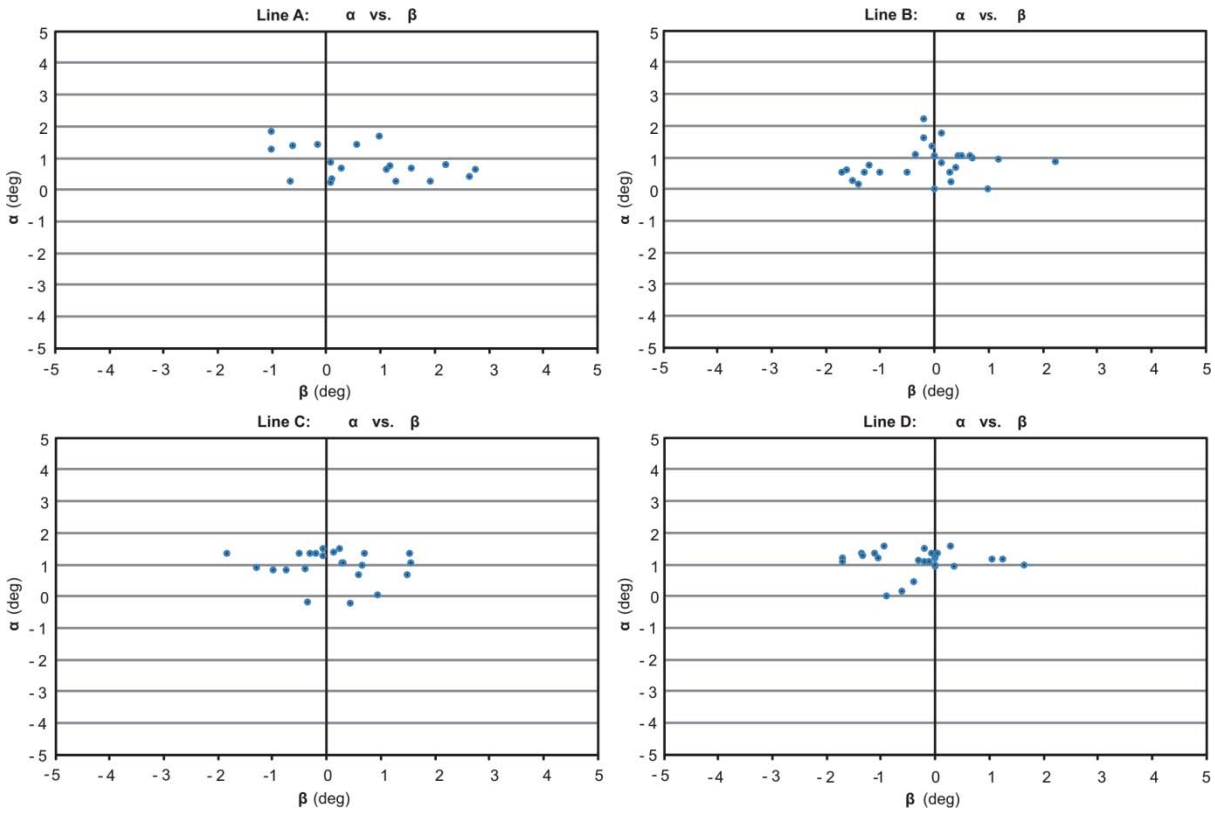

Figure 14: Alpha vs. beta plots for seismic lines A-D (Figures 6-9) illustrating a scattered effect from the measured values of alpha and beta. The clear inverse relationship between alpha and beta observed in previous studies (i.e. Bilotti and Shaw, 2005) is not always observed in every plot, likely due to the localised variations in detachment and seabed angles along the 2D seismic lines.

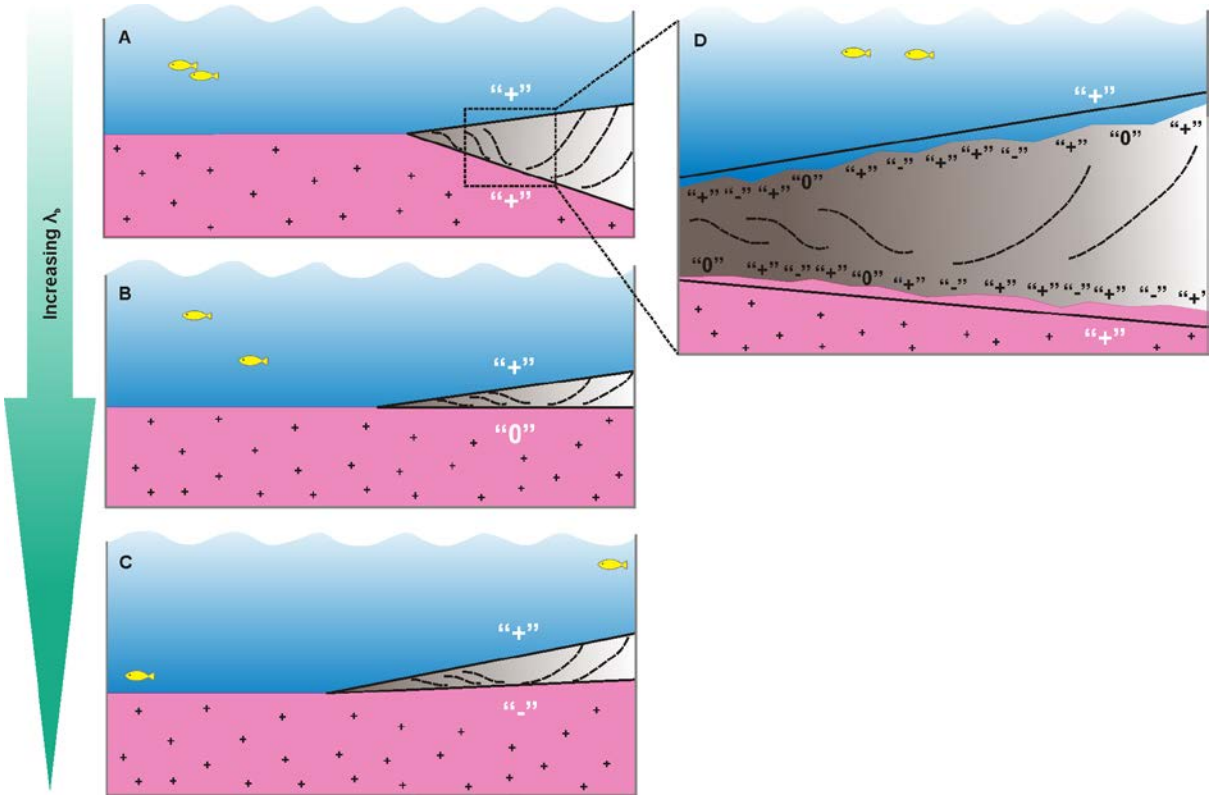

Figure 15: Schematic of changing taper angle within a series of idealised submarine wedges. Positive alpha and beta in a submarine wedge (a) will result in a sublithostatic λ_b value. With a flat basal detachment (b) or beta = 0 degrees and a positive alpha angle we see an increase in λ_b value. Finally, a negative beta or seaward dipping basal detachment (c) will result in an increased λ_b value (see Figure 13; sensitivity analysis). Along each scenario at the kilometre scale there are often small fluctuations in both alpha and beta angles (d) where parts of an overall positive beta will exhibit small patches of negative beta, such as is observed in Figures 6-9. The methodology used in this study is detailed enough to capture these small fluctuations rather than simply averaging the entire wedge profile (i.e. d; solid black line vs. actual profile marked with "-" and "+" symbols).

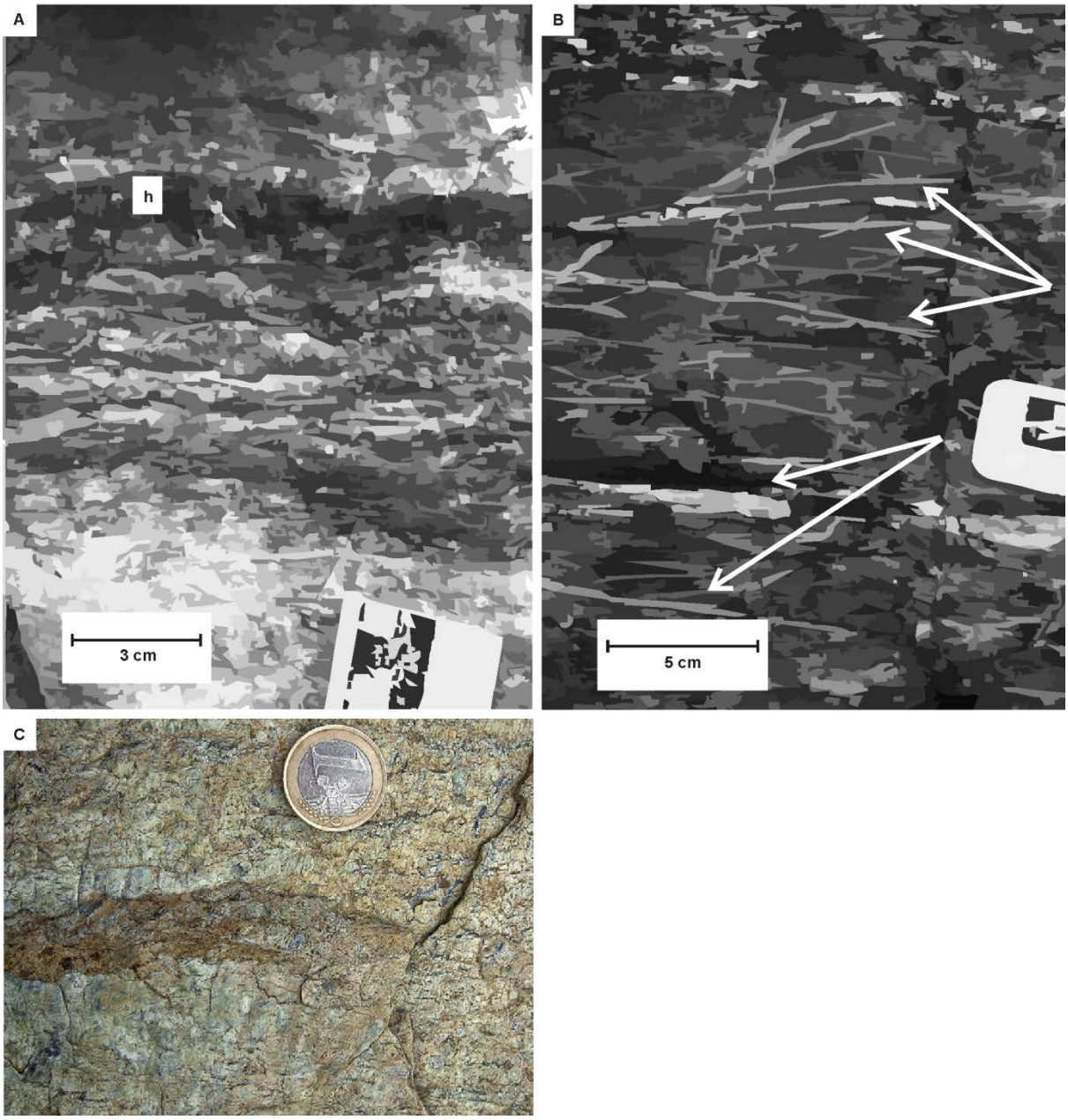

Figure 16: Photo trace of the Larra Thrust fault zone (top) and trench parallel veining in a subducted slab (bottom). Dense veining at the fault zone centre (a) is dominantly parallel to the bedding and thrust. Veins compose almost 100% of the rock volume with minor slivers of limestone preserved (labelled h). View of damage zone (b) 110-140 cm above the reference fault zone centre. Horizontal veins (white arrows) present are again parallel to thrust (after Teixell et al. 2000). Vein in bottom image (c) contains olivine (light brown), clinohumite (dark red), clinopyroxene and opaque oxides. The host rock is an antigorite mylonite with a strong mineral stretching lineation oriented at high angle to the vein margins (elongate blue crystal aggregates). The vein assemblage records a prograde dehydration with respect to the host rock and metamorphic conditions have been estimated at P¼ 2–2.5 GPa and T ¼550–600 C, i.e. eclogite facies. The curved vein tips, sharp vein margins and narrow apophyses attest to the brittle origin of the vein fracture. Prograde dehydration of the serpentinite in a subduction zone led to brittle hydrofracture (Healy, 2011).

Table Captions

Table 1

Parameter		Input Value	Method of Determination
Density of wedge material	ρ	2400 kg/m^3	Deepwater well-density logs (approximate; Bilotti and Shaw, 2005)
Fluid pressure ratio	λ	0.54 ± 0.15	Pressure data from 13 deepwater wells (Bilotti and Shaw, 2005)
Basal step-up angle	S_b	22°	Measured from seismic data (Bilotti and Shaw, 2005)
Internal coefficient of friction	μ	0.91 ± 0.06	Calculated from basal step-up angle (Bilotti and Shaw, 2005)
Basal coefficient of friction	μ_b	0.91 ± 0.3	Similar to wedge material strength and Byerlee's Law (Byerlee, 1978)
Wedge cohesion	C	10 MPa	Hoshino et al. (1972)
Gravitational Acceleration Constant	g	9.81 m/s^2	Gravitational Constant
Density of Water Column	ρ_f	1.02 g/cm ^{3}	Density of seawater

Table 1: *title:* Critical Taper Wedge Equation Parameters. *Description*: Table 1 displays each parameter of the Critical Taper Wedge equation, the input value used in our model and the method of determination of the input value. Due to lack of public domain data for the deepwater Niger Delta Toe, most input values were based on published values by Bilotti and Shaw (2005).

Table 2

Location	α (deg)	β (deg)	Observed λ	λ Source
Barbados overall taper	1.0 ± 0.5	8.0 ± 0.8	0.8 ± 0.05	Mud weight in a well on Barbados (Moore & von Huene, 1980)
Barbados toe	0.7 ± 0.2	4.5 ± 0.5	≈ 1	Inadvertent packer experiment in hole 542 (Davis et al., 1983; Moore et al., 1982)
Makran	1.6 ± 0.3	2.0 ± 1.0	≈ 1	Mud weight in a well offshore Pakistan Makran accretionary wedge (Davis et al., 1983)
Corsica & Italy	-	-	Supralithostatic	Dehydration induced extensional veins in subducted slab (Healy et al., 2009; Healy, 2011)
Pyrenees	-	-	Supralithostatic	Detachment parallel extensional veins in limestone on Larra Thrust (Teixell et al., 2000)
Abitibi Au-Qtz veins	-	-	Supralithostatic	Horizontal gold-quartz veins, Abitibi greenstone belt, Canada (Sibson et al., 1988)

Table 2: *title:* Evidence for Observed Fluid Pressure Ratios $\lambda = \lambda_b$. *Description*: Table 2 illustrates worldwide areas that have demonstrated evidence for lithostatic to supralithostatic pore fluid pressure, either by drilling measurements in sedimentary basins or physical examples in outcrop. Measured values for alpha and beta, the observed lamda value and the source of the data are presented for each area.

4.2 Paper 2

MacDonald, J.D., King, R., Hillis, R.R., and Backé, G., (2010): Structural style of the White Pointer and Hammerhead Delta—Deepwater Fold-Thrust Belts, Bight Basin, Australia. *The Australian Association of Petroleum Production and Exploration Journal*, v 50, 487-510.

Lead author
Justin MacDonald

STRUCTURAL STYLE OF THE WHITE POINTER AND HAMMERHEAD DELTA—DEEPWATER FOLD-THRUST BELTS, BIGHT BASIN, AUSTRALIA

J.D. MacDonald, R.C. King, R.R. Hillis and G. Backé
Australian School of Petroleum
Centre for Tectonics, Resources and Exploration (TRaX)
University of Adelaide
North Terrace
Adelaide SA 5005
jmacdonald@asp.adelaide.edu.au
rking@asp.adelaide.edu.au
rhillisdetcrc@gmail.com
guillaume.backe@adelaide.edu.au

ABSTRACT

The White Pointer and Hammerhead delta—deepwater fold-thrust belts (DDWFTBs) are located in the Ceduna Sub-basin of the Bight Basin, offshore southern Australia. These DDWFTB systems are structurally independent deltaic wedges of late Albian-Santonian and late Santonian-Maastrichtian age, which detach above Santonion-Albian marine shales of the Blue Whale and Tiger supersequences, respectively. The DDWFTBs are constrained by the position of the delta lobes, one in the east and one in the west, each of which are defined by the position of their associated fold-thrust belts. Geometry of the structures in the DDWFTBs are dependent on the interaction of numerous variables including sediment input, amount of progradation, shape and depth of the detachment, thickness and lithology of the detachment substrate, overpressure development and presence of basement structures. Geometric differences between the two DDWFTBs, particularly the two deepwater fold-thrust belts, results in different styles of deformation and creates different potential hydrocarbon trap geometries.

The White Pointer DDWFTB contains up to three levels of detachment, while the Hammerhead DDWFTB changes from a single level of detachment in the west to two in the east. Both DDWFTBs are composed of an extensional, transitional and compressional province whereby the extensional province is consistent with the delta top and the compressional province with the deepwater fold-thrust belt. The extensional provinces are characterised by regional listric, normal, growth faults and, rarely, counter-regional faults. The transitional provinces are composed of large-scale (< 15 km wavelength) detachment folds, minor thrust faults and chaotic folding of deltaic sediments where imaged. The compressional provinces are defined by imbricate thrust faults and associated folds of various geometries, spacing and scale. All structures in the DDWFTBs sole out or are rooted at or above the level of the basal detachment; thus, deformation is constrained to within the deltaic wedge.

Deformation observed in these DDWFTBs has produced likely hydrocarbon traps that could form viable exploration targets in the future, but excessive water depths would preclude the use of existing drilling technology. Nevertheless the DDWFTBs from the Ceduna Sub-basin provide a good example of the style of tectonism associated with distal parts of marine deltas and is useful for the development of structural models that could be applied elsewhere.

KEYWORDS

Great Australian Bight, Bight Basin, Ceduna Sub-basin, Hammerhead Delta, White Pointer Delta, hydrocarbon trap geometry, structural geometry, detachment.

INTRODUCTION

The Bight Basin is located in the centre of the southern margin of Australia and is host to the Ceduna Sub-basin—a significantly underexplored, yet prospective, hydrocarbon province (Fig. 1). The Ceduna Sub-basin has an area of approximately 90,000 km^2 with water depths ranging from 200 m to more than 5,000 m. The thickness of Middle Jurassic to Tertiary sedimentary rocks exceeds 12 km (Struckmeyer et al, 2001; Krassay and Totterdell, 2003).

The southern margin of Australia, between Kangaroo Island and Cape Leeuwin (Western Australia), covers a distance in excess of 3,000 km, with only 12 exploration wells drilled to date, two of which were drilled in the Ceduna Sub-basin. Indications of past hydrocarbon accumulation were observed in the Potoroo–1 well (Totterdell et al, 2000; Struckmeyer et al, 2001; Somerville, 2001) and in the Jerboa–1 well from the adjacent Eyre Sub-basin (Ruble et al, 2001).

The Ceduna Sub-basin contains two spatially and temporally separate Cretaceous delta—deepwater fold-thrust belt (DDWFTB) systems: the late Albian-Santonian White Pointer DDWFTB and the late Santonian-Maastrichtian Hammerhead DDWFTB. These systems detach above the mud-rich Blue Whale and Tiger supersequences, respectively (Fig. 2). These DDWFTBs vary in both size and geometry, and produce hydrocarbon trap styles whose geometries are controlled by the lithology and thickness of the underlying detachments. Exploration success has been lacking on

Figure 1. Location map showing the position of the Ceduna Sub-basin in the Bight Basin on the southern Australian margin (from Totterdell and Bradshaw, 2004).

the near shore delta top but with constant improvements in drilling technology and seismic imaging, higher risk deepwater fold-thrust belt targets could become prospective for exploration in the future.

Previous work completed by Geoscience Australia (in 1999–2008) and Woodside Energy Limited (including drilling of the most recent well, Gnarlyknots–1) resulted in an improved understanding of the hydrocarbon prospectivity of the Bight Basin, particularly the Ceduna Sub-basin. This work focused on the sequence stratigraphy, tectonics and petroleum systems of the Sub-basin to identify probable organic-rich supersequences, understand the regional maturity of these rocks, and identify suitable traps and seals for hydrocarbon accumulation (Blevin et al, 2000; Totterdell et al, 2000; Somerville, 2001; Ruble et al, 2001; Struckmeyer et al, 2001; Sayers et al, 2001; Struckmeyer et al, 2002; Krassay and Totterdell, 2003; Totterdell and Krassay, 2003; Totterdell and Bradshaw, 2004; King and Mee, 2004; Tapley et al, 2005; Totterdell et al, 2008).

In this paper, we describe the structural framework of the White Pointer and Hammerhead DDWFTBs and their associated potential hydrocarbon traps, with particular emphasis on the less widely addressed compressional provinces. We describe the style and nature of deformation, identify the regional structural controls, and discuss the potential to create viable hydrocarbon trap geometries.

TECTONO-STRATIGRAPHIC FRAMEWORK

The Bight Basin is located in the Great Australian Bight and underlies a broad bathymetric terrace (Ceduna Terrace) forming the continental slope and rise on the southern Australian margin (Totterdell et al, 2000). The basin is bound to the north by Proterozoic and older terranes and to the east by the Proterozoic of the Gawler Craton (Krassay and Totterdell, 2003). The Eyre Sub-basin defines the western limit of the Bight Basin while the Duntroon Basin forms the southeast boundary, and to the south it tapers out onto the thin oceanic crust of the South Australian Abyssal Plain (Fraser and Tilbury, 1979; Bein and Taylor, 1981; Willcox and Stagg, 1990; Hill, 1995; Norvick and Smith, 2001; Totterdell and Krassay, 2003). The Bight Basin developed during Late Jurassic to Early Cretaceous rifting and continued to develop with the breakup of Gondwana, separating Australia and Antarctica during the Late Cretaceous (Totterdell et al, 2000; Sayers et al, 2001; Fig. 3). Late Cretaceous break-up resulted in the separation of the basin into three structurally controlled sub-basins: the Eyre, Ceduna and Recherche—the Ceduna Sub-basin being the largest depocentre (Totterdell et al, 2000; Krassay and Totterdell, 2003; Fig.1). The sub-basins are separated by northwest striking accommodation zones, which were formed by the rifting and crustal thinning of the Australian Plate (Stagg et al, 1990; Wilcox and Stagg, 1990; Totterdell et al, 2000).

The Ceduna Sub-basin stratigraphy is divided into 10 supersequences, which relate to the four basin phases first described by Totterdell et al (2000) who proposed a new nomenclature for the Bight Basin sequence stratigraphy (Fig. 2). The basin evolution involved two successive periods of extension and thermal subsidence that commenced in the Late Jurassic (Totterdell et al, 2000; Totterdell and Krassay, 2003). Basin Phase 1 marks the onset of sedimentation in the basin during the Middle–Late Jurassic

Figure 2. Sequence stratigraphic framework (supersequences) for the Bight Basin with basin phases represented by numbers 1–4. Predicted timing of hydrocarbon expulsion is represented by the arrows, with base of arrow as the onset and arrowhead as the end (from Blevin et al, 2000).

Figure 3. Plate tectonic reconstructions for the Australian-Antarctic conjugate margin (after Norvick and Smith, 2001). Red polygons represent approximate location of Bight Basin.

extension, with the contemporaneous formation of a series of extensional and transtensional half-graben structures. Pre-existing basement trends appear to have focused the deformation during this phase (Totterdell et al, 2000). Basin Phase 2 records the slow thermal subsidence during the Early Cretaceous, which ended abruptly with the onset of rapid subsidence (Basin Phase 3) during the late Albian (Totterdell et al, 2000). Sea-floor spreading in the late Santonian caused the breakup of Australia and Antarctica (Fig. 3) and marks the end of Basin Phase 3; it is followed by a period of thermal subsidence (Basin Phase 4), marking the initiation of the late Santonian south Australian passive margin (Totterdell and Krassay, 2003).

Of the ten supersequences defined in Totterdell et al (2000) the supersequences of most importance to this study are the stratigraphic units with recognised potential for hydrocarbon generation (Blevin et al, 2000; Totterdell et al, 2008). At the northern margin of the Bight Basin these include: the Late Jurassic to Early Cretaceous Sea Lion and Minke supersequences; the Early Cretaceous Southern Right, Bronze Whaler and Blue Whale supersequences; and the Late Cretaceous White Pointer, Tiger and Hammerhead supersequences (Blevin et al, 2000). Basin modelling for the distal parts of the Sub-basin indicate that the uppermost Bronze Whaler, Blue Whale, White Pointer and Tiger supersequences are most prospective in terms of source rocks (Blevin et al, 2000). Dredging by Geoscience Australia in the Bight Basin in 2007 found that late Cenomanian–early Turonian rocks (White Pointer and Tiger supersequences) have high organic carbon contents (2.1–6.2% total organic carbon [TOC]), and the potential to generate liquid hydrocarbons (hydrocarbon index [HI] values ranging from 274–479 mg hydrocarbons/gTOC) (Totterdell et al, 2008).

The relevant supersequence lithology descriptions below come from Totterdell et al (2000), who used well data from the Bight, Eyre and Duntroon basins. The oldest unit relevant to this study is the Valanginian to middle Albian Bronze Whaler supersequence, which is largely composed of an aggradational succession of fluvial and lacustrine sandstone and mudstone with intermittent marine influence. Above this, the middle Albian–Cenomanian Blue Whale supersequence records the first major marine

flooding event with the deposition of restricted marine siltstones nearest the palaeo-shelf and an inferred thick package of marine mudstones in the basin. This package of marine mudstone forms the detachment for the overlying Cenomanian White Pointer DDWFTB, comprising the White Pointer supersequence (Totterdell and Bradshaw, 2004). Rapid (~5 million years [My]) deposition of the aggradational White Pointer supersequence likely produced overpressure in the underlying ductile marine mudstone enabling gravity-driven deformation, which resulted in the formation growth faults and toe thrusts that sole out or are rooted in the Blue Whale mudstone and form the DDWFTB (Totterdell and Krassay, 2003). The White Pointer supersequence is composed primarily of fluvial to lagoonal siltstone and mudstone intercalated with minor sandstone and coal units. An angular unconformity in the White Pointer supersequence where a package of reflections that diverge towards the bounding faults from an overlying flat-lying unit is thought to be related to cessation of growth fault activity (Totterdell et al, 2000). Dewatering of the underlying shale resulting and an associated loss of overpressure (Totterdell et al, 2000; Totterdell and Krassay, 2003) provided the likely mechanism for the cessation of all gravity-driven deformation.

Overlying the White Pointer DDWFTB is the Turonian–Santonian Tiger supersequence, containing an aggradational package of what is suggested to be marine shale based on seismic sequence stratigraphy and extrapolation of well data from Potoroo–1 in the northern Ceduna Sub-basin (Totterdell et al, 2000). The unit is heavily faulted in the Ceduna Sub-basin due to reactivation of older faults (Mulgara Fault Family) controlled by the underlying ductile shales of the Blue Whale supersequence. The timing of this fault reactivation is well constrained to the late Santonian because this faulting had ceased before deposition of the overlying Hammerhead supersequence.

The Santonian–Maastrichtian Hammerhead supersequence has an overall progradational to aggradational character and is likely composed almost entirely of channel sandstones near the present-day shelf in the Ceduna Sub-basin (Totterdell et al, 2000). Three major successions have been interpreted from seismic, with the lowermost and middle sections being progradational and the uppermost being aggradational. The lowermost two sequences of the Hammerhead supersequence show seismic facies character (lack of strong stratal geometries observed on the shelf, more homogeneous seismic character) that is consistent with a basinward change to a more shale-rich system. The 19 My period of progradation of the Hammerhead DDWFTB across the palaeo-shelf resulted in the initiation of gravity-driven deformation with the top of the underlying Tiger supersequence forming the detachment surface. The gravitational tectonics initiated at the palaeo-shelf margin where the Hammerhead supersequence is the thickest (~5,000 m at this location; Totterdell and Krassay, 2003).

The Hammerhead supersequence is overlain by the Paleocene–early Eocene Wobbegong supersequence, which consists of marginal marine-to-deltaic sandstone and siltstone that was deposited on a hiatus that is believed to represent 5–7 million years. Above this, the Middle Eocene to Pleistocene Dugong supersequence is present, consisting of a basal coarse sandstone and thick uniform carbonate succession related to the development of a stable carbonate shelf.

STRUCTURAL GEOMETRY OF DELTA—DEEPWATER FOLD-THRUST BELTS

The structural geometry of delta—deepwater fold-thrust belts has been widely studied where they form prolific hydrocarbon provinces such as the Niger (e.g. Doust and Omatsola, 1990; Morley and Guerin, 1996; Cohen and McClay, 1996) and Baram DDWFTBs (e.g. James, 1984; Koopman et al, 1996; Sandal, 1996; Schreurs, 1997; Van Rensbergen et al, 1999). Delta—deepwater fold-thrust belts typically form at continental margins where rapid progradation of deltaic sediments over salt or water-prone mud results in overpressure development (in water-prone mud) and deformation under gravitational forces (Morley, 2003a). The result is a broad segregation of the delta into extensional and compressional provinces, whereby margin-parallel gravitational extensional stresses on the delta top drive down-dip, margin-normal, compressional stresses in the deepwater fold-thrust belt (Yassir and Zerwer, 1997; Corredor et al, 2005; King et al, 2009).

The delta-top is typically characterised by regional and counter-regional listric, normal, growth faults that sole out at the level of the underlying pro-delta sediments (salt or shale)(Morley and Guerin, 1996). These extensional structures are balanced by the deepwater fold-thrust belt, which is composed of imbricate thrust sheets and associated fault propagation folds rooted at the basal detachment (Morley and Guerin, 1996; McClay et al, 2003; King et al, 2009). The extensional and compressional provinces are commonly separated by a transitional province that is characterised by detachment folds and reactive, active and passive diapirs of shale or salt (Morley and Guerin, 1996).

The detachment horizons are dependent on the development and maintenance of overpressure, with rapid progradation of delta sediments over the water-prone mud or salt contributing the initial overpressure due to disequilibrium compaction of the muds. Overpressure is not required for salt as it is naturally weak and mobile, whereas shale requires overpressure to induce weakness and mobility. Subsequent inflationary overpressures can also develop, most often by dewatering during the smectite-illite transition and volume increase due to hydrocarbon generation; these serve to maintain overpressure (Morley and Guerin, 1996; Osborne and Swarbrick, 1997). Variations in sediment supply, detachment parameters such as lithology and thickness of the detachment horizon(s), and development of overpressure are some of the key factors that contribute to the varied structural styles observed in DDWFTBs worldwide.

Delta—deepwater fold-thrust belts often form excellent hydrocarbon provinces due to the generation of hydrocarbons from marine sediments and an abundance of

trapping mechanisms in the deltaic sediments as a result of the gravity-driven deformation. There are numerous structures formed in these settings, many of which have excellent hydrocarbon trapping potential. For example, rollover antiforms and tilted fault blocks develop in the extensional province (Finkbeiner et al, 2001). Hanging-wall and footwall folds developed due to thrust fault propagation in a deepwater fold-thrust belt also form excellent fault-independent and dependent traps (Cobbold et al, 2009). The imbricate thrusts can provide fluid pathways from the often hydrocarbon generating, detachment horizon into the overlying traps (Cobbold et al, 2009). Deepwater fold-thrust belts are proven hydrocarbon provinces worldwide, such as deepwater Nigeria (Briggs et al, 2006), deepwater Gulf of Mexico (Fiduk et al, 1999) and deepwater northwest Borneo (Tingay et al, 2009).

STRUCTURAL FRAMEWORK OF THE WHITEPOINTER AND HAMMERHEAD DELTA—DEEPWATER FOLD-THRUST BELTS

The Ceduna Sub-basin

The Ceduna Sub-basin contains two Cretaceous DDWFTBs: the late Albian-Cenomanian White Pointer and the late Santonian-Maastrichtian Hammerhead. The geometry of the Ceduna DDWFTBs was first recognised by Boeuf and Doust (1975) and Fraser and Tilbury (1979) and have since been investigated by several authors including Totterdell and Krassay (2003), Totterdell and Bradshaw (2004), Espurt et al (2009) and King and Backé (in press).

The Ceduna Sub-basin provides a unique opportunity to study two separate progradational DDWFTB systems that are independent in size, shape and structural geometry. Both DDWFTBs exhibit well-developed gravity-driven deformation structures, making them analogous to other delta systems around the world. The deepwater fold-thrust belts that form the down-dip compressional provinces of the White Pointer and Hammerhead DDWFTBs are of particular interest to this study.

The structural interpretation of the White Pointer and Hammerhead DDWFTBs is based on public domain time-migrated 2D seismic data. It is important to note that true dip and interlimb angles can be uncertain in the time domain and those quoted in the following descriptions are a guide for the reader; however, the overall structural style will not be modified by migration of the data in depth domain.

Our interpretation of the nine seismic lines provided by Geoscience Australia enabled us to precisely map the extent of both the White Pointer and Hammerhead DDWFTBs (Fig. 4). While the lines to the northwest clearly display the White Pointer DDWFTB and the lines to the southeast display the Hammerhead DDWFTB, the central seismic line S65r 065-15 does not evidence such deformation (Fig. 5). In addition, evidence for White Pointer DDWFTB in the southeast and Hammerhead DDWFTB in the northwest are limited—if not non-existent—from our interpretation. On the contrary, the time-equivalent stratigraphy of the White Pointer and Hammerhead DDWFTBs is stacked throughout the Ceduna Sub-basin; however these are lacking the gravity-driven compressional structures that are needed to classify them as part of the DDWFTBs.

It was previously known that these DDWFTBs represent successive periods of time (Totterdell et al, 2000), but our analysis shows that they are also geographically separated. The White Pointer DDWFTB is only present in the northwest, while the Hammerhead DDWFTB is only formed in the southeast (Fig. 4). These two DDWFTBs are separated in the Bight Basin by a 1.5 s basement high, clearly demonstrated on the time grid interpreted from the seismic reflection data. This is in opposition with the interpretation of one seismic line from Espurt et al (2009), who propose a system of two stacked DDWFTBs. Our interpretation however, bears a drastic resemblance to the regional geometry of the Niger DDWFTB, where the Charcot Fracture Zone separates the western from the eastern lobe (Cobbold et al, 2009). We propose that the basement high may have influenced the location of the depocentres for the White Pointer and Hammerhead deltas (Fig. 4).

WHITE POINTER DELTA—DEEPWATER FOLD-THRUST BELT

The late Albian–Cenomanian White Pointer supersequence rapidly prograded over a thick package of mostly mud-prone Blue Whale supersequence over a period of about 5 My (Totterdell et al, 2000). The delta system can be approximately divided into three tectonic provinces: an extensional province, associated with the delta top; a poorly developed transitional province between the delta top and deepwater fold-thrust belt; and a compressional province, related to the deepwater fold-thrust belt (Fig. 6). We interpreted 10 seismic lines to constrain the transitional and compressional provinces of the White Pointer DDWFTB. For clarity, we present the three most representative lines in this paper (S65r 065-02,065-07 and 065-03; Fig. 4). These lines display a well constrained seaward-dipping basal detachment underlying the delta in the southwest of the Ceduna Sub-basin that is located at or near the base of the Blue Whale supersequence. The gravity-driven deformation in the delta includes both the sediments of the Blue Whale and White Pointer supersequences, and a second and third level of detachment can be observed in both the upper Blue Whale and upper White Pointer supersequences (Fig. 6).

The extensional province of the White Pointer DDWFTB is dominated by a series of northwest–southeast striking, seaward dipping, strongly listric, normal, growth faults that were active in the Cenomanian (Totterdell and Krassay, 2003). This fault system is widespread and controlled the depocentres for deltaic sediments of the White Pointer supersequence, with faults displaying up to 1,500–2,500 m of vertical displacement and spaced 5–10 km apart (as determined from depth-converted seismic of Totterdell and Krassay, 2003). These large-scale faults sole out in the underlying detachment in the Blue Whale supersequence.

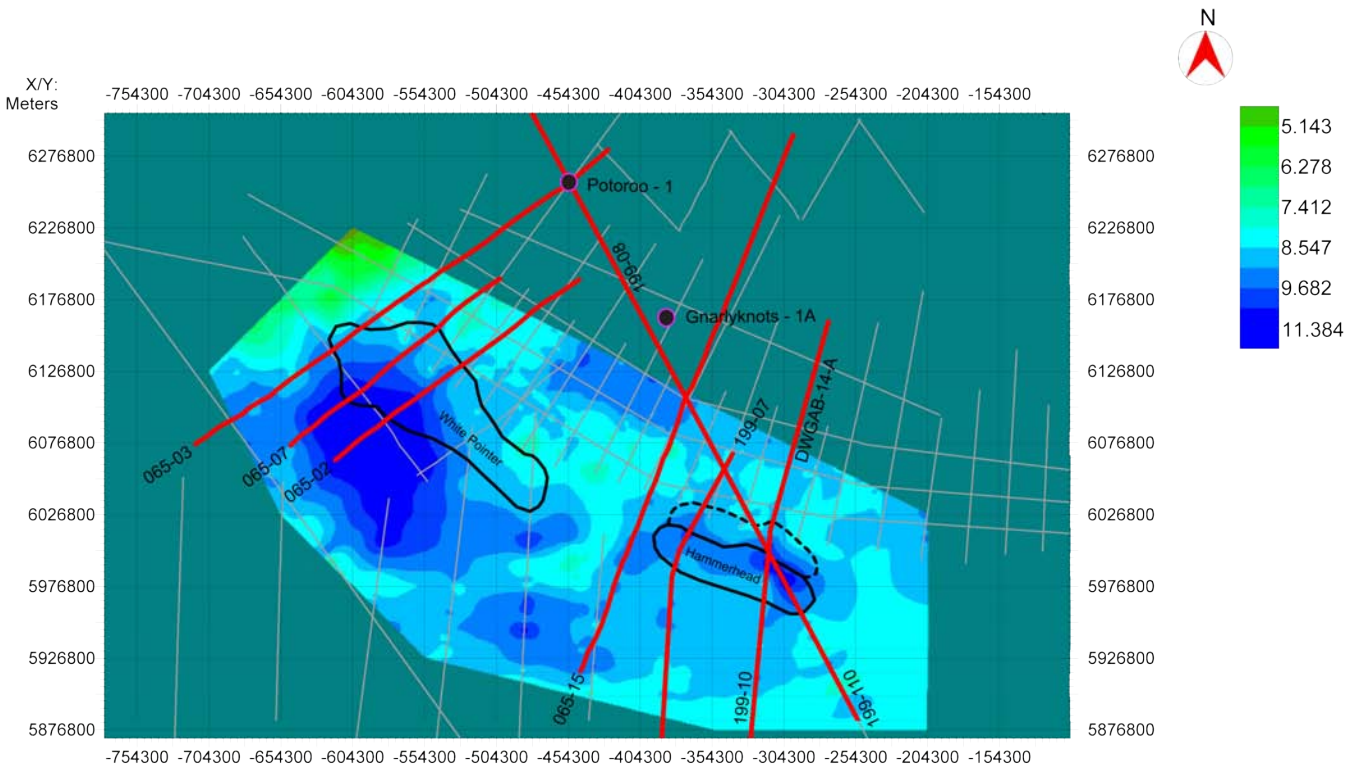

Figure 4. Isochron map (two-way time) of Ceduna Sub-basin basement as interpreted by Geoscience Australia, showing a prominent basement high dividing the White Pointer deepwater fold-thrust belt to the west from the Hammerhead deepwater fold-thrust belt to the east. Seismic profile locations for Figures 5–15 are indicated. Hammerhead transitional zone (top polygon) and deepwater fold-thrust belt (bottom polygon) is shown to the east of the basement high, while the White Pointer deepwater fold-thrust belt is displayed to the west.

It is important to note that there are very few counter-regional faults developed in the extensional province of the White Pointer DDWFTB (Fig. 6). Totterdell and Krassay (2003) suggest that the often thin substrate of the Blue Whale (average 2 km thickness) inhibited the formation of these counter-regional faults that are commonly observed where DDWFTBs overlie thick shales (up to 6 km thick) such as in the Niger DDWFTB (Morley and Guerin, 1996).

As opposed to the Hammerhead DDWFTB and other large deltas systems such as the Niger DDWFTB, The White Pointer DDWFTB does not have a well-defined transition province (Morley and Guerin, 1996; McClay et al, 2003; Corredor et al, 2005). The most likely constraint on the poorly defined transitional province is the nature of the detachment in the Blue Whale supersequence. The detachment has a much steeper dip where it cuts through the marine sediments of the Blue Whale supersequence—a transition that is clearly supported by strongly dipping reflectors below the detachment (Fig 6). This sudden change in the dip of the detachment initiates the deformation in the Blue Whale supersequence sediments seaward, explaining the often chaotic nature of this unit above the detachment in the transitional to compressional provinces (Figs 6 and 7). Totterdell and Krassay (2003) suggested that possible mobile shales and diapiric structures in the transition zone of the White Pointer Delta indicate excessive overpressure similar to the Niger Delta; however, we suggest that although some shale mobilisation may have occurred, these structures are more suitably attributed to reverse/thrust faulting and detachment folding, as fold-limb reflectors are observed throughout (Fig. 7). It is evident that the poorly developed transition zone in the White Pointer DDWFTB is an artifact of the uppermost detachment position; minor offset thrust splays coupled with minor detachment folding work to accommodate strain seaward of the extensional faults rather than forming a large domal detachment fold. Overall, the transitional province of the White Pointer DDWFTB is, in places, poorly developed with few continuous seismic reflectors, likely due to minor shale mobility. One exception to this is observed in Figure 8, where a large, 5–10 km wavelength broad antiformal detachment fold with shallowly dipping limbs is present in the footwall of the highest detachment. This discontinuity along strike in the transitional province of the White Pointer DDWFTB may be attributed to a change in lithology of the Blue Whale supersequence between seismic profiles 065-07 (west) and 065-02 (east) in Figure 6. The top profile (065-07) shows continuous reflectors in the transitional province whereas in the bottom profile (065-02) the seismic reflections are chaotic and poorly constrained.

The compressional province of the White Pointer DDWFTB is represented nearest the edges of the delta lobe by a few small thrust faults and associated folding, while the centre of the lobe is extensively shortened with

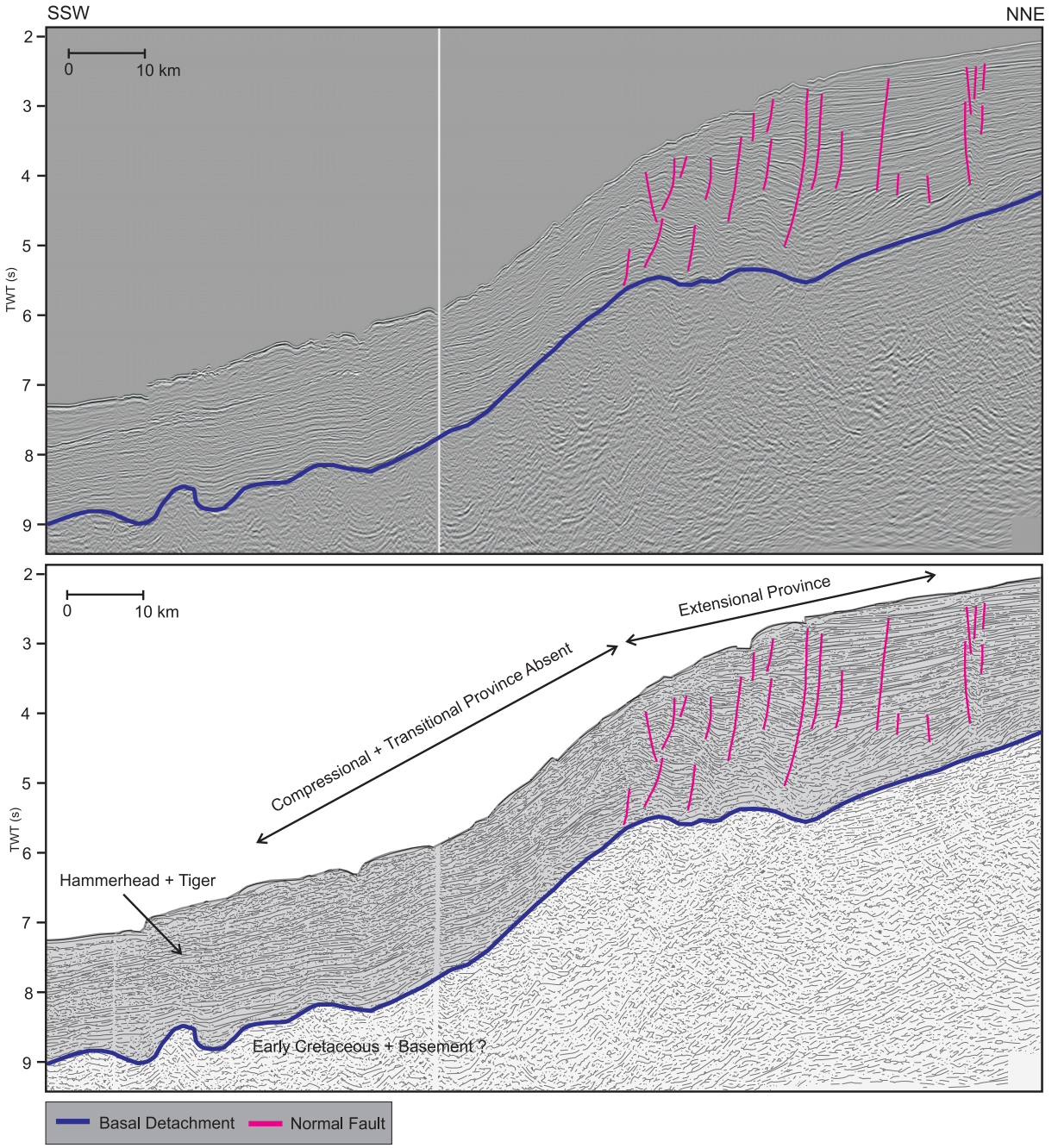

Figure 5. Seismic profile 065-15, showing an absence of transitional or compressional provinces between the White Pointer and Hammerhead DDWFTBs, indicating that the systems are both temporally and spatially separate. The purple line represents basement contact. The position of potential compressional province is indicated.

imbricate thrusting and fault propagation folding over a 75 km compressional zone. Faults in the deepwater fold-thrust belt range from moderate to low-angle landward dips with associated seaward-verging, often symmetrical, hanging-wall anticlines and less commonly asymmetric synclinal footwall cutoffs (Figs 9a and 9b). The imbricate thrust sheets are spaced 2–10 km, variability being controlled by the dip and thickness of the detachment horizon. Footwall fault panels rarely display minor back-thrusting between thrust ramps (Figs 7 and 9b) and are gently folded, rarely with small antiforms that show no evidence for crestal faults (Fig. 10). Ponded basins in the footwall synclines are common, where growth strata slump off the anticline forelimb with ongoing deformation. Ponded mini-basins are also present on the backlimbs of major hanging-wall anticlines, with the syn-kinematic sedimentary package typically sealing the fault tip of the preceding thrust fault (Fig. 10).

The nature of the detachment and the lithology together with the thickness of the substrate are the major controls

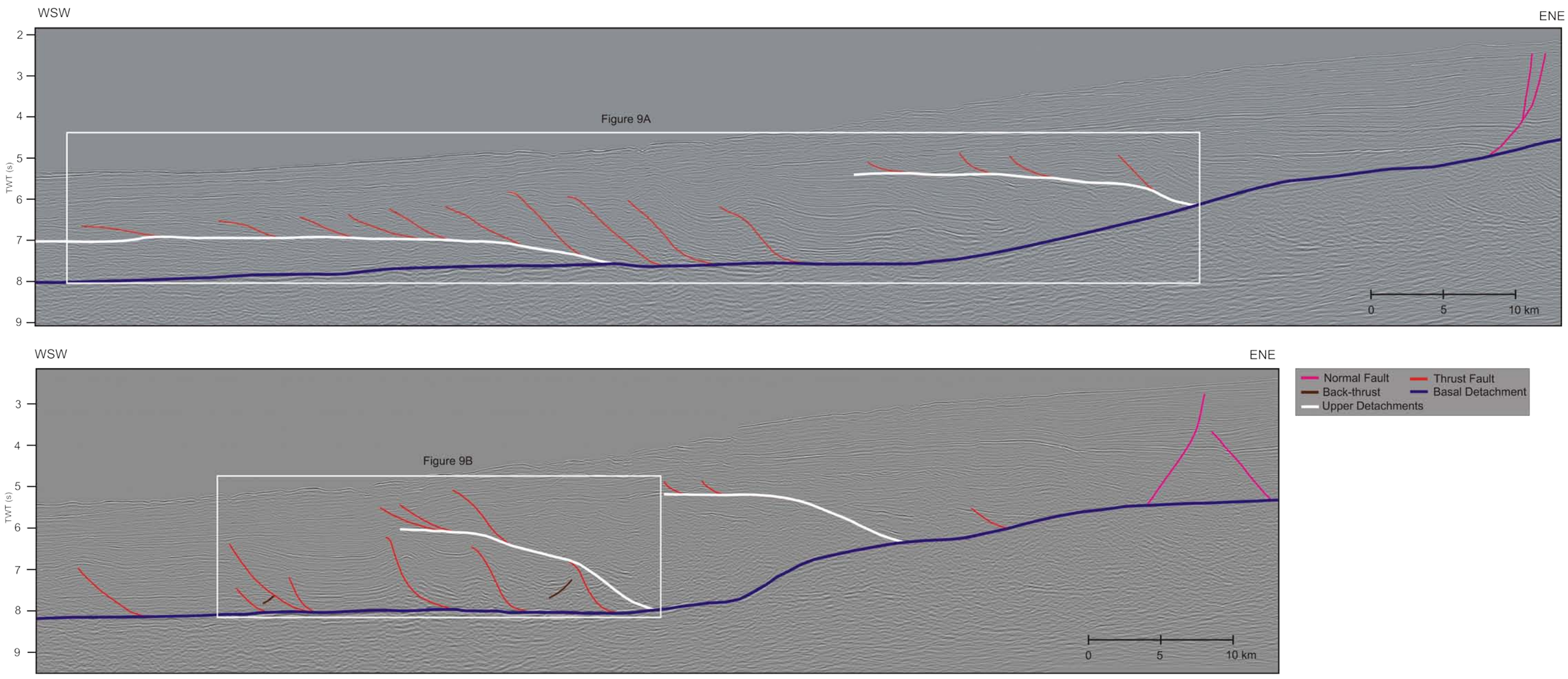

Figure 6. Two regional seismic profiles 065-07 (top) and 065-02 (bottom), showing the geometry of the White Pointer DDWFTB system with an extensional province to extreme ESE and a compressional province extending to the WSW. The transitional province is poorly developed and three levels of detachment can be observed in the top section with the basal detachment at the base of the Blue Whale supersequence. Note the strong reflectors located beneath the steep seaward dip in the basal detachment and the variability in thrust fault angles throughout and between the profiles.

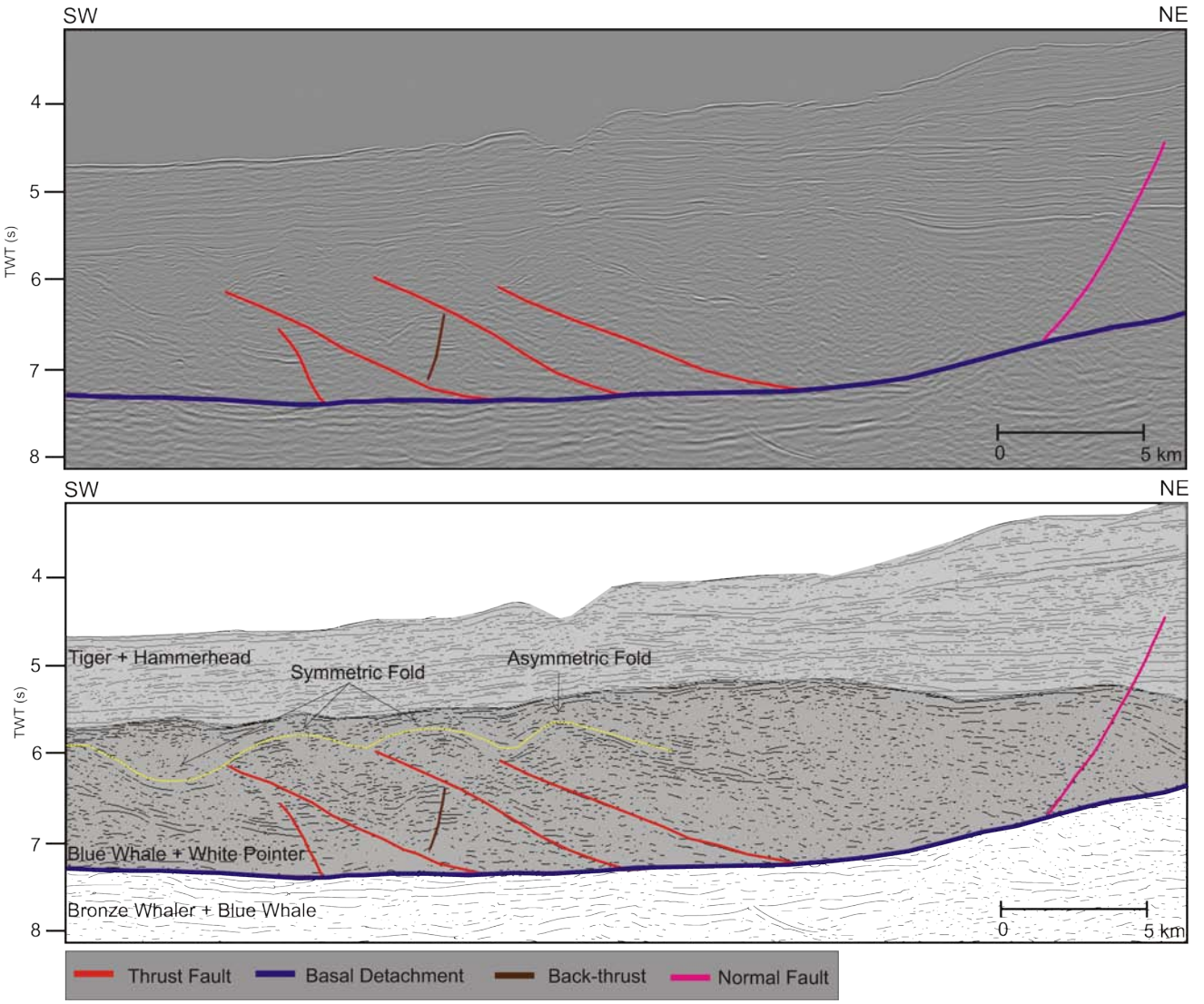

Figure 7. Seismic profile 065-03, displayed with basic (upper) and detailed interpretation (lower). Asymmetric and symmetric folding, thrust faulting and minor back-thrust formation are shown in the poorly developed transitional province of the White Pointer DDWFTB. The yellow line represents trace of folds and supersequences names are displayed on the left of the diagram.

on the geometry of the overlying deepwater fold-thrust belt, and consequently, the structural style of the White Pointer DDWFTB.

HAMMERHEAD DELTA—DEEPWATER FOLD-THRUST BELT

The late Santonian–Maastrichtian Hammerhead DDWFTB is composed of up to 5,000 m of the Hammerhead supersequence in the southeast Ceduna Sub-basin. The Hammerhead DDWFTB is divided into three provinces—extensional, transitional and compressional—all of which are well developed and easily mapped throughout the southeast Ceduna Sub-basin (Totterdell and Krassay, 2003) (Fig. 11). A continuous basal detachment forms at the base of the Tiger supersequence (Figs 11 and 12) and an upper detachment occurs near the top of the Tiger supersequence (Fig. 12). The latter detachment is present only below the transition and compressional zones to the southeast. A total of three regional seismic lines (S199-07, 199-10 and 199-110) display the extent of the gravity-driven deformation in the DDWFTB, two of which are roughly perpendicular to the structural grain (west-northwest–east-southeast) (Fig 4). Seismic line S199-07 is the western most control on the Hammerhead DDWFTB in the southern portion of the Ceduna Sub-basin (Fig. 11). This seismic profile demonstrates the seaward dipping detachment above which the extensional, transitional and compressional provinces are displayed.

The eastern control on the Hammerhead DDWFTB is provided by the remaining two regional seismic lines (199-10 and 199-110; Fig. 12). The profiles show the change in

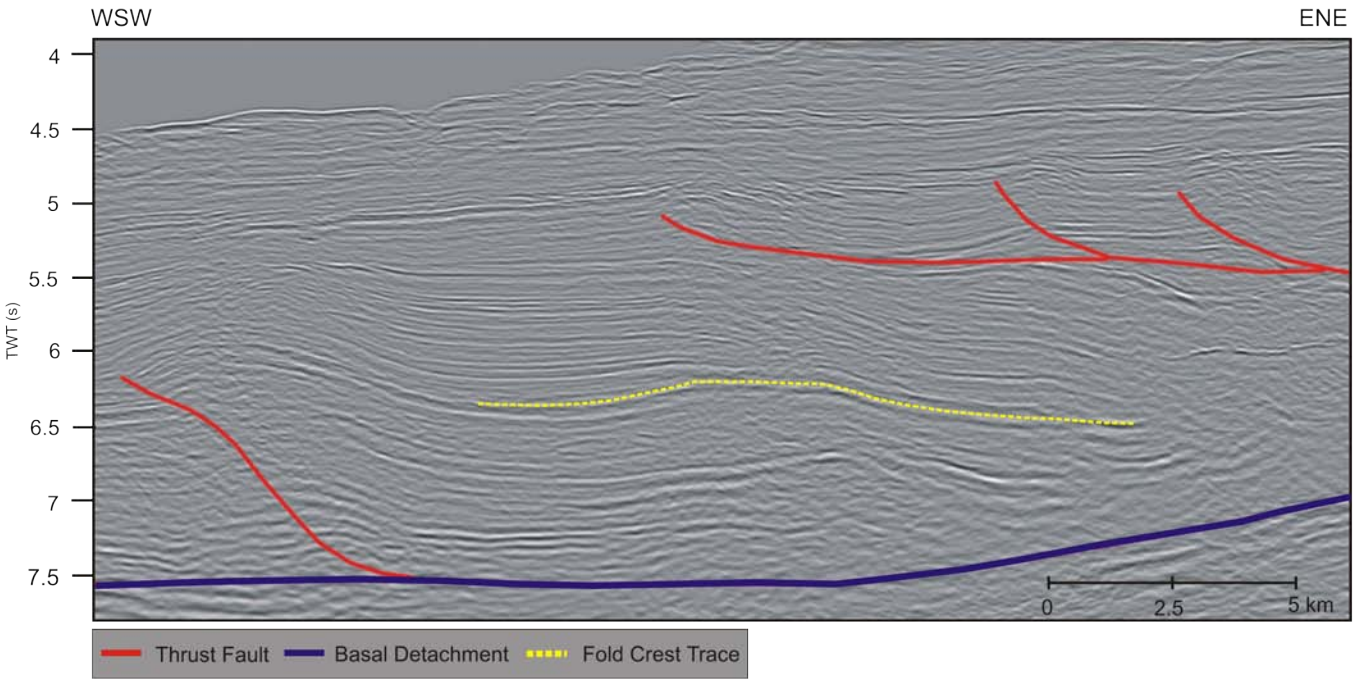

Figure 8. Seismic profile 065-07 shows a large (10 km) gentle detachment fold in the poorly developed White Pointer transitional province with the intact fold crest being favourable for hydrocarbon trap formation.

the detachment from seaward dipping to a spoon shape, with the detachment dipping landward near the delta toe. We interpret the landward dip of the detachment to be controlled by a slight basement high beneath the deepwater fold-thrust belt, which most likely provides the control on formation of the second level of detachment across the DDWFTB (Fig. 12). The three provinces identified in seismic profiles are characterised by a series of structures that sole out or are rooted in the underlying basal and upper detachment levels (Fig. 13, 14).

The extensional province in the Hammerhead DDWFTB varies in fault geometry across the shelf to shelf edge, where it is composed of mainly regional planar faults in the northwest and steep, seaward-dipping listric, normal, growth faults in the south and southwest (Figs 11, 12 and 13c). The regional planar faults are late Maastrichtian–Paleocene and are either reactivated Cenomanian growth faults or have initiated at the tips of earlier faults that were last active during the Turonian–Santonian extension (Totterdell and Krassay, 2003). The growth faults in the south and southwest parts of the basin are of Campanian age and are complimented down-dip by the detachment folding in the transitional province, and toe thrusting and associated folding in the compressional province (Totterdell and Krassay, 2003; Fig. 13a). The extensional stresses in the delta-top are inferred to drive the compressional stresses responsible for the structures observed down dip in the transitional and compressional provinces (Yassir and Zerwer, 1997; Corredor et al, 2005; King et al, 2009).

The transitional province is characterised in the Hammerhead DDWFTB by large-scale detachment folding bounded by growth strata to the north and the hanginwall of the first thrust to the south. The province ranges from ~15–25 km in width and contains a large-scale open concentric anticline, which is periclinal in the east (Figs 14b and 14d) and is composed of an open to gentle, concentric anticline with gently dipping limbs in the west (Fig. 13b). This detachment fold has been thrusted by a large backthrust in the southeast limb that is rooted at the basal detachment and may correspond to an accommodation structure for the possible mobile shale package of Tiger supersequence occupying the core of the anticline (Figs 14b and 14d). Given that there are some 40 km between seismic lines displayed in Figures 11 and 12, and the system is open to the southeast, there is a high probability that detachment folds are continuous in the transition province.

The compressional province of the Hammerhead DDWFTB is well imaged in seismic lines 199-07, 199-10 and 199-110, and is composed of a series of northeast dipping imbricate thrust sheets that are generally steepest in the hinterland and shallow out in the foreland, separated into 2–10 km panels (Figs 11, 12, 13a, 14a and 14c). Thrust faults control the hanging-wall anticlines, which are commonly paired with an asymmetric footwall syncline and less commonly with footwall anticline (Fig. 14c). Hanging-wall anticlines are commonly tight to open symmetric concentric folds that exhibit intact limbs with proportionally steep dips on forelimbs and backlimbs. There are variations in fold geometry, such as minor asymmetry due to parasitic folding and box-shaped folds (Figs 13a and 14a); however, these structures are not representative of the entirety of the deepwater-fold-thrust belt. There is significant evidence for slumping and growth strata shedding from both the forelimbs and backlimbs resulting in ponded or mini-basin development (Fig. 15). This suggests the upper Hammerhead supersequence was syn-kinematic. Thrust tips are

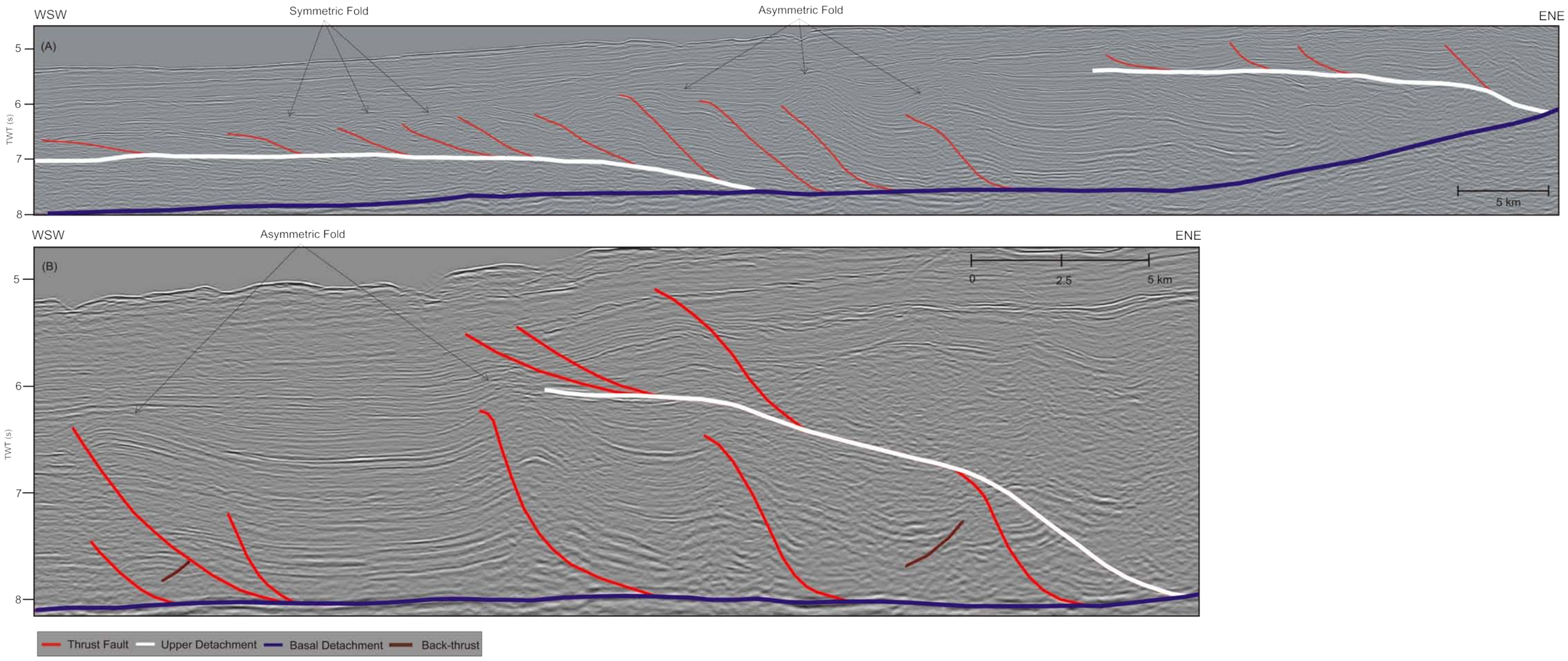

Figure 9. A) Seismic profile 065-07 from the central part of the White Pointer DDWFTB showing variability in hanging-wall anticlines from symmetric folds toward the basin to asymmetric folds toward the shelf, which corresponds with decrease in dip of thrust faults from shelf to basin. B) Seismic profile 065-02 shows the clear transition between the basal detachment and overlying Blue Whale and White Pointer supersequences with asymmetric and symmetric hanging-wall anticlines and minor back-thrust development in footwall strata.

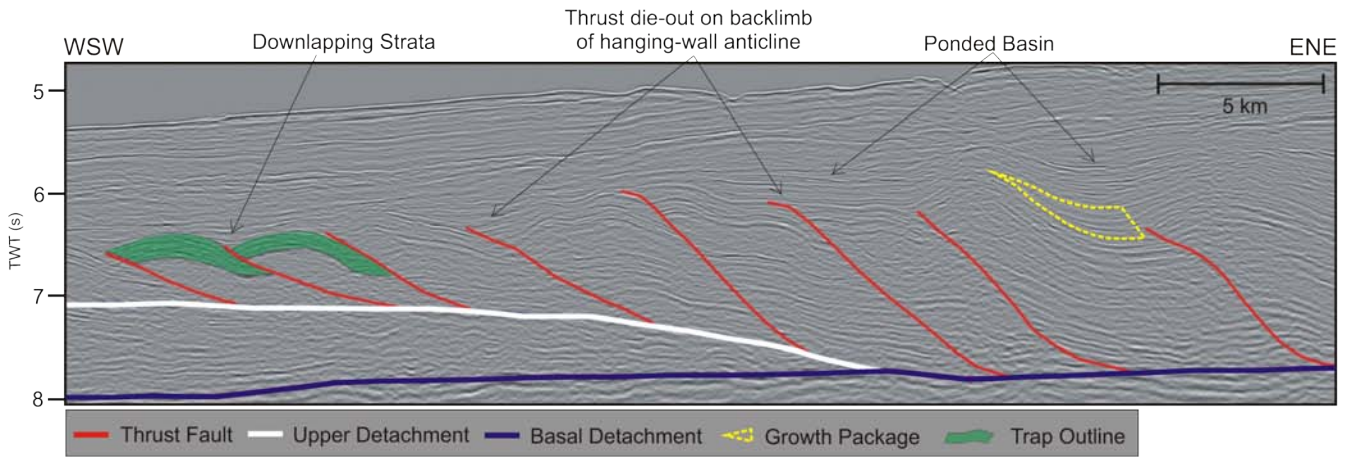

Figure 10. Seismic profile 065-07 from the White Pointer deepwater fold-thrust belt showing faults dying out in backlimb of hanging-wall anticlines, growth strata in footwall synclines, ponded basin and mini-basin development as well as down-lapping of strata of the upper White Pointer supersequence acting to seal potential fluid migration pathways. Green polygons show examples of symmetric hanging-wall anticlines that display excellent hydrocarbon trap potential due to fault independent nature.

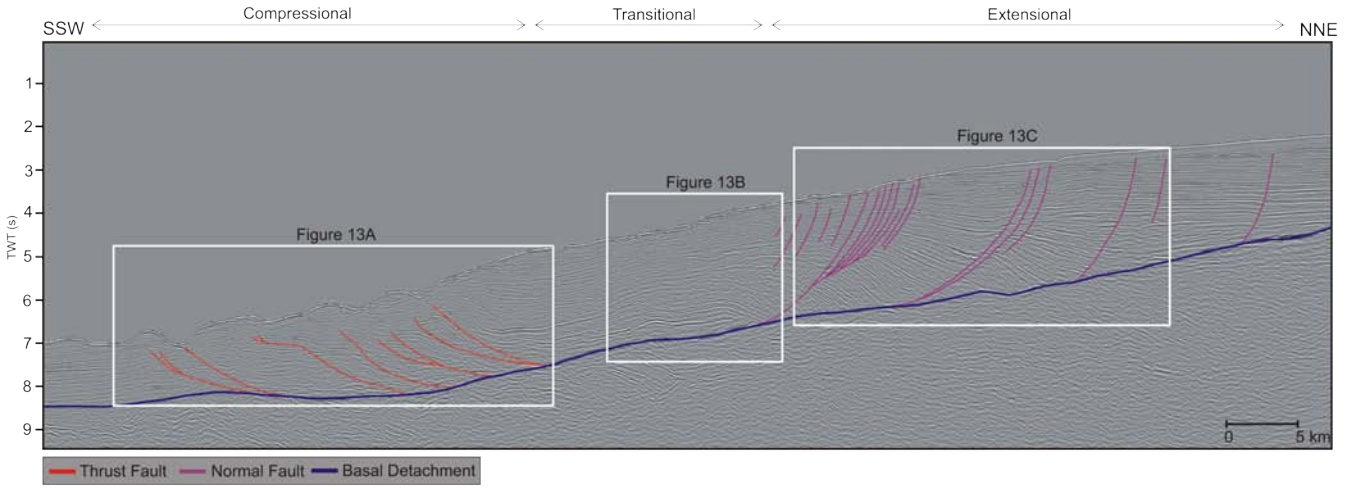

Figure 11. Seismic profile 199-07 of the Hammerhead DDWFTB with well-developed extensional, transitional and compressional provinces. Basal detachment at top of the Tiger supersequence has a seaward dip in the western extent of the deepwater fold-thrust belt.

commonly invisible as they end in trishear zones (Fig. 15), which are characterised by upward thickening wedges of reduced seismic amplitude caused by shearing nearest the thrust tips, a feature that is often recorded in outcrop (Erslev, 1991; Briggs et al, 2006). These trishear zones are often overlapped by growth strata that thicken with ongoing deformation and deposition (Fig. 15).

The faulted hanging-wall anticlines are demonstrated to develop from folds along strike in the transfer zone (Figs 14a and 14c). The fact that thrust faults develop into fault-propagation folds along strike suggests lobate rather than conical thrust/fold geometry. There is no visible evidence for crestal faulting in folds that occur in the Hammerhead deepwater fold-thrust belt, and the majority of thrusts die out within growth strata that accumulate in the cores of synclines and backlimbs of anticlines (Fig. 15).

There are notable similarities between the White Pointer DDWFTB and the Hammerhead DDWFTB, in particular in the fold-thrust belt. These similarities include the geometry of listric normal growth faults, thrust sheet spacing and variation in dip of thrust faults, hanging-wall anticline geometry, ponded basin development adjacent to the forelimb and backlimbs of folds, and the initiation of structures in an underlying ductile detachment unit. Axial traces/planes of the folds are likely curved for both DDWFTBs—an artifact of the lobate nature of the thrust sheets; however, due to the spacing of the available seismic lines it is not possible to trace the folds/faults across the deepwater fold-thrust belt with certainty.

Major differences in the two systems include size, age, detachment lithology and thickness, deltaic lithology, thickness, shear modulus and the position of the delta lobes; however, the most important of these differences is the nature of the detachment. The White Pointer has a sea-

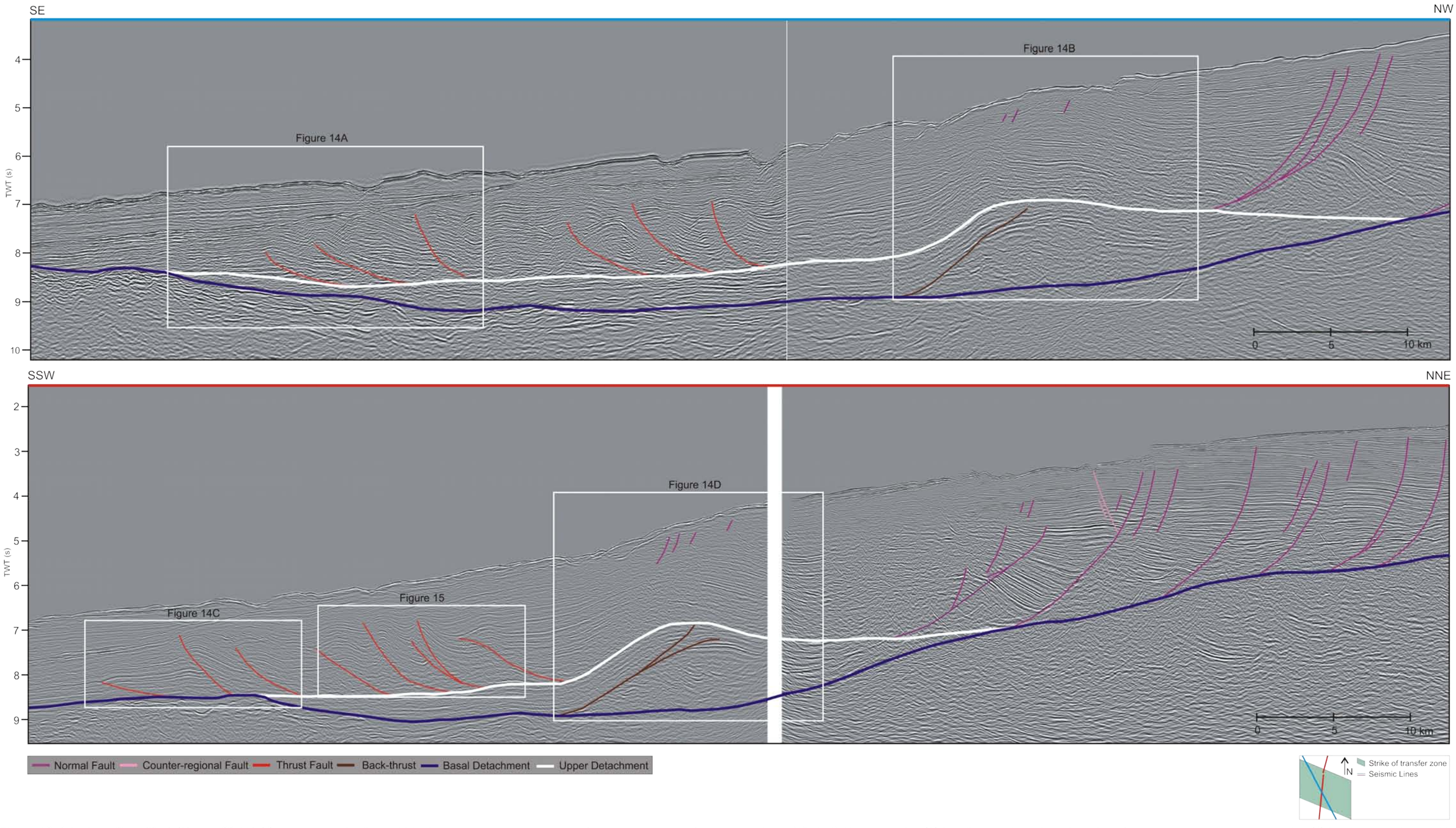

Figure 12. Seismic profiles 199-10 (A) and 199-110 (B) are cross-cutting lines, which display the structural geometry of the eastern extent of the Hammerhead DDWFTB. The top section (A) is oblique to the strike orientation of thrusts, whereas the bottom section (B) is sub-perpendicular, which infers that the detachment fold in the transitional province is most likely to be 4-way closed (i.e. a pericline).

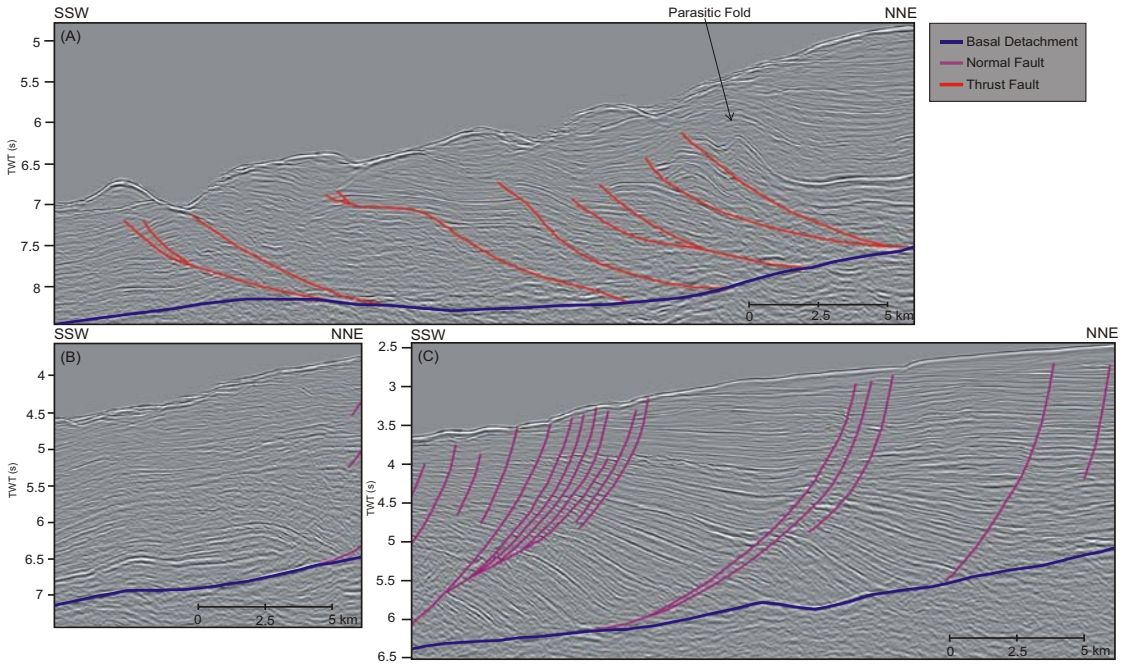

Figure 13. Detailed images of the western Hammerhead seismic profile (Fig. 11; 199-07) displaying: (A) the western Hammerhead deep-water fold-thrust belt with asymmetric hanging-wall anticlines displaying parasitic folding and no breach of potential traps; (B) large (10 km wavelength) gentle detachment fold with no evidence for crestal breach and a minimum 2-way closure; and, (C) the listric, normal growth faults in the extensional province with strata roll over into footwall.

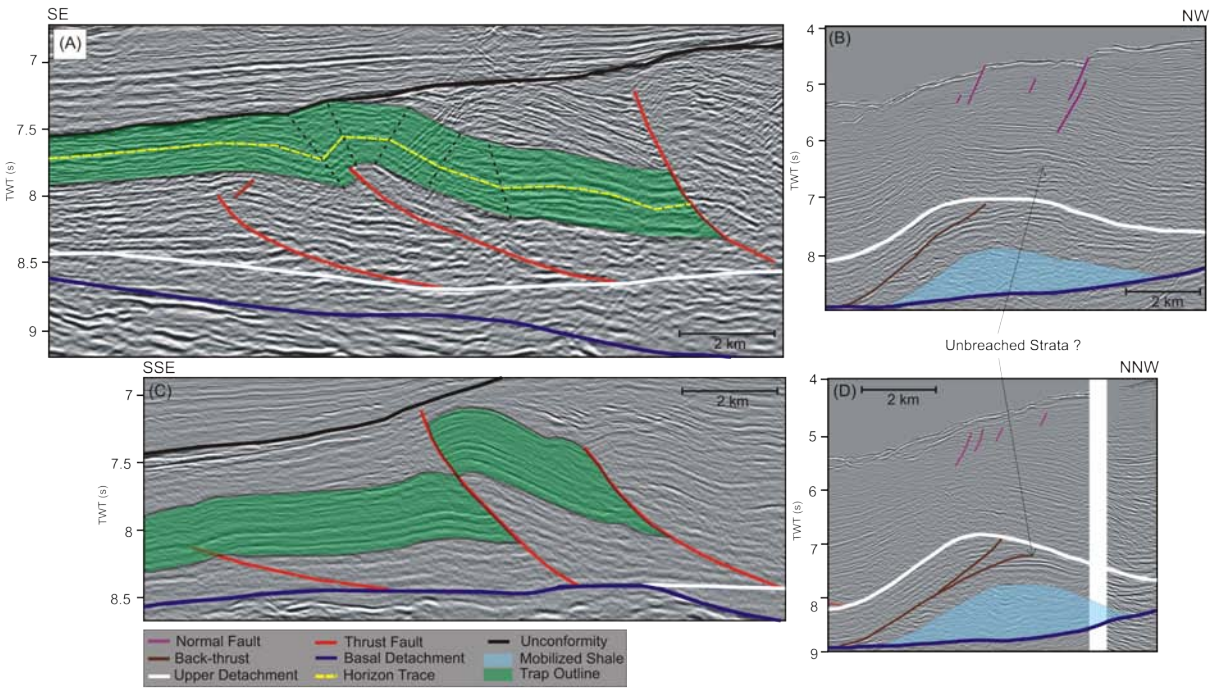

Figure 14. Detailed images of the eastern Hammerhead DDWFTB (Fig. 12; 199-10, 199-110), displaying variation of thrust sheet along strike from high angle thrust (C) to box-shaped fold (A). Flat-lying upper detachment (blue line) in (A) distributes strain homogeneously among the thrusts in this section whereas a slight basement high in (C) results in increased shortening directly above termination of upper detachment. The open detachment fold displays a back-thrust accommodation structure (continuous along strike; A and D), which is related to possible mobile shales in the core of the fold (chaotic reflections; light blue polygon). Crestal breach is evident in both (A) and (D), however small flexures in strata remain intact in the core of the fold above and beneath the upper detachment (blue line). Potential traps are represented by green polygons, which marks the same horizon across the ~10 km distance between (A) and (C).

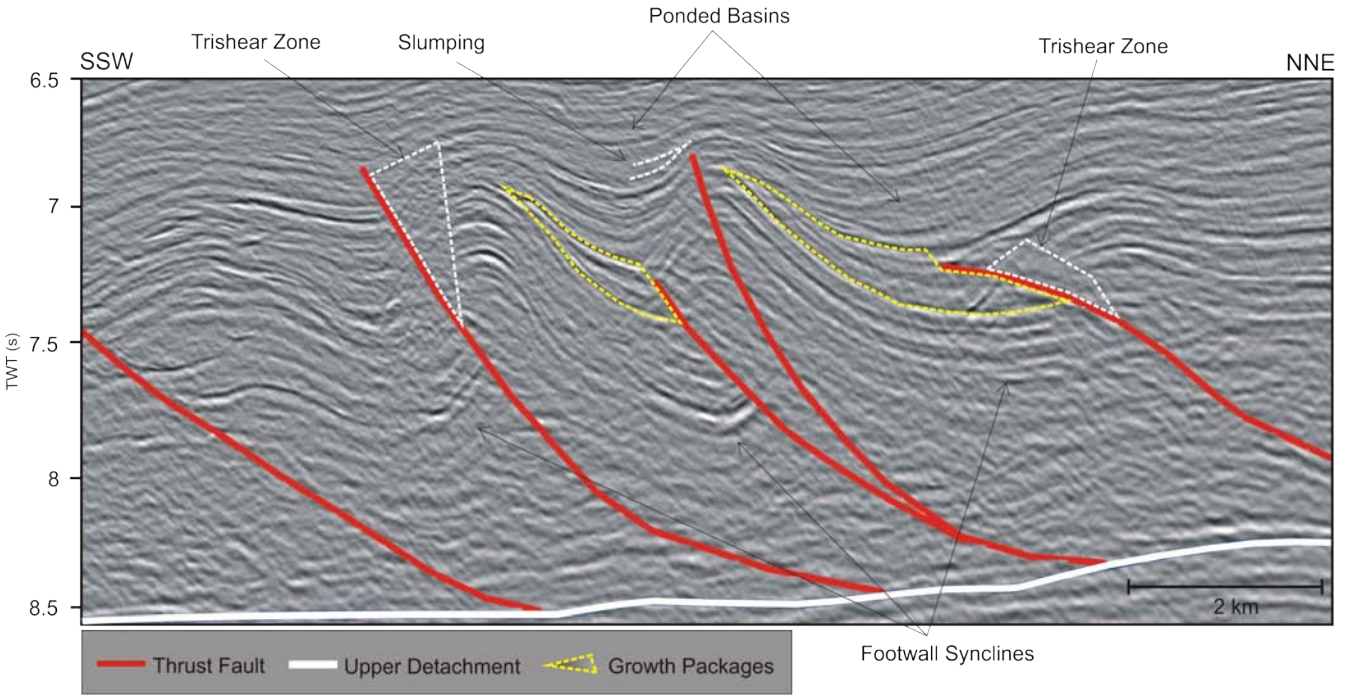

Figure 15. Seismic profile enlargement from Figure 12 (199-110) showing syn-kinematic features such as ponded basin or mini-basin development, slumping of sediments off the crests of hanging-wall anticlines, growth strata, termination of fault tips in footwall synclines and trishear zones. Inferred mud-rich upper Hammerhead supersequence strata drape over structures, resulting in possible regional seal development for underlying traps. Note also the variability in geometry of the asymmetric footwall synclines.

ward dipping detachment in/below the Blue Whale supersequence with a steep ramp (Fig. 16), resulting in second and third level detachments higher up in the stratigraphy; the detachment beneath the Hammerhead is in/below the Tiger supersequence and has variable dips, from seaward dipping in the west to landward dipping in the east forming a spoon shape (Fig. 16). The detachments directly influence the development of the transitional province in the Hammerhead and the lack of this feature in the White Pointer.

PROSPECTIVITY AND POTENTIAL HYRDOCARBON TRAPPING IN THE WHITE POINTER AND HAMMERHEAD DDWFTBS

Identifying prospective targets for hydrocarbon trapping in the White Pointer and Hammerhead DDWFTBs is difficult with the present data set, which is comprised of wide spaced 2D seismic and limited well data from Potoroo–1 and Gnarlyknots–1A. This work aims to identify potential hydrocarbon trap geometries from seismic data only, by presenting a series of structures that are located primarily in the transitional and compressional provinces of the White Pointer and Hammerhead DDWFTBs. Potential hydrocarbon traps in the extensional province or shelf of the two DDWFTBs have been presented by previous authors and are therefore not a focus of the following descriptions (e.g. Blevin et al, 2000; Totterdell et al, 2000; Somerville, 2001; Ruble et al, 2001; Struckmeyer et al, 2001; Struckmeyer et al, 2002; King and Mee, 2004; Tapley et al, 2005; Totterdell et al, 2008).

The aim of this section is to present structures that have the potential—based on position, quality of fold closure and presence of seals—to contain hydrocarbons provided they are continuous and close along strike. As the seismic lines that cover the transitional and compressional provinces are broadly spaced (average of 25–50 km; Fig. 4), it is very difficult to predict with any certainty how structures will continue along strike. Fortunately, two lines (199-10 and 199-110) cross-cut the Hammerhead DDWFTB and provide a good visualisation of the structures along strike with some degree of certainty (Figs 12 and 14). Our interpretation of these seismic lines (Figs 12 and 14) provide evidence of potential 4-way closures along strike, both in the detachment folds (Figs 12, 14b and 14d) of the transitional province and in the lobate thrust sheets (Figs 12,14a and 14c) of the compressional province. The existence of these structures provide the basis for identifying similar structures between seismic lines—as well as to the east of the Hammerhead DDWFTB—and classifying them as potential hydrocarbon traps.

White Pointer DDWFTB prospectivity

As the White Pointer DDWFTB is an entirely separate DDWFTB than the Hammerhead DDWFTB, and no cross-cutting seismic lines are available to provide evidence for 4-way closure of structures along strike, the following interpretations can only be based on the assumption that thrust sheets in DDWFTBs have curved axial traces and

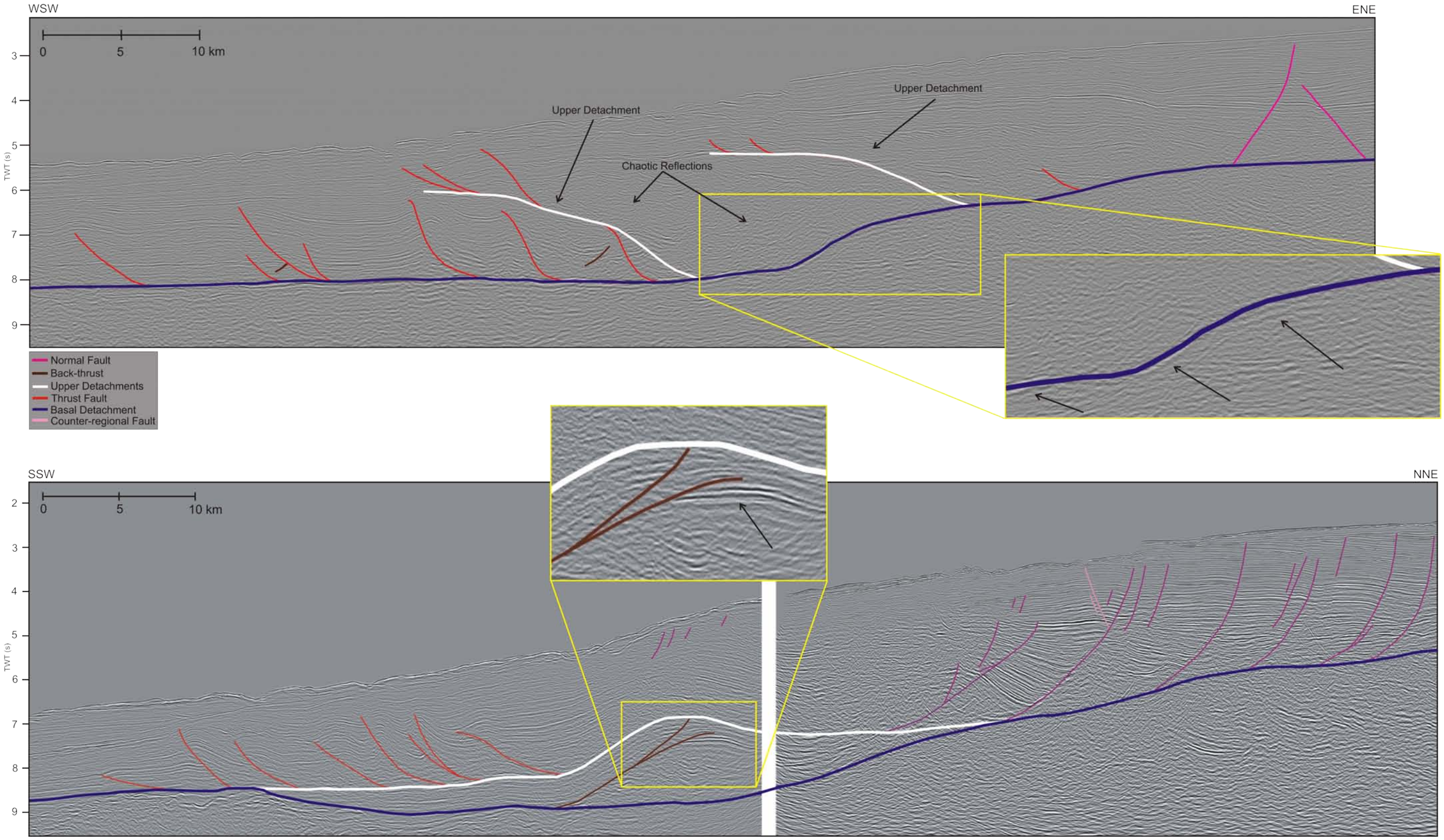

Figure 16. Seismic sections, from top to bottom, of White Pointer (065-02) and Hammerhead (199-110) DDWFTBs, showing main features of the systems. Top insert shows position of strong reflectors that define the dip of the detachment, as well as the position of chaotic reflections adjacent to the steep ramp in the basal (purple) detachment. Bottom insert shows interpreted periclinal detachment fold in the transitional province with back-thrust in core as defined by strong set of reflectors. The top profile displays the seaward dip of the White Pointer basal detachment (purple) while the bottom profile displays the spoon-shaped basal detachment (purple) of the Hammerhead DDWFTB.

are commonly lobate as observed in other DDWFTBs such as the Niger (e.g. Cobbold et al, 2009) and Baram deltas (e.g. Van Rensbergen and Morley, 2003) and in analogue models of DDWFTBs (McClay et al, 2003). This geometry is essential for 4-way closure of both fault-propagation folds and hanging-wall anticlines where, with a sufficient seal mechanism, potential fluids may be isolated in the crest of the fold in the fold-thrust belt (Cobbold et al, 2009). Based on the available seismic data, we interpret the transitional province of the White Pointer DDWFTB to be lacking suitable fold structures, possibly due to the influence of detachment geometry on the DDWFTB, as was previously described (Fig. 6).

We interpret the fold-thrust belt of the White Pointer DDWFTB to contain a number of structures that provide a realistic geometry for hydrocarbon traps (Figs 6, 9a, 9b and 10), based on comparison with similar structures in hydrocarbon producing DDWFTBs such as the Baram (e.g. Van Rensbergen and Morley, 2003) and Niger DDWFTBs (e.g. Cobbold et al, 2009). We suggest that the traps with greatest potential are related to the fault-dependent and fault-independent hanging-wall anticlines that are generally open to tight concentric folds, which can be grouped into two styles (Figs 9a, 9b and 10). The difference between the styles is solely attributed to the dip of the forelimb where one set is asymmetric (Figs 9a and 9b) with a steeper forelimb (typically faults with steeper geometry) and the other is symmetrical (Figs 9a and 10). The latter are often associated with shallower thrust faults (Figs 9a and 10) and are interpreted to provide better potential trap geometries as they are broad (~5 km), show no signs of crestal breach and are largely fault independent, mitigating the risk of fault breach.

There are two possibilities for trap seal mechanisms for the White Pointer DDWFTB based on both well data (Potoroo–1) and interpretation of seismic data by Totterdell et al (2000). The first potential seal mechanism is the intercalated strata of the White Pointer supersequence (Figs 8, 9 and 10), which is primarily composed of lagoonal siltstone and mud, with minor sandstone and coal, as it is observed in wells of both the Bight and Duntroon basins (Totterdell et al, 2000). In addition to the potential intra-stratal seals, the entirety of the White Pointer deepwater fold-thrust belt is draped with shales of the Tiger supersequence, which unconformably overlie the delta in the southwest and may act as a regional seal (Totterdell et al, 2000).

In terms of potential reservoir, the White Pointer supersequence contains sandstone intervals, which are interbedded with muds, siltstones and coals providing potential reservoir-seal pairs. Platypus–1 in the Duntroon Basin contains high-energy fluvial sandstone facies that may also act as potential reservoirs, provided they are represented to the west in the Ceduna Sub-basin (Totterdell et al, 2000).

Hammerhead DDWFTB prospectivity

Our interpretation of the cross-cutting seismic lines that cover the Hammerhead DDWFTB (Fig. 4) demonstrate the potential for structures in both the transitional and compressional provinces to exhibit 4-way closure and continuity along strike (Figs 12 and 14). The transitional province of the Hammerhead DDWFTB is well imaged in the five lines that were interpreted for this paper, displaying detachment folding (Figs 11 and 12) that is represented across the minimum ~75 km strike length of the DDWFTB (Fig. 4). The interpreted pericline in the east, which is imaged by two cross-cutting seismic lines (199-10+DWG14-A and 199-110+199-08; Fig. 12), has likely been breached by faults nearest the top of the structure; however, strong seismic reflectors indicate several zones in the core of the fold that appear intact (Figs 14b, 14d and 16). More importantly, the presence of this interpreted pericline demonstrates the overall structural style of the transitional province of the Hammerhead DDWFTB.

We interpret the detachment fold in the western seismic line 199-07 (Figs 4, 11 and 13b) to have a 5–8 km-wide trap area, with potential 4-way closure; however, this is dependent on the structural style of the Hammerhead DDWFTB being homogeneous across the system, as 4-way closure is demonstrated in the east (Figs 12 and 14).

Our interpretation of cross-cutting seismic lines (199-10+DWG14-A and 199-110+199-08) in the compressional province of the Hammerhead DDWFTB demonstrates the potential for lobate thrust sheet geometry, which in the Niger DDWFTB (e.g. Cobbold et al, 2009) provides 4-way closure along strike (Figs 12, 14a and 14c). We interpret the fold-thrust belt structures to include fault-propagation folds (Fig. 14a) and hanging-wall anticlines (Figs 13a and 14c), as well as minor footwall synclines and anticlines (Figs 13a, 14c and 15). Many of these interpreted structures display fault dependent and/or independent geometry, and have fold crests that appear unbreached (Figs 15 and 17). Cobbold et al (2009) provides evidence in the Niger DDWFTB for hydrocarbons migrating along existing thrust faults, and charging associated anticlines. This could provide a mechanism for fluid migration from the potential source rocks of the Tiger supersequence, where thrust faults are rooted (Figs 14a, 14c and 16), to the overlying structures in the Hammerhead DDWFTB (Totterdell et al, 2000; Totterdell et al, 2008).

Potential seal mechanisms for the Hammerhead DDWFTB would likely be provided by the intra-stratal muds that are present in several Duntroon Basin wells that penetrated the supersequence (Blevin et al, 2000; Totterdell et al, 2000; Krassay and Totterdell, 2004). Totterdell and Krassay (2003) indicate that the Hammerhead supersequence is comprised of basinward-thinning wedges of marine shale at the toe of slope, and our interpretation of seismic data indicates that the Hammerhead supersequence may become shale prone with proximity to the basin (Figs 12 and 17). This is based on seismic reflections near the terminus of the DDWFTB, whereby intra-stratal packages become increasingly chaotic, characteristic of shale rather than the thick sands that represent the supersequence closer to the shelf (Totterdell et al, 2000).

In terms of reservoir for the Hammerhead DDWFTB, the Hammerhead supersequence itself displays the best potential, with Gnarlyknots–1A intersecting blocky sandstone

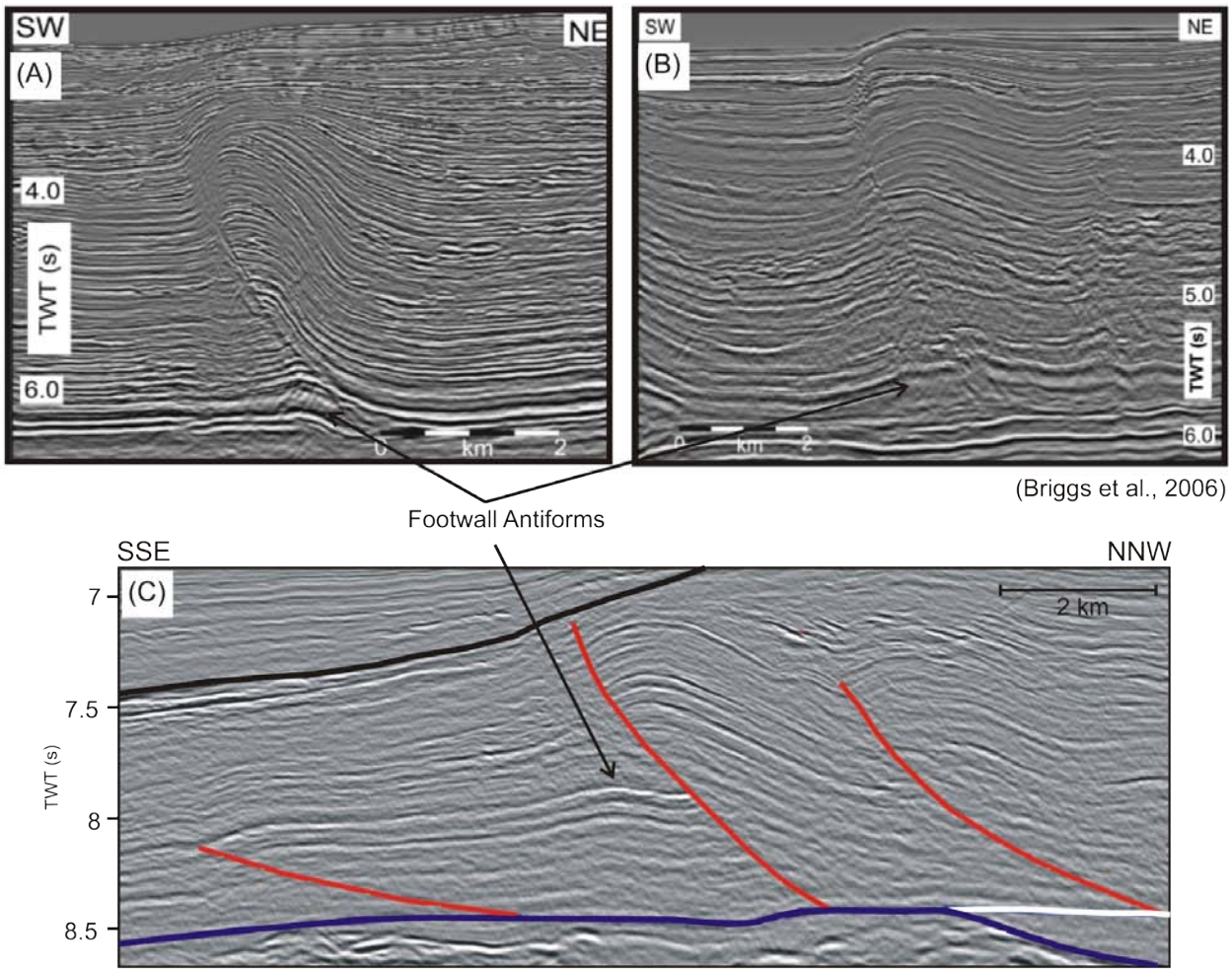

Figure 17. Seismic sections from Niger (A and B; after Briggs et al, 2006) and Hammerhead (199-110) (C) DDWFTBs showing hanging-wall anticlines with ~2 km wavelength and minor footwall antiforms.

and a seismic character indicative of strongly prograding stratal geometries nearest the shelf (Totterdell et al, 2000; Totterdell et al, 2008).

Regional structural controls on trap style

In the broadest sense, regional basement rift structures that developed along the southern margin control the distribution of the prospective Mesozoic to Cainozoic depocenters (Fraser and Tilbury, 1979; Willcox and Stagg, 1990; Stagg et al, 1990; Hill, 1995; Totterdell et al, 2000; Norvick and Smith, 2001; Totterdell and Bradshaw, 2004). The basement control on the location of depocentres for the sedimentary wedge at the time of deposition ultimately controlled the location of the White Pointer and Hammerhead DDWFTBs, and therefore any potential hydrocarbon trapping mechanisms therein. This is displayed in Figure 12 (bottom) whereby the basement high below the leading edge of the Hammerhead fold-thrust belt influences the geometry of the upper detachment and consequently the toe-thrust directly above it (Fig. 14c). This structure is represented in Figure 14c by a steeply dipping hanging-wall anticline, whereas in the next seismic line to the east where there is no basement high below the fold-thrust belt (Fig. 12, top), the structure is a fault-bend fold with box-fold geometry (Fig. 14a).

Regional stratigraphy plays a major role as overpressure development is important in initiating deformation in the delta wedge (Morley and Guerin, 1996). Salt (which is rheologically weak) and mudstone (which is commonly water-prone and becomes overpressured due to rapid burial) tend to flow and deform plastically initiating gravity-deformation along a detachment (Morley and Guerin, 1996).

The detachment is perhaps the most direct control on hydrocarbon trap geometry in that the deltaic wedge is often highly influenced by the lithology and thickness of the detachment horizon (Morley and Guerin, 1996; Rowan et al, 2004). Detachment folds form in preference to thrust faults where the underlying substrate is thick enough to allow excess material to be squeezed into the core of the antiform(s) to accommodate the shortening (Stewart, 1996; Simpson, 2009). This indicates that one should observe detachment folds where the lithology of the detachment horizon(s) is thickest and mobile. Other systems such as

the Niger and Baram DDWFTBs have structures that are controlled by the nature or lithology of the substrate; in these cases it is thick shale (Morley and Guerin, 1996; Morley, 2003; Briggs et al, 2006).

The major difference between the White Pointer and Hammerhead DDWFTBs is the thickness of the underlying supersequences, which form the detachment horizons. The Blue Whale supersequence is on average 2 km thick (and up to 4 km thick in places), while the Tiger supersequence is on average 1 km thick (rarely up to 4.5 km in the central Ceduna Sub-basin), thus restricting the amount of secondary overpressure that can form (i.e. from hydrocarbon generation, conversion of illite to montmorillonite; Morley, 2003; Osborne and Swarbrick, 1998) and limiting the initial volume of mobile material to accommodate the structures above (i.e. detachment folds).

The expectation that detachment folds form where the lithology of the detachment horizon(s) is thickest and mobile is not met for the White Pointer DDWFTB, where thrusting takes precedent to detachment folding despite a thick (>2 km) horizon of Blue Whale supersequence (Fig. 16). This may be influenced by the steep step in the detachment, driving the system to deform by thrusting rather than folding, or it may be attributed to the Blue Whale supersequence having a different lithology in this particular area. In contrast, the Hammerhead DDWFTB shows excellent evidence for shale mobilisation into the core of the detachment antiform, thus conforming to the models proposed by Stewart (1996) and Simpson (2009) (Figs 14b and 14d).

The detachment can also affect the transfer of strain along strike such as in the Hammerhead deepwater fold-thrust belt transfer zone, where a steep detachment has resulted in increased displacement immediately adjacent to the step in the detachment (Fig. 14c). A shallow detachment angle results in a more homogeneous distribution of strain amongst the structures of the deepwater fold-thrust belt. Figure 14a demonstrates how the same structure changes from a thrust fault where the detachment ramp is high angle to a box-shaped fault-propagation fold where the detachment is relatively flat lying, over a distance of ~10 km.

COMPARISON OF STRUCTURES FROM THE CEDUNA SUB-BASIN DELTA—DEEPWATER FOLD-THRUST BELTS TO THE NIGER DELTA—DEEPWATER FOLD-THRUST BELT

The Niger DDWFTB is one of the most prolific and structurally complex hydrocarbon provinces in the world with estimated oil reserves quoted to be 35 x 10^9 barrels, and gas reserves quoted to be 120 x 10^{12} standard cubic feet (SCF) or 66 x 10^9 barrels of oil equivalent (Cobbold et al, 2009; Ekweozor and Daukoru, 1994; Saugy and Eyer, 2003). The Niger DDWFTB consists of primarily Eocene to Recent sediments, which have prograded over the thick (3–4 km) Akata Shale Formation that forms both the source rock and the main detachment horizon for the gravity-driven deformation in the ~10 km-thick deltaic wedge (Cobbold et al, 2009). Although differences between Ceduna and Nigeria exist (such as degree of shale mobility, back-thrusting, counter-regional faulting, diapirism and the presence of two identifiable fold-thrust belts in the Niger DDWFTB), there are notable structural elements that make the systems analogous. The Niger DDWFTB is composed of two prominent lobes (western and southern)—a similar scenario to the White Pointer and Hammerhead DDWFTBs, respectively. The lobes of Niger DDWFTB are separated by a basement high known as the Charcot Fracture Zone. Above the Charcot Fracture Zone there is no diapir development and the leading-edges of the western and southern deepwater fold-thrust belts are lobate in shape where they border either side of the zone (Morley and Guerin, 1996; Cobbold et al, 2009). This is similar to the spatial configuration of the Ceduna Sub-basin, where a basement high separates the depocentres of the White Pointer and Hammerhead DDWFTBs, resulting in two separated delta systems whose structures have different orientations and geometries. If the basement high had not been present the system may have resulted in two stacked progradational delta systems similar to analogue models by McClay et al (2003).

Other similarities include a thick shale detachment and geometry of toe-thrusts and hanging-wall anticlines, the latter of which are proven hydrocarbon traps in the Niger DDWDTBs and are structurally analogous to several folds identified in the Ceduna Sub-basin DDWFTBs (Fig. 17). In the Niger DDWFTB, targets in the deepwater fold-thrust belt have been the source of significant reserves with eight deepwater discoveries estimated to contain over 10^9 barrel of oil equivalent each, concentrated in hanging-wall anticlines (Cobbold et al, 2009).

The Ceduna Sub-basin deepwater fold-thrust belts are located at considerable depths in deepwater (6–8 seconds two-way time [TWT] for the White Pointer, and 7–8.5 seconds TWT for the Hammerhead), however, drilling capabilities may someday be sufficient to explore such targets; the limits of deepwater drilling are constantly pushed, as is the case with deepwater Gulf of Mexico (JPT Online). Further exploration of the northern Ceduna Sub-basin may result in significant hydrocarbon discoveries and eventually lead to the exploration of deepwater targets to the south.

CONCLUSIONS

The White Pointer and Hammerhead DDWFTBs are separated temporally by ~20 My and spatially by a small basement high (approximately 1.5 seconds TWT). Evidence for gravity-driven tectonics is present nearest the centre of the depocentres, where the deltaic wedges are thickest and sediment supply was sufficient to initiate deformation. The DDWFTBs exhibit different structural geometries, which are controlled primarily by the thickness and lithology of the underlying detachment horizons.

The White Pointer DDWFTB has three provinces: ex-

tensional, transitional and compressional. The extensional province is dominated by listric, normal, growth faults, the transitional province is poorly developed due to a steep ramp in the seaward-dipping basal detachment and the compressional province is characterised by a series of imbricate thrust faults and folds of varying geometry and scale. There are two higher levels of detachment that distribute the compressional deformation across a larger area, resulting in a wider deepwater fold-thrust belt with imbricate thrust sheets of varying dip. The Hammerhead DDWFTB also contains extensional, transitional and compressional provinces with a gentle seaward dipping to landward dipping detachment. The extensional province is characterised by widely spaced listric growth faults with large vertical displacement. The transitional province is dominated by large antiformal detachment folds that show evidence for 4-way closure. The compressional province is dominated by a series of imbricate thrust faults and accompanying folds of varying geometry and scale (Figs 11 and 12).

The different structural styles displayed by the two DDWFTBs result in the creation of different potential hydrocarbon traps. A variety of trap styles are present in all three provinces of the White Pointer and Hammerhead DDWFTBs—particularly the deepwater fold-thrust belts—as these structures are best preserved with minimal crestal collapse and increased shale in the system for potential source/seals due to their more proximal positions in the basin. Numerous hanging-wall anticlines provide potential traps that range in width from 2–5 km and are demonstrated to develop into fault-propagation folds along strike as displacement on each lobate thrust sheet decreases (Figs 9a, 9c, 14a and 14c). Large-scale (<15 km wavelength) detachment folds also provide viable traps as structures display two-way and four-way closure in intersecting seismic profiles (Figs 8, 13b, 14b and 14d).

Ultra-deep water presently precludes the traps recognised in this study from being tested as exploration prospects, but information on the structural style associated with DDWFTBs of this type is readily exportable to other locations where a contribution to the assessment of prospectivity could be made more effectively.

ACKNOWLEDGEMENTS

The authors wish to thank Geoscience Australia for contribution of data for this project. The authors thank the Australian Research Council for their continuing support. This paper forms TRaX record #72.

REFERENCES

BEIN, J. AND TAYLOR, M.L., 1981—The Eyre Sub-basin: recent exploration results. APEA Journal, 21 (1), 91–8.

BOUEF, M.G., AND DOUST, H., 1975—Structure and development of the southern margin of Australia. APEA Journal, 15 (1), 33–43.

BLEVIN, J.E., TOTTERDELL, J.M., LOGAN, G.A., KENNARD, J.M., STRUCKMEYER, H.I.M. AND COLWELL, J.B., 2000—Hydrocarbon prospectivity of the Bight Basin—petroleum systems analysis in a frontier basin. In: 2nd Sprigg Symposium—Frontier Basins, Frontier Ideas, Adelaide, 29–30 June. Geological Society of Australia, Abstracts 60, 24–29.

BRIGGS, S.E., DAVIES, R.J., CARTWRIGHT, J.A. AND MORGAN, R., 2006—Multiple detachment levels and their control on fold styles in the compressional domain of the deepwater west Niger Delta. Basin Research, 18, 435–50. DOI:10.1111/j.1365-2117.2006.00300.x.

COBBOLD, P.R., CLARKE, B.J. AND LØSETH, H., 2009—Structural consequences of fluid overpressure and seepage forces in the outer thrust belt of the Niger Delta. Petroleum Geoscience, 15, 3–15. DOI: 10.1144/1354-079309-784

COHEN, H.A. AND MCCLAY, K., 1996—Sedimentation and shale tectonics of the northwestern Niger Delta front. Marine and Petroleum Geology, 13, 313–28.

CORREDOR, F., SHAW, J. H., AND BILOTTI, F., 2005—Structural styles in the deep-water fold and thrust belts of the Niger Delta. American Association of Petroleum Geologists Bulletin, 89, 753–80.

DOUST, H. AND OMATSOLA, E., 1990—Niger Delta. In: Edwards, J.D. and Santogrossi, P.A. (eds), Divergent/passive margin basins. American Association of Petroleum Geologists Memoir, 48, 201–38.

EKWEOZOR, C.M. AND DAUKORU, E.M., 1994—Northern delta depobelt portion of the Akata–Agbada petroleum system, Niger Delta, Nigeria. In: Magoon, L.B. & Dow, W.G. (eds), The petroleum system—from source to trap. American Association of Petroleum Geologists Memoir, 460, 599–613

ERSLEV, E.A., 1991—Trishear fault-propagation folding. Geology, 19, 617–20.

ESPURT, N., CALLOT, J.-P., TOTTERDELL, J., STRUCKMEYER, H. AND VIALLY, R., 2009—Interactions between continental breakup dynamics and large-scale delta system evolution: Insights from the Cretaceous Ceduna delta system, Bight Basin, Southern Australia margin. Tectonics, 28, TC6002. DOI:10.1029/2009TC002447.

FIDUK, J.C., WEIMER, P., TRUDGILL, B.D., ROWAN, M.G., GALE, P.E., PHAIR, R.L., KORN, B.E., ROBERTS, G.R., GAFFORD, W.T., LOWE, R.S. AND QUEFFELEC, T.A., 1999—The Perdido Fold Belt, Northwestern Deep Gulf of Mexico, Part 2: Seismic Stratigraphy and Petroleum Systems. American Association of Petroleum Geologists Bulletin, 83 (4), 578–612.

FINKBEINER, T., ZOBACK, M., FLEMINGS, P. AND STUMP, B., 2001—Stress, pore pressure, and dynamically

constrained hydrocarbon columns in the South Eugene Island 330 field, northern Gulf of Mexico. American Association of Petroleum Geologists Bulletin, 85 (6), 1,007–31.

FRASER, A.R. AND TILBURY, L.A., 1979—Structure and stratigraphy of the Ceduna Terrace region, Great Australian Bight. APEA Journal, 19 (1), 53–65.

HILL, A.J., 1995—Bight Basin. In: Drexel, J.F. and Preiss, W.V. (eds), The geology of South Australia. Vol. 2, The Phanerozoic. South Australia, Geological Survey, Bulletin 54, 133–149.

JAMES, D.M.D., 1984—The geology and hydrocarbon resources of Negara Brunei Darussalam. Muzium Brunei and Brunei Shell Petroleum Company Berhad, Special Publication, 8, 2–21.

KING, R.C. AND BACKÉ, G., in press—A balanced 2D structural model of Hammerhead Delta—Deepwater Fold-Thrust Belt, Bight Basin, Australia. Australian Journal of Earth Sciences.

KING, R.C., HILLIS, R.R. AND TINGAY, M.R.P., 2009—Present-day stress and neotectonic provinces of the Baram Delta and deepwater fold-thrust belt. Journal of the Geological Society, London, 166, 197–200.

KING, S.J. AND MEE, B.C., 2004—The seismic stratigraphy and petroleum potential of the Late Cretaceous Ceduna Delta, Ceduna Sub-basin, Great Australian Bight. In: Boult, P.J., Johns, D.R. and Lang, S.C. (eds), Eastern Australasian Basins Symposium II. Petroleum Exploration Society of Australia, Special Publication, 63–73.

KRASSAY, A.A. AND TOTTERDELL, J.M., 2003—Seismic stratigraphy of a large, Cretaceous shelf-margin delta complex, offshore southern Australia. American Association of Petroleum Geologists Bulletin, 87 (6), 935–63.

KOOPMAN, A., SCHREURS, J. AND ELLENOR. D.W., 1996—The oil and gas resources of Brunei Darussalam—the coastal and offshore oil and gas fields. In: Sandal, S.T. (ed.), Geology and Hydrocarbon Resources of Negara Brunei Darussalam. Chapter 5, 155–92. Bandar Seri Begawan: Syabas.

MCCLAY, K., DOOLEY, T. AND ZAMORA, G., 2003—Analogue models of delta systems above ductile substrates. In: Van Rensbergen, P., Hillis, R.R., Maltman, A.J. and Morley, C.K. (eds), Subsurface sediment mobilization. Geological Society, London, Special Publication, 216, 411–28.

MORLEY, C.K., 2003—Mobile shale related deformation in large deltas developed on passive and active margins. In: van Rensbergen, P., Hillis, R.R., Maltman, A.J. and Morley, C.K. (eds), Subsurface Sediment Mobilization. Geological Society, London, Special Publication, 216, 335–57.

MORLEY, C.K. AND GUERIN, G., 1996—Comparison of gravity-driven deformation styles and behaviour associated with mobile shales and salt. Tectonics, 15, 1,154–70.

NORVICK, M.S. AND SMITH, M.A., 2001—Mapping the plate tectonic reconstruction of southern and southeastern Australia and implications for petroleum systems. APPEA Journal, 41 (1), 15–35.

OSBORNE, M.J., AND SWARBRICK, R.E., 1998—Mechanisms for Generating Overpressure in Sedimentary Basins: A Re-evaluation. American Association of Petroleum Geologists Bulletin, 81 (6), 1,023–41.

ROWAN, M.G, PEEL, F.J. AND VENDEVILLE, B.C., 2004—Gravity-driven fold belts on passive margins. In: K.R. McClay (ed.), Thrust tectonics and hydrocarbons systems. American Association of Petroleum Geologists Memoir, 82, 157–82.

RUBLE, T.E., LOGAN, G.A., BLEVIN, J.E., STRUCKMEYER, H.I.M., LIU, K., AHMED, M., EADINGTON, P.J. AND QUEZADA, R.A., 2001—Geochemistry and charge history of a palaeo-oil column: Jerboa–1, Eyre Sub-basin, Great Australian Bight. In: Hill, K.C. and Bernecker, T. (eds), Eastern Australasian Basins Symposium—A Refocused Energy Perspective for the Future. Petroleum Exploration Society of Australia, Special Publication, 521–30.

SANDAL, S.T., 1996—The Geology and Hydrocarbon Resources of Negara Brunei Darussalam. Brunei Shell Petroleum Company and Brunei Museum. Bandar Seri Begawan: Syabas.

SAUGY, L. AND EYER, J.A., 2003—Fifty years of exploration in the Niger Delta (West Africa). In: Halbouty, M.T. (ed.), Giant Oil and Gas Fields of the Decade 1990–1999. American Association of Petroleum Geologists Memoir, 78, 211–26.

SAYERS, J., SYMONDS, P., DIREEN, N.G. AND BERNARDEL, G., 2001—Nature of the continent-ocean transition on the non-volcanic rifted margin of the central Great Australian Bight. In: Wilson, R.C.L., Whitmarsh, R.B., Taylor, B. and Froitzheim, N. (eds), Non-volcanic rifting of continental margins: a comparison of evidence from land and sea. Geological Society, London, Special Publication, 187, 51–76.

SCHREURS, G., 1997—The petroleum geology of Negara Brunei Darussalem; an update. In: Howes, J.V.C. and Noble, R.A. (eds), Proceedings of the Indonesian Petroleum Association Petroleum Systems of SE Asia and Australasia Conference, Jakarta, Indonesia, 21–23 May, 751–66.

SIMPSON, G.D.H., 2009—Mechanical modelling of folding versus faulting in brittle-ductile wedges. Journal of Structural Geology, 31, 369–81.

SOMERVILLE, R., 2001—The Ceduna Sub-basin—a snapshot of prospectivity. APPEA Journal, 41 (1), 321–46.

STAGG, H.M.V., COCKSHELL, C.D., WILLCOX, J.B., HILL, A.J., NEEDHAM, D.V.L., THOMAS, B., O'BRIEN, G.W. AND HOUGH, L.P., 1990—Basins of the Great Australian Bight region: geology and petroleum potential. Bureau of Mineral Resources, Australia, Continental Margins Program, Folio 5.

STEWART, S.A., 1996—Influence of detachment layer thickness on style of thin-skinned shortening. Journal of Structural Geology, 18 (10), 1,271–74.

STRUCKMEYER, H.I.M., TOTTERDELL, J.M., BLEVIN, J.E., LOGAN, G.A., BOREHAM, C.J., DEIGHTON, I., KRASSAY, A.A. AND BRADSHAW, M.T., 2001—Character, maturity and distribution of potential Cretaceous oil source rocks in the Ceduna Sub-basin, Bight Basin, Great Australian Bight. In: Hill, K.C. and Bernecker, T. (eds), Eastern Australasian Basin Symposium, a refocused energy perspective for the future. Petroleum Exploration Society of Australia, Special Publication, 543–52.

STRUCKMEYER, H.I.M., WILLIAMS, A.K., COWLEY, R., TOTTERDELL, J.M., LAWRENCE, G. AND O'BRIEN, G.W., 2002—Evaluation of hydrocarbon seepage in the Great Australian Bight. APPEA Journal, 42 (1), 371–85.

TAPLEY, D., MEE, B.C., KING, S.J., DAVIS, R.C. AND LEISCHNER, K.R., 2005—Petroleum potential of the Ceduna Sub-basin: impact of Gnarlyknots–1A. APPEA Journal, 45 (1), 365–80.

TINGAY, M., HILLIS, R., MORLEY, C., KING, R., SWARBRICK, R. AND DAMIT, A., 2009—Present-day stress and neotectonics of Brunei: implications for petroleum exploration and production. American Association of Petroleum Geologists Bulletin, 93 (1), 75–100.

TOTTERDELL, J.M., BLEVIN, J.E., STRUCKMEYER, H.I.M., BRADSHAW, B.E., COLWELL, J.B. AND KENNARD, J.M., 2000—A new sequence framework for the Great Australian Bight: starting with a clean slate. APPEA Journal, 40 (1), 95–117.

TOTTERDELL, J.M. AND KRASSAY, A.A., 2003—The role of shale deformation and growth faulting in the Late Cretaceous evolution of the Bight Basin, offshore southern Australia. In: Van Rensbergen, P., Hillis, R.R., Maltman, A.J. and Morley, C.K. (eds), Subsurface sediment mobilisation. Geological Society, London, Special Publication 216, 429–42.

TOTTERDELL, J.M. AND BRADSHAW, B.E., 2004—The structural framework and tectonic evolution of the Bight Basin. In: Boult, P.J., Johns, D.R. and Lang, S.C. (eds), Eastern Australasian Basins Symposium II. Petroleum Exploration Society of Australia, Special Publication, 41–61.

TOTTERDELL, J.M., STRUCKMEYER, H.I.M., BOREHAM, C.J., MITCHELL, C.H., MONTEIL, E. AND BRADSHAW, B.E., 2008—Mid–Late Cretaceous organic-rich rocks from the eastern Bight Basin: implications for prospectivity. PESA Eastern Australasian Basins Symposium III, 137–58.

VAN RENSBERGEN, P., MORLEY, C. K., ANG, D.W., HOAN, T.Q. AND LAM, N.T., 1999—Structural evolution of shale diapirs from reactive rise to mud volcanism: 3D seismic data from the Baram delta, offshore Brunei Darussalam. Journal of the Geological Society, London, 156, 633–50.

VAN RENSBERGEN, P. AND MORLEY, C.K., 2003—Re-evaluation of mobile shale occurrences on seismic sections of the Champion and Baram deltas, offshore Brunei. Geological Society, London, Special Publication, 216, 395–409.

WILLCOX, J.B. AND STAGG, H.M.J., 1990—Australia's southern margin: a product of oblique extension. Tectonophysics, 173, 269–81.

YASSIR, N.A. AND ZERWER, A., 1997—Stress regimes in the Gulf Coast, offshore Louisiana: data from well-bore breakout analysis. AAPG Bulletin, 81, 293–307.

Authors' biographies next page.

THE AUTHORS

Justin MacDonald is a PhD student at the Australian School of Petroleum. He is a graduate of Memorial University of Newfoundland and the University of Waterloo and holds a BSc (Hons) and a MSc. Justin recently completed his MSc, which involved structural analyses of the Mackenzie Mountains foreland fold and thrust belt in northern Canada. Over the last few years he has worked in base and precious metals exploration in western and northern Canada and for the Northwest Territories Geoscience Office. Justin's current research interests pertain to structural controls on delta—deepwater fold-thrust belts with particular emphasis on the Ceduna Delta systems of the Bight Basin. Student member: AAPG, PESA, SPE, ASEG and SEG.

Rosalind King successfully completed her BSc (Hons) and PhD at the University of Liverpool in 2001 and 2005, respectively. Her PhD research was the Structural Evolution of the Cape Fold Belt, South Africa. Since 2005, she has been working at the Australian School of Petroleum (University of Adelaide) as a post-doctoral researcher. Ros's current research include the present-day stresses of northwest Borneo and the tectonics of delta—deepwater fold-thrust belts. Ros currently serves as the vice-president of the South Australian Branch of the Petroleum Exploration Society of Australia (PESA). Member: the GSL, AAPG and PESA.

Richard Hillis is CEO of the Deep Exploration Technologies CRC. He graduated with a BSc (Hons) from Imperial College (London, 1985), and a PhD from the University of Edinburgh (1989) and was until recently State of South Australia Professor of Petroleum Geology and Head of the Australian School of Petroleum (University of Adelaide). He has published over 100 papers in the areas of petroleum geomechanics and basin tectonics and has consulted extensively to, and run short courses for, the petroleum industry on these topics. Richard is a non-executive director of JRS Petroleum Research (privately owned image log and geomechanics consultancy), Petratherm (ASX-listed geothermal company) and AuScope (national research facility in the earth sciences). Member: AAPG, AGU, ASEG, EAGE, GSA, GSL, PESA, SEG and SPE.

Guillaume Backé recently joined the Australian School of Petroleum, following a two year post doctoral research position at the Centre for Mineral Exploration Under Cover (CMXUC) of the University of Adelaide. He obtained his Master of Geophysics at the University of Toulouse III in France in June 2002, and completed his PhD at the University of Pau et des Pays de l'Adour in December 2006 with a dissertation on the tectonic evolution of the Venezuelan Andes (Venezuela), the Southern Central Andes and the Neuquén basin (Argentina). Guillaume's main research interests lie in the integration of geophysics and geology for the construction of accurate and validated three-dimensional models of the Earth's sub-surface, in particular for petroleum, geothermal or geological storage of carbon dioxide applications. Member: AGU, GSA. Active committee member: PESA.

APPEA

4.3 Paper 3

MacDonald, J.D., Backé, G., King, R., Holford, S., and Hillis, R.R., (2012): Geomechanical modelling of fault reactivation in the Ceduna Sub-basin, Bight Basin, Australia, *in*: Healy, D., Butler, R. W. H., Shipton, Z. K. & Sibson, R. H. (eds) 2012. Faulting, Fracturing and Igneous Intrusion in the Earth's Crust. *Geological Society, London, Special Publications*, 367, 71–89.

Geomechanical modelling of fault reactivation in the Ceduna Sub-basin, Bight Basin, Australia

J. MACDONALD[1]*, G. BACKÉ[1], R. KING[2], S. HOLFORD[1] & R. HILLIS[3]

[1]*Australian School of Petroleum, University of Adelaide, Santos Petroleum Engineering Building, Adelaide, 5005, Australia*

[2]*School of Earth and Environmental Sciences, University of Adelaide, Mawson Laboratories, Adelaide, 5005, Australia*

[3]*Deep Exploration Technologies Cooperative Research Centre, University of Adelaide, Mawson Laboratories, Adelaide, 5005, Australia*

**Corresponding author (e-mail: jmacdonald@asp.adelaide.edu.au)*

Abstract: The Ceduna Sub-basin is located within the Bight Basin on the Australian southern margin. Recent structural analysis using newly acquired two-dimensional (2D) and three-dimensional (3D) seismic data demonstrates two Late Cretaceous delta–deepwater fold–thrust belts (DDWFTBs), which are overlain by Cenozoic sediments. The present-day normal fault stress regime identified in the Bight Basin indicates that the maximum horizontal stress (S_{Hmax}) is margin parallel; Andersonain faulting theory therefore suggests the delta-top extensional faults are oriented favourably for reactivation. A breached hydrocarbon trap encountered in the Jerboa-1 well demonstrates this fault reactivation. Faults interpreted from 3D seismic data were modelled using the Poly3D© geomechanical code to determine the risk of reactivation. Results indicate delta-top extensional faults that dip 40–70° are at moderate–high risk of reactivation, while variations in the orientation of the fault planes results in an increased risk of reactivation. Two pulses of inversion are identified in the Ceduna Sub-basin and correlate with the onset of rifting and fault reactivation in the Santonian. We propose a ridge-push mechanism for this stress which selectively reactivates extensional faults on the delta-top, forming inversion anticlines that are prospective for hydrocarbon exploration.

Indications of past hydrocarbon accumulations have been found in the Jerboa-1 well of the Eyre Sub-basin on the southern margin of Australia (Totterdell *et al.* 2000; Ruble *et al.* 2001; Somerville, 2001; Struckmeyer *et al.* 2001; Fig. 1). However, exploration success has been lacking in the Ceduna Sub-basin due to geographic constraints such as water depth and accessibility, as well as failure to identify a significant hydrocarbon system in only two exploration wells (Potoroo-1 and Gnarlyknots-1; Figs 1 & 2).

The Ceduna Sub-basin is located in the Bight Basin at the centre of the southern margin of Australia, which is defined by the bathymetry of the Ceduna Terrace (Fig. 2). The Bight Basin is significantly underexplored yet is a prospective hydrocarbon province that extends along the coast between Port Lincoln (South Australia) and Cape Leeuwin (Western Australia), a distance in excess of 3000 km, and offshore for hundreds of kilometres (Fig. 1). Only 12 exploration wells have been drilled to date in the Bight Basin, two of which were drilled in the Ceduna Sub-basin. The Ceduna Sub-basin covers an area of approximately 90 000 km^2 with water depths ranging from 200 m to more than 5000 m.

The thickness of Middle Jurassic–Cenozoic sedimentary rocks in the Ceduna Sub-basin exceeds 12 km (Struckmeyer *et al.* 2001; Krassay & Totterdell 2003). The Ceduna Sub-basin contains two spatially and temporally separate Cretaceous delta–deepwater fold–thrust belt (DDWFTB) systems: the late Albian–Santonian White Pointer DDWFTB and the late Santonian–Maastrichtian Hammerhead DDWFTB. These systems detach above the mud-rich Blue Whale and Tiger supersequences, respectively (Fig. 3).

Previous work completed by Geoscience Australia (in 1999–2008) and Woodside (including drilling of the most recent well, Gnarlyknots-1) resulted in an improved understanding of the hydrocarbon prospectivity of the Bight Basin, particularly the Ceduna Sub-basin. This work focused on the sequence stratigraphy, tectonics and petroleum systems of the Bight Basin to identify organic-rich supersequences, understand the regional maturity of these rocks and identify suitable traps and seals for hydrocarbon accumulation (Blevin *et al.* 2000;

From: HEALY, D., BUTLER, R. W. H., SHIPTON, Z. K. & SIBSON, R. H. (eds) 2012. *Faulting, Fracturing and Igneous Intrusion in the Earth's Crust*. Geological Society, London, Special Publications, **367**, 71–89. http://dx.doi.org/10.1144/SP367.6

Fig. 1. Location map showing the position of the Ceduna Sub-basin in the Bight Basin on the southern Australian margin (from Totterdell & Bradshaw 2004).

Totterdell *et al.* 2000, 2008; Ruble *et al.* 2001; Sayers *et al.* 2001; Somerville 2001; Struckmeyer *et al.* 2001, 2002; Krassay & Totterdell 2003; Totterdell & Krassay 2003; King & Mee 2004; Totterdell & Bradshaw 2004; Tapley *et al.* 2005).

In this paper, we demonstrate that extensional faults on the delta top are optimally oriented for fault reactivation, based on the current understanding of the *in situ* stress regime in the Ceduna Sub-basin. Using 3D seismic data and Poly3D© (Maerten

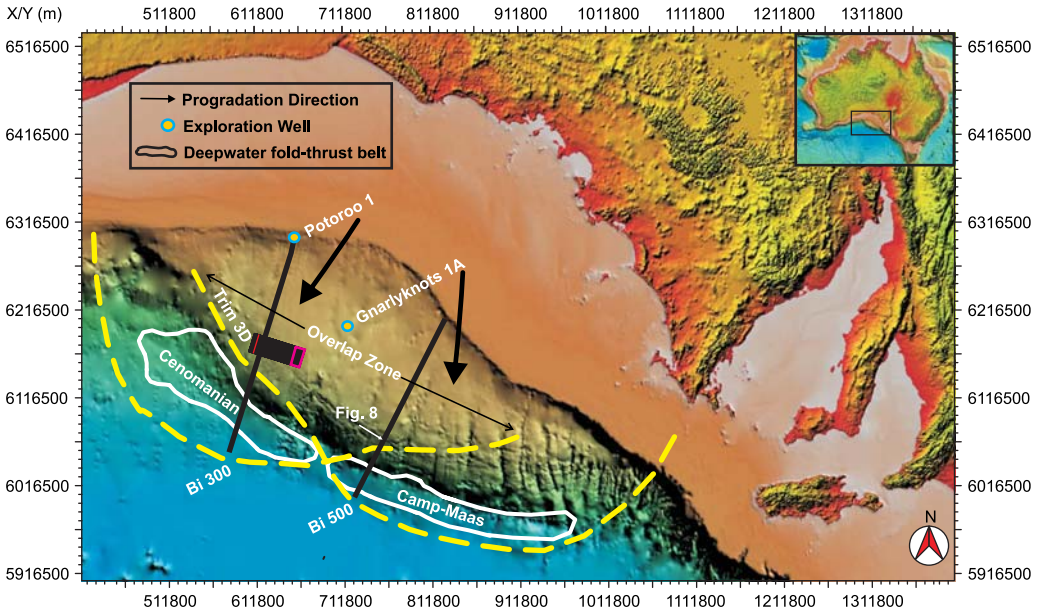

Fig. 2. Digital elevation model demonstrating the broad bathymetry of the Ceduna Terrace, outline of delta lobes and overlap zone (yellow dashed line) with approximate progradation direction, location of delta–deepwater fold–thrust belts (DDWFTBs), well locations and location of seismic surveys used in this study.

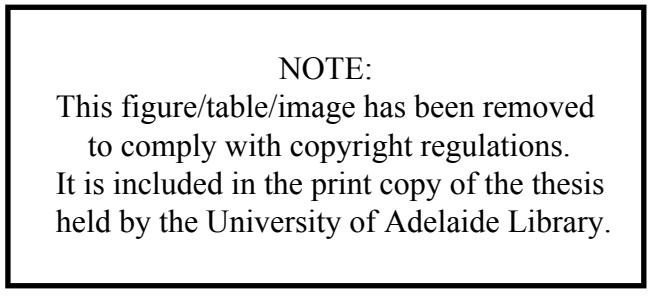

Fig. 3. Sequence stratigraphic framework (supersequences) for the Bight Basin with basin phases represented by numbers 1–4. Global sea level curve on right side from Haq *et al.* (1988). Modified from Krassay & Totterdell (2003).

et al. 2005, 2009), we demonstrate the geometry and reactivation potential of the extensional faults in the delta top. We apply this model as a proxy to further assess the reactivation risk of the extensional faults for the regional 2D seismic data.

Tectono-stratigraphic framework

The Bight Basin is located in the Great Australian Bight (Fig. 1) and demonstrates a broad bathymetric terrace (the Ceduna Terrace; Fig. 2) which forms the continental slope and rise of the southern Australian margin (Totterdell *et al.* 2000). The Bight Basin developed during Late Jurassic–Early Cretaceous rifting and continued to develop with the break-up of Gondwana, separating Australia and Antarctica during the Late Cretaceous (Totterdell *et al.* 2000; Sayers *et al.* 2001). Late Cretaceous break-up resulted in the separation of the basin into three structurally controlled sub-basins: the Eyre, Ceduna and Recherche (Fig. 1). The Ceduna Sub-basin is the largest depocentre and the focus of this study

(Totterdell *et al.* 2000; Krassay & Totterdell 2003; Fig. 1). The sub-basins are separated by NW-striking accommodation zones, which were formed by the rifting and crustal thinning of the Australian Plate (Stagg *et al.* 1990; Willcox & Stagg 1990; Totterdell *et al.* 2000).

The Ceduna Sub-basin is bound to the north by Proterozoic and older terranes and to the east by the Proterozoic of the Gawler Craton (Krassay & Totterdell 2003; Fig. 1). The Eyre Sub-basin defines the western limit of the Ceduna Sub-basin while the Duntroon Basin forms the SE boundary; to the south it tapers out onto the thin oceanic crust of the South Australian Abyssal Plain (Fraser & Tilbury 1979; Bein & Taylor 1981; Willcox & Stagg 1990; Hill 1995; Norvick & Smith 2001; Totterdell & Krassay 2003; Fig. 1).

The stratigraphy of the Ceduna Sub-basin comprises 10 supersequences which relate to the four Bight Basin phases first described by Totterdell *et al.* (2000; Fig. 3). The sub-basin evolution involved two successive periods of extension and thermal subsidence that commenced in the Late Jurassic (Totterdell *et al.* 2000; Totterdell & Krassay 2003). Basin Phase 1 marks the onset of sedimentation in the Bight Basin during the Middle–Late Jurassic extension, with the contemporaneous formation of a series of extensional and transtensional half-graben structures. Pre-existing basement trends appear to have focused the deformation during this phase (Totterdell *et al.* 2000). Basin Phase 2 records the slow thermal subsidence during the Early Cretaceous, which ended abruptly with the onset of rapid subsidence (Basin Phase 3) during the Late Albian (Totterdell *et al.* 2000). Seafloor spreading in the Late Santonian caused the break-up of Australia and Antarctica and marks the end of Basin Phase 3 in the Bight Basin. A period of thermal subsidence (Basin Phase 4) followed, which marks the initiation of the Late Santonian South Australian passive margin (Totterdell & Krassay 2003). These four Bight Basin phases are observed in the Ceduna Sub-basin (Fig. 3).

Of the ten supersequences defined in Totterdell *et al.* (2000), those of most importance to this study are the stratigraphic units that comprise the two DDWFTB systems and their respective detachments. At the northern margin of the Ceduna Sub-basin these include: the Albian Blue Whale supersequence; Cenomanian White Pointer supersequence; Turonian–Santonian Tiger supersequence; Campanian–Maastrichtian Hammerhead supersequence; and the Cenozoic rocks above the intra-Maastrichtian regional unconformity (Fig. 3). Basin modelling of the distal parts of the sub-basin indicates that the Blue Whale, White Pointer and Tiger supersequences are most prospective in terms of source rocks (Blevin *et al.* 2000).

The supersequence lithology descriptions below come from Totterdell *et al.* (2000), who used well data from the Bight, Eyre and Duntroon sub-basins. The oldest unit relevant to this study is the Middle Albian–Cenomanian Blue Whale supersequence, which records the first major marine flooding event with the deposition of restricted marine siltstones nearest the palaeoshelf and an inferred thick package of marine mudstones in the basin. This package of marine mudstone forms the detachment for the overlying Cenomanian White Pointer DDWFTB, comprising the White Pointer supersequence (Totterdell & Bradshaw 2004). Rapid (*c*. 5 Ma) deposition of the aggradational White Pointer supersequence likely produced overpressure in the underlying ductile marine mudstone, enabling gravity-driven deformation which resulted in the formation of growth faults and toe thrusts that sole out or are rooted in the Blue Whale mudstone and form the White Pointer DDWFTB (Totterdell & Krassay 2003). The White Pointer supersequence is composed primarily of fluvial to lagoonal siltstone and mudstone intercalated with minor sandstone and coal units. Dewatering of the underlying shale resulted in a loss of overpressure (Totterdell *et al.* 2000; Totterdell & Krassay 2003) and provided the likely mechanism for the cessation of all gravity-driven deformation.

Overlying the White Pointer DDWFTB is the Turonian–Santonian Tiger supersequence, containing an aggradational package of what is suggested to be marine shale based on seismic sequence stratigraphy and extrapolation of well data from Potoroo-1 in the northern Ceduna Sub-basin (Totterdell *et al.* 2000). The unit is heavily faulted in the Ceduna Sub-basin due to reactivation of older faults (Mulgara Fault Family), controlled by the underlying ductile shales of the Blue Whale supersequence. The timing of this fault reactivation is well constrained to the Late Santonian as this faulting had ceased before deposition of the overlying Hammerhead supersequence (Totterdell *et al.* 2000).

The Santonian–Maastrichtian Hammerhead supersequence has an overall progradational to aggradational character and is believed to be almost entirely composed of channel sandstones near the present-day shelf in the Ceduna Sub-basin (Totterdell *et al.* 2000). Three stratigraphic sequences have been interpreted in the Hammerhead supersequence from seismic data: the lowermost and middle sequences are progradational and the uppermost sequence is aggradational. The lowermost and middle sequences of the Hammerhead supersequence show seismic facies character that lack strong stratal geometries on the shelf and are homogeneous. This seismic character is consistent with a basinward change to a more shale-rich system. The 19 Ma period of progradation of the Hammerhead

DDWFTB across the palaeoshelf resulted in the initiation of gravity-driven deformation with the top of the underlying Tiger supersequence forming the detachment surface (Totterdell & Krassay 2003; King & Backé 2010). The gravitational tectonics initiated at the palaeoshelf margin, where the Hammerhead supersequence is thickest (*c.* 5000 m at this location; Totterdell & Krassay 2003).

The Hammerhead supersequence is overlain by the Paleocene–Early Eocene Wobbegong supersequence, which consists of marginal marine-to-deltaic sandstone and siltstone that was deposited on a hiatus which is believed to represent 5–7 Ma. Above this, the Middle Eocene–Pleistocene Dugong supersequence is present, consisting of a basal coarse sandstone and thick uniform cold water carbonate succession related to the development of a stable carbonate shelf.

Structural geometry of delta–deepwater fold–thrust belts

The structural geometry of delta–deepwater fold–thrust belts has been widely studied where they form prolific hydrocarbon provinces such as the Niger (e.g. Doust & Omatsola 1990; Morley & Guerin 1996; Briggs *et al.* 2006) and Baram DDWFTBs (e.g. Tingay *et al.* 2005, 2009; King *et al.* 2010; Morley *et al.* 2011). Delta–deepwater fold–thrust belts typically form at continental margins where rapid progradation of deltaic sediments over salt or water-prone mud results in overpressure development (in water-prone mud) and deformation under gravitational forces (Morley & Guerin 1997; Morley 2003; Rowan *et al.* 2004). The result is a broad segregation of the delta into extensional and compressional provinces, whereby margin-parallel gravitational extensional stresses on the delta top drive downdip margin-normal compressional stresses in the deepwater fold–thrust belt (Yassir & Zerwer 1997; Corredor *et al.* 2005; King *et al.* 2009).

The delta top is typically characterized by regional and counter-regional listric normal growth faults that sole out at the level of the underlying pro-delta sediments (salt or shale; Mandl & Crans 1981; Morley & Guerin 1996; Rowan *et al.* 2004). These extensional structures are balanced by the deepwater fold–thrust belt, which is composed of imbricate thrust sheets and associated fault-propagation folds rooted at the basal detachment (Morley & Guerin 1996; McClay *et al.* 2003; King *et al.* 2009). The extensional and compressional provinces are commonly separated by a transitional province that is characterized by detachment folds and reactive, active and passive diapirs of shale or salt (Jackson *et al.* 1994; Morley & Guerin 1996).

Shale detachment horizons are dependent on the development and maintenance of overpressure, with rapid progradation of delta sediments over the water-prone mud contributing the initial disequilibrium compaction overpressure of the muds (Morley *et al.* 2008, 2011). Overpressure is not required for salt as it is naturally weak and mobile, whereas shale requires overpressure to induce weakness and mobility (Davis & Engelder 1985; Morley & Guerin 1996; Costa & Vendeville 2002; Rowan *et al.* 2004; Bilotti & Shaw 2005). Subsequent inflationary overpressures can also develop, most often by dewatering during the smectite–illite transition and volume increase due to hydrocarbon generation; these serve to maintain overpressure (Morley & Guerin 1996; Osborne & Swarbrick 1997; Morley *et al.* 2011).Variations in sediment supply and detachment parameters [such as lithology and thickness of the detachment horizon(s)] and development of overpressure are some of the key factors that contribute to the varied structural styles observed in DDWFTBs worldwide.

Delta–deepwater fold–thrust belts often form excellent hydrocarbon provinces due to the generation of hydrocarbons from marine sediments and an abundance of trapping mechanisms in the deltaic sediments, as a result of the gravity-driven deformation (Morley *et al.* 2011). There are numerous structures formed in these settings, many of which have excellent hydrocarbon-trapping potential. For example, rollover antiforms and tilted fault blocks develop in the extensional province (Finkbeiner *et al.* 2001). Hanging-wall and footwall folds developed due to thrust fault propagation in a deepwater fold–thrust belt also form excellent fault-independent and -dependent traps (Ingram *et al.* 2004; Cobbold *et al.* 2009). The imbricate thrusts can provide fluid pathways from the often hydrocarbon-generating shale detachment horizon into the overlying traps (Ingram *et al.* 2004; Cobbold *et al.* 2009).

Regional structural style of the Ceduna Sub-basin

The Ceduna Sub-basin contains two Cretaceous DDWFTBs: the late Albian–Cenomanian White Pointer and the Late Santonian–Maastrichtian Hammerhead. The geometry of the Ceduna DDWFTBs was first recognized by Boeuf & Doust (1975) and Fraser & Tilbury (1979) and has since been investigated by several authors including Totterdell & Krassay (2003), Totterdell & Bradshaw (2004), Espurt *et al.* (2009), King & Backé (2010) and MacDonald *et al.* (2010).

The Ceduna Sub-basin provides a unique opportunity to study two separate progradational

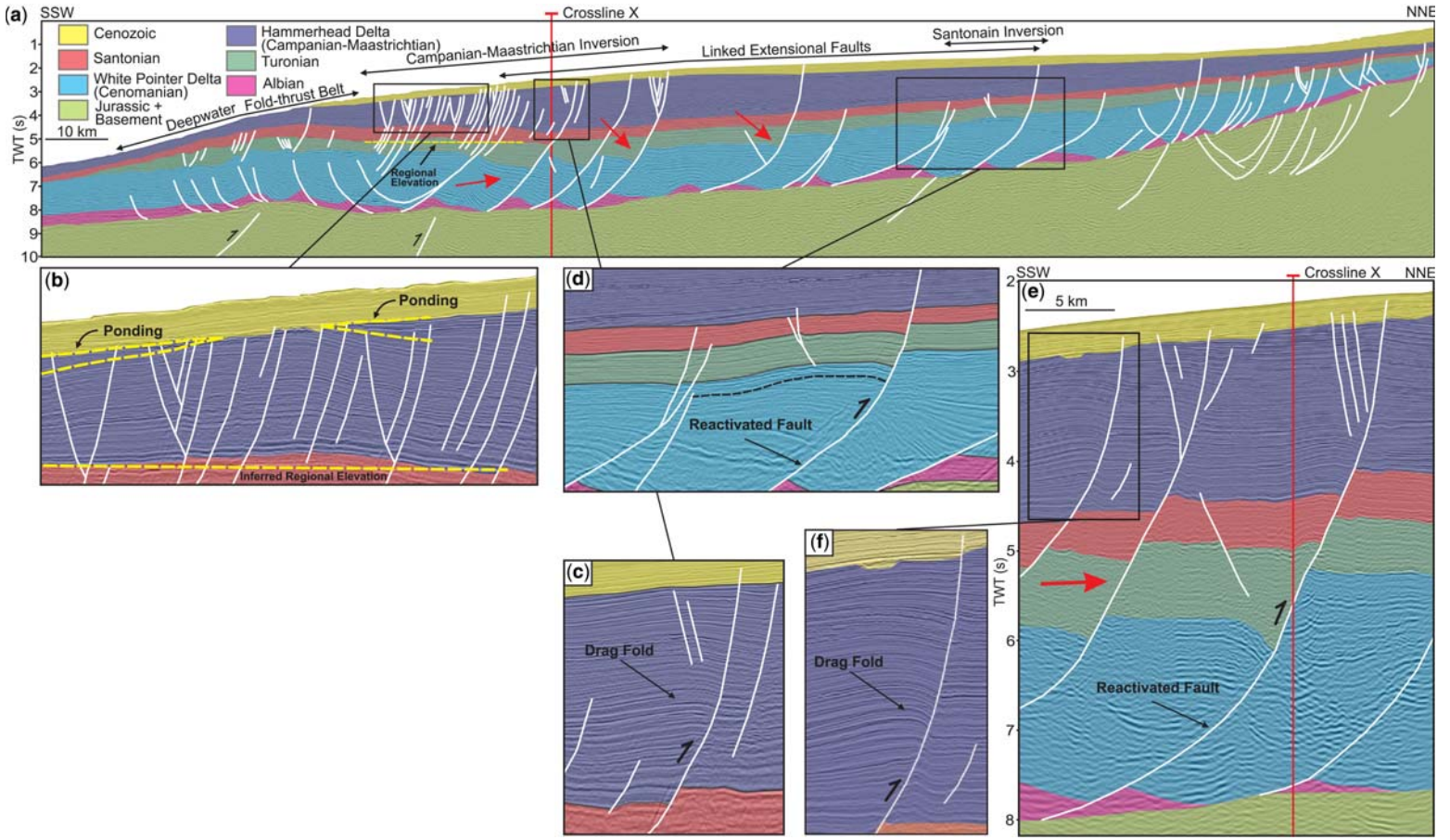

Fig. 4. Seismic line Bi 300. (**a**) Sequence stratigraphic framework for the western Ceduna Sub-basin including the White Pointer DDWFTB (blue) with extensional (delta top) and shortening (delta toe) provinces. Two phases of inversion are indicated: (**b**) the Campanian–Maastrichtian (purple) inversion resulting in broad uplift and erosion and (**c**) selected fault reactivation forming an inversion anticline. Inset (b) demonstrates that the boundary between the Santonian (orange) and Campanian (purple) is structurally elevated above the regional level (yellow dashed line) while there is minor erosion and ponding on the flanks of the inversion anticline at the top of the Campanian–Maastrichtian

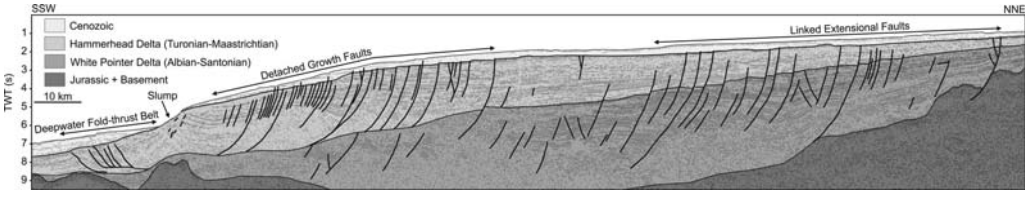

Fig. 5. Seismic line Bi 500 from the eastern Ceduna Sub-basin demonstrating growth of deeper White Pointer DDWFTB extensional faults upwards into the Hammerhead DDWFTB nearest the margin. Outboard of this, extensional listric growth faults of the Hammerhead DDWFTB detach above Turonian–Santonian strata and are linked downdip to a deepwater fold–thrust belt (delta toe). The White Pointer supersequence images well-developed extensional faults, but is missing a linked downdip delta toe.

DDWFTB systems that are independent in size, shape and structural geometry (MacDonald *et al.* 2010). Both DDWFTBs exhibit well-developed gravity-driven deformation structures, making them analogous to other delta systems around the world (Totterdell & Krassay 2003; MacDonald *et al.* 2010). The structural interpretation of the White Pointer and Hammerhead DDWFTBs is based on newly acquired 2D BightSPAN© seismic data and a public domain Trim3D seismic dataset. Both 2D and 3D seismic datasets were interpreted in the time domain while the fault model from the 3D dataset was depth converted. Depth conversion employed a simple velocity model due to the lack of well data available in the Ceduna Sub-basin. Water depth varies considerably along the regional 2D seismic lines from several hundred metres to over four kilometres, which can result in dramatic differences in dip of structures towards the basin due to the simple velocity model used in depth conversion. It is important to note that true dip and interlimb angles are apparent in the time domain. However, the overall structural style will not be modified by migration of the data in the depth domain. In this study the fault reactivation analysis is based on a depth-migrated fault model where true, rather than apparent, dips and geometries are displayed. This fault model has been used as a proxy for similar geometry faults elsewhere in the basin, which are imaged in the time domain on the regional 2D seismic lines.

In this study, we present two representative 2D seismic lines that demonstrate the regional variation in the structural style of the Late Cretaceous DDWFTB systems (Figs 4 & 5). In addition to this, we examine a 3D dataset on the delta top to constrain fault geometry in three dimensions. Results from previous interpretation of the public domain 2D seismic data covering the Ceduna Sub-basin were considered when picking the representative 2D regional seismic lines.

Seismic line Bi 300 (Fig. 4a) images the western side of the Ceduna Sub-basin and illustrates a linked system of extension and shortening within the Cenomanian White Pointer DDWFTB. This linked system is overlain by the Tiger supersequence (Turonian–Santonian) and the Hammerhead supersequence (Campanian–Maastrichtian). However, in the western Ceduna Sub-basin the Hammerhead supersequence did not develop into a DDWFTB system (MacDonald *et al.* 2010). In the eastern Ceduna Sub-basin, seismic line Bi 500 (Fig. 5) illustrates a linked system of extension and shortening within the Hammerhead supersequence, forming a DDWFTB system. In this section, the Cenomanian White Pointer supersequence is purely an extensional system that is lacking a downdip deepwater fold–thrust belt (Espurt *et al.* 2009; MacDonald *et al.* 2010). It therefore cannot be classified as a linked DDWFTB system at this location.

Examination of additional regional 2D seismic data indicates that the White Pointer and Hammerhead DDWFTBs prograded in slightly different directions based on the positions of their deepwater fold–thrust belts (Fig. 2). Overlap occurs between the lobes on the delta top (Fig. 2; yellow dashed line) due to proximity to the source and the deeper Mulgara Fault System, which developed in the White Pointer supersequence, is shared at this location (MacDonald *et al.* 2010). Linkage between the White Pointer, Tiger and Hammerhead supersequences on the delta top is achieved via the Mulgara Fault System, whereby optimally oriented faults were reactivated as the Hammerhead

Fig. 4. (*Continued*) (purple) strata. (**d**) The centre fault block in inset demonstrates a Santonian aged inversion anticline. (**e**) Along-strike seismic data demonstrates the continuation of the inversion anticline imaged in inset (c) (red vertical line where projected crossline X would intersect both). (**f**) A second inversion anticline with excellent fault-independent closure is shown basinwards of the structure imaged in (e). Scale and legend for inset images as per (a). Red arrows indicate examples of growth faults that show no evidence for inversion.

supersequence prograded over the existing White Pointer system. This selective reactivation is evidenced by the growth strata in the Tiger and Hammerhead supersequences and is localized to areas where the sedimentary wedge is thickest (Figs 4a, e & 5). In areas where the Mulgara Faults are observed to propagate through the Tiger and Hammerhead supersequences but do not demonstrate evidence for growth, these faults are interpreted as a result of ongoing compaction of the existing White Pointer DDWFTB below. To the east and west of the overlap zone between the DDWFTB systems, the linked faults become less prominent and the extensional faults that belong to each respective system become more abundant. This is observed in Figure 5 where the outboard growth faults within the Hammerhead DDWFTB detach at the level of the Tiger supersequence, rather than linking to the existing Mulgara Fault System below.

The limited 3D seismic survey in the Ceduna Sub-basin is located in the overlap zone (Fig. 2) where the Mulgara Fault System has been reactivated by the presence of the Tiger and Hammerhead supersequences above. This presents an excellent opportunity to map these linked faults and determine the reactivation risk by applying the present-day stress regime of the Bight Basin (after Reynolds *et al.* 2003) to the 3D fault models using Poly3D© (Maerten *et al.* 2005), a 3D boundary element code for heterogeneous, linear and elastic whole or half-space developed by Igeoss/Schlumberger.

Inversion in the Ceduna Sub-basin

Although the southern margin of Australia is a rifted margin, it has been subjected to episodic compressional forces since early rifting in the Late Jurassic (Teasdale *et al.* 2003; Holford *et al.* 2011). These forces have been attributed to ridge push, which imposes a compressional stress on a rifted margin upon initiation of seafloor spreading (cf. Bott 1991), as well as compressional forces transmitted through the Indo-Australian plate via collisions along its northern and eastern boundaries during the Cenozoic (Reynolds *et al.* 2002; Sandiford *et al.* 2004). Inversion structures in the Ceduna Sub-basin were first identified by Totterdell & Bradshaw (2004), who attributed the reverse reactivation of some normal faults to minor compressional forces in the basin, possibly coupled with Cenozoic magmatic activity, resulting in the formation of slight hanging-wall anticlines. The subtle inversion structures described here are interpreted as Late Cretaceous in age, and thus most likely resulted from ridge-push forces generated following progressive separation between the Australian and Antarctic plates. Of the four examples of inverted normal faults described here, three still retain net-normal displacement with all marker horizons exhibiting net-normal offset but appearing to have been uplifted above their original regional elevation (cf. Williams *et al.* 1989; Cooper & Warren 2010). Although this inversion is relatively minor, it indicates that some faults in the Ceduna Sub-basin have undergone reactivation (with opposing sense of slip) in response to changing stress field conditions, subsequent to their formation. Detailed mapping of the newly acquired 2D BightSPAN© seismic data and existing 3D seismic data has enabled identification and relative timing of two pulses of Late Cretaceous inversion in the Ceduna Sub-basin.

Santonian inversion

The oldest phase of inversion in the Ceduna Sub-basin is displayed in seismic line Bi 300 (Fig. 4a, d) whereby a Cenomanian growth fault (Mulgara Fault System) within the White Pointer DDWFTB is reactivated in the inboard part of the basin. Here, uplift and erosion of the Santonian Tiger supersequence resulted in a thinning of the Santonian above the core of the inversion anticline (Fig. 4d). The displacement on the fault is net normal, but the structure has been subjected to minor inversion as the geometry of the hanging-wall anticline is such that the south side of the fault block is structurally lower than the north side (within a south-facing growth fault). The geometry of the hanging-wall anticline in Figure 4d is unique in that whereas most of the hanging-wall rollover anticlines in the basin (Fig. 4a, red arrows) have a gentle south limb and steeper north limb, this anticline displays nearly equal dips on both limbs. These three relationships (the thinning of Santonian strata, structurally elevated boundaries and near-equal limb dips) suggest this first identifiable phase of inversion occurred within the Santonian, which directly corresponds to the onset of Late Cretaceous seafloor spreading (Sayers *et al.* 2001). Due to the timing of the inversion we propose a ridge-push mechanism for the compressional stress required to form this structure. This example provides a unique view into the history of the Ceduna Sub-basin in that the Santonian inversion, albeit minimal, is preserved. Subsequent to this phase of inversion, many of the linked Mulgara Faults in the overlap zone (Fig. 2 & 4e) would have accommodated sediment input from the Hammerhead DDWFTB. At this stage, the stress field due to external ridge-push forcing was likely overwhelmed due to the internal forces resulting from sediment loading. This may indicate that inversion in the Santonian was more widespread than what we observe today; however, the deposition of the Hammerhead supersequence would have effectively destroyed much of this

evidence through subsequent 'negative inversion' or restoration of hanging-wall strata.

Campanian–Maastrichtian inversion

The most recent episode of inversion evidenced in the Ceduna Sub-basin, also attributed to be the result of a ridge-push mechanism due to contemporaneous seafloor spreading, is demonstrated in Figure 4a, b. Here, a Cenomanian growth fault (Mulgara Fault System) of the White Pointer DDWFTB has been reactivated resulting in broad uplift of the Campanian–Maastrichtian strata in the hanging wall of the fault. In Figure 4a the boundary between the Santonian Tiger supersequence and Campanian–Maastrichtian Hammerhead supersequence is structurally elevated above the regional level to the north by *c.* 0.5 s (two-way time), suggesting fairly mild inversion compared to more severe examples from the St George's Channel Basin, offshore UK (Williams *et al.* 2005) or the East Java Sea Basin (Turner & Williams 2004). The contact between the Campanian–Maastrichtian and the Tertiary strata exhibits minor erosion of the inversion anticline with slight ponding of growth strata on both flanks of the structure (Fig. 4b). Further to the north along seismic line Bi 300, there is an additional inversion anticline (Fig. 4c) which again shows net-normal displacement and is controlled by a Cenomanian growth fault (Mulgara Fault System). Here, the displacement occurs primarily near the top of the reactivated growth fault, resulting in a characteristic drag-fold hanging-wall anticline (Fig. 4c). There therefore exists evidence of two faults in seismic line Bi 300 (Fig. 4a), with Campanian–Maastrichtian-aged inversion anticlines at a more distal location to the Santonian-aged inversion anticline described above.

Along-strike to the west of Figure 4a, a crossline from the Trim 3D seismic dataset (Fig. 2 red line; Fig. 4e) also images the same fault and associated inversion anticline interpreted in Figure 4c. The anticline has undergone more displacement here, although still retaining net-normal offset, and has steeper limb dips (Fig. 4g). Drag-fold geometry is observed at the Cenomanian–Turonian, Turonian–Santonian and Santonian–Campanian boundaries along the fault in this location, indicating increased reverse displacement along the fault to the west. In addition to this structure, Figure 4e, f demonstrates that the adjacent basinwards fault has undergone slight reactivation resulting in an inversion anticline. This anticline also has a net-normal displacement which occurs nearest the top of the fault, indicating the continuity of these inversion anticlines along-strike for *c.* 12 km. The inverted growth faults described above have a very different geometry to the other growth faults in the basin, which are indicated in Figure 4a by the red arrows.

The inversion structure imaged in Figure 4c, f displays potential to trap hydrocarbons for a number of reasons: it displays four-way closure along-strike with a significant fault-independent volume (from 3D seismic); it is linked to potential source rocks of the Albian Blue Whale, Cenomanian White Pointer and Turonian–Santonian Tiger supersequences; and formed in the upper Campanian or Maastrichtian. This age is based on the thickness of the Hammerhead supersequence and position of the inverted strata within the upper portion of this sedimentary package (Fig. 4c). Some structures with similar geometries in the Otway Basin (to the east of the Ceduna Sub-basin) contain significant volumes of methane gas, although these structures formed during younger Mid–Late Cenozoic inversion episodes (Holford *et al.* 2010).

From a regional standpoint, seismic line Bi 500 (Fig. 5) does not reveal any evidence for inversion which may be attributed to the geometry of the Cenomanian faults in the eastern part of the Ceduna Sub-basin. Here, the Mulgara Fault System is not commonly linked to the above fault system within the Hammerhead DDWFTB. On the eastern side of the sub-basin, the Hammerhead DDWFTB is composed of growth faults that sole out or detach within the formerly mobile shales of the Turonian–Santonian Tiger supersequence. It is plausible that any minor pulse of Santonian-aged reactivation and inversion in this area may be obscured by the thickness and ductility of the Tiger supersequence, given that there is a well-established gravity-sliding DDWFTB actively deforming above it. Any inversion structure that began to propagate upwards into the Tiger or Hammerhead supersequences may subsequently have been effectively accommodated by remobilization of the overpressured shale. Other possible explanations for the lack of inversion of the Cenomanian White Pointer faults (Mulgara Fault System) in the east may be the slight change in strikes of the fault system there, rotating azimuths slightly from their position in the overlap zone between the two DDWFTB systems (i.e. Fig. 4a) or the occurrence of sub-seismic scale inversion that has not been imaged (Holford *et al.* 2009).

Fault orientation analysis

The Trim3D seismic survey (Fig. 2) was used to constrain the orientation of the extensional faults (Fig. 6a) in the overlap zone between the two DDWFTB systems. The major faults (Fig. 6b, c) within the eastern side of the Trim3D survey were

mapped and a 3D fault model was constructed for both orientation and fault reactivation analysis. The faults within the 3D seismic survey were simplified such that only the large synthetic (Faults 2 and 4) and antithetic (Faults 1 and 3) faults were mapped (Fig. 6b, c). The fault model was then depth converted to show true rather than apparent orientations, and imported into 3D MOVE© for the structural analysis (Fig. 6a).

The analysis of the depth-converted faults shows an excellent correlation between the orientations of both the synthetic and antithetic faults (Fig. 6a). Faults 2 and 4, the synthetic growth faults, show a wider dip-azimuth distribution on the rose diagrams yet very similar averages (Fault 2: 228°; Fault 4: 224°; Fig. 6a) and a larger point cluster (Fig. 6a) due to the larger size and strike length of these faults. Fault 4 displays the largest point cluster, due to the slightly deeper detachment level (Fig. 6b). The mean principal poles for Faults 2 and 4 are also slightly different, again due to the larger surface area and increased variability in dip of Fault 4.

The antithetic faults are very similar in orientation (dip-azimuth) in both the rose diagrams with 052° (Fault 1) and 048° (Fault 3; Fig. 6a) and in terms of point cluster size (Fig. 6a). The mean principal pole for Faults 1 and 3 are almost exactly the same, indicating very similar geometries along both strike and dip of the faults (Fig. 6b, c). The similarity of these two structures, with nearly identical orientations, is observed elsewhere in the Ceduna Sub-basin in regional 2D seismic data (Figs 4a & 5).

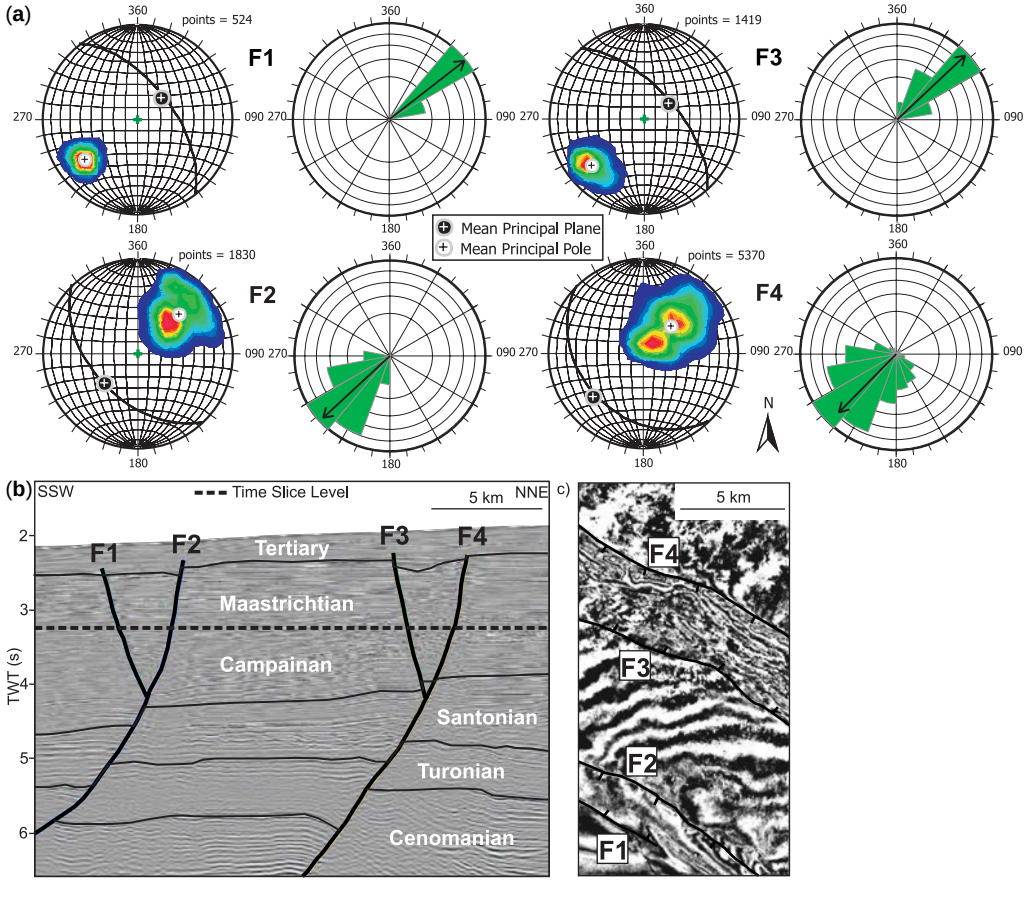

Fig. 6. (**a**) Fault analysis data plotted on equal-area stereographic projections for 3D fault model shows similarity between antithetic (Faults 1 and 3) and synthetic (Faults 2 and 4) faults with rose diagram (dip-azimuth) and contoured poles to plane (dip-azimuth). (**b**) Interpreted seismic section from Trim3D showing extensional Faults 1–4 in 2D with black dashed line indicating observation grid level at 1000 m below seabed. (**c**) Time slice from Trim3D survey at −1000 m observation level, showing extensional faults used for 3D fault model.

Regional stress regime of the Bight Basin

The first investigation of the *in situ* stress regime of the Bight Basin was conducted by Reynolds *et al.* (2003), whereby the stress tensor was calculated from the available well data in the Bight Basin and a fault reactivation analysis was completed. The absence of additional well data in the basin since this work was completed limits our ability to further refine the *in situ* stress analysis. However, with newly acquired 2D and 3D seismic data allowing for detailed investigation of the 3D fault geometries and new techniques for modelling fault reactivation using Poly3D©, we can more accurately predict the risk of reactivation in the basin. The reactivation risk for a well-constrained fault model can then be used as a proxy for other faults in data-poor areas of the basin. The following fault reactivation risk analysis is therefore based entirely on the *in situ* stress regime as it was calculated in Reynolds *et al.* (2003).

The *in situ* stress regime was calculated using the drilling and logging data from ten open file exploration wells within the Bight Basin, particularly the Duntroon and eastern Ceduna sub-basins and the Polda Trough to the north (Reynolds *et al.* 2003; Figs 1 & 7). The variation in water depth across the Bight Basin from several hundred metres to over four kilometres posed a significant problem for calculating the total stress in the basin; the analyses are therefore based on effective stress (total stress minus pore pressure; Reynolds *et al.* 2003).

Reynolds *et al.* (2003) determined the maximum horizontal stress (S_{Hmax}) orientation in the Bight Basin by interpreting borehole breakout directions in high-resolution 4-arm dipmeter (HDT) logs from four wells (Fig. 7)–Echidna-1 (Duntroon Sub-basin), Duntroon-1, Platypus-1 (Ceduna Sub-basin) and Columbia-1 (Polda Basin)–and image log data (Formation Microscanner, FMS) from two wells (Greenly-1 and Borda-1; eastern Ceduna Sub-basin).

To determine the S_{Hmax} value for the Bight Basin, Reynolds *et al.* (2003) used a total of 78 breakouts with a combined length of 1208 m from the six wells in the basin covering a depth range 1460–4791 m below rotary table. The average S_{Hmax} orientation calculated from the six wells was N130°E (130). The interpreted stress data from Reynolds *et al.* (2003) is plotted on Figure 7 along with the Australian stress map, demonstrating the sparse data coverage in the western Ceduna Sub-basin. The average S_{Hmax} orientation of N130°E (130) for the available wells in the Bight Basin is consistent with S_{Hmax} orientations in the Otway Basin to the east (Fig. 7).

The stress trajectories or regionally averaged stress orientations for the Australian stress field have been modelled by Hillis & Reynolds (2000) and plotted in Figure 7. These trajectories allow for a better understanding of the regional stress field over the entire Bight Basin rather than any one sub-basin. On the western side of the Bight Basin, the stress trajectories indicate a more east–west orientation which reflects the (data constrained) east–west S_{Hmax} orientation in the Perth Basin to the west (Hillis & Reynolds 2000; Reynolds & Hillis 2000; King *et al.* 2008). Due to the lack of available well data in the western Bight Basin, Reynolds *et al.* (2003) were unable to verify if the S_{Hmax} orientation rotates to an east–west orientation in the western part of the Bight Basin. An average S_{Hmax} orientation of N130°E (130) was therefore used for the entire Bight Basin.

Reynolds *et al.* (2003) determined the magnitudes of the vertical stress (S_v), minimum horizontal stress (S_{hmin}) and S_{Hmax} from the petroleum wells in the Bight Basin. They integrated density logs and check-shot data to determine S_v at 10.5 MPa km^{-1}. They used leak-off tests and formation integrity tests to calculate S_{hmin} at 6.0 MPa km^{-1} and used frictional limits calculations to determine the upper limit of S_{Hmax} at 18.7 MPa km^{-1}. However, Reynolds *et al.* (2003) were unable to define S_{Hmax} any further. They therefore concluded that the Bight Basin may demonstrate a normal fault stress regime ($S_v > S_{Hmax} > S_{hmin}$), a borderline normal fault to strike-slip fault stress regime ($S_v \geq S_{Hmax} > S_{hmin}$) or a strike-slip fault stress regime ($S_{Hmax} > S_v > S_{hmin}$; Fig. 8; Table 1).

For details of the calculation of individual stress tensor components and their magnitudes, including the vertical stress, minimum horizontal stress, maximum horizontal stress and pore pressure, we refer the reader to Reynolds *et al.* (2003).

Fault reactivation in the Ceduna Sub-basin

Previous work completed on fault reactivation in the Bight Basin utilized the FAST technique (Fault Analysis Seal Technology, Mildren *et al.* 2002; Reynolds *et al.* 2003). In the FAST technique, the risk of fault reactivation is determined using the stress tensor (Mohr circle) and fault-rock strength (failure envelope). This technique was applied to regional faults from the Bight Basin whereby strike and dip data were determined from regional 2D seismic mapping. The analysis completed in the Reynolds *et al.* (2003) work is therefore based on generalized fault orientations rather than a precise fault model from 3D seismic data, which includes combined mechanical interaction due to fault slip.

To evaluate fault reactivation, Reynolds *et al.* (2003) investigated three stress regimes: (1)

Fig. 7. Upper: Australian stress map (A–D quality) with the Bight Basin stress data with superimposed stress trajectory map from Hillis & Reynolds (2000) demonstrates the regional trends across the Australian continent. The S_{Hmax} orientation for the Bight Basin is reasonably consistent with the stress trajectories in the region. Lower: smaller-scale stress map of the Bight Basin showing A–D quality stress indicators and well names used in this study. Orientation and length of vector represents the data quality, while wells with no data or E-quality data are represented by a dot (after Reynolds *et al.* 2003).

Fig. 8. Location in stress space of the three *in situ* stress cases evaluated (Table 1; after Reynolds *et al.* 2003).

strike-slip fault stress regime ($S_{hmin} < S_v < S_{Hmax}$); (2) normal fault stress regime ($S_{hmin} < S_{Hmax} < S_v$); and (3) borderline normal fault to strike-slip fault stress regime (Fig. 8; Table 1). The magnitude of the *in situ* stress field for the three cases was determined at a depth of 1000 m below seabed; an observation grid at this depth was therefore used for the Poly3D© analysis.

Geomechanical stress analysis

We used the boundary element code Poly3D to characterize the reactivation risk along the faults interpreted from the 3D seismic cube in the Ceduna Delta. Poly3D© utilizes polygon elements and linear elasticity theory (Thomas 1993; Maerten *et al.* 2000, 2002; Fiore *et al.* 2006). Models are simplified in the boundary element method (BEM) as only the discontinuities (such as faults) are gridded and therefore taken into account in the calculation. The faults were meshed using a 500 m triangular mesh size, which was a good compromise between precision and computation time. Specific boundary conditions were applied, which govern how the elements should respond to far-field stress or strain states. Different attributes can be used or studied to describe the propensity of a fault to slip under a given stress field (e.g. Morris *et al.* 1996; Ferrill & Morris 2003; Healy 2009; Morris & Ferrill 2009). Here, we used the total displacements (total, vertical or horizontal displacements) calculated along the fault planes when subjected to the known present-day stress field in order to estimate the reactivation potential of the listric faults imaged by the Trim3D 3D seismic cube. The displacements were computed for cohesionless fault surfaces, with boundary conditions set on the triangular boundary elements making up the faults as follows.

- The traction components parallel to the element plane in the dip direction and in the strike direction are both set to zero so the element surfaces may slip freely.
- The displacement discontinuity component normal to the element plane is set to zero to avoid opening or interpenetration of the fault surfaces.

After depth conversion using a simple velocity model, the faults surfaces were imported and remeshed in Poly3D©. We also created an observation grid where attributes such as total displacement, direction and magnitudes of stresses were also computed close to and away from the faults. The results of the models allow the reactivation potential of the main faults in the Trim3D 3D seismic cube to be investigated.

The fault reactivation analysis is based on two independent fault sets (Fig. 6b) from the overlap zone between the two DDWFTB systems (Fig. 2). These two fault sets were selected as a proxy as they are well imaged in the Trim3D seismic dataset (Fig. 2) and are representative of growth fault geometries on the delta top(s). To utilize the calculated stress magnitudes for each component of the stress tensor (Table 1), we have used the same observation level of 1000 m below seabed

Table 1. *Calculated stress magnitudes of Reynolds* et al. *(2003), used to model fault reactivation risk with the geomechanical modelling software Poly3D©*

for this analysis as for the stress analysis (Fig. 6b) of Reynolds *et al.* (2003). Figure 6c represents a time slice through this observation level (1000 m below seabed), where the four faults that were analysed are shown (Faults 1–4). Faults 1 and 3 are antithetic faults while Faults 2 and 4 are synthetic growth faults (Fig. 6c).

The synthetic growth faults (Fault 2 and 4; Figs 6b & 9a) detach within the Albian Blue Whale supersequence and were reactivated, likely after the Santonian, allowing for growth to occur along the faults within the Campanian–Maastrichtian section (Fig. 4a, e). The antithetic faults formed as a result of increased offset on the synthetic faults and are relatively shallow and younger (Figs 6b & 9a). The fault model was depth converted, triangulated and imported into Poly3D© and three fault regime scenarios were run on the model (Figs 8 & 9a–f).

The orientation of S_{Hmax} was set at N130°E (130) for each fault regime scenario and the calculated stress magnitudes from Reynolds *et al.* (2003) were used (Table 1) starting with Case I strike-slip fault stress regime ($S_{hmin} < S_v < S_{Hmax}$; Fig. 9a). Case II normal fault stress regime ($S_{hmin} < S_{Hmax} < S_v$; Fig. 9b) was run next followed by Case III (Fig. 9c), the borderline normal fault to strike-slip fault stress regime. The results (Fig. 9a–c) demonstrate that variability in the stress magnitudes has only a minor effect on reactivation risk. All three cases demonstrate that the antithetic faults are optimally oriented for reactivation (Faults 1 and 3; Fig. 9a–c) while the larger synthetic growth faults are less optimally oriented for reactivation and demonstrate a moderate to low risk (Faults 2 and 4; Fig. 9a–c).

An important consideration that was not addressed in the work of Reynolds *et al.* (2003) was fault plane roughness, likely due to the lack of data and scope of the study. With the Poly3D© fault model constrained from 3D seismic data, we can demonstrate that variability in fault plane roughness affects reactivation along the strike of the fault (e.g. in Figure 9b where the east side of Fault 4 is at a high risk of reactivation in the normal fault stress regime but is only at moderate risk of reactivation in the other two scenarios; Fig. 9a, c). Depending on the orientation of the structure with respect to S_{Hmax}, the fault plane roughness can have a significant impact on reactivation risk

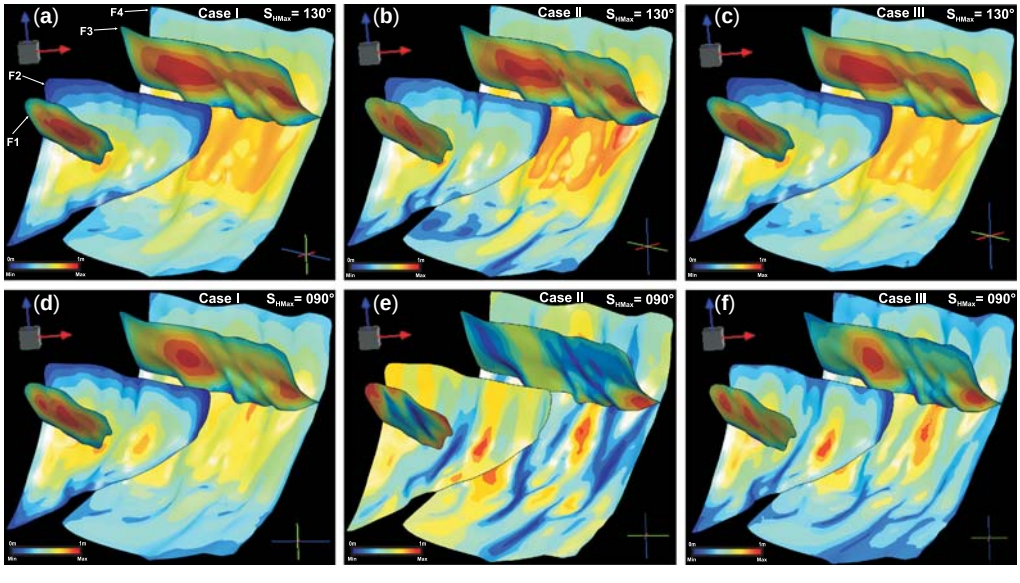

Fig. 9. Modelled 3D antithetic (Faults 1 and 3) and synthetic (Faults 2 and 4) faults from Trim3D seismic data (Figs 2 & 6). Modelled S_{Hmax} orientation of (**a–c**) N130°E (130) and (**d–f**) N090°E (090). Three cases were modelled for each S_{Hmax} orientation: (a, d) Case I strike-slip faulting stress regime ($S_{hmin} < S_v < S_{Hmax}$); (b, e) Case II normal faulting stress regime ($S_{hmin} < S_{Hmax} < S_v$); and (c, f) Case III strike-slip normal faulting boundary. Orientation in space is shown by grey cube in top left corner where blue arrow is *z* axis, green is *y* axis (north) and red is *x* axis. Orientation and relative magnitude of stress field are shown in bottom-right corner where blue represents maximum horizontal stress, red represents minimum horizontal stress and green represents vertical stress as per Table 1 calculated values. Contours define the modelled displacement in metres as a result of the stress applied to the boundary of the model and along the faults.

across the fault as demonstrated when the orientation of S_{Hmax} is rotated to east–west or N090°E (090; Fig. 9d–f).

Previous Finite Element Method (FEM) modelling of the Australian stress field incorporating all plate boundary forces that act on the Indo-Australian Plate indicates an *c.* east–west S_{Hmax} for the Bight Basin (Reynolds *et al.* 2003; Fig. 7). As the individual principal stress axis (averaged by black lines; Fig. 7) demonstrates a more east–west S_{Hmax} orientation in the FEM model, the Poly3D© fault model was also run with this orientation (N090°E) using the same three fault regimes and magnitudes as the initial model [with a S_{Hmax} orientation of N130°E (130)]. Here, Figure 9d–f demonstrates the same fault model, fault regimes and stress magnitudes with a rotated S_{Hmax} orientation to N090°E (090). There are two reasons for running a second model with a rotated S_{Hmax} orientation: (1) to investigate the difference in the modelled (FEM) versus calculated present-day stress field from Reynolds *et al.* (2003); and (2) to demonstrate that even a rotation of 40° from the interpreted plate scale stress trajectory (Fig. 7) would still infer that the Ceduna Sub-basin faults are at moderate to high risk of reactivation (Fig. 9d–f).

By changing the S_{Hmax} orientation to N090°E (090), we can now investigate the risk of reactivation for the three fault regimes (Case I–Case III; Fig. 9d–f). This model demonstrates that Faults 1 and 3 in Case I and Case III (Fig. 9d, f) remain at a moderate to high reactivation risk, albeit lower than for the S_{Hmax} orientation of N130°E (130) scenario (Fig. 9a, c). Case II faults demonstrate a much lower risk of reactivation in this scenario (Fig. 9e) with a low to moderate risk rather than a high risk as in the orientation of N130°E (130) scenario (Fig. 9b). The fault plane roughness has a more acute effect on reactivation risk; a modelled S_{Hmax} orientation of N090°E (090) with select areas of the fault plane demonstrates a high risk of reactivation (Fig. 9f) compared to moderate risk in the S_{Hmax} orientation of N130°E (130) scenario (Fig. 9c).

In both scenarios described so far, the antithetic faults (Faults 1 and 3) display a high risk of reactivation (aside from Fig. 9e) relative to the synthetic faults (Fig. 9). This is again a result of the fault plane roughness along Faults 1 and 3 as the 'bullseye' occurs in the same place each time (Fig. 9a–c). The uneven nature of the fault surface is represented clearly on Faults 1 and 3; Faults 2 and 4 display smoother fault planes and therefore have an overall lower risk of reactivation (Fig. 9).

The two examples of varying the S_{Hmax} orientation described above demonstrate that the orientation of the structure with respect to S_{Hmax} is more substantial for fault reactivation risk than changing the stress magnitude. This is justified by the absence of significant change between the three cases and corresponding stress magnitudes tested in the model (Fig. 9). This analysis also suggests that the moderately dipping (40–70°) segments of Faults 2 and 4 are at a higher risk of reactivation than the shallow (<40°) or steeply dipping (>70°) portions of the fault, which is in agreement with the results of Reynolds *et al.* (2003). This evidence suggests that dips of the fault surfaces do play a role in the reactivation risk. However, the variability of the fault plane roughness has a more substantial effect on risk of reactivation along any single fault, especially when the variability occurs in the moderately dipping section of the fault (Fig. 9).

The fault sets modelled above are orientated approximately N140°E (140; synthetic) and N320°E (320; antithetic). The S_{Hmax} orientation of N130°E (130) therefore produces a small angle between the modelled faults and the S_{Hmax} orientation (*c.* 10°), which is a generally favourable fault reactivation (Anderson 1951; Healy *et al.* 2006). The second orientation of S_{Hmax} at N090°E (090) results in a larger angle between the modelled faults and the S_{Hmax} orientation (*c.* 50°), which is reflected in the modelled decrease in risk of reactivation with this scenario (Fig. 9d–f).

Given that the majority of the faults in the Mulgara Fault System and Hammerhead DDWFTB system have a similar strike and dip (Figs 4a & 5) and a 40° rotation of the S_{Hmax} orientation only minimally reduces the reactivation risk (Fig. 9), this fault model allows us to extrapolate risk of reactivation to include other similarly oriented faults in the Ceduna Sub-basin.

Fault model implications

From the calculated and modelled stress orientation(s) and magnitude(s) from Reynolds *et al.* (2003) and the 3D fault geometries and fault reactivation analysis described above, we can now examine the implications for regional fault reactivation in the Ceduna Sub-basin. Because we have 3D seismic control on the delta-top extensional faults, emphasis will be placed on comparison to other extensional faults in the sub-basin given that these are likely targets for exploration (Totterdell *et al.* 2000).

The regional extensional faults in the Ceduna Sub-basin have an average strike of N140°E–N320°E (140–320) and are listric normal growth faults associated with two periods of delta-top extension (Fig. 6). The majority of the potential hydrocarbon trap geometries in the Ceduna Sub-basin are within the extensional delta top(s) and rely at least partially on fault seal for viability. Understanding the reactivation risk is therefore

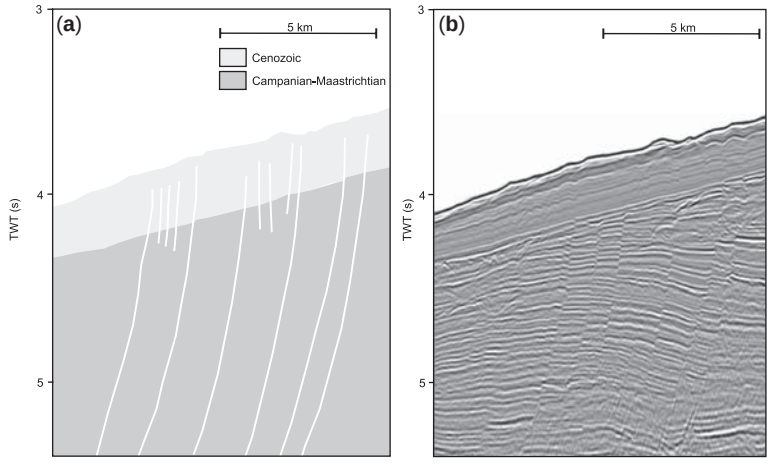

Fig. 10. (**a**) Interpreted and (**b**) un-interpreted 2D seismic image of Campanian–Maastrichtian faults intersecting the Cenozoic strata and reaching the seabed. This represents post-Maastrichtian fault reactivation in the Ceduna Sub-basin.

essential (Blevin *et al.* 2000; Totterdell *et al.* 2000, 2008; Ruble *et al.* 2001; Somerville 2001; Struckmeyer *et al.* 2001; 2002; King & Mee 2004; Tapley *et al.* 2005). Given that the modelled extensional faults from the 3D seismic data demonstrate a moderate to high risk of reactivation along the centre of the fault surfaces, where they are moderately dipping ($>40^\circ$ and $<70^\circ$; Fig. 9) it is possible that these and other extensional faults on the delta top (Figs 4a & 5) are either at risk of reactivation or have already been reactivated. There is evidence for fault seal breach having occurred in the Bight Basin, such as the failure of Jerboa-1 well that demonstrated a charged and breached petroleum trap, likely due to Late Cretaceous reactivation (described above; Totterdell *et al.* 2000; Ruble *et al.* 2001; Somerville 2001; Struckmeyer *et al.* 2001). Strong evidence for fault reactivation is demonstrated where delta-top extensional faults are observed to disrupt the Cenozoic sediments and, in some cases, result in seafloor topography (Fig. 10).

The presence of Late Cretaceous inversion structures in the Ceduna Sub-basin (Fig. 4) indicates that far-field stresses affected isolated extensional structures, creating another potential reactivation mechanism in the area prior to establishment of the present-day stress regime. The exact orientation of this mechanism is unknown; however, if the stress was due to ridge push as proposed here, the extensional faults would have been optimally oriented for reactivation during the Late Cretaceous. In addition, it may be possible that this inversion pulse created fault-independent traps that could be prospective targets for hydrocarbon exploration in the Ceduna Sub-basin (Fig. 4c–f).

Conclusions

The Ceduna Sub-basin is composed of two temporally and spatially separate DDWFTBs, each demonstrating updip extension and downdip shortening (Figs 2, 4a & 5). From detailed mapping of two fault sets (in the extensional delta-top regions) from 3D seismic data and regional 2D seismic data we can now accurately model fault plane geometries at N320°E (320) and N140°E (140) orientations (Fig. 9). The detailed mapping of 3D and 2D seismic data has demonstrated the approximate timing of two newly identified phases of inversion in the Ceduna Sub-basin during the Santonian and Campanian–Maastrichtian. Both inversion events correspond to the initiation of sustained rifting of the Australian Southern Margin. These inversion structures may be responsible for the breach of the Jerboa-1 well in the Late Cretaceous and may also provide potential fault-independent trapping mechanisms via inversion anticlines (Fig. 4).

Using the fault plane geometries in combination with the previously calculated *in situ* stress regime and new geomechanical modelling, we can now determine the risk of fault reactivation in the Ceduna Sub-basin (Fig. 9). The results indicate that moderately dipping faults and/or areas of the fault planes are at the highest reactivation risk while the shallow ($<40^\circ$) and steeply ($>70^\circ$) dipping fault and/or areas of fault planes have a lower reactivation risk. The modelled antithetic faults have a higher risk of reactivation for both S_{Hmax} orientations [N130°E (130) and N090°E (090)] due to a combination of acute fault plane roughness, causing heterogeneities along the fault

surface and the moderate dips between 40° and 70°. In addition, the modelling also demonstrates that for both S_{Hmax} orientations of N130°E (130) and N090°E (090) all three stress regime scenarios pose a moderate to high risk of fault reactivation; this indicates that fault reactivation is less sensitive to stress magnitude and most sensitive to the orientation of S_{Hmax} and fault plane roughness. Presence of fault reactivation is also identified in 2D seismic data (Fig. 10), indicating post-Maastrichtian fault reactivation and establishment of a normal or strike-slip normal faulting stress regime in the basin. Our results demonstrate reactivation is still likely to occur at present day, leading to potential seal breach and hydrocarbon migration in the Bight Basin.

Further exploration will ultimately lead to better data coverage, which will allow for more accurate depth conversions and additional well data for regional stress analysis.

The authors would like to thank the Australian Research Council and the University of Adelaide for their financial support of this study. The authors would also like to thank Igeoss/Schlumberger, Ion Geophysical, Midland Valley, SMT and PIRSA for the data and software used in this study. The authors would especially like to thank the reviewers of this paper for the constructive and thoughtful comments. This forms TRaX record 142.

References

Anderson, E. M. 1951. *The Dynamics of Faulting and Dyke Formation with Applications to Britain*. 2nd edn. Oliver and Boyd, Edinburgh.

Bein, J. & Taylor, M. L. 1981. The Eyre Sub-basin: recent exploration results. *The Australian Petroleum Production and Exploration Association Journal*, **21**, 91–98.

Bilotti, F. & Shaw, J. H. 2005. Deep-water Niger Delta fold and thrust belt modeled as a critical taper wedge: the influence of elevated basal fluid pressure on structural styles. *American Association of Petroleum Geologists Bulletin*, **89**, 1475–1491.

Blevin, J. E., Totterdell, J. M., Logan, G. A., Kennard, J. M., Struckmeyer, H. I. M. & Colwell, J. B. 2000. Hydrocarbon prospectivity of the Bight Basin – petroleum systems analysis in a frontier basin. *In*: *2nd Spring Symposium – Frontier Basins, Frontier Ideas, Adelaide, June 29–30th, 2000*. Geological Society of Australia, Abstracts, **60**, 24–29.

Bott, M. H. P. 1991. Ridge push and associated plate interior stress in normal and hot spot regions. *Tectonophysics*, **200**, 17–32.

Boeuf, M. G. & Doust, H. 1975. Structure and development of the southern margin of Australia. *The Australian Petroleum Production and Exploration Association Journal*, **15**, 33–43.

Briggs, S. E., Davies, R. J., Cartwright, J. A. & Morgan, R. 2006. Multiple detachment levels and their control on fold styles in the compressional domain of the deepwater west Niger Delta. *Basin Research*, **18**, 435–450, doi: 10.1111/j.1365-2117. 2006.00300.x.

Cobbold, P. R., Clarke, B. J. & Løseth, H. 2009. Structural consequences of fluid overpressure and seepage forces in the outer thrust belt of the Niger Delta. *Petroleum Geoscience*, **15**, 3–15, doi: 10.1144/1354-079309-784.

Cooper, M. & Warren, M. J. 2010. The geometric characteristics, genesis and petroleum significance of inversion structures. *In*: Law, R. D., Butler, R. W. H., Holdsworth, R. E., Krabbendam, M. & Strachan, R. A. (eds) *Continental Tectonics and Mountain Building: The Legacy of Peach and Horne*. Geological Society, London, Special Publications, **335**, 827–846.

Corredor, F., Shaw, J. H. & Bilotti, F. 2005. Structural styles in the deep-water fold and thrust belts of the Niger Delta. *American Association of Petroleum Geologists Bulletin*, **89**, 753–780.

Costa, E. & Vendeville, B. C. 2002. Experimental insights on the geometry and kinematics of fold-and-thrust belts above weak, viscous evaporitic décollement. *Journal of Structural Geology*, **24**, 1729–1739.

Davis, D. M. & Engelder, T. 1985. The role of salt in fold-and-thrust belts. *Tectonophysics*, **199**, 67–88.

Doust, H. & Omatsola, E. 1990. Niger delta. *In*: Edwards, J. D. & Santogrossi, P. A. (eds) *Divergent/Passive Margin Basins*. American Association of Petroleum Geologists, Boulder, Memoir, **48**, 201–238.

Espurt, N., Callot, J.-P., Totterdell, J., Struckmeyer, H. & Vially, R. 2009. Interactions between continental breakup dynamics and large-scale delta system evolution: Insights from the Cretaceous Ceduna delta system, Bight Basin, Southern Australia margin. *Tectonics*, **28**, TC6002, doi: 10.1029/2009TC002447.

Ferrill, D. A. & Morris, A. P. 2003. Dilational normal faults. *Journal of Structural Geology*, **25**, 183–196.

Finkbeiner, T., Zoback, M., Flemings, P. & Stump, B. 2001. Stress, pore pressure, and dynamically constrained hydrocarbon columns in the South Eugene Island 330 field, northern Gulf of Mexico. *American Association of Petroleum Geologists Bulletin*, **85**, 1007–1031.

Fiore, P. E., Pollard, D. D., Currin, W. R. & Miner, D. M. 2006. Mechanical and stratigraphic constraints on the evolution of faulting at Elk hills, California. *American Association of Petroleum Geologists Bulletin*, **91**, 321–341.

Fraser, A. R. & Tilbury, L. A. 1979. Structure and stratigraphy of the Ceduna Terrace region, Great Australian Bight. *The Australian Petroleum Production and Exploration Association Journal*, **19**, 53–65.

Haq, B. U., Hardenbol, J. & Vail, P. R. 1988. Mesozoic and Cenozoic chronostratigraphy and eustatic cycles. *In*: Wilgus, C. K., Hastings, B. S., Kendall, C. G. St. C., Posamentier, H. W., Ross, C. A. & Van Wagoner, J. C. (eds) *Sea-Level Changes: An Integrated Approach*. Society of Economic Paleontologists and Mineralogists, Tulsa, Special Publication, **42**, 71–108.

Healy, D. 2009. Anisotropy, pore fluid pressure and low angle normal faults. *Journal of Structural Geology*, **31**, 561–574.

HEALY, D., JONES, R. R. & HOLDSWORTH, R. E. 2006. Three-dimensional brittle shear fracturing by tensile crack interaction. *Nature*, **439**, 64–67.

HILLIS, R. R. & REYNOLDS, S. D. 2000. The Australian stress map. *Journal of the Geological Society, London*, **157**, 915–921.

HOLFORD, S. P., TURNER, J. P., GREEN, P. F. & HILLIS, R. R. 2009. Signature of cryptic sedimentary basin inversion revealed by shale compaction data in the Irish Sea, western British Isles. *Tectonics*, **28**, TC4011, doi: 10.1029/2008TC002359.

HOLFORD, S. P., HILLIS, R. R., DUDDY, I. R., GREEN, P. F., TUITT, A. K. & STOKER, M. S. 2010. Impacts of neogene-recent compressional deformation and uplift on hydrocarbon prospectivity of the 'passive' southern Australian margin. *The Australian Petroleum Production and Exploration Association Journal*, **50**, 267–284.

HOLFORD, S. P., HILLIS, R. R. *ET AL.* 2011. Cenozoic post-breakup compressional deformation and exhumation of the southern Australian margin. *The Australian Petroleum Production and Exploration Association Journal*, **51**, 613–638.

INGRAM, G. M., CHISHOLM, T. J., GRANT, C. J., HEDLUND, C. A., STUART-SMITH, P. & TEASDALE, J. 2004. Deepwater North West Borneo: hydrocarbon accumulation in an active fold thrust belt. *Marine and Petroleum Geology*, **21**, 879–887.

JACKSON, M. P. A., VENDEVILLE, B. C. & SCHULZ-ELA, D. D. 1994. Salt-related structures in the Gulf of Mexico: a field guide for geophysicists. *The Leading Edge*, **13**, 837–842.

KING, S. J. & MEE, B. C. 2004. The seismic stratigraphy and petroleum potential of the Late Cretaceous Ceduna Delta, Ceduna Sub-basin, Great Australian Bight. *In*: BOULT, P. J., JOHNS, D. R. & LANG, S. C. (eds) *Eastern Australasian Basins Symposium II*. Petroleum Exploration Society of Australia, Special Publication, 63–73.

KING, R. C. & BACKÉ, G. 2010. A balanced 2D structural model of Hammerhead Delta – deepwater fold–thrust belt, Bight Basin, Australia. *Australian Journal of Earth Sciences*, **57**, 1005–1012.

KING, R. C., HILLIS, R. R. & REYNOLDS, S. D. 2008. In situ stresses and natural fractures in the Northern Perth Basin, Australia. *Australian Journal of Earth Sciences*, **55**, 685–701.

KING, R. C., HILLIS, R. R. & TINGAY, M. R. P. 2009. Present-day stress and neotectonic provinces of the Baram Delta and deepwater fold–thrust belt. *Journal of the Geological Society, London*, **166**, 197–200.

KING, R. C., BACKÉ, G., MORLEY, C. K., HILLIS, R. R. & TINGAY, M. R. P. 2010. Balancing deformation in NW Borneo: quantifying plate-scale v. gravitational tectonics in a delta and deepwater fold–thrust belt systems. *Marine and Petroleum Geology*, **27**, 238–246.

KRASSAY, A. A. & TOTTERDELL, J. M. 2003. Seismic stratigraphy of a large, Cretaceous shelf-margin delta complex, offshore southern Australia. *American Association of Petroleum Geologists Bulletin*, **87**, 935–963.

MACDONALD, J. D., KING, R., HILLIS, R. R. & BACKÉ, G. 2010. Structural style of the white pointer and Hammerhead Delta – deepwater fold–thrust belt, Bight Basin, Australia. *The Australian Petroleum Production and Exploration Association Journal*, **50**, 487–510.

MAERTEN, F. 2010. Adaptive cross-approximation applied to the solution of system of equations and post-processing for 3D elastostatic problems using the boundary element method. *Engineering Analysis with Boundary Elements*, **34**, 483–491.

MAERTEN, L., GILLEPIE, P. & POLLARD, D. D. 2002. Effects of local stress perturbation on secondary fault development. *Journal of Structural Geology*, **24**, 145–153.

MAERTEN, F., RESOR, P. G., POLLARD, D. D. & MAERTEN, L. 2005. Inverting for slip on three dimensional fault surfaces using angular dislocations. *Bulletin of the Seismological Society of America*, **95**, 1654–1665.

MAERTEN, F., MAERTEN, L. & COOKE, M. 2009. Solving 3d boundary element problems using constrained iterative approach. *Computational Geosciences*, **14**, 551–564.

MANDL, G. & CRANS, W. 1981. Gravitational gliding in deltas. *In*: PRICE, N. J. & MCCLAY, K. R. (eds) *Nappe and Thrust Tectonics*. The Geological Society, London, Special Publications, **9**, 41–54.

MCCLAY, K., DOOLEY, T. & ZAMORA, G. 2003. Analogue models of delta systems above ductile substrates. *In*: VAN RENSBERGEN, P., HILLIS, R. R., MALTMAN, A. J. & MORLEY, C. K. (eds) *Subsurface Sediment Mobilization*. Geological Society, London, Special Publications, **216**, 411–428.

MILDREN, S. D., HILLIS, R. R. & KALDI, J. 2002. Calibrating predictions of fault seal reactivation in the Timor Sea. *The Australian Petroleum Production and Exploration Association Journal*, **42**, 187–202.

MORLEY, C. K. 2003. Mobile shale related deformation in large deltas developed on passive and active margins. *In*: VAN RENSBERGEN, P., HILLIS, R. R., MALTMAN, A. J. & MORLEY, C. K. (eds) *Subsurface Sediment Mobilization*. Geological Society, London, Special Publications, **216**, 335–357.

MORLEY, C. K. & GUERIN, G. 1996. Comparison of gravity-driven deformation styles and behaviour associated with mobile shales and salt. *Tectonics*, **15**, 1154–1170.

MORLEY, C. K., TINGAY, M. R. P., HILLIS, R. R. & KING, R. C. 2008. Relationship between structural style, overpressures and modern stress, Baram Delta province, NW Borneo. *Journal of Geophysical Research*, **113**, BO9410, doi: 10.1029/2007JB005324.

MORLEY, C. K., KING, R. C., HILLIS, R. R., TINGAY, M. R. P. & BACKÉ, G. 2011. Deepwater fold and thrust belt classification and hydrocarbon prospectivity. *Earth Science Reviews*, **104**, 41–91.

MORRIS, A. & FERRILL, D. A. 2009. The importance of the effective intermediate principal stress (s'_2) to fault slip patterns. *Journal of Structural Geology*, **31**, 950–959.

MORRIS, A. P., FERRILL, D. A. & HENDERSON, D. B. 1996. Slip tendency and fault reactivation. *Geology*, **24**, 275–278.

NORVICK, M. S. & SMITH, M. A. 2001. Mapping the plate tectonic reconstruction of southern and southeastern Australia and implications for petroleum systems. *The Australian Petroleum Production and Exploration Association Journal*, **41**, 15–35.

OSBORNE, M. J. & SWARBRICK, R. E. 1997. Mechanisms for generating overpressure in Sedimentary Basins: a reevaluation. *American Association of Petroleum Geologists Bulletin*, **81**, 1023–1041.

REYNOLDS, S. D. & HILLIS, R. R. 2000. The in situ stress field of the Perth Basin, Australia. *Geophysical Research Letters*, **27**, 3421–3424.

REYNOLDS, S. D., COBLENTZ, D. D. & HILLIS, R. R. 2002. Tectonic forces controlling the regional intraplate stress field in continental Australia: results from new finite element modelling. *Journal of Geophysical Research*, **107B**, 21–31.

REYNOLDS, S. D., HILLIS, R. R. & PARASCHIVOIU, E. 2003. The in situ stress field, fault reactivation and seal integrity in the Bight Basin, South Australia, Australia. *Exploration Geophysics*, **34**, 174–181.

ROWAN, M. G., PEEL, F. J. & VENDEVILLE, B. C. 2004. Gravity-driven fold belts on passive margins. *In*: MCCLAY, K. R. (ed.) *Thrust Tectonics and Hydrocarbon Systems*. American Association of Petroleum Geologists, Boulder, Memoir, **82**, 157–182.

RUBLE, T. E., LOGAN, G. A. *ET AL*. 2001. Geochemistry and charge history of a paleo-oil column: Jerboa-1, Eyre Sub-basin, Great Australian Bight. *In*: HILL, K. C. & BERNECKER, T. (eds) *Eastern Australasian Basins Symposium. A Refocused Energy Perspective for the Future*. Petroleum Exploration Society of Australia, Special Publication, 521–530.

SANDIFORD, M., WALLACE, M. & COBLENTZ, D. 2004. Origin of the in situ stress field in south-eastern Australia. *Basin Research*, **16**, 325–338.

SAYERS, J., SYSMONDS, P., DIREEN, N. G. & BERNARDEL, G. 2001. Nature of the continent–ocean transition on the non-volcanic rifted margin of the central Great Australian Bight. *In*: WILSON, R. C. L., WHITMARSH, R. B., TAYLOR, B. & FROITZHEIM, N. (eds) *Non-Volcanic Rifting of Continental Margins: A Comparison of Evidence from Land and Sea*. Geological Society, London, Special Publications, **187**, 51–76.

SOMERVILLE, R. 2001. The Ceduna Sub-basin – a snapshot of prospectivity. *The Australian Petroleum Production and Exploration Association Journal*, **41**, 321–346.

STAGG, H. M. V., COCKSHELL, C. D. *ET AL*. 1990. Basins of the Great Australian Bight region: geology and petroleum potential. *Bureau of Mineral Resources, Australia, Continental Margins Program, Folio 5*.

STRUCKMEYER, H. I. M., TOTTERDELL, J. M. *ET AL*. 2001. Character, maturity and distribution of potential Cretaceous oil source rocks in the Ceduna Sub-basin, Bight Basin, Great Australian Bight. *In*: HILL, K. C. & BERNECKER, T. (eds) *Eastern Australasian Basin Symposium, a Refocused Energy Perspective for the Future*. Petroleum Exploration Society of Australia, Special Publication, 543–552.

STRUCKMEYER, H. I. M., WILLIAMS, A. K., COWLEY, R., TOTTERDELL, J. M., LAWRENCE, G. & O'BRIEN, G. W. 2002. Evaluation of hydrocarbon seepage in the Great Australian Bight. *The Australian Petroleum Production and Exploration Association Journal*, **42**, 371–385.

TAPLEY, D., MEE, B. C., KING, S. J., DAVIS, R. C. & LEISCHNER, K. R. 2005. Petroleum potential of the Ceduna Sub-basin: impact of Gnarlyknots-1A. *The Australian Petroleum Production and Exploration Association Journal*, **45**, 365–380.

TEASDALE, J. P., PRYER, L. L., STUART-SMITH, P. G., ROMINE, K. K., ETHERIDGE, M. A., LOUTIT, T. S. & KYAN, D. M. 2003. Structural framework and basin evolution of Australia's southern margin. *The Australian Petroleum Production and Exploration Association Journal*, **43**, 13–37.

THOMAS, A. L. 1993. Poly3D: *A three-dimensional, polygonal element, displacement discontinuity boundary element computer program with applications to fractures, faults, and cavities in the Earth's crust*. MSc thesis, Stanford University.

TINGAY, M. R. P, HILLIS, R. R., MORLEY, C. K., SWARBRICK, R. E. & DRAKE, S. J. 2005. Present-day stress orientation in Brunei: a snapshot of 'prograding tectonics' in a Tertiary delta. *Journal of the Geological Society, London*, **162**, 39–49.

TINGAY, M., HILLIS, R., MORLEY, C., KING, R., SWARBRICK, R. & DAMIT, A. 2009. Present-day stress and neotectonics of Brunei: implications for petroleum exploration and production. *American Association of Petroleum Geologists Bulletin*, **93**, 75–100.

TOTTERDELL, J. M. & KRASSAY, A. A. 2003. The role of shale deformation and growth faulting in the Late Cretaceous evolution of the Bight Basin, offshore southern Australia. *In*: VAN RENSBERGEN, P., HILLIS, R. R., MALTMAN, A. J. & MORLEY, C. K. (eds) *Subsurface Sediment Mobilisation*. Geological Society, London, Special Publications, **216**, 429–442.

TOTTERDELL, J. M. & BRADSHAW, B. E. 2004. The structural framework and tectonic evolution of the Bight Basin. *In*: BOULT, P. J., JOHNS, D. R. & LANG, S. C. (eds) *Eastern Australasian Basins Symposium II*. Petroleum Exploration Society of Australia, Special Publication, 41–61.

TOTTERDELL, J. M., BLEVIN, J. E., STRUCKMEYER, H. I. M., BRADSHAW, B. E., COLWELL, J. B. & KENNARD, J. M. 2000. A new sequence framework for the Great Australian Bight: starting with a clean slate. *The Australian Petroleum Production and Exploration Association Journal*, **40**, 95–117.

TOTTERDELL, J. M., STRUCKMEYER, H. I. M., BOREHAM, C. J., MITCHELL, C. H., MONTEIL, E. & BRADSHAW, B. E. 2008. Mid–Late Cretaceous organic-rich rocks from the eastern Bight Basin: implications for prospectivity. *PESA Eastern Australasian Basins Symposium III*, 137–158.

TURNER, J. P. & WILLIAMS, G. D. 2004. Sedimentary basin inversion and intra-plate shortening. *Earth-Science Reviews*, **65**, 277–304.

WILLCOX, J. B. & STAGG, H. M. J. 1990. Australia's southern margin: a product of oblique extension. *Tectonophysics*, **173**, 269–281.

WILLIAMS, G. A., TURNER, J. P. & HOLFORD, S. P. 2005. Inversion and exhumation of the St Georges Channel Basin, offshore Wales, UK. *Journal of the Geological Society, London*, **162**, 97–110.

WILLIAMS, G. D., POWELL, C. M. & COOPER, M. A. 1989. Geometry and kinematics of inversion tectonics. *In*: COOPER, M. A. & WILLIAMS, G. D. (eds) *Inversion Tectonics*. Geological Society, London, Special Publications, **44**, 3–15.

YASSIR, N. A. & ZERWER, A. 1997. Stress regimes in the Gulf Coast, offshore Louisiana: data from well-bore breakout analysis. *American Association of Petroleum Geologists Bulletin*, **81**, 293–307.

4.4 Paper 4

MacDonald, J.D., Holford, S., Green, P.F., Duddy, I., King, R., and Backé, G., (2013): Detrital Zircon Data Reveal the Origin of Australia's Largest Delta System. *Journal of the Geological Society, London*.

NOTE:
Statements of authorship appear on pages 159-160 in the print copy of the thesis held in the University of Adelaide Library.

Journal of the Geological Society, London, Vol. **170**, 2013, pp. 3–6. doi: 10.1144/jgs2012-093.

SPECIAL

Detrital zircon data reveal the origin of Australia's largest delta system

JUSTIN D. MACDONALD[1]*, SIMON P. HOLFORD[1], PAUL F. GREEN[2], IAN R. DUDDY[2], ROSALIND C. KING[3] & GUILLAUME BACKÉ[4]

[1]*ConocoPhillips Company, Geological Technology, Houston, TX, 77079, USA*

[2]*Geotrack International Pty Ltd, 37 Melville Rd, Victoria 3055, Australia*

[3]*School of Earth and Environmental Sciences, University of Adelaide, SA 5005, Australia*

[4]*BP Exploration Co Ltd, Subsurface Technology, Sunbury on Thames, TW16 7LN, UK*

**Corresponding author (e-mail: Justin.D.MacDonald@conocophillips.com)*

The Late Cretaceous Ceduna Delta is the largest deltaic system on the Australian continent, yet its source is unknown. Apatite fission-track data reveal widespread Late Cretaceous exhumation across the southern Australian margin. New detrital zircon analysis of 786 grains from the Gnarlyknots-1 well, which penetrated the offshore delta top, show that the upper part of the delta (Santonian–Maastrichtian) was sourced largely from recycled Permian to Early Cretaceous cover and underlying basement eroded from the margin, proximal to the basin. This challenges the widely accepted model involving distal provenance of >2000 km from the eastern margin of Australia.

Supplementary material The 2D seismic reflection data, results for detrital zircon LA-ICP-MS and zircon fission-track analyses, including the LA-ICP-MS method, and a list of sample intervals and ages are available at www.geolsoc.org.uk/SUP18582.

The Ceduna Delta, offshore South Australia, is the largest delta located along the rifted continental margins of Australia and is comparable in size with the contemporary Niger Delta. The conspicuous bathymetric expression of the delta extends for *c*. 700 km along the southern Australian margin, covering an area of *c*. 126000 km^2, with the Late Cretaceous (Albian–Maastrichtian) sedimentary succession reaching an estimated 12–15 km in thickness (Fig. 1; Totterdell *et al*. 2000). Despite the enormous size of this delta system, both its origin and the cause of its demise are poorly understood, because to date, no data on the provenance of the deltaic sediments have been available. This is mainly due to the limited well coverage in the basin (Fig. 1).

Several studies have suggested that the Ceduna Delta system was deposited by a SW-flowing, continent-scale river system delivering erosional detritus either from the Eromanga Basin (King & Mee 2004) or the Australian Eastern Highlands (Veevers 2000). However, the well-documented (though under-appreciated) exhumation of the arcuate South Australian margin is contemporaneous with deposition of this delta system, providing a possible alternative source, which we evaluate here.

Geological setting. The Ceduna sub-basin formed along the southern Australian rifted margin during late Jurassic–Cenozoic separation from Antarctica. MacDonald *et al*. (2012) used seismic data to demonstrate that the Ceduna Delta can be subdivided into two structurally distinct delta lobes, a Cenomanian lobe in the west (D2; thickness >5000 m in places) and a Santonian–Maastrichtian lobe in the east (D1; thickness up to 5000 m). The two delta lobes are separated by a Turonian–Santonian package of intercalated deltaic material and marine mudstone of varying thickness and distribution. Unfortunately, there has been limited exploration drilling in this sub-basin, and the deepest well to date, Gnarlyknots-1A, did not penetrate D2 (Fig. 1). Thus we have focused on the data-rich D1 lobe and can only speculate on the origin of the D2 lobe based on regional geological constraints.

Dataset and results. For detrital zircon dating, 10 composite samples were collected over *c*. 100 m intervals from the D1 succession in Gnarlyknots-1A, yielding 786 U–Pb laser ablation inductively coupled plasma mass spectrometry (LA-ICP-MS) ages and 179 zircon fission-track ages. All 10 samples show essentially similar spectra of U–Pb ages regardless of stratigraphic age and are thus presented in a single probability density plot to highlight the dominant populations within the dataset (Fig. 2). Combining all U–Pb ages into a single composite sample of D1 reveals a range from late Cretaceous to Archaean (40% are Phanerozoic, 58% Proterozoic and 2% Archaean). In detail, the youngest age populations in deeper samples (*c*. 85–100 Ma) are distinctly younger than the corresponding populations in the shallowest samples (*c*. 100–120 Ma) (Fig. 3).

Zircon fission-track analysis (ZFTA) results from Gnarlyknots-1A show a similar range of ages to the younger Palaeozoic U–Pb ages (Fig. 3). The older ages are not represented, partly because of the greater stability of U–Pb ages but also because track densities in grains with Precambrian fission-track ages would be too high to allow reliable track counting. The youngest zircon fission-track ages in each sample tend to be slightly younger than the youngest U–Pb ages, although remaining in agreement with the stratigraphic age (Fig. 3).

Detrital zircon populations, Gnarlyknots-1A. In the U–Pb data from Gnarlyknots-1A we have identified six significant (>5% of sample) detrital zircon populations (Fig. 2) indicative of source terranes in southeastern, eastern and central Australia (Fig. 1). The youngest population of ages (23%) range from 83 to 200 Ma (Fig. 2), and, as above, the youngest ages within this population are very close to the depositional ages of these samples. We interpret these grains as derived from erosion of Early Cretaceous volcanogenic sediments that are widely distributed across central eastern and southeastern Australia (Gleadow & Duddy 1982; Duddy 2003). Although zircons in this age range have previously been attributed to a source from the Whitsunday Volcanic Province, far to the east (Veevers 2000), Duddy (2003) demonstrated that Early Cretaceous explosive volcanism was prolific across southeastern Australia, resulting in widespread volcanogenic sedimentary sequences derived from a large number of easily eroded local sources that have not been preserved. The main phase of this volcanism occurred during the Aptian–Albian and is identified by petrographical and fission-track studies of the Lower Cretaceous volcanogenic sediments in central and southern Australia, particularly the Otway and Strzelecki Groups (Gleadow & Duddy

Fig. 1. Compilation digital elevation model of Australia showing detrital zircon provenance terranes (after Veevers 2000) and relevant basin locations. The inset of Ceduna Terrace (bottom centre) shows the bathymetric expression of the Ceduna Delta at the present day. The Late Cretaceous Exhumation Limit is defined by published onshore AFTA studies cited in the text. The Gnarlyknots-1A well log (bottom left) shows the position of detrital zircon composite samples (red bars) and sample numbers, where yellow indicates sand and grey indicates shale.

1982) and Winton Formation (Alley *et al*. 2011). The presence of chemically unstable volcanic minerals including clinopyroxene and amphiboles and diagenetic zeolites following dissolution of volcanic glass, as well as detrital apatites and zircons with well-defined crystal forms, in these rocks requires a proximal source (Duddy 2003), rather than transport from a volcanic arc >1500 km to the east (Veevers 2000). Thus there is abundant evidence in central–east and southeastern Australia for proximal volcanism as the source for major Cretaceous sediment accumulations in adjacent basins (Duddy 2003).

The next youngest population of ages (200–300 Ma) comprises *c*. 17% of the total ages. Ages in this range have previously been interpreted as derived from the New England Fold Belt, which extends along the eastern Australian coast and is characterized by zircon ages of *c*. 200–300 Ma (Fig. 2; Veevers 2000; Veevers *et al*. 2006). However, zircons with U–Pb ages in this range have been identified in Eocene sandstones of local derivation in palaeochannels on the Eyre Peninsula that are clearly not directly derived from the east coast of Australia by an extensive river system (Reid *et al*. 2009). We suggest that grains with these ages are derived principally from Permian sandstones formerly present across the onshore margin, which would have contributed zircons originally derived from a broad range of sources (Veevers 2000). A further contribution of grains with ages in the younger part of the range could come from erosion of Triassic volcanogenic sandstones, which also contain a major contribution of detritus from contemporaneous volcanism (Duddy 2003).

Minor populations of ages in the range of *c*. 300–450 Ma (6% of ages) and 485–514 Ma (<5% of ages) could be derived from the Lachlan Fold Belt and Delamerian Granites in South Australia (respectively) (Fig. 2; Veevers *et al*. 2006), whereas a much more dominant population in the 500–700 Ma range makes up 27% of the zircon grains analysed (Fig. 2). Sources in this age range are recognized in the Flinders Ranges (Reid *et al*. 2009), and Veevers *et al*. (2006) suggested that such grains could also be derived from Antarctic sources and these could also easily have been recycled through Permian clastic sediments.

A 900–1000 Ma population may have been originally sourced from the Rayner Province in Antarctica and represent recycled zircons from Permian rocks or from the Flinders Ranges (Veevers *et al*. 2006). A *c*. 5% Mesoproterozoic (1000–1300 Ma) population (Fig. 2) is most probably originally sourced from the equivalent aged Musgrave Block in central Australia, the Lachlan Fold Belt and possibly from the Albany–Fraser Orogen, which borders the eastern Yilgarn Craton (Veevers 2000; Fig. 1).

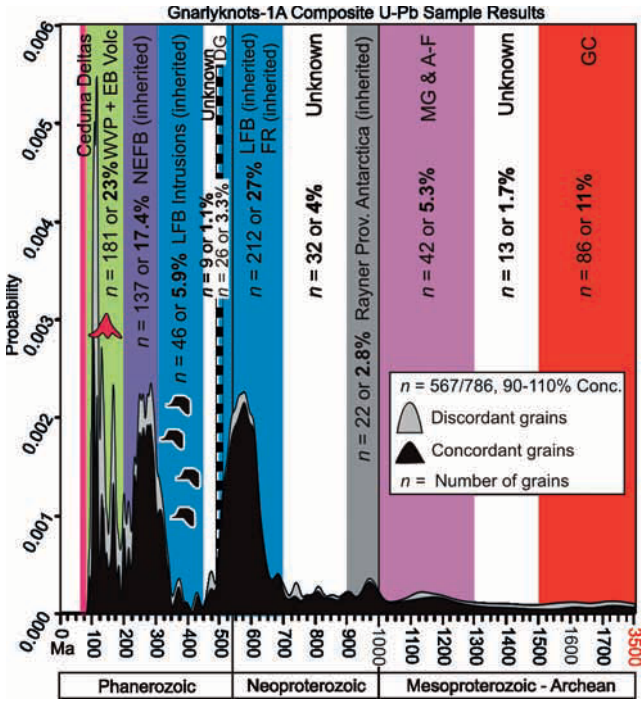

Fig. 2. Composite sample results of Gnarlyknots-1A U–Pb data displayed on a probability density–time plot. The legend and colour scheme on the plots correspond to zircon provenance terranes shown in Figure 1, and *n* is the number of grains that for each population and the corresponding percentage of the total sample.

The oldest population of zircons (1500–3400 Ma) accounts for 11% of all grains (Fig. 2), with the proposed source in the Archaean–early Mesoproterozoic Gawler Craton, which is the most proximal source terrane to the Ceduna Delta and was exposed by the end of the Cretaceous (Reid *et al*. 2009).

Origin of the Santonian–Maastrichtain delta lobe. Seismic reflection data (Totterdell *et al*. 2000; MacDonald *et al*. 2012) provide evidence for a significant change in sediment input at the start of the Santonian, from a marine flooding surface (Turonian–Santonian) to deltaic progradation (D1). During this change in depositional setting, the South Australian margin was undergoing a change in tectonic regime. Significant evidence exists from apatite fission-track analysis (AFTA) for a late Cretaceous exhumation event that resulted in 1–2 km of erosion (Fig. 1) across a broad arcuate-shaped region encompassing the southern Musgrave Block, western Eromanga Basin, Officer Basin, Flinders Ranges (Blinman-2 well; Fig. 1), Yorke Peninsula, Southern Adelaide Fold Belt and Kangaroo Island (Fig. 1; Gibson & Stuwe 2000; Tingate & Duddy 2002; Tingate *et al*. 2007). AFTA data show that this regional exhumation event began between 100 and 80 Ma, probably resulting in the erosion of significant volumes of existing Permian glacial sediments, Jurassic and early Cretaceous volcanogenic sediments that covered the margin at this time (Veevers 2000), plus underlying basement. Reworked Permian, Jurassic and early Cretaceous palynomorphs are present in dredged samples of the Campanian–Maastrichtian Potoroo Formation throughout the Ceduna and Duntroon Sub-basins (Alley & Clarke 1992), indicating erosion of Permian to early Cretaceous rocks in the hinterland at the time of deposition. This hypothesis is supported by the seismic character of the delta, which indicates a rapid deposition rate consistent with high-angle drainages, as shown by steep clinoforms, regional incision and the geometry of the deltaic lobe (Totterdell *et al*. 2000).

Whereas our results indicate that much of the D1 lobe was derived from erosion of Early Cretaceous volcanogenic sediments, samples from Gnarlyknots-1A indicate >75% quartz content in most of the sands and typically <5% volcanic rock fragments (Baker 2003). This apparent contradiction arises because, out of the original Early Cretaceous recognizable volcanic components that survived Early Cretaceous transport and diagenetic alteration, including some ferromagnesian minerals, plagioclase feldspars and volcanic rock fragments (Duddy 2003), few survive a second phase of weathering and transport, so that only resistant grains from the original Early Cretaceous volcano-sedimentary provenance (i.e. quartz, apatite, zircon and some glassy or flow-banded volcanic rock fragments; Baker 2003) are redeposited in the delta. The 'younging downward' pattern of the youngest populations of zircon U–Pb ages in Gnarlyknots-1A clearly shows a progressive unroofing of a sedimentary pile, with progressively older units being eroded from the onshore shelf through time (Fig. 3). The significant component (*c*. 10%) of Gawler Craton ages in the results also shows that erosion of the proximal Eyre Peninsula crystalline basement was taking place during deposition of the delta (Fig. 2). The demise of the D1 lobe in the intra-Maastrichtian is thus a direct

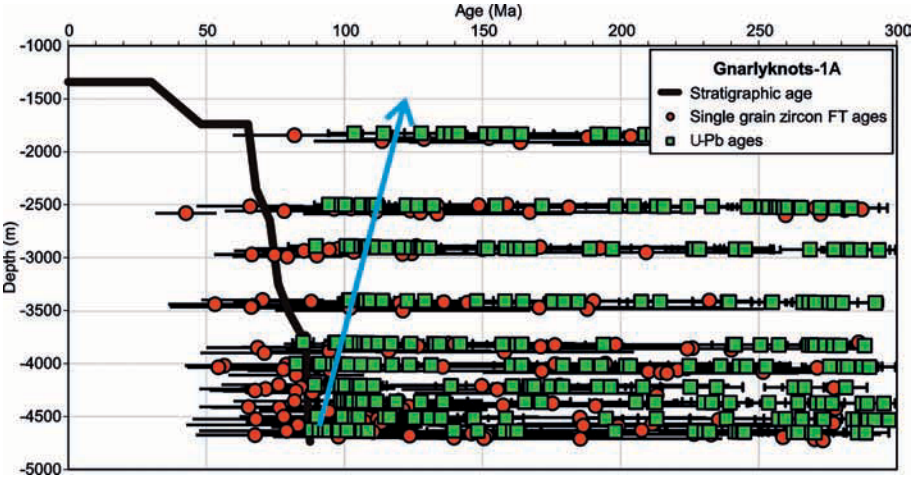

Fig. 3. Depth v. age plot showing correlation between zircon fission-track data (red squares), U–Pb data (green circles) and stratigraphic age (bold continuous line) from Gnarlyknots-1A well. The blue arrow indicates a reverse stratigraphy pattern with youngest zircons at the base of well and progressively older zircons toward the top of the well in the 85–120 Ma age range.

result of cessation of exhumation, and therefore sediment source, on the margin. This is consistent with observations from the Otway and Gippsland basins that show a progressive reduction in clastic sediment flux throughout the late Cretaceous following peak sediment flux at *c*. 90–95 Ma, which accompanied major inversion and exhumation (Duddy 2003).

The Cenomanian delta lobe. With little extant geological or geomorphological evidence for the Cenomanian delta lobe, we can only speculate on its origin based on regional geological constraints. The Eromanga Basin in eastern Australia hosts the only known post-Albian Cretaceous strata preserved onshore between the central–east and southeastern source terranes and the Ceduna Delta (Fig. 1). The Winton Formation is an Albian–Cenomanian fluvial–lacustrine package, containing abundant volcaniclastic material, deposited in a swampy, flat, low-energy environment following the retreat of an inland sea in the early Cenomanian (Alley *et al*. 2011). Petrographic studies of the Aptian–Cenomanian stratigraphy of the Eromanga Basin indicate an almost exclusive volcanogenic source for the sandstones within this formation (Alley *et al*. 2011), implying that eruption and deposition continued until cessation of volcanic activity in the Cenomanian (Fig. 1). A recent analysis of detrital zircon in a sample of Winton Formation (Bryan *et al*. 2012) revealed 107 concordant U–Pb ages ranging from 95 to 2800 Ma, with *c*. 35% of the ages between 95 and 102 Ma. The absence of 105–95 Ma ages in the Whitsunday Volcanic Province (Bryan *et al*. 2012), and the euhedral nature of 105–95 Ma grains in the Winton Formation, provides further evidence for a proximal volcanic source for the Winton Formation rather than the Whitsunday Volcanic Province some 700 km to the east. We speculate that the Winton Formation was deposited in the catchment area of a major river system (i.e. Ceduna River; Fig. 1). Thus the D2 lobe is probably a direct product of a short-lived river system, supplying fresh volcaniclastic sediment and underlying basement to the Ceduna Delta with continuing eruption. By the Turonian–Coniacian, the volcanism had ceased in the catchment area (*c*. 90 Ma), explaining the termination of deposition offshore.

Although purely speculative, if the 'younging downward' pattern observed in the Gnarlyknots-1A well is representative of the overall late Cretaceous basin fill, we would expect to see Albian–Cenomanian aged zircons in D2, coeval with the continuing volcanism in the Eromanga Basin catchment area. This then would require a significant river system to transport sediment from the Eromanga Basin catchment area to the Ceduna Delta. If exhumation of the margin began after 90 Ma, when the volcanism waned in the east, this may have allowed a river system to pass over the margin, before exhumation could inhibit flow. If that was the case, the remaining evidence for any fluvial system would be eradicated by the regional exhumation event evidenced in the AFTA data, as is confirmed by the absence of any Late Cretaceous strata onshore South Australia.

Conclusions. The first study of the origin of the Ceduna Delta system indicates that regional uplift and exhumation that began between 100 and 80 Ma resulted in the removal of 1–2 km of existing Permian to mid-Cretaceous strata from the South Australian margin to produce the D1 lobe. This study demonstrates that understanding the tectonic history of Australia has profound implications for reconstructing its palaeogeography, and that a simple source-to-sink model cannot fully explain the origin of the Ceduna Delta.

We thank the Australian Research Council (ARC Discovery Grants DP0878258 and DP0897612) and the University of Adelaide for their financial support of this study, B. Henderson and E. Alexander for help with the LA-ICP-MS analysis, A. Collins for discussion on source terranes, and Ion Geophysical for supplying the BightSPAN seismic dataset. The journal reviewers, P. Hayman and C. Fergusson, provided useful comments, which led to a better paper. This article forms TRaX #260.

References

Alley, N.F. & Clarke, J.D.A. 1992. Stratigraphy and palynology of Mesozoic sediments from the Great Australian Bight area, southern Australia. *BMR Journal of Australian Geology and Geophysics*, **13**, 113–130.

Alley, N.F., Sheard, M.J., White, M.R. & Krieg, G.W. 2011. The sedimentology and stratigraphic significance of Cretaceous sediments at Mt Howie, NE South Australia. *Transactions of the Royal Society of South Australia*, **135**, 12–25.

Baker, J.C. 2003. *Petrology, diagenesis and reservoir quality of sidewall cores from Gnarlyknots-1A, EPP-29, Great Australian Bight*. Woodside Energy Ltd, Perth, Australia, 29pp.

Bryan, S.E., Cook, A.G., *et al*. 2012. Early–mid Cretaceous tectonic evolution of eastern Gondwana: From silicic LIP magmatism to continental rupture. *Episodes*, **35**, 142–152.

Duddy, I.R. 2003. Mesozoic, a time of change in tectonic regime. *In*: Birch, W.D. (ed.) *Geology of Victoria*. Geological Society of Australia Special Publication, **23**, 239–286.

Gibson, H.J. & Stuwe, K. 2000. Multiphase cooling and exhumation of the southern Adelaide Fold Belt: constraints from apatite fission track data. *Basin Research*, **12**, 31–45.

Gleadow, A.J.W. & Duddy, I.R. 1982. A natural long-term track annealing experiment for apatite. *Nuclear Tracks*, **5**, 169–174.

King, S.J. & Mee, B.C. 2004. The seismic stratigraphy and petroleum potential of the Late Cretaceous Ceduna Delta, Ceduna Sub-basin, Great Australian Bight. *In*: Boult, P.J., Johns, D.R. & Lang, S.C. (eds) *Eastern Australasian Basins Symposium II*. Petroleum Exploration Society of Australia, Special Publication, 63–73.

Macdonald, J., Backé, G., King, R., Holford, S. & Hillis, R. 2012. Geomechanical modelling of fault reactivation in the Ceduna Sub-basin, Bight Basin, Australia. *In*: Healy, D., Butler, R.W.H., Shipton, Z.K. & Sibson, R.H. (eds) *Faulting, Fracturing and Igneous Intrusion in the Earth's Crust*. Geological Society, London, Special Publications, **367**, 71–89.

Reid, A.J., Korsch, R.J., Hou, B. & Black, L.P. 2009. Sources of sediment in the Eocene Garford paleovalley, South Australia, from detrital-zircon geochronology. *Australian Journal of Earth Sciences*, **56**, 125–137.

Tingate, P.R. & Duddy, I.R. 2002. The thermal history of the eastern Officer Basin (South Australia): evidence from apatite fission track analysis and organic maturity data. *Tectonophysics*, **349**, 251–275.

Tingate, P., Green, P.F., Lemon, N.M. & McKirdy, D.M. 2007. Insight into the tectonic development and hydrocarbon potential of the Flinders Ranges South Australia based on AFTA and organic maturity data from the Blinman-2 borehole. *In*: Munson, T.J. & Ambrose, G.J. (eds) *Conference Proceedings of the Central Australian Basins Symposium*. Northern Territory Geological Survey Special Publication, **2**, 71–81.

Totterdell, J.M., Blevin, J.E., Struckmeyer, H.I.M., Bradshaw, B.E., Colwell, J.B. & Kennard, J.M. 2000. A new sequence framework for the Great Australian Bight: starting with a clean slate. *Australian Petroleum Production and Exploration Association Journal*, **40**, 95–117.

Veevers, J.J. (ed.) 2000. *Billion-Year Earth History of Australia and Neighbours in Gondwanaland*. Geochemical Evolution and Metallogeny of Continents (GEMOC) Press, Macquarie University, Sydney.

Veevers, J.J., Belousova, E.A., Saeed, A., Sircombe, K., Cooper, A.F. & Read, S.E. 2006. Pan-Gondwanaland detrital zircons from Australia analysed for Hf-isotopes and trace elements reflect an ice-covered Antarctic provenance of 700–500 Ma age, T_{DM} of 2.0−1.0 Ga, and alkaline affinity. *Earth-Science Reviews*, **76**, 135–174.

Received 6 August 2012; revised typescript accepted 26 October 2012.
Scientific editing by Andrew Carter.

4.4.1 Paper 4 – Supplementary Data

Supplementary Data

Seismic Reflection Data

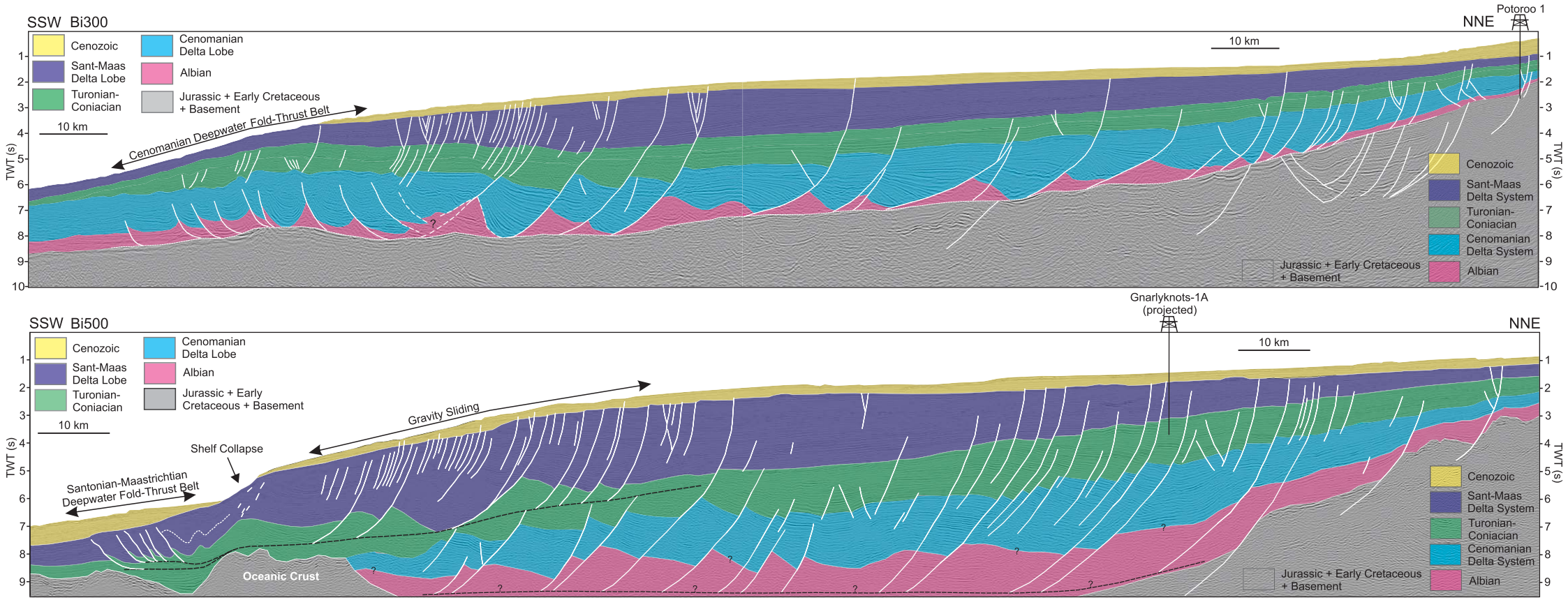

Fig. 1. Two dimensional seismic reflection data from the western (top) and eastern (bottom) Ceduna Sub-basin delta system showing two separate delta deepwater fold-thrust belt systems with extensional faults on the delta top(s) and thrust faults in the delta toe(s). Of particular importance is the Santonian-Maastrichtian delta system (purple) which is thicker in the east where it developed a deepwater fold-thrust belt (bottom) and the Cenomanian delta system (blue) which is better preserved in the west (top). Here, the system developed a deepwater fold-thrust belt whereas in the east the deepwater fold-thrust belt was likely uplifted by oceanic crust and eroded prior to deposition of the Santonian-Maastrichtian delta system leaving only the delta top faults preserved. The projected position of Gnarlyknots-1A is illustrated on the eastern seismic line where it penetrated the Santonian-Maastrichtian delta top and was abandoned within the Coniacian-Turonian section (green) before penetrating the older Cenomanian delta top. Potoroo-1 well (top) penetrated the entire section from Cenozoic to basement however limited sample material was available and thus insufficient sample size prevented U-Pb or ZFT dating in this study.

Supplementary Data

U-Pb LA-ICP-MS Data

Sample_ Grain #	Pb207/ Pb206	± 1σ	Pb208/ Th232	± 1σ	Pb207/ U235	± 1σ	Pb206/ U238	± 1σ	rho	Conc. (%)	Pb207/Pb206	± 1σ	Pb206/U238	± 1σ	Pb207/ U235	± 1σ	Pb208/Th232	± 1σ	Age
74317_01	0.05193	0.00249	0.01404	0.00091	0.28885	0.01354	0.04034	0.00082	0.433642	101	282.5	106.18	255	5.06	257.7	10.67	281.9	18.1	**255**
74317_02	0.05533	0.00193	0.02123	0.00121	0.48116	0.01669	0.06307	0.00112	0.511951	101	425.5	75.66	394.3	6.78	398.9	11.44	424.6	24	**394.3**
74317_03	0.04979	0.01354	0.00597	0.00109	0.1462	0.03855	0.0213	0.00148	0.263515	102	185.2	534	135.9	9.34	138.6	34.15	120.3	21.91	**135.9**
74317_04	0.05264	0.00286	0.01633	0.00113	0.36102	0.0191	0.04974	0.00106	0.402808	100	313.4	118.74	312.9	6.54	313	14.25	327.3	22.49	**312.9**
74317_05	0.06231	0.00311	0.0331	0.00227	0.94483	0.0457	0.10999	0.00241	0.453003	100	684.7	102.98	672.7	13.97	675.4	23.86	658.1	44.44	**672.7**
74317_06	0.05591	0.00217	0.01115	0.00067	0.25372	0.00969	0.03292	0.00061	0.485178	110	448.5	83.73	208.8	3.82	229.6	7.85	224.2	13.38	**208.8**
74317_07	0.07808	0.00196	0.06642	0.00419	2.02596	0.05231	0.18821	0.00311	0.639976	97	1148.9	49.06	1111.7	16.89	1124.3	17.55	1299.9	79.34	**1148.9**
74317_08	0.0569	0.00222	0.03159	0.00239	0.64844	0.02497	0.08267	0.00156	0.490036	99	486.9	84.57	512	9.27	507.5	15.38	628.6	46.81	**512**
74317_09	0.05608	0.0024	0.02928	0.00224	0.66111	0.02777	0.08551	0.00168	0.467725	97	455.1	92.65	528.9	9.99	515.3	16.98	583.4	43.99	**528.9**
74317_10	0.05519	0.00206	0.01432	0.00108	0.29942	0.01108	0.03935	0.00072	0.494457	107	419.8	81.04	248.8	4.47	265.9	8.66	287.3	21.53	**248.8**
74317_11	0.0577	0.00492	0.0076	0.00165	0.35548	0.0291	0.04469	0.00136	0.37175	110	518	177.37	281.8	8.39	308.8	21.8	153.1	33.09	**281.8**
74317_12	0.05664	0.00322	0.01562	0.00138	0.35858	0.01971	0.04592	0.00105	0.415994	108	477	121.54	289.4	6.49	311.2	14.73	313.2	27.43	**289.4**
74317_13	0.05968	0.00152	0.02553	0.00225	0.70808	0.01869	0.08607	0.0014	0.616239	102	591.8	54.41	532.2	8.3	543.6	11.11	509.6	44.25	**532.2**
74317_14	0.05939	0.00252	0.02762	0.00259	0.65953	0.02747	0.08055	0.0016	0.476903	103	581.4	89.67	499.4	9.53	514.3	16.81	550.6	50.92	**499.4**
74317_15	0.05227	0.00172	0.0215	0.00201	0.42134	0.01394	0.05847	0.00102	0.527275	97	297.2	73.36	366.3	6.23	357	9.96	430	39.81	**366.3**
74317_16	0.05164	0.00519	0.00975	0.00079	0.17741	0.01724	0.02492	0.00079	0.326227	104	269.3	214.92	158.7	4.94	165.8	14.86	196.1	15.86	**158.7**
74317_17	0.09865	0.00347	0.09558	0.00664	3.30906	0.11402	0.24327	0.00486	0.579791	88	1598.7	64.3	1403.7	25.22	1483.2	26.87	1845.1	122.54	**1598.7**
74317_18	0.05913	0.00154	0.03416	0.00223	0.76444	0.02042	0.09375	0.00151	0.602967	100	571.9	55.51	577.7	8.87	576.6	11.75	679	43.5	**577.7**
74317_19	0.05146	0.00604	0.0156	0.00192	0.35063	0.03951	0.04942	0.00187	0.3358	98	261.3	248.75	310.9	11.49	305.2	29.7	312.8	38.3	**310.9**
74317_20	0.05111	0.00328	0.01302	0.00111	0.25663	0.01597	0.03641	0.00085	0.375146	101	246	141.19	230.5	5.28	231.9	12.9	261.5	22.1	**230.5**
74317_21	0.04983	0.00217	0.01332	0.00107	0.27253	0.01165	0.03966	0.00075	0.442381	98	187.1	98.22	250.7	4.67	244.7	9.3	267.4	21.36	**250.7**
74317_22	0.0527	0.00303	0.00762	0.00063	0.17229	0.0096	0.02371	0.00053	0.401174	107	315.9	125.32	151	3.32	161.4	8.31	153.4	12.59	**151**
74317_23	0.05124	0.0035	0.01013	0.00095	0.23574	0.01558	0.03336	0.00082	0.371924	102	251.7	150.12	211.6	5.15	214.9	12.8	203.6	19.08	**211.6**
74317_24	0.05333	0.00829	0.00472	0.0007	0.11902	0.01782	0.01619	0.00074	0.305279	110	342.6	318.1	103.5	4.67	114.2	16.17	95.2	14.03	**103.5**
74317_25	0.05152	0.00258	0.01557	0.00141	0.32251	0.01574	0.0454	0.00093	0.419726	99	263.9	110.81	286.2	5.73	283.8	12.08	312.3	28.06	**286.2**
74317_26	0.11543	0.00326	0.08649	0.00786	4.24276	0.12075	0.26655	0.00454	0.598465	81	1886.6	50.03	1523.3	23.09	1682.3	23.39	1676.7	146.28	**1886.6**
74317_27	0.05941	0.00188	0.02574	0.00251	0.67866	0.02151	0.08285	0.0014	0.533147	103	582	67.31	513.1	8.35	526	13.01	513.6	49.55	**513.1**
74317_28	0.05265	0.00246	0.00983	0.00098	0.21893	0.00998	0.03015	0.0006	0.436555	105	313.9	102.84	191.5	3.73	201	8.32	197.7	19.52	**191.5**
74317_29	0.20753	0.00713	0.07964	0.00886	7.18946	0.23847	0.25127	0.00506	0.607117	50	2886.3	54.7	1445	26.08	2135.2	29.57	1548.9	165.89	**2886.3**
74317_30	0.06072	0.00306	0.03057	0.00327	0.82838	0.04043	0.09895	0.00211	0.436911	101	629.3	104.94	608.3	12.4	612.7	22.45	608.7	64.19	**608.3**
74317_31	0.04807	0.00561	0.00713	0.00065	0.13268	0.0149	0.02001	0.00074	0.329309	99	102.9	254.89	127.7	4.65	126.5	13.36	143.5	13	**127.7**

74317_32	0.05525	0.00575	0.00922	0.00094	0.1964	0.01952	0.02577	0.00093	0.363103	111	422.3	217.06	164	5.82	182.1	16.57	185.4	18.75	**164**
74317_33	0.05865	0.00151	0.0246	0.00191	0.66311	0.01762	0.08198	0.00134	0.615144	102	554.3	55.09	507.9	7.98	516.5	10.76	491.1	37.77	**507.9**
74317_34	0.05081	0.00293	0.01329	0.00099	0.28257	0.01583	0.04032	0.00092	0.407298	99	232.2	127.85	254.8	5.68	252.7	12.53	266.9	19.67	**254.8**
74317_35	0.06006	0.00244	0.02799	0.00233	0.80105	0.03205	0.0967	0.0019	0.491087	100	605.9	85.55	595	11.16	597.4	18.07	557.9	45.78	**595**
74317_36	0.05345	0.00316	0.01225	0.00097	0.26567	0.01522	0.03604	0.00084	0.406839	105	347.8	127.67	228.2	5.23	239.2	12.21	246.1	19.39	**228.2**
74317_37	0.08162	0.00691	0.05823	0.00603	2.41578	0.19405	0.21461	0.00783	0.454209	101	1236.3	157.69	1253.4	41.55	1247.3	57.68	1143.9	115.15	**1236.3**
74317_38	0.05141	0.00257	0.01434	0.00126	0.34627	0.01697	0.04884	0.00104	0.434501	98	259.1	111	307.4	6.38	301.9	12.8	287.9	25.02	**307.4**
74317_39	0.05682	0.00244	0.02909	0.00258	0.72235	0.03059	0.09218	0.00186	0.47648	97	484	92.8	568.4	10.98	552.1	18.03	579.6	50.75	**568.4**
74317_40	0.05514	0.00379	0.0302	0.00292	0.73113	0.04867	0.09615	0.00254	0.396842	94	417.7	146.87	591.8	14.94	557.2	28.55	601.4	57.37	**591.8**
74317_41	0.05814	0.00226	0.01293	0.0045	0.71862	0.02776	0.08963	0.00175	0.505434	99	534.5	83.3	553.3	10.33	549.9	16.4	259.6	89.72	**553.3**
74317_42	0.06329	0.00316	0.03338	0.00361	0.98034	0.04775	0.11232	0.00254	0.46428	101	718	102.52	686.2	14.71	693.8	24.48	663.7	70.56	**686.2**
74317_43	0.0458	0.00287	0.01615	0.00172	0.31712	0.01942	0.05021	0.0012	0.39027	89	0.1	132.09	315.8	7.37	279.7	14.97	323.9	34.21	**315.8**
74317_44	0.05417	0.00312	0.00858	0.00174	0.28747	0.01613	0.03848	0.00091	0.421468	105	378.1	124.12	243.4	5.63	256.6	12.72	172.7	34.96	**243.4**
74317_45	0.05042	0.00228	0.01429	0.00159	0.3618	0.01627	0.05204	0.00108	0.461496	96	214.5	101.59	327	6.61	313.6	12.13	286.8	31.61	**327**
74317_46	0.04985	0.00202	0.00796	0.00058	0.1719	0.0069	0.02503	0.00046	0.457851	101	187.9	91.84	159.3	2.88	161.1	5.98	160.3	11.59	**159.3**
74317_47	0.04911	0.00583	0.00646	0.00059	0.14695	0.01675	0.02171	0.00083	0.335408	101	153.2	256.72	138.5	5.22	139.2	14.82	130.2	11.86	**138.5**
74317_48	0.05203	0.00281	0.01351	0.0011	0.30268	0.01592	0.04222	0.00091	0.409792	101	286.5	119	266.6	5.61	268.5	12.41	271.2	21.88	**266.6**
74317_49	0.04849	0.00853	0.00878	0.00161	0.22652	0.03836	0.0339	0.00174	0.303094	96	123.3	368.28	214.9	10.87	207.3	31.76	176.8	32.26	**214.9**
74317_50	0.05687	0.00177	0.02849	0.0034	0.69281	0.02178	0.08842	0.00146	0.525241	98	485.9	67.85	546.2	8.66	534.5	13.07	567.8	66.73	**546.2**
74317_51	0.05073	0.00171	0.01511	0.00142	0.33589	0.01135	0.04806	0.00081	0.498772	97	228.5	76.04	302.6	4.96	294	8.63	303	28.21	**302.6**
74317_52	0.05862	0.00326	0.0277	0.00334	0.65789	0.03544	0.08146	0.00184	0.419308	102	553	117.12	504.8	11	513.3	21.71	552.2	65.76	**504.8**
74317_53	0.13717	0.00426	0.11228	0.01211	7.37948	0.22872	0.39047	0.00681	0.562705	97	2191.7	52.97	2125	31.58	2158.5	27.72	2150.9	219.99	**2191.7**
74317_54	0.09625	0.003	0.07412	0.00855	3.15717	0.0983	0.23807	0.00396	0.534238	89	1552.6	57.49	1376.6	20.62	1446.8	24.01	1445.2	160.94	**1552.6**
74317_55	0.05603	0.00302	0.01189	0.00147	0.27519	0.01431	0.03564	0.00077	0.415476	109	453.3	115.77	225.8	4.79	246.8	11.4	238.8	29.35	**225.8**
74317_56	0.05981	0.00211	0.02995	0.00383	0.75549	0.02617	0.09166	0.00156	0.491326	101	596.8	74.81	565.3	9.23	571.4	15.14	596.5	75.11	**565.3**
74317_57	0.04973	0.00327	0.01304	0.00184	0.26525	0.01674	0.0387	0.00092	0.376684	98	182.5	146.21	244.8	5.72	238.9	13.44	262	36.65	**244.8**
74317_58	0.04916	0.0033	0.01342	0.00198	0.25481	0.0164	0.0376	0.00092	0.380165	97	155.6	150.22	237.9	5.69	230.5	13.27	269.5	39.45	**237.9**
74317_59	0.04922	0.0033	0.01299	0.00195	0.24543	0.01573	0.03617	0.00088	0.379606	97	158.1	149.95	229.1	5.46	222.9	12.82	260.9	38.92	**229.1**
74317_60	0.04785	0.00392	0.00743	0.0012	0.14617	0.0114	0.02215	0.00062	0.358898	98	90.8	184.25	141.3	3.9	138.5	10.1	149.7	24.08	**141.3**
74317_71	0.15994	0.00905	0.11671	0.03011	9.65061	0.53084	0.4377	0.01047	0.434872	95	2455	92.63	2340.3	46.95	2402	50.61	2231.2	545.05	**2455**
74317_72	0.08154	0.00731	0.07351	0.01932	2.19548	0.18748	0.1953	0.00709	0.425127	93	1234.6	166.46	1150	38.23	1179.6	59.57	1433.8	363.68	**1234.6**
74317_73	0.06008	0.00386	0.03406	0.00895	0.7314	0.04543	0.0883	0.00229	0.417529	102	606.5	133.35	545.5	13.55	557.4	26.65	677	174.95	**545.5**
74317_74	0.09869	0.00647	0.09978	0.02648	3.66213	0.23097	0.26917	0.00738	0.434718	96	1599.5	117.69	1536.6	37.47	1563.2	50.3	1922.3	486.7	**1599.5**

74317_75	0.07514	0.00466	0.06704	0.01787	1.93943	0.11608	0.18723	0.00474	0.42298	103	1072.2	119.81	1106.4	25.74	1094.8	40.1	1311.6	338.58	**1072.2**
74317_76	0.09358	0.00584	0.08301	0.0223	2.76186	0.16624	0.21408	0.00544	0.422172	83	1499.6	113.68	1250.5	28.87	1345.3	44.87	1611.8	416.15	**1499.6**
74317_77	0.07256	0.00518	0.05052	0.01384	1.6069	0.10998	0.16065	0.00456	0.414724	101	1001.6	138.59	960.4	25.31	972.9	42.84	996.1	266.2	**960.4**
74317_78	0.11515	0.00765	0.09952	0.02715	4.58138	0.29183	0.2886	0.00779	0.423748	87	1882.2	115.08	1634.5	38.95	1745.9	53.09	1917.6	499.18	**1882.2**
74317_79	0.05368	0.00397	0.01657	0.00456	0.37661	0.02669	0.05089	0.00144	0.399276	101	357.6	158.67	320	8.81	324.5	19.69	332.2	90.59	**320**
74317_80	0.05405	0.0044	0.01442	0.00404	0.29413	0.02292	0.03947	0.00119	0.386905	105	373	173.82	249.6	7.38	261.8	17.98	289.4	80.51	**249.6**
74318_01	0.06082	0.00361	0.00929	0.0007	0.27115	0.0155	0.03228	0.00075	0.406449	119	633	122.93	204.8	4.67	243.6	12.38	186.9	14.08	**204.8**
74318_02	0.05432	0.00239	0.01266	0.00069	0.31493	0.0136	0.04202	0.00074	0.407803	105	384.4	95.3	265.3	4.56	278	10.5	254.3	13.77	**265.3**
74318_03	0.05253	0.00129	0.01572	0.00081	0.37466	0.00938	0.0517	0.00075	0.579436	99	308.5	54.88	325	4.59	323.1	6.93	315.3	16.05	**325**
74318_04	0.06119	0.00533	0.00505	0.00046	0.12455	0.01048	0.01474	0.00041	0.330574	126	646.1	176.76	94.3	2.62	119.2	9.46	101.9	9.35	**94.3**
74318_05	0.06404	0.00161	0.01378	0.00094	0.58962	0.01522	0.06669	0.00103	0.598321	113	742.8	52.31	416.2	6.24	470.6	9.72	276.7	18.82	**416.2**
74318_06	0.05119	0.00142	0.01193	0.00065	0.27476	0.00772	0.0389	0.00059	0.539807	100	249.4	62.52	246	3.64	246.5	6.15	239.8	13.08	**246**
74318_07	0.04402	0.00336	0.00461	0.00033	0.09388	0.00708	0.01546	0.00031	0.265884	92	0.1	67.78	98.9	1.99	91.1	6.57	93	6.65	**98.9**
74318_08	0.07592	0.00221	0.04894	0.0047	1.80496	0.05403	0.17222	0.00296	0.57417	~~94~~	1092.9	57.35	1024.3	16.27	1047.3	19.56	965.8	90.55	**1092.9**
74318_09	0.06432	0.00233	0.0239	0.00208	0.78884	0.02843	0.08885	0.00159	0.496537	108	752.3	74.81	548.7	9.4	590.5	16.14	477.3	40.96	**548.7**
74318_10	0.0635	0.0013	0.04694	0.00354	0.71467	0.0159	0.08156	0.00122	0.672343	108	724.9	42.96	505.4	7.3	547.5	9.41	927.2	68.31	**505.4**
74318_11	0.10303	0.00345	0.01388	0.00093	0.48353	0.01588	0.03402	0.00061	0.54597	186	1679.5	60.45	215.6	3.78	400.5	10.87	278.6	18.57	**215.6**
74318_12	0.05305	0.00184	0.01222	0.00086	0.2936	0.01026	0.04011	0.00066	0.470869	103	331	76.9	253.5	4.12	261.4	8.05	245.5	17.13	**253.5**
74318_13	0.05348	0.00248	0.01243	0.00136	0.36635	0.0167	0.04964	0.00094	0.415409	101	349	101.2	312.3	5.79	316.9	12.41	249.6	27.05	**312.3**
74318_14	0.05684	0.00297	0.00561	0.00055	0.13673	0.00704	0.01744	0.00036	0.40091	117	484.5	112.14	111.5	2.29	130.1	6.29	113	11.13	**111.5**
74318_15	0.05431	0.00203	0.01785	0.00203	0.44026	0.01627	0.0588	0.00107	0.492411	101	383.9	81.28	368.3	6.49	370.4	11.47	357.6	40.39	**368.3**
74318_16	0.0631	0.00252	0.00746	0.00092	0.21166	0.0083	0.02433	0.00046	0.482144	126	711.6	82.67	155	2.9	194.9	6.95	150.2	18.52	**155**
74318_17	0.09392	0.00302	0.06981	0.00818	3.25254	0.10409	0.25119	0.00443	0.55108	96	1506.6	59.49	1444.6	22.83	1469.8	24.85	1363.9	154.59	**1506.6**
74318_18	0.05303	0.0032	0.01545	0.00273	0.32855	0.01916	0.04494	0.00106	0.404463	102	329.8	130.5	283.4	6.55	288.5	14.65	309.9	54.25	**283.4**
74318_19	0.11053	0.00434	0.08235	0.01252	4.71976	0.1824	0.30973	0.00607	0.507108	96	1808.1	69.71	1739.4	29.86	1770.8	32.38	1599.5	233.9	**1808.1**
74318_20	0.05015	0.00198	0.00519	0.00053	0.11873	0.00462	0.01717	0.0003	0.449024	104	202	89.01	109.7	1.88	113.9	4.19	104.6	10.68	**109.7**
74318_21	0.05032	0.00194	0.01195	0.00168	0.28243	0.01074	0.04072	0.00076	0.490809	98	209.7	86.92	257.3	4.7	252.6	8.5	240.1	33.63	**257.3**
74318_22	0.05081	0.00584	0.01221	0.00287	0.28699	0.03174	0.04096	0.00152	0.335539	99	232.2	244.86	258.8	9.39	256.2	25.04	245.3	57.25	**258.8**
74318_23	0.04863	0.002	0.00549	0.00071	0.11581	0.00467	0.01727	0.00032	0.459501	101	130.2	93.75	110.4	2.03	111.3	4.25	110.6	14.3	**110.4**
74318_24	0.05777	0.00221	0.00545	0.00058	0.13222	0.00497	0.0166	0.00029	0.464762	119	521	82.01	106.1	1.84	126.1	4.45	109.9	11.56	**106.1**
74318_25	0.05715	0.0045	0.01175	0.00258	0.34658	0.02623	0.04401	0.00129	0.387296	109	496.8	165.07	277.6	7.97	302.1	19.78	236.1	51.63	**277.6**
74318_26	0.05884	0.00276	0.02969	0.00336	0.75109	0.03437	0.09257	0.00176	0.415485	100	561.3	98.91	570.7	10.39	568.9	19.93	591.4	65.95	**570.7**
74318_27	0.08066	0.00259	0.05661	0.00622	2.16234	0.06865	0.19441	0.00329	0.533041	94	1213.2	61.79	1145.2	17.77	1169	22.04	1113.1	119	**1213.2**

74318_28	0.05205	0.00195	0.01564	0.00178	0.36555	0.01347	0.05094	0.00088	0.468817	99	287.5	83.32	320.3	5.37	316.3	10.02	313.7	35.38	**320.3**
74318_29	0.06845	0.00474	0.03064	0.00742	1.03189	0.069	0.10938	0.003	0.410174	108	882.2	137.11	669.1	17.43	719.9	34.48	610	145.47	**669.1**
74318_30	0.11992	0.00635	0.08918	0.01995	4.93885	0.25517	0.29865	0.00682	0.441996	86	1955	91.62	1684.6	33.85	1808.9	43.63	1726.6	370.23	**1955**
74318_31	0.0628	0.00394	0.03073	0.00851	0.89983	0.05486	0.10391	0.0026	0.410413	102	701.6	128.23	637.3	15.19	651.6	29.32	611.7	166.79	**637.3**
74318_32	0.0572	0.0028	0.02367	0.00498	0.62122	0.0298	0.07877	0.00164	0.434022	100	498.9	105.01	488.8	9.83	490.6	18.66	472.9	98.42	**488.8**
74318_33	0.05142	0.00333	0.00607	0.00133	0.14661	0.00925	0.02068	0.00048	0.367885	105	259.7	142.43	132	3.05	138.9	8.19	122.3	26.64	**132**
74318_34	0.05658	0.00328	0.02309	0.00532	0.58411	0.03292	0.07488	0.00171	0.405196	100	474.6	124.12	465.5	10.26	467.1	21.1	461.4	105.07	**465.5**
74318_35	0.05128	0.00273	0.01202	0.00262	0.281	0.01455	0.03974	0.00086	0.41794	100	253.5	117.81	251.2	5.35	251.5	11.53	241.4	52.41	**251.2**
74318_36	0.05354	0.00332	0.01752	0.00408	0.41714	0.02507	0.05651	0.00132	0.388666	100	351.6	133.68	354.4	8.08	354	17.96	351	81.08	**354.4**
74318_37	0.07641	0.00414	0.05113	0.01213	1.8146	0.09537	0.17225	0.00381	0.420857	93	1105.8	104.68	1024.5	20.95	1050.7	34.41	1007.8	233.25	**1105.8**
74318_38	0.07856	0.00416	0.05474	0.01289	1.81054	0.093	0.16716	0.00362	0.421601	105	1161.1	101.56	996.5	20.02	1049.3	33.6	1077.2	247.07	**996.5**
74318_39	0.05976	0.0031	0.02983	0.00666	0.83538	0.04207	0.10139	0.00218	0.426946	99	594.7	108.99	622.5	12.75	616.6	23.27	594.2	130.69	**622.5**
74318_40	0.05878	0.00308	0.02657	0.00588	0.72905	0.03706	0.08997	0.00194	0.424186	100	559	110.41	555.3	11.49	556	21.76	530	115.84	**555.3**
74318_41	0.05117	0.00281	0.01332	0.00304	0.3042	0.01615	0.04312	0.00095	0.414984	99	248.3	121.48	272.2	5.87	269.7	12.58	267.4	60.67	**272.2**
74318_42	0.07671	0.00211	0.04443	0.00216	1.80238	0.0483	0.17053	0.00283	0.619277	91	1113.6	53.85	1015	15.58	1046.3	17.5	878.7	41.87	**1113.6**
74318_43	0.05953	0.00103	0.02838	0.00131	0.8022	0.0146	0.09779	0.00134	0.752905	99	586.5	37.09	601.4	7.88	598.1	8.22	565.6	25.67	**601.4**
74318_44	0.1654	0.00289	0.05114	0.00297	4.15331	0.07749	0.18221	0.00265	0.779511	43	2511.7	29.05	1079.1	14.44	1664.9	15.27	1008.1	57.15	**2511.7**
74318_45	0.07763	0.00143	0.03725	0.0022	1.72423	0.03387	0.16116	0.00236	0.745478	106	1137.5	36.28	963.2	13.1	1017.6	12.63	739.2	42.93	**963.2**
74318_46	0.05782	0.0021	0.03343	0.002	0.60323	0.02101	0.0757	0.00139	0.5272	102	522.6	77.84	470.4	8.34	479.3	13.31	664.7	39.1	**470.4**
74318_47	0.06333	0.00298	0.01131	0.00084	0.30903	0.01381	0.0354	0.00079	0.49938	122	719.2	96.9	224.3	4.93	273.4	10.72	227.4	16.84	**224.3**
74318_49	0.05185	0.00182	0.0122	0.00075	0.29307	0.01005	0.041	0.00072	0.512099	101	278.9	78.47	259	4.43	261	7.89	245	14.92	**259**
74318_50	0.10566	0.00352	0.06397	0.00724	3.65315	0.12136	0.25079	0.00503	0.60374	84	1725.9	59.92	1442.5	25.9	1561.2	26.48	1253.3	137.51	**1725.9**
74318_51	0.05988	0.00219	0.02443	0.00185	0.68522	0.02442	0.083	0.00158	0.53415	103	599.2	77.34	514	9.4	529.9	14.71	487.9	36.42	**514**
74318_52	0.05654	0.00154	0.016	0.00117	0.39375	0.01075	0.05051	0.00083	0.601884	106	472.7	59.54	317.7	5.09	337.1	7.83	320.7	23.24	**317.7**
74318_53	0.06804	0.00168	0.03561	0.00308	1.11533	0.0285	0.11889	0.00196	0.645163	105	869.7	50.46	724.2	11.32	760.7	13.68	707.2	60.06	**724.2**
74318_54	0.05154	0.00154	0.01132	0.00121	0.28819	0.00844	0.04055	0.00068	0.572604	100	264.9	67.34	256.2	4.22	257.1	6.66	227.6	24.15	**256.2**
74318_55	0.05265	0.0023	0.01058	0.00139	0.2994	0.01256	0.04122	0.00086	0.497339	102	313.9	96.46	260.4	5.34	265.9	9.81	212.7	27.88	**260.4**
74318_56	0.08643	0.00383	0.05142	0.00799	2.2841	0.09607	0.19161	0.00436	0.540998	84	1347.7	83.18	1130.1	23.57	1207.4	29.7	1013.4	153.63	**1347.7**
74318_57	0.06057	0.00184	0.02229	0.00277	0.76408	0.02263	0.09147	0.00159	0.586912	102	624.1	64.14	564.2	9.39	576.4	13.02	445.6	54.67	**564.2**
74318_58	0.07806	0.00219	0.05298	0.0062	2.0803	0.05694	0.19329	0.00319	0.602962	99	1148.3	54.8	1139.2	17.25	1142.3	18.77	1043.5	119.01	**1148.3**
74318_59	0.15733	0.00714	0.0828	0.01437	6.29646	0.27081	0.2902	0.00661	0.529585	68	2427.2	74.96	1642.5	33.02	2018	37.69	1608	268.19	**2427.2**
74318_60	0.07468	0.00217	0.04758	0.00588	1.78745	0.05047	0.17359	0.00291	0.593703	97	1059.9	57.47	1031.8	15.96	1040.9	18.39	939.6	113.44	**1059.9**
74318_61	0.06638	0.00317	0.01207	0.00158	0.36684	0.01656	0.04008	0.0009	0.497429	125	818.5	96.81	253.3	5.56	317.3	12.3	242.5	31.62	**253.3**

74318_62	0.04808	0.002	0.00539	0.00065	0.13122	0.00524	0.0198	0.00038	0.480604	99	103	95.47	126.4	2.4	125.2	4.71	108.6	13.08	**126.4**
74318_63	0.05487	0.00209	0.02311	0.00282	0.63466	0.02319	0.08389	0.00157	0.512189	96	406.8	82.44	519.3	9.37	499	14.4	461.9	55.73	**519.3**
74318_64	0.04744	0.00297	0.00912	0.00127	0.21976	0.01321	0.0336	0.0008	0.396092	95	70.8	143.3	213	5	201.7	10.99	183.5	25.34	**213**
74318_65	0.05477	0.00326	0.01156	0.00198	0.35874	0.02005	0.0475	0.00124	0.467082	104	403	127.68	299.1	7.66	311.3	14.99	232.3	39.51	**299.1**
74318_66	0.14255	0.00536	0.05644	0.0083	3.82301	0.13629	0.19448	0.00382	0.550972	51	2258.5	63.49	1145.6	20.62	1597.6	28.69	1109.8	158.88	**2258.5**
74318_67	0.05855	0.00271	0.03544	0.00731	0.67451	0.02966	0.08353	0.00186	0.506393	101	550.4	98.12	517.2	11.05	523.4	17.99	704	142.71	**517.2**
74318_68	0.07984	0.00481	0.03022	0.00708	1.81261	0.10191	0.16457	0.00448	0.484189	107	1193	114.35	982.1	24.81	1050	36.79	601.8	138.88	**982.1**
74318_70	0.05985	0.00707	0.02326	0.01023	0.67246	0.07364	0.08149	0.00397	0.444876	103	598.2	237.12	505	23.69	522.2	44.71	464.7	202.09	**505**
74318_71	0.0694	0.00403	0.00875	0.00178	0.25798	0.01408	0.02695	0.0007	0.475908	136	910.7	115.15	171.5	4.38	233	11.36	176.1	35.73	**171.5**
74318_72	0.17222	0.00747	0.10247	0.0186	7.50304	0.30812	0.31593	0.00671	0.517189	69	2579.4	70.72	1769.8	32.89	2173.4	36.79	1971.8	341.02	**2579.4**
74318_73	0.05986	0.00589	0.0054	0.00116	0.12938	0.01214	0.01567	0.00053	0.360459	123	598.6	199.93	100.2	3.38	123.5	10.91	108.9	23.31	**100.2**
74318_74	0.05985	0.00497	0.01266	0.00361	0.30385	0.02356	0.03681	0.00128	0.448465	116	598	170.31	233	7.93	269.4	18.35	254.2	72	**233**
74318_75	0.12386	0.00578	0.06806	0.01293	4.71517	0.20714	0.27607	0.00605	0.49885	78	2012.6	80.49	1571.6	30.54	1769.9	36.8	1330.8	244.6	**2012.6**
74318_76	0.05724	0.00371	0.00721	0.00142	0.19141	0.01169	0.02425	0.00064	0.432134	115	500.3	137.04	154.5	4.02	177.8	9.96	145.3	28.45	**154.5**
74318_77	0.06552	0.00337	0.03382	0.00623	1.14951	0.05563	0.12726	0.00297	0.482246	101	791	104.33	772.2	16.99	777	26.28	672.3	121.77	**772.2**
74318_78	0.10733	0.00643	0.01425	0.00283	0.46209	0.02553	0.03122	0.00086	0.498587	195	1754.6	105.75	198.2	5.39	385.7	17.73	286.1	56.39	**198.2**
74318_79	0.0656	0.00435	0.03038	0.00793	0.92862	0.05767	0.10264	0.00296	0.464369	106	793.7	133.37	629.9	17.3	666.9	30.36	605	155.47	**629.9**
74318_80	0.05293	0.00326	0.01189	0.00242	0.30561	0.01759	0.04188	0.00109	0.452191	102	325.6	133.32	264.5	6.74	270.8	13.68	238.8	48.33	**264.5**
74319_01	0.0513	0.00274	0.00581	0.00032	0.14228	0.0074	0.02012	0.00036	0.344022	105	254.3	118.08	128.4	2.29	135.1	6.58	117.1	6.34	**128.4**
74319_02	0.05983	0.00146	0.02651	0.00146	0.76767	0.01859	0.09307	0.00129	0.572368	101	597.3	51.83	573.7	7.62	578.4	10.68	528.9	28.79	**573.7**
74319_03	0.05743	0.00313	0.00595	0.00037	0.15832	0.00838	0.02	0.00038	0.358959	117	507.6	116.05	127.6	2.41	149.2	7.35	120	7.47	**127.6**
74319_04	0.04944	0.00525	0.0076	0.00071	0.16243	0.01677	0.02383	0.00068	0.276387	101	168.6	231.47	151.8	4.27	152.8	14.64	153	14.23	**151.8**
74319_05	0.05386	0.00195	0.00619	0.00037	0.14732	0.00521	0.01984	0.00031	0.441819	110	365	79.32	126.6	1.95	139.5	4.61	124.7	7.41	**126.6**
74319_06	0.0622	0.00155	0.02805	0.00171	0.84086	0.02072	0.09804	0.00137	0.567089	103	681	52.24	602.9	8.02	619.6	11.43	559.2	33.55	**602.9**
74319_07	0.05652	0.00122	0.02531	0.00162	0.66421	0.01451	0.08524	0.00114	0.612209	98	472	47.75	527.3	6.8	517.2	8.85	505.2	31.95	**527.3**
74319_08	0.05118	0.00218	0.00626	0.00044	0.14457	0.00603	0.02049	0.00034	0.39783	105	248.8	95.34	130.7	2.12	137.1	5.35	126.1	8.88	**130.7**
74319_09	0.05476	0.0033	0.00553	0.00063	0.12746	0.00733	0.01688	0.00037	0.381153	113	402.6	129.01	107.9	2.32	121.8	6.6	111.5	12.65	**107.9**
74319_10	0.06032	0.00155	0.02921	0.00209	0.78171	0.01995	0.09398	0.00134	0.558692	101	615.2	54.53	579	7.91	586.5	11.37	581.9	41.09	**579**
74319_11	0.04855	0.00475	0.00568	0.00064	0.12045	0.01143	0.01799	0.00048	0.281171	100	126.4	215.3	115	3.06	115.5	10.36	114.4	12.84	**115**
74319_12	0.05297	0.00137	0.01714	0.00135	0.39028	0.01	0.05343	0.00075	0.547838	100	327.6	57.66	335.6	4.57	334.6	7.3	343.5	26.74	**335.6**
74319_13	0.0766	0.00247	0.05679	0.00647	1.97111	0.06217	0.18662	0.00303	0.379584	99	1110.8	63.19	1103.1	16.46	1105.7	21.25	1116.4	123.73	**1110.8**
74319_14	0.05552	0.00423	0.00701	0.0013	0.19031	0.01391	0.02487	0.00069	0.416448	112	432.9	161.35	158.4	4.33	176.9	11.87	141.2	26.18	**158.4**
74319_15	0.05212	0.00233	0.01638	0.00199	0.35844	0.01553	0.04988	0.0009	0.493743	99	290.7	98.82	313.8	5.53	311.1	11.61	328.4	39.52	**313.8**

74319_16	0.05887	0.00192	0.0284	0.00347	0.71645	0.02285	0.08827	0.00139	0.420294	101	562.3	69.4	545.3	8.24	548.6	13.52	566	68.17	**545.3**
74319_17	0.05962	0.00323	0.05327	0.01151	0.73854	0.03871	0.08988	0.00198	0.448838	101	589.8	113.51	554.8	11.7	561.6	22.61	1049.1	220.84	**554.8**
74319_18	0.06197	0.00269	0.02705	0.00395	0.79341	0.0335	0.09287	0.00176	0.466721	104	672.9	90.38	572.5	10.38	593.1	18.96	539.4	77.68	**572.5**
74319_19	0.14898	0.00542	0.08057	0.01294	6.00537	0.21168	0.29238	0.00481	0.393187	71	2334.2	61.04	1653.4	24.01	1976.6	30.68	1566.2	242.12	**2334.2**
74319_20	0.06014	0.00314	0.02686	0.00369	0.75088	0.03795	0.09058	0.0018	0.482028	102	608.8	109.06	558.9	10.66	568.7	22.01	535.8	72.58	**558.9**
74319_21	0.08093	0.00284	0.05964	0.00872	2.19543	0.07498	0.19681	0.00324	0.491476	95	1219.8	67.45	1158.1	17.44	1179.6	23.82	1170.8	166.34	**1219.8**
74319_22	0.06824	0.00237	0.04462	0.00659	1.41542	0.04805	0.15044	0.00251	0.503585	99	875.8	70.28	903.4	14.08	895.4	20.2	882.4	127.57	**903.4**
74319_23	0.07273	0.00238	0.04942	0.00692	1.61363	0.05156	0.16096	0.00259	0.473022	101	1006.4	64.93	962.1	14.36	975.5	20.03	975.1	133.21	**962.1**
74319_24	0.10125	0.00466	0.07972	0.01313	3.83896	0.16994	0.27508	0.00576	0.481401	95	1647.1	83.04	1566.5	29.11	1601	35.66	1550.4	245.73	**1647.1**
74319_25	0.05002	0.00167	0.01135	0.00058	0.24871	0.00836	0.03607	0.00061	0.503119	99	195.9	75.95	228.4	3.8	225.5	6.8	228.1	11.61	**228.4**
74319_26	0.0644	0.00107	0.04195	0.00193	0.99955	0.01839	0.11261	0.00159	0.767437	102	754.7	34.7	687.9	9.23	703.6	9.34	830.6	37.49	**687.9**
74319_27	0.0598	0.0012	0.02669	0.0011	0.77735	0.0166	0.09431	0.00139	0.690185	101	596.4	42.75	581	8.18	584	9.49	532.5	21.64	**581**
74319_28	0.1186	0.00172	0.09118	0.00402	5.60156	0.09403	0.34267	0.00481	0.836203	98	1935.2	25.73	1899.5	23.08	1916.3	14.46	1763.7	74.41	**1935.2**
74319_29	0.05282	0.0011	0.01288	0.00064	0.31997	0.00705	0.04394	0.00064	0.661059	102	321.2	46.42	277.2	3.98	281.9	5.42	258.6	12.72	**277.2**
74319_30	0.05497	0.00164	0.01298	0.00068	0.35287	0.01066	0.04657	0.00076	0.540213	105	410.8	64.7	293.4	4.7	306.9	8	260.7	13.67	**293.4**
74319_31	0.16475	0.00733	0.06049	0.00579	1.70601	0.07005	0.07514	0.00183	0.593135	216	2505	72.97	467	10.97	1010.8	26.29	1187	110.32	**467**
74319_32	0.05108	0.00159	0.00885	0.00068	0.25147	0.00798	0.03572	0.00062	0.54697	101	244.2	70.11	226.2	3.85	227.8	6.47	178	13.53	**226.2**
74319_33	0.06016	0.00287	0.01482	0.00112	0.40109	0.01863	0.04836	0.00097	0.431832	112	609.4	100	304.4	5.95	342.4	13.5	297.4	22.33	**304.4**
74319_34	0.05935	0.0029	0.00694	0.00052	0.19351	0.00921	0.02365	0.0005	0.444204	119	580.1	102.76	150.7	3.17	179.6	7.84	139.9	10.48	**150.7**
74319_35	0.04942	0.00225	0.00721	0.00044	0.17296	0.00781	0.02539	0.00046	0.401227	100	168	102.9	161.6	2.87	162	6.76	145.2	8.82	**161.6**
74319_36	0.08945	0.00219	0.05338	0.00414	2.74785	0.07095	0.22284	0.0037	0.643057	92	1413.7	46.05	1296.8	19.5	1341.5	19.22	1051	79.49	**1413.7**
74319_37	0.05223	0.00164	0.00816	0.00071	0.22348	0.00721	0.03103	0.00054	0.539406	104	295.7	70.16	197	3.39	204.8	5.98	164.2	14.17	**197**
74319_38	0.06699	0.00361	0.00564	0.00087	0.16128	0.00835	0.01746	0.00039	0.431434	136	837.3	108.37	111.6	2.46	151.8	7.3	113.6	17.39	**111.6**
74319_39	0.04946	0.00278	0.00504	0.00068	0.13262	0.00726	0.01945	0.00044	0.413243	102	169.9	126.03	124.2	2.75	126.5	6.51	101.6	13.66	**124.2**
74319_40	0.20382	0.00481	0.14225	0.01352	15.68809	0.38686	0.55833	0.00885	0.642789	100	2857	37.92	2859.7	36.6	2858	23.54	2688.1	239.25	**2857**
74319_41	0.04859	0.00345	0.00539	0.00087	0.11261	0.00779	0.01681	0.00042	0.361178	101	128.1	159.2	107.5	2.65	108.4	7.11	108.6	17.57	**107.5**
74319_42	0.07961	0.00226	0.05264	0.00508	2.14913	0.06204	0.19582	0.00329	0.582009	97	1187.4	55.15	1152.8	17.71	1164.8	20	1036.9	97.5	**1187.4**
74319_43	0.05898	0.00395	0.00568	0.00087	0.14141	0.00914	0.01739	0.00044	0.39146	121	566.4	139.44	111.1	2.82	134.3	8.13	114.4	17.56	**111.1**
74319_44	0.06873	0.00454	0.01137	0.00186	0.36181	0.023	0.03819	0.00101	0.41603	130	890.6	130.84	241.6	6.27	313.6	17.15	228.4	37.14	**241.6**
74319_45	0.06563	0.00245	0.03745	0.00551	1.17971	0.04376	0.1304	0.00247	0.510643	100	794.6	76.34	790.1	14.11	791.2	20.39	743.2	107.34	**790.1**
74319_46	0.06124	0.00658	0.00474	0.00081	0.14676	0.01526	0.01738	0.00058	0.320946	125	647.8	215.46	111.1	3.66	139	13.51	95.6	16.24	**111.1**
74319_47	0.05086	0.00324	0.0051	0.0007	0.12211	0.00757	0.01741	0.0004	0.37061	105	234.6	140.38	111.3	2.56	117	6.85	102.9	14.14	**111.3**
74319_48	0.05309	0.00186	0.01341	0.00159	0.32762	0.01146	0.04476	0.00078	0.498185	102	332.8	77.58	282.3	4.8	287.7	8.76	269.3	31.71	**282.3**

74319_49	0.05354	0.00292	0.0114	0.0017	0.28596	0.01519	0.03875	0.00082	0.398373	104	351.6	117.99	245.1	5.08	255.4	11.99	229.1	33.89	**245.1**
74319_50	0.05111	0.0034	0.00524	0.00079	0.11081	0.00718	0.01573	0.00037	0.363017	106	245.6	146.32	100.6	2.35	106.7	6.56	105.6	15.83	**100.6**
74319_51	0.05685	0.00195	0.02287	0.00278	0.57576	0.01974	0.07347	0.00129	0.512123	101	484.9	74.74	457	7.78	461.7	12.72	457	54.92	**457**
74319_52	0.28376	0.01652	0.06871	0.01704	11.35074	0.64137	0.29015	0.00703	0.01704	49	3383.7	87.95	1642.3	35.13	2552.4	52.73	1343.2	322.23	**3383.7**
74319_53	0.08169	0.0036	0.05911	0.01044	2.15084	0.09265	0.19098	0.00389	0.01044	91	1238.1	84	1126.7	21.07	1165.3	29.86	1160.8	199.14	**1238.1**
74319_54	0.06475	0.00273	0.03351	0.00587	0.97519	0.04037	0.10924	0.00214	0.00587	103	766.3	86.48	668.3	12.44	691.1	20.75	666.2	114.79	**668.3**
74319_55	0.05952	0.00249	0.02986	0.0053	0.81329	0.03337	0.09912	0.00193	0.0053	99	586	88.19	609.2	11.3	604.3	18.69	594.7	104.03	**609.2**
74319_56	0.04865	0.00354	0.00557	0.00109	0.11559	0.00813	0.01723	0.00044	0.00109	101	131.1	162.51	110.1	2.77	111.1	7.4	112.2	21.94	**110.1**
74319_57	0.17444	0.00727	0.0833	0.01509	6.94145	0.28343	0.28864	0.00565	0.01509	63	2600.7	67.84	1634.7	28.28	2104	36.24	1617.2	281.48	**2600.7**
74319_58	0.08368	0.00529	0.05671	0.01369	2.26867	0.13811	0.19664	0.00513	0.01369	90	1285	118.51	1157.3	27.63	1202.6	42.9	1114.9	261.83	**1285**
74319_59	0.05841	0.00277	0.02935	0.00551	0.78967	0.03647	0.09807	0.00203	0.00551	98	545.2	100.41	603.1	11.93	591	20.69	584.7	108.19	**603.1**
74319_60	0.0506	0.00237	0.01261	0.00231	0.29666	0.01353	0.04252	0.00087	0.00231	98	222.7	104.64	268.5	5.38	263.8	10.59	253.2	46.05	**268.5**
74319_61	0.03973	0.00363	0.00488	0.00096	0.0932	0.00831	0.01702	0.00046	0.00096	83	0.1	0	108.8	2.93	90.5	7.71	98.5	19.35	**108.8**
74319_62	0.08839	0.00433	0.01107	0.00215	0.36216	0.01717	0.02972	0.00064	0.00215	166	1391.1	91.1	188.8	3.98	313.8	12.8	222.5	42.91	**188.8**
74319_63	0.06131	0.00303	0.02831	0.00531	0.82536	0.03956	0.09764	0.00208	0.00531	102	650.2	102.59	600.6	12.2	611	22.01	564.2	104.3	**600.6**
74319_64	0.07448	0.00334	0.04937	0.00916	1.83767	0.08031	0.17898	0.00361	0.00916	101	1054.1	88.09	1061.4	19.74	1059	28.74	974	176.38	**1054.1**
74319_65	0.05387	0.00339	0.01091	0.00238	0.26586	0.01626	0.0358	0.00085	0.388211	106	365.3	135.47	226.8	5.31	239.4	13.04	219.3	47.56	**226.8**
74319_66	0.10083	0.00651	0.07804	0.02122	3.74695	0.23375	0.2696	0.00704	0.418581	94	1639.5	115.25	1538.8	35.74	1581.5	50	1518.8	397.8	**1639.5**
74319_67	0.10674	0.01184	0.01039	0.00374	0.38665	0.04029	0.02627	0.00116	0.423759	199	1744.4	190.43	167.2	7.27	331.9	29.5	208.9	74.77	**167.2**
74319_68	0.04978	0.00422	0.00506	0.00114	0.1157	0.00957	0.01686	0.00045	0.322683	103	184.6	186.3	107.8	2.83	111.2	8.71	102	22.86	**107.8**
74319_69	0.07686	0.00431	0.05667	0.01175	2.07179	0.11262	0.19553	0.00459	0.431847	103	1117.7	107.99	1151.3	24.76	1139.5	37.23	1114.2	224.83	**1117.7**
74319_70	0.08607	0.00435	0.06244	0.01396	2.14932	0.10557	0.18116	0.00395	0.44391	80	1339.7	94.59	1073.3	21.57	1164.8	34.04	1224.3	265.54	**1339.7**
74319_71	0.05389	0.00715	0.00374	0.0011	0.12329	0.01569	0.0166	0.00071	0.33609	111	366.5	274.41	106.1	4.51	118	14.18	75.5	22.18	**106.1**
74319_72	0.05849	0.00331	0.01402	0.00322	0.36686	0.02007	0.0455	0.00104	0.417806	111	548.2	118.86	286.8	6.44	317.3	14.91	281.4	64.15	**286.8**
74319_73	0.05009	0.00378	0.00555	0.00155	0.13077	0.00949	0.01894	0.00053	0.385601	103	199.3	166.19	120.9	3.35	124.8	8.52	111.9	31.16	**120.9**
74319_74	0.05163	0.00536	0.00526	0.00135	0.11402	0.01149	0.01602	0.0005	0.309719	107	269.2	221.66	102.4	3.17	109.6	10.48	106	27.06	**102.4**
74319_75	0.0687	0.00372	0.04082	0.00956	1.21157	0.06335	0.12793	0.00289	0.432043	104	889.7	107.94	776.1	16.51	805.9	29.08	808.6	185.75	**776.1**
74319_76	0.09317	0.00831	0.00945	0.00272	0.33031	0.02801	0.02572	0.00087	0.398893	177	1491.3	160.11	163.7	5.47	289.8	21.38	190.2	54.55	**163.7**
74319_77	0.09259	0.0055	0.07787	0.02037	3.21651	0.18373	0.252	0.00608	0.422384	98	1479.4	108.73	1448.8	31.29	1461.1	44.25	1515.7	381.96	**1479.4**
74319_78	0.05073	0.00336	0.0142	0.00386	0.31432	0.01998	0.04494	0.00113	0.395569	98	228.8	145.89	283.4	6.99	277.5	15.44	284.9	76.89	**283.4**
74319_79	0.08655	0.01326	0.00475	0.00222	0.16703	0.02409	0.014	0.00078	0.3863	175	1350.5	270.12	89.6	4.99	156.8	20.96	95.8	44.75	**89.6**
74319_80	0.05967	0.00352	0.02758	0.00686	0.72117	0.04091	0.08767	0.00207	0.416224	102	591.6	123.05	541.8	12.28	551.4	24.13	549.9	134.98	**541.8**
74320_01	0.05702	0.00107	0.02036	0.00068	0.62934	0.01194	0.08006	0.00098	0.645196	100	491.8	40.86	496.5	5.88	495.7	7.44	407.3	13.38	**496.5**

74320_02	0.24574	0.00387	0.12024	0.00401	4.08477	0.06357	0.12058	0.00158	0.841971	23	3157.5	24.76	733.9	9.11	1651.3	12.69	2294.9	72.44	**733.9**
74320_03	0.07621	0.00398	0.00472	0.00021	0.16765	0.00858	0.01596	0.00026	0.318315	65	1100.5	101.13	102.1	1.67	157.4	7.46	95.2	4.23	**102.1**
74320_04	0.14063	0.00192	0.05597	0.002	2.22586	0.03182	0.11481	0.00139	0.846901	59	2235	23.48	700.6	8.02	1189.2	10.02	1100.8	38.25	**700.6**
74320_05	0.50418	0.00643	0.13279	0.00492	5.60762	0.07567	0.08068	0.00097	0.890965	26	4253.5	18.65	500.2	5.76	1917.3	11.63	2520.2	87.73	**500.2**
74320_07	0.10712	0.00172	0.05728	0.00238	1.79691	0.02951	0.12168	0.00152	0.760644	71	1751	29.06	740.2	8.72	1044.3	10.71	1125.9	45.51	**740.2**
74320_08	0.16567	0.00258	0.05283	0.00228	2.04829	0.03254	0.08968	0.00113	0.793153	49	2514.4	25.97	553.6	6.67	1131.7	10.84	1040.6	43.8	**553.6**
74320_09	0.05652	0.00162	0.00766	0.00035	0.22632	0.00646	0.02905	0.00039	0.470337	89	472.1	62.46	184.6	2.42	207.2	5.35	154.2	7.1	**184.6**
74320_10	0.06699	0.0012	0.02303	0.00109	0.795	0.01454	0.08608	0.00108	0.686	90	837.6	36.98	532.3	6.4	594	8.23	460.2	21.56	**532.3**
74320_12	0.05579	0.00234	0.01074	0.0006	0.31011	0.01284	0.04032	0.00059	0.353413	93	443.8	90.39	254.8	3.68	274.3	9.95	216	11.93	**254.8**
74320_13	0.13594	0.00421	0.06305	0.0067	6.87592	0.20742	0.36687	0.0058	0.524078	96	2176.1	52.9	2014.7	27.33	2095.6	26.74	1235.8	127.47	**2176.1**
74320_14	0.06058	0.00354	0.02419	0.00313	0.72897	0.04174	0.08727	0.00155	0.310187	97	624.5	121.07	539.4	9.16	556	24.51	483.1	61.87	**539.4**
74320_15	0.06473	0.00272	0.02178	0.00293	0.81756	0.03319	0.09163	0.00171	0.459696	93	765.5	86.11	565.1	10.1	606.7	18.54	435.4	57.91	**565.1**
74320_16	0.06759	0.00281	0.01797	0.0021	0.91474	0.03689	0.09819	0.0018	0.454563	92	855.9	84.08	603.8	10.56	659.6	19.56	360	41.7	**603.8**
74320_17	0.06269	0.00261	0.02199	0.00277	0.94406	0.03829	0.10925	0.00206	0.4649	99	697.7	86.44	668.4	11.96	675	20	439.7	54.86	**668.4**
74320_18	0.13252	0.00889	0.01452	0.00235	0.79824	0.05073	0.04369	0.00126	0.453792	46	2131.7	112.85	275.6	7.79	595.8	28.65	291.3	46.72	**275.6**
74320_19	0.12609	0.0079	0.01676	0.00237	0.77202	0.04593	0.04442	0.00119	0.450299	48	2044.2	106.78	280.2	7.32	580.9	26.32	336	47.07	**280.2**
74320_20	0.11764	0.01185	0.00638	0.00089	0.27128	0.02652	0.01673	0.00047	0.287373	44	1920.7	170.4	106.9	3	243.7	21.18	128.5	17.88	**106.9**
74320_22	0.0607	0.00316	0.0208	0.00329	0.77806	0.03946	0.093	0.00192	0.407075	98	628.6	108.39	573.2	11.33	584.4	22.54	416.2	65.14	**573.2**
74320_23	0.05362	0.00225	0.01008	0.00131	0.31397	0.01295	0.04247	0.00069	0.393899	97	355.1	91.81	268.2	4.26	277.3	10.01	202.7	26.22	**268.2**
74320_24	0.07442	0.00628	0.00461	0.00063	0.1701	0.01411	0.01658	0.00036	0.261755	66	1053	161.35	106	2.26	159.5	12.24	92.9	12.58	**106**
74320_25	0.06466	0.00312	0.01934	0.00323	0.67347	0.03167	0.07554	0.00141	0.396929	90	763.3	98.68	469.5	8.46	522.8	19.22	387.1	63.96	**469.5**
74320_26	0.06228	0.0039	0.0082	0.00134	0.2807	0.01718	0.03269	0.00064	0.319878	83	683.6	128.25	207.4	4	251.2	13.62	165	26.82	**207.4**
74320_27	0.09019	0.00426	0.04971	0.00873	2.31236	0.10608	0.18596	0.00367	0.430198	90	1429.5	87.71	1099.5	19.94	1216.1	32.52	980.6	168.05	**1429.5**
74320_28	0.06261	0.00416	0.00519	0.00083	0.20035	0.01301	0.02321	0.00048	0.318477	80	694.9	135.71	147.9	3.01	185.4	11.01	104.7	16.6	**147.9**
74320_29	0.06448	0.00473	0.01188	0.00242	0.50365	0.0352	0.05667	0.00157	0.396399	86	757.3	147.46	355.3	9.57	414.2	23.77	238.6	48.4	**355.3**
74320_30	0.1927	0.01287	0.00965	0.00165	0.73258	0.04569	0.02758	0.00079	0.459269	31	2765.3	105.58	175.4	4.94	558.1	26.78	194.2	33.11	**175.4**
74320_31	0.06644	0.005	0.01057	0.00231	0.34621	0.02491	0.0378	0.00105	0.386068	79	820.1	149.77	239.2	6.49	301.9	18.79	212.5	46.27	**239.2**
74320_32	0.09437	0.0049	0.02109	0.0035	0.61809	0.03085	0.0475	0.00099	0.417579	61	1515.6	94.88	299.2	6.12	488.7	19.36	421.9	69.28	**299.2**
74320_33	0.05251	0.00262	0.00878	0.00143	0.34951	0.01681	0.04828	0.00096	0.413424	100	307.5	109.58	304	5.92	304.4	12.65	176.6	28.7	**304**
74320_34	0.05809	0.00532	0.0111	0.00283	0.55148	0.04795	0.06885	0.00225	0.375854	96	532.5	189.39	429.2	13.57	446	31.38	223.2	56.49	**429.2**
74320_35	0.07996	0.00558	0.02379	0.00447	2.0628	0.13665	0.18702	0.00494	0.398737	97	1196.1	131.62	1105.2	26.82	1136.5	45.3	475.3	88.2	**1196.1**
74320_36	0.05002	0.00511	0.00401	0.00104	0.11787	0.01165	0.01709	0.00052	0.30785	97	195.8	221.36	109.3	3.32	113.1	10.58	80.9	21.01	**109.3**
74320_37	0.06044	0.00276	0.02488	0.00482	0.80457	0.03563	0.09658	0.00178	0.41618	99	619.4	95.61	594.3	10.48	599.4	20.05	496.7	95.01	**594.3**

74320_38	0.05977	0.004	0.00935	0.00205	0.39249	0.02538	0.04766	0.00121	0.392616	89	594.8	139.12	300.1	7.45	336.2	18.5	188.1	41	**300.1**
74320_39	0.08124	0.00452	0.03352	0.00677	1.78833	0.09633	0.15976	0.00352	0.409035	92	1227.3	105.44	955.4	19.58	1041.2	35.08	666.4	132.39	**955.4**
74320_40	0.05906	0.00272	0.01859	0.00355	0.67179	0.02999	0.08252	0.00153	0.415326	98	569.4	97.15	511.1	9.13	521.8	18.21	372.4	70.38	**511.1**
74320_41	0.10755	0.00716	0.04048	0.00849	2.82982	0.18133	0.19091	0.00495	0.404637	83	1758.3	117.06	1126.3	26.8	1363.5	48.08	802	164.88	**1126.3**
74320_42	0.39109	0.02003	0.02391	0.00448	1.39377	0.06681	0.02585	0.00061	0.492288	19	3875.2	75.08	164.5	3.81	886.3	28.34	477.6	88.51	**164.5**
74320_43	0.11314	0.00641	0.05047	0.01076	2.95543	0.16118	0.18954	0.00427	0.413082	80	1850.4	99.14	1118.9	23.13	1396.2	41.38	995.2	207	**1118.9**
74320_44	0.06605	0.00537	0.01613	0.0038	1.02934	0.07983	0.11305	0.0034	0.387794	96	807.9	161.38	690.4	19.69	718.6	39.94	323.4	75.52	**690.4**
74320_45	0.06703	0.00585	0.00456	0.00103	0.15567	0.01311	0.01685	0.00048	0.338254	73	838.6	172.05	107.7	3.07	146.9	11.52	91.9	20.8	**107.7**
74320_46	0.06193	0.00459	0.00449	0.00104	0.16404	0.01169	0.01922	0.0005	0.36505	80	671.8	150.99	122.7	3.15	154.2	10.2	90.5	20.84	**122.7**
74320_47	0.12777	0.01637	0.04255	0.01196	1.76536	0.21702	0.10026	0.0041	0.332652	60	2067.5	209.97	615.9	24.01	1032.8	79.68	842.2	231.88	**615.9**
74320_48	0.08523	0.00652	0.00728	0.00176	0.2916	0.02131	0.02483	0.00069	0.380256	61	1320.6	141.35	158.1	4.34	259.8	16.75	146.5	35.35	**158.1**
74320_49	0.07067	0.00491	0.04188	0.01206	1.66396	0.11053	0.17082	0.00444	0.391297	102	947.9	136.19	1016.6	24.42	994.9	42.13	829.3	233.95	**947.9**
74320_50	0.08695	0.00481	0.06111	0.0137	2.26473	0.12047	0.18896	0.00406	0.403918	93	1359.5	102.99	1115.7	21.99	1201.4	37.47	1198.9	260.92	**1359.5**
74320_51	0.06548	0.00452	0.0502	0.01592	0.85525	0.05679	0.09474	0.00228	0.362429	93	789.9	138.54	583.5	13.41	627.5	31.08	990.1	306.38	**583.5**
74320_52	0.07502	0.00565	0.0453	0.01442	1.72962	0.12377	0.16723	0.00463	0.386903	98	1069.2	144.39	996.9	25.59	1019.6	46.04	895.4	278.75	**996.9**
74320_53	0.10035	0.01078	0.06928	0.03371	2.82591	0.28943	0.20429	0.00777	0.371355	88	1630.5	187.44	1198.3	41.59	1362.4	76.81	1353.9	637.15	**1630.5**
74320_54	0.04952	0.00144	0.00315	0.0001	0.19263	0.00572	0.02821	0.00052	0.620766	100	172.6	66.47	179.4	3.24	178.9	4.87	63.5	2.05	**179.4**
74320_55	0.07121	0.00133	0.01764	0.0005	0.73897	0.0154	0.07527	0.00122	0.777757	83	963.3	37.78	467.8	7.33	561.8	8.99	353.4	9.85	**467.8**
74320_56	0.07869	0.00111	0.04331	0.00103	2.06539	0.03498	0.19036	0.00284	0.880897	96	1164.4	27.79	1123.3	15.37	1137.4	11.59	856.9	19.97	**1164.4**
74320_57	0.09036	0.00266	0.005	0.00016	0.25193	0.0074	0.02022	0.00038	0.639809	57	1432.9	55.31	129.1	2.42	228.1	6	100.8	3.19	**129.1**
74320_58	0.05296	0.00124	0.00995	0.00031	0.31288	0.00777	0.04284	0.0007	0.657969	98	327.2	52.2	270.4	4.35	276.4	6.01	200	6.13	**270.4**
74320_59	0.05762	0.0026	0.00504	0.00036	0.12683	0.00559	0.01596	0.00035	0.49756	84	515	96.37	102.1	2.22	121.2	5.03	101.6	7.18	**102.1**
74320_60	0.05166	0.00114	0.01039	0.00033	0.31296	0.00737	0.04394	0.0007	0.676487	100	270.3	49.69	277.2	4.32	276.5	5.7	209	6.57	**277.2**
74320_61	0.04759	0.00132	0.00351	0.00012	0.10427	0.00299	0.01589	0.00027	0.592554	101	78.3	65.33	101.6	1.71	100.7	2.74	70.9	2.39	**101.6**
74320_62	0.0601	0.00179	0.01528	0.00083	0.38422	0.01152	0.04638	0.00078	0.560908	89	607.3	63.07	292.2	4.8	330.1	8.45	306.4	16.62	**292.2**
74320_63	0.07977	0.00103	0.04751	0.00144	2.13524	0.03531	0.19415	0.00294	0.915712	96	1191.3	25.26	1143.8	15.88	1160.3	11.43	938.2	27.74	**1191.3**
74320_64	0.06651	0.00107	0.02868	0.00085	1.2761	0.02403	0.13917	0.00217	0.828028	101	822.4	33.28	840	12.3	835.1	10.72	571.6	16.77	**840**
74320_65	0.06465	0.00087	0.03518	0.00112	0.82394	0.01398	0.09244	0.00142	0.905351	93	763	28.13	570	8.36	610.2	7.78	698.8	21.87	**570**
74320_67	0.10359	0.00261	0.06255	0.00465	4.15625	0.10975	0.29101	0.00508	0.661078	97	1689.4	45.76	1646.6	25.39	1665.4	21.61	1226.2	88.52	**1689.4**
74320_68	0.07384	0.00247	0.02577	0.0023	1.64787	0.05542	0.16188	0.00317	0.582267	98	1037.1	66.11	967.2	17.58	988.7	21.25	514.3	45.26	**1037.1**
74320_69	0.14019	0.00397	0.05218	0.00443	6.90949	0.202	0.35749	0.00653	0.624804	88	2229.5	48.24	1970.3	31	2099.9	25.93	1028.1	85.02	**2229.5**
74320_70	0.13795	0.01325	0.0263	0.00511	6.72413	0.6078	0.3542	0.01522	0.475381	89	2201.7	157.87	1954.6	72.46	2075.8	79.9	524.7	100.64	**2201.7**
74320_71	0.05293	0.00168	0.00821	0.00066	0.27526	0.00888	0.03772	0.00069	0.567032	97	325.6	70.56	238.7	4.28	246.9	7.07	165.3	13.15	**238.7**

74320_72	0.05753	0.00188	0.01791	0.00143	0.65155	0.02148	0.08214	0.00153	0.565002	100	511.5	70.44	508.9	9.09	509.4	13.21	358.8	28.41	**508.9**
74320_73	0.10598	0.00419	0.04295	0.00461	4.61961	0.18112	0.31617	0.00675	0.54453	102	1731.4	70.84	1771	33.07	1752.8	32.73	850	89.34	**1731.4**
74320_74	0.08804	0.00546	0.0219	0.00327	3.15273	0.18848	0.25983	0.0075	0.482829	108	1383.3	114.62	1489	38.36	1445.7	46.08	437.9	64.67	**1383.3**
74320_75	0.10947	0.0115	0.00287	0.00063	0.2043	0.02002	0.01355	0.0006	0.451873	46	1790.6	180.07	86.8	3.83	188.8	16.88	57.8	12.62	**1790.6**
74320_76	0.06017	0.00405	0.00596	0.00093	0.28028	0.0181	0.03378	0.00094	0.430905	85	609.8	139.04	214.2	5.89	250.9	14.35	120.1	18.75	**214.2**
74320_77	0.05127	0.00193	0.00384	0.00043	0.1258	0.0047	0.0178	0.00035	0.526297	95	252.8	84.43	113.7	2.2	120.3	4.24	77.5	8.74	**113.7**
74320_78	0.05669	0.00218	0.01515	0.00179	0.63961	0.02439	0.08185	0.00165	0.528651	101	478.6	83.55	507.1	9.83	502.1	15.1	303.9	35.73	**507.1**
74320_79	0.11942	0.01058	0.02033	0.00373	3.28122	0.27201	0.19942	0.0075	0.453673	60	1947.6	150.41	1172.2	40.33	1476.6	64.51	406.9	73.86	**1947.6**
74320_80	0.05326	0.00395	0.00707	0.00119	0.53761	0.03789	0.07322	0.00227	0.439885	104	340	159.12	455.5	13.61	436.8	25.02	142.5	23.96	**455.5**
74320_81	0.06149	0.0023	0.01775	0.00208	0.68164	0.02544	0.08041	0.00159	0.529816	94	656.3	78.37	498.6	9.5	527.8	15.36	355.6	41.31	**498.6**
74320_82	0.05166	0.00376	0.00461	0.00076	0.29991	0.02077	0.04212	0.00129	0.442238	100	270.3	158.61	266	7.96	266.3	16.22	92.9	15.28	**266**
74321_01	0.05858	0.00292	0.00472	0.00028	0.12188	0.00587	0.0151	0.00029	0.398763	121	552	105.28	96.6	1.83	116.8	5.31	95.3	5.56	**96.6**
74321_02	0.07774	0.00149	0.04064	0.00215	1.43324	0.02865	0.13381	0.00187	0.699113	112	1140	37.57	809.6	10.62	902.9	11.96	805.1	41.83	**809.6**
74321_03	0.05999	0.00172	0.02563	0.0013	0.72274	0.02045	0.08742	0.00131	0.529602	102	603	60.78	540.3	7.78	552.3	12.06	511.6	25.68	**540.3**
74321_04	0.15299	0.00239	0.09794	0.00476	7.78262	0.12923	0.36908	0.00476	0.776692	85	2380	26.34	2025.1	22.41	2206.2	14.94	1888.5	87.54	**2379.6**
74321_05	0.06777	0.00188	0.01885	0.00127	0.55757	0.01546	0.0597	0.00094	0.567863	120	862	56.64	373.8	5.69	449.9	10.08	377.5	25.19	**373.8**
74321_06	0.2485	0.00545	0.11906	0.00902	15.29997	0.34189	0.44679	0.00679	0.680096	75	3175	34.32	2381	30.26	2834.1	21.3	2273.6	162.86	**3175.2**
74321_07	0.0906	0.00331	0.05225	0.00434	2.38408	0.08508	0.1909	0.00368	0.540176	78	1438	68.14	1126.2	19.91	1237.8	25.53	1029.4	83.35	**1438.2**
74321_08	0.05348	0.00416	0.00497	0.00036	0.1249	0.00947	0.01694	0.00039	0.303643	110	349	166.85	108.3	2.46	119.5	8.55	100.2	7.16	**108.3**
74321_09	0.07126	0.0024	0.01776	0.00113	0.43516	0.01439	0.0443	0.00071	0.484666	131	965	67.4	279.4	4.36	366.8	10.18	355.8	22.52	**279.4**
74321_10	0.05484	0.00235	0.01157	0.00076	0.28845	0.01201	0.03815	0.00068	0.428097	107	406	92.66	241.4	4.22	257.3	9.46	232.5	15.2	**241.4**
74321_11	0.07184	0.00138	0.03155	0.00196	1.31335	0.02618	0.13261	0.00179	0.677154	106	981	38.67	802.7	10.19	851.6	11.49	627.9	38.34	**802.7**
74321_12	0.07766	0.00322	0.05076	0.00505	2.01109	0.08152	0.18786	0.00372	0.488513	98	1138	80.34	1109.8	20.17	1119.3	27.49	1000.8	97.12	**1138.1**
74321_13	0.06286	0.00208	0.02787	0.00321	0.83104	0.02699	0.09592	0.00158	0.507186	104	703	68.83	590.5	9.27	614.2	14.97	555.7	63.12	**590.5**
74321_14	0.05875	0.00197	0.02546	0.00286	0.68665	0.02256	0.08479	0.00137	0.491782	101	558	71.6	524.6	8.11	530.8	13.58	508.2	56.28	**524.6**
74321_15	0.11921	0.00322	0.09625	0.01072	5.77918	0.15463	0.35167	0.00517	0.549449	100	1944	47.59	1942.6	24.65	1943.3	23.16	1857.5	197.65	**1944.4**
74321_16	0.05305	0.00187	0.01177	0.00134	0.27818	0.00959	0.03804	0.00061	0.465154	104	331	78.1	240.7	3.82	249.2	7.62	236.5	26.77	**240.7**
74321_17	0.07302	0.00556	0.00802	0.00133	0.25954	0.01892	0.02579	0.00073	0.388289	143	1014	147.18	164.1	4.57	234.3	15.25	161.5	26.74	**164.1**
74321_18	0.0618	0.002	0.02804	0.0033	0.83227	0.02632	0.09769	0.00155	0.501718	102	667	67.65	600.9	9.1	614.9	14.59	559	64.82	**600.9**
74321_19	0.13372	0.00551	0.08816	0.01485	4.99188	0.19762	0.27077	0.00487	0.45432	72	2147	70.26	1544.7	24.72	1817.9	33.49	1707.8	275.84	**2147.4**
74321_20	0.06172	0.00316	0.02551	0.00309	0.74331	0.03682	0.08737	0.00173	0.399733	105	664	105.94	539.9	10.27	564.3	21.45	509.2	60.81	**539.9**
74321_21	0.07161	0.00316	0.02883	0.0039	0.83667	0.03566	0.08477	0.00162	0.448379	118	975	87.4	524.5	9.65	617.3	19.71	574.5	76.67	**524.5**
74321_22	0.05073	0.0019	0.01254	0.00175	0.30371	0.01102	0.04343	0.00072	0.456899	98	229	84.13	274	4.47	269.3	8.58	251.9	34.88	**274**

74321_23	0.05254	0.00208	0.00966	0.00132	0.22095	0.0085	0.03051	0.00052	0.443033	105	309	87.79	193.7	3.26	202.7	7.07	194.4	26.38	**193.7**
74321_24	0.0952	0.00297	0.07925	0.01023	3.65434	0.11188	0.27845	0.00438	0.513787	103	1532	57.58	1583.5	22.1	1561.5	24.41	1541.4	191.54	**1532.1**
74321_25	0.05527	0.00268	0.01358	0.00248	0.32502	0.01513	0.04265	0.00084	0.423089	106	423	104.69	269.3	5.2	285.8	11.59	272.7	49.47	**269.3**
74321_26	0.18762	0.01039	0.12348	0.02874	11.63598	0.6135	0.44983	0.00994	0.419108	88	2721	88.46	2394.5	44.18	2575.6	49.3	2353.4	517.04	**2721.4**
74321_27	0.17265	0.00765	0.08628	0.01604	7.39922	0.31441	0.31086	0.00593	0.448931	68	2584	72.13	1744.9	29.15	2160.9	38.01	1672.8	298.46	**2583.5**
74321_28	0.05264	0.00305	0.02151	0.00504	0.33189	0.01833	0.04574	0.00105	0.415647	101	313	126.32	288.3	6.47	291	13.98	430.2	99.71	**288.3**
74321_29	0.11227	0.00726	0.07176	0.0194	4.02208	0.24742	0.25994	0.00637	0.398366	81	1837	112.71	1489.6	32.59	1638.7	50.02	1400.7	365.86	**1836.5**
74321_30	0.05779	0.00337	0.02498	0.00569	0.71391	0.03983	0.08962	0.00201	0.401998	99	522	123.43	553.3	11.91	547.1	23.6	498.7	112.17	**553.3**
74321_31	0.09568	0.01001	0.07724	0.02956	3.54561	0.35164	0.26888	0.01062	0.398253	100	1542	184.79	1535.1	53.94	1537.5	78.55	1503.8	554.55	**1541.5**
74321_32	0.12385	0.00571	0.08486	0.01609	5.71988	0.25377	0.33499	0.00654	0.44004	93	2012	79.56	1862.5	31.58	1934.4	38.35	1646.4	299.74	**2012.4**
74321_33	0.05777	0.0036	0.02197	0.00471	0.61574	0.03686	0.07731	0.00181	0.391097	102	521	131.55	480	10.83	487.2	23.17	439.3	93.12	**480**
74321_34	0.05565	0.00374	0.02526	0.00629	0.69661	0.04495	0.09081	0.00225	0.38398	96	438	143.42	560.3	13.33	536.8	26.9	504.2	124.04	**560.3**
74321_35	0.07761	0.00387	0.05504	0.01128	2.10689	0.10115	0.19691	0.00405	0.428414	102	1137	96.08	1158.7	21.79	1151.1	33.06	1082.9	216.16	**1137**
74321_36	0.0707	0.00502	0.00544	0.00139	0.17837	0.0121	0.0183	0.0005	0.402768	143	949	138.9	116.9	3.15	166.7	10.42	109.7	27.95	**116.9**
74321_37	0.0615	0.0043	0.01473	0.00434	0.44227	0.02954	0.05217	0.00136	0.390297	113	657	143.17	327.8	8.31	371.8	20.8	295.6	86.49	**327.8**
74321_38	0.05812	0.00417	0.02533	0.00763	0.70644	0.04846	0.08817	0.00234	0.386889	100	534	150.37	544.7	13.87	542.6	28.84	505.6	150.4	**544.7**
74321_39	0.25233	0.01979	0.13087	0.04216	20.40977	1.52861	0.58673	0.01703	0.387541	93	3200	118.85	2976.1	69.17	3111	72.5	2485.8	753.6	**3199.5**
74321_40	0.06115	0.00523	0.025	0.00901	0.69385	0.05663	0.08231	0.00254	0.378094	105	645	173.95	509.9	15.15	535.1	33.94	499.1	177.71	**509.9**
74321_41	0.08224	0.00607	0.05409	0.01738	2.0839	0.14662	0.1838	0.00498	0.385095	87	1251	137.91	1087.7	27.09	1143.5	48.27	1064.7	333.2	**1251.2**
74321_42	0.07091	0.00526	0.04498	0.01459	1.50489	0.10635	0.15394	0.00418	0.384231	101	955	144.67	923	23.36	932.4	43.11	889.2	282.2	**923**
74321_43	0.0678	0.00558	0.0265	0.00864	0.87482	0.06856	0.0936	0.0028	0.381707	111	862	162.03	576.8	16.53	638.2	37.13	528.7	170.06	**576.8**
74321_44	0.05331	0.00995	0.01342	0.00938	0.31479	0.05587	0.04284	0.00268	0.352474	103	342	374.88	270.4	16.58	277.9	43.15	269.3	187.03	**270.4**
74321_45	0.05764	0.00603	0.00653	0.00257	0.16489	0.01642	0.02075	0.00072	0.348446	117	516	214.75	132.4	4.56	155	14.31	131.6	51.55	**132.4**
74321_46	0.07496	0.00603	0.04705	0.01657	1.67514	0.12792	0.16209	0.00469	0.378904	103	1068	153.74	968.4	26.03	999.1	48.56	929.3	319.78	**968.4**
74321_47	0.05282	0.0044	0.00812	0.00067	0.18561	0.01503	0.02551	0.00064	0.309822	106	321	178.55	162.4	4.02	172.9	12.87	163.4	13.5	**162.4**
74321_48	0.05532	0.00181	0.0065	0.00029	0.16072	0.00519	0.02107	0.00033	0.485011	113	425	70.91	134.4	2.06	151.3	4.54	131	5.86	**134.4**
74321_49	0.05086	0.00223	0.00798	0.00052	0.17294	0.00738	0.02467	0.00044	0.417948	103	235	97.9	157.1	2.76	162	6.39	160.6	10.53	**157.1**
74321_51	0.05208	0.00262	0.00523	0.00031	0.10908	0.00535	0.01519	0.00028	0.37583	108	289	111.19	97.2	1.76	105.1	4.89	105.5	6.33	**97.2**
74321_52	0.05595	0.00281	0.0081	0.00054	0.1408	0.0069	0.01825	0.00034	0.380163	115	450	108.25	116.6	2.14	133.8	6.14	163.1	10.85	**116.6**
74321_53	0.26391	0.00388	0.16837	0.00868	21.23709	0.33824	0.58348	0.00748	0.804907	91	3270	22.93	2962.9	30.43	3149.5	15.44	3145.2	150.24	**3270.2**
74321_54	0.05291	0.00313	0.00705	0.00045	0.14163	0.0082	0.01941	0.00036	0.320345	109	325	128.6	123.9	2.29	134.5	7.29	142	9.05	**123.9**
74321_55	0.09915	0.00183	0.08749	0.00492	3.97424	0.07569	0.29068	0.00395	0.713506	102	1608	33.93	1644.9	19.74	1629	15.45	1695.2	91.43	**1608.2**
74321_56	0.04986	0.00193	0.00529	0.00042	0.10905	0.00414	0.01587	0.00027	0.448138	104	188	87.72	101.5	1.69	105.1	3.79	106.7	8.51	**101.5**

74321_57	0.04888	0.00415	0.00432	0.00031	0.08948	0.00744	0.01328	0.0003	0.271692	102	142	188.12	85	1.88	87	6.94	87.1	6.34	**85**
74321_58	0.05258	0.00204	0.01414	0.001	0.29507	0.01122	0.0407	0.00066	0.426463	102	311	85.86	257.2	4.07	262.5	8.8	283.7	19.97	**257.2**
74321_59	0.13328	0.00272	0.11406	0.00865	7.11511	0.1505	0.38723	0.00559	0.682477	99	2142	35.24	2110	25.98	2125.9	18.83	2183.2	156.92	**2141.6**
74321_60	0.08926	0.00375	0.0078	0.00057	0.25645	0.01035	0.02084	0.00039	0.463692	174	1410	78.35	133	2.46	231.8	8.37	157	11.51	**133**
74321_61	0.06742	0.00135	0.02181	0.00092	0.39465	0.00833	0.04247	0.00063	0.70279	126	851	41.15	268.1	3.91	337.8	6.06	436.1	18.3	**268.1**
74321_62	0.05896	0.00178	0.00494	0.00017	0.13005	0.00391	0.016	0.00025	0.519701	121	566	64.42	102.3	1.56	124.1	3.52	99.7	3.34	**102.3**
74321_63	0.06452	0.00134	0.02769	0.00128	0.73254	0.01565	0.08237	0.00117	0.664866	109	759	43.1	510.2	6.99	558	9.17	552	25.26	**510.2**
74321_64	0.14392	0.00359	0.01133	0.00039	0.34816	0.00837	0.01755	0.00028	0.663643	271	2275	42.39	112.1	1.8	303.3	6.3	227.8	7.71	**112.1**
74321_65	0.06411	0.00122	0.02704	0.00112	0.89413	0.01824	0.10116	0.00149	0.722027	104	745	39.73	621.2	8.73	648.6	9.78	539.4	22.03	**621.2**
74321_66	0.08078	0.00124	0.0496	0.00205	2.21209	0.03832	0.19868	0.00282	0.819355	96	1216	29.79	1168.2	15.19	1184.9	12.11	978.5	39.48	**1216.1**
74321_67	0.11367	0.00325	0.00667	0.00028	0.25852	0.00724	0.0165	0.00029	0.627581	221	1859	50.81	105.5	1.81	233.5	5.85	134.4	5.69	**105.5**
74321_68	0.06337	0.00126	0.02599	0.00097	0.80424	0.01676	0.09205	0.0013	0.67769	106	721	41.73	567.6	7.66	599.2	9.43	518.6	19.12	**567.6**
74321_69	0.05141	0.00089	0.01341	0.00054	0.31116	0.00577	0.0439	0.00059	0.724762	99	259	39.23	277	3.65	275.1	4.46	269.2	10.87	**277**
74321_70	0.06058	0.00091	0.02412	0.0009	0.7507	0.01269	0.08988	0.00123	0.809556	102	624	31.99	554.8	7.29	568.6	7.36	481.7	17.78	**554.8**
74321_71	0.06478	0.00208	0.00551	0.00024	0.15193	0.00486	0.01701	0.00027	0.496211	132	767	66.17	108.7	1.72	143.6	4.28	111	4.89	**108.7**
74321_72	0.06774	0.0023	0.00727	0.00037	0.20779	0.00698	0.02224	0.00036	0.481878	135	861	69.01	141.8	2.3	191.7	5.87	146.4	7.33	**141.8**
74321_73	0.06046	0.00188	0.02563	0.00303	0.75366	0.02342	0.0904	0.00153	0.544643	102	620	65.85	557.9	9.07	570.3	13.56	511.4	59.67	**557.9**
74321_74	0.16433	0.00624	0.15774	0.02272	3.21566	0.12002	0.14194	0.0027	0.509654	171	2501	62.54	855.6	15.24	1460.9	28.91	2960.4	396.63	**855.6**
74321_75	0.06902	0.00167	0.04331	0.00428	1.47813	0.03649	0.15533	0.00236	0.615454	99	900	49.23	930.8	13.19	921.5	14.95	856.9	82.94	**930.8**
74321_76	0.05212	0.00165	0.01167	0.00135	0.28479	0.00897	0.03963	0.00066	0.528752	102	291	70.49	250.6	4.12	254.5	7.09	234.5	26.92	**250.6**
74321_77	0.0597	0.00212	0.02421	0.0032	0.80125	0.0281	0.09736	0.00178	0.521316	100	593	74.66	598.9	10.45	597.5	15.84	483.5	63.21	**598.9**
74321_78	0.07835	0.00444	0.01022	0.00125	0.18072	0.00997	0.01673	0.00035	0.379213	158	1156	108.57	107	2.21	168.7	8.57	205.6	25.1	**107**
74321_79	0.06059	0.00183	0.02627	0.00288	0.77602	0.02338	0.0929	0.00152	0.543071	102	625	63.79	572.6	8.97	583.2	13.37	524	56.75	**572.6**
74321_80	0.06137	0.0017	0.029	0.00327	0.85727	0.02391	0.10133	0.00161	0.569673	101	652	58.46	622.2	9.43	628.6	13.07	577.7	64.3	**622.2**
74322_01	0.07454	0.00108	0.0515	0.00172	1.75806	0.02974	0.17108	0.00246	0.850019	96	1055.8	29.22	1018	13.56	1030.1	10.95	1015	33.07	**1055.8**
74322_02	0.05714	0.00118	0.02405	0.00092	0.62678	0.0138	0.07956	0.00121	0.690759	100	496.5	44.86	493.5	7.21	494.1	8.61	480.4	18.07	**493.5**
74322_03	0.07649	0.00183	0.05455	0.00212	1.93292	0.04772	0.18329	0.00298	0.658553	98	1107.9	47.15	1084.9	16.22	1092.5	16.52	1073.6	40.57	**1107.9**
74322_04	0.05991	0.00134	0.03188	0.00131	0.8581	0.0201	0.1039	0.00162	0.665643	99	600.2	47.61	637.2	9.44	629.1	10.98	634.3	25.72	**637.2**
74322_05	0.05833	0.0054	0.00539	0.0005	0.12587	0.01112	0.01565	0.00051	0.36887	120	541.6	191.18	100.1	3.25	120.4	10.03	108.7	9.97	**100.1**
74322_06	0.08287	0.00226	0.05416	0.00231	2.23742	0.06169	0.19583	0.00337	0.624142	91	1266.2	52.25	1152.9	18.16	1192.8	19.35	1066.1	44.35	**1266.2**
74322_07	0.13719	0.00226	0.085	0.0037	6.11903	0.11324	0.32352	0.00489	0.816752	82	2192	28.34	1806.9	23.82	1993	16.15	1648.8	69.01	**2192**
74322_08	0.06231	0.0018	0.02839	0.00147	0.85192	0.02485	0.09916	0.00168	0.580825	103	684.9	60.41	609.5	9.85	625.7	13.62	565.9	28.89	**609.5**
74322_09	0.05914	0.00154	0.02848	0.00152	0.77922	0.02082	0.09556	0.00156	0.610981	99	572.4	55.59	588.3	9.19	585	11.88	567.6	29.78	**588.3**

74322_10	0.05938	0.00447	0.00537	0.00037	0.14167	0.01022	0.01731	0.00048	0.384389	122	581.1	155.55	110.6	3.05	134.5	9.09	108.2	7.51	**110.6**
74322_11	0.0623	0.0053	0.00637	0.00051	0.16615	0.01346	0.01934	0.00061	0.38934	126	684.4	171.83	123.5	3.85	156.1	11.72	128.4	10.34	**123.5**
74322_12	0.05434	0.00265	0.00507	0.00032	0.13744	0.00653	0.01835	0.00038	0.43586	112	385.1	105.39	117.2	2.4	130.8	5.83	102.2	6.5	**117.2**
74322_13	0.04954	0.00188	0.00573	0.00036	0.14059	0.00532	0.02058	0.00037	0.475115	102	173.5	86.13	131.3	2.32	133.6	4.73	115.4	7.25	**131.3**
74322_14	0.0565	0.00485	0.00442	0.00038	0.11647	0.00957	0.01495	0.00046	0.374472	117	471.1	180.25	95.7	2.92	111.9	8.71	89.1	7.65	**95.7**
74322_15	0.06304	0.00247	0.02374	0.00147	0.75902	0.02928	0.08733	0.0017	0.504624	106	709.7	81.16	539.7	10.11	573.4	16.9	474.2	29.08	**539.7**
74322_16	0.04813	0.00504	0.00429	0.00039	0.10111	0.01022	0.01524	0.00051	0.331077	100	105.5	230.52	97.5	3.22	97.8	9.43	86.5	7.91	**97.5**
74322_17	0.05745	0.00152	0.02388	0.00128	0.72102	0.01978	0.09103	0.00152	0.608667	98	508.5	57.49	561.6	8.96	551.3	11.67	476.9	25.36	**561.6**
74322_18	0.05997	0.00132	0.02622	0.00134	0.7945	0.01874	0.0961	0.00154	0.679394	100	602.4	46.89	591.5	9.03	593.7	10.6	523.1	26.45	**591.5**
74322_19	0.06064	0.00221	0.02224	0.00128	0.72322	0.02619	0.08651	0.00162	0.517111	103	626.4	76.59	534.9	9.61	552.6	15.43	444.6	25.23	**534.9**
74322_20	0.09947	0.00169	0.06955	0.00368	3.76852	0.07331	0.2748	0.0042	0.78567	97	1614.2	31.34	1565.1	21.25	1586.1	15.61	1359.1	69.55	**1614.2**
74322_21	0.04973	0.00239	0.00663	0.00044	0.1728	0.00816	0.0252	0.00051	0.428571	101	182.4	108.29	160.5	3.2	161.8	7.06	133.7	8.75	**160.5**
74322_22	0.05924	0.00166	0.02282	0.00138	0.71075	0.02039	0.08703	0.00147	0.588773	101	575.9	59.71	537.9	8.72	545.2	12.1	456.1	27.28	**537.9**
74322_23	0.06001	0.00265	0.02206	0.00153	0.66456	0.02873	0.08032	0.00163	0.469421	104	604	92.64	498.1	9.72	517.4	17.53	441	30.25	**498.1**
74322_24	0.06182	0.00148	0.02616	0.00174	0.82772	0.02078	0.09712	0.00157	0.643916	102	667.8	50.44	597.5	9.24	612.3	11.54	521.9	34.31	**597.5**
74322_25	0.06649	0.00207	0.01202	0.00086	0.36636	0.01143	0.03997	0.0007	0.56134	125	821.7	63.55	252.6	4.36	317	8.49	241.5	17.09	**252.6**
74322_26	0.04696	0.0069	0.00382	0.00056	0.10206	0.01451	0.01577	0.00065	0.289914	98	46.7	318.1	100.8	4.14	98.7	13.37	77	11.37	**100.8**
74322_27	0.06019	0.00213	0.02107	0.00167	0.62671	0.02208	0.07552	0.00138	0.518662	105	610.4	74.82	469.3	8.28	494	13.78	421.5	33.02	**469.3**
74322_28	0.06042	0.00483	0.00377	0.00037	0.1073	0.00819	0.01288	0.00038	0.38653	125	618.6	163.62	82.5	2.42	103.5	7.51	76	7.47	**82.5**
74322_29	0.05833	0.00139	0.02524	0.00249	0.70335	0.0175	0.08747	0.0014	0.643283	100	541.3	52.23	540.5	8.32	540.8	10.43	503.9	49.11	**540.5**
74322_30	0.0626	0.00193	0.02778	0.00246	0.85309	0.02647	0.09884	0.00171	0.557576	103	694.7	64.46	607.6	10.05	626.3	14.51	553.8	48.29	**607.6**
74322_31	0.08258	0.00224	0.04857	0.00262	2.19072	0.06045	0.19238	0.00339	0.638602	90	1259.3	51.94	1134.3	18.31	1178.1	19.24	958.6	50.43	**1259.3**
74322_32	0.0775	0.00137	0.05073	0.00279	2.05373	0.04058	0.19215	0.00297	0.782253	100	1134.2	34.7	1133	16.04	1133.5	13.49	1000.2	53.69	**1134.2**
74322_33	0.0519	0.00223	0.01005	0.00064	0.26699	0.01135	0.03731	0.00071	0.447643	102	280.8	95.36	236.1	4.4	240.3	9.1	202.1	12.87	**236.1**
74322_34	0.0852	0.00343	0.05448	0.00352	2.26242	0.08838	0.19255	0.0041	0.545079	86	1320	76.09	1135.2	22.18	1200.7	27.51	1072.2	67.42	**1320**
74322_35	0.05162	0.00272	0.00459	0.00033	0.1099	0.00563	0.01544	0.00033	0.417211	107	268.5	116.48	98.8	2.11	105.9	5.15	92.6	6.72	**98.8**
74322_36	0.05317	0.0036	0.00989	0.00079	0.28463	0.0186	0.03882	0.00099	0.390254	104	335.9	146.11	245.5	6.13	254.3	14.71	198.9	15.72	**245.5**
74322_37	0.06496	0.00553	0.02745	0.00328	0.85883	0.06982	0.09587	0.00307	0.393897	107	773.1	169.52	590.1	18.07	629.5	38.14	547.4	64.53	**590.1**
74322_38	0.05181	0.0035	0.01087	0.00097	0.27718	0.01809	0.0388	0.00097	0.383057	101	276.9	147.7	245.4	6.04	248.4	14.38	218.5	19.32	**245.4**
74322_39	0.06027	0.00324	0.02241	0.00204	0.71852	0.03725	0.08646	0.00196	0.437274	103	613.2	111.92	534.6	11.64	549.8	22.01	448.1	40.25	**534.6**
74322_40	0.10644	0.00273	0.07404	0.00594	4.27366	0.11075	0.29119	0.00489	0.64802	95	1739.3	46.18	1647.5	24.43	1688.3	21.32	1443.6	111.76	**1739.3**
74322_41	0.05674	0.00303	0.01139	0.00067	0.24891	0.01288	0.03182	0.0007	0.425133	112	480.9	114.13	201.9	4.36	225.7	10.47	228.9	13.34	**201.9**
74322_42	0.07092	0.00138	0.05284	0.00278	1.5609	0.03285	0.15965	0.00241	0.717279	100	955	39.33	954.8	13.39	954.8	13.03	1040.7	53.39	**954.8**

74322_43	0.06327	0.00304	0.03163	0.00205	0.88348	0.04116	0.10129	0.00217	0.459848	103	717.3	98.8	621.9	12.68	642.9	22.19	629.4	40.23	**621.9**
74322_44	0.05568	0.00166	0.01489	0.00094	0.35326	0.01066	0.04602	0.00077	0.554474	106	439.2	64.96	290	4.72	307.2	7.99	298.7	18.69	**290**
74322_45	0.05428	0.00204	0.01834	0.00117	0.38185	0.01421	0.05103	0.00093	0.489729	102	382.6	81.71	320.8	5.68	328.4	10.44	367.4	23.22	**320.8**
74322_46	0.05231	0.0024	0.01098	0.00075	0.219	0.00982	0.03037	0.0006	0.440595	104	299	101.12	192.9	3.76	201.1	8.18	220.7	15.01	**192.9**
74322_47	0.05144	0.00187	0.00949	0.00063	0.18268	0.00658	0.02576	0.00046	0.495766	104	260.7	81.17	164	2.87	170.4	5.65	190.8	12.69	**164**
74322_48	0.05315	0.00405	0.00531	0.00049	0.1159	0.0085	0.01582	0.00043	0.370618	110	335.1	163.72	101.2	2.74	111.3	7.74	107.1	9.92	**101.2**
74322_49	0.06454	0.0044	0.00682	0.00064	0.14754	0.00961	0.01658	0.00044	0.407431	132	759.5	137.61	106	2.81	139.7	8.51	137.4	12.86	**106**
74322_50	0.05042	0.00163	0.01075	0.00081	0.19584	0.00637	0.02818	0.00048	0.523675	101	214.2	73.24	179.1	3.01	181.6	5.41	216.1	16.17	**179.1**
74322_51	0.05246	0.00531	0.01065	0.00124	0.23185	0.02251	0.03206	0.0011	0.353395	104	305.5	215.49	203.4	6.89	211.7	18.55	214.1	24.79	**203.4**
74322_52	0.06076	0.00151	0.04	0.00329	0.92235	0.02392	0.1101	0.00177	0.619898	99	630.8	52.79	673.3	10.27	663.6	12.64	792.8	63.93	**673.3**
74322_53	0.07276	0.00211	0.0579	0.00501	1.64882	0.04853	0.16437	0.00282	0.582894	101	1007.3	57.69	981	15.6	989.1	18.6	1137.6	95.64	**981**
74322_54	0.09028	0.00433	0.03639	0.00339	1.11962	0.05149	0.08996	0.00209	0.505178	137	1431.3	89.05	555.3	12.33	762.8	24.67	722.5	66.11	**555.3**
74322_55	0.05941	0.00221	0.02988	0.00288	0.68936	0.0255	0.08417	0.00156	0.501041	102	582	78.88	520.9	9.3	532.4	15.33	595.2	56.54	**520.9**
74322_56	0.0578	0.00183	0.03243	0.00194	0.71547	0.0228	0.08979	0.00156	0.545197	99	521.9	68.21	554.3	9.22	548	13.5	645	38.03	**554.3**
74322_57	0.11266	0.00224	0.1184	0.00643	5.1947	0.11158	0.33445	0.00529	0.736374	101	1842.7	35.56	1859.9	25.57	1851.7	18.29	2261.7	116.17	**1842.7**
74322_58	0.0636	0.00136	0.03969	0.00256	0.97636	0.02229	0.11135	0.00174	0.684477	102	728.4	44.65	680.6	10.08	691.7	11.45	786.7	49.7	**680.6**
74322_59	0.06426	0.0033	0.01618	0.00107	0.34037	0.01688	0.03842	0.00086	0.451357	122	750.4	104.91	243	5.32	297.5	12.79	324.4	21.24	**243**
74322_60	0.05907	0.00193	0.03654	0.00226	0.85377	0.02796	0.10483	0.00185	0.538877	98	569.7	69.51	642.7	10.8	626.7	15.32	725.3	44.09	**642.7**
74322_61	0.05064	0.00347	0.01735	0.0014	0.31077	0.02056	0.04451	0.00113	0.38374	98	224.5	150.85	280.7	6.95	274.8	15.93	347.7	27.72	**280.7**
74322_62	0.05794	0.00216	0.03367	0.00224	0.73741	0.02726	0.0923	0.00172	0.504092	99	527.3	80.04	569.2	10.13	560.9	15.93	669.4	43.87	**569.2**
74322_63	0.16888	0.00376	0.08874	0.00594	6.55552	0.15274	0.28156	0.00467	0.711869	63	2546.5	36.82	1599.2	23.5	2053.4	20.53	1718.4	110.33	**2546.5**
74322_64	0.06523	0.00226	0.03581	0.00276	0.91877	0.03164	0.10216	0.00187	0.531534	106	781.8	71.15	627.1	10.96	661.7	16.74	711.1	53.88	**627.1**
74322_65	0.0632	0.00199	0.03623	0.00262	0.8654	0.0274	0.09932	0.00174	0.553323	104	715	65.52	610.4	10.23	633.1	14.91	719.3	51.19	**610.4**
74322_66	0.07615	0.00295	0.05835	0.00473	1.83861	0.06995	0.17512	0.00351	0.526833	95	1099.1	75.66	1040.3	19.23	1059.4	25.02	1146.3	90.25	**1099.1**
74322_67	0.05169	0.00154	0.01241	0.00095	0.25288	0.00766	0.03548	0.0006	0.558282	102	271.8	66.97	224.8	3.73	228.9	6.21	249.2	18.99	**224.8**
74322_68	0.05468	0.00233	0.00549	0.00044	0.10675	0.00447	0.01416	0.00028	0.472232	114	399.2	92.19	90.6	1.76	103	4.1	110.7	8.88	**90.6**
74322_69	0.06089	0.00322	0.0175	0.0015	0.38271	0.01956	0.04559	0.00103	0.442047	114	635.5	109.75	287.4	6.32	329	14.36	350.7	29.75	**287.4**
74322_70	0.05971	0.00167	0.03472	0.00336	0.80358	0.02301	0.09761	0.00164	0.586762	100	593.5	59.32	600.4	9.63	598.8	12.95	689.8	65.65	**600.4**
74322_71	0.12468	0.00289	0.12697	0.00942	6.17892	0.15222	0.35943	0.00617	0.696806	98	2024.3	40.46	1979.5	29.25	2001.5	21.53	2416.1	169	**2024.3**
74322_72	0.06031	0.00151	0.03994	0.00331	0.82466	0.02173	0.09917	0.00168	0.642901	100	614.8	53.25	609.5	9.83	610.6	12.09	791.5	64.27	**609.5**
74322_73	0.06673	0.00526	0.00701	0.00072	0.14244	0.01067	0.01548	0.00048	0.41394	137	829.4	156.29	99	3.04	135.2	9.49	141.2	14.39	**99**
74322_74	0.05136	0.00184	0.01784	0.00162	0.30943	0.01109	0.04369	0.00081	0.51729	99	257	80.3	275.7	5	273.7	8.6	357.5	32.13	**275.7**
74322_75	0.05792	0.00439	0.01114	0.00116	0.23564	0.01713	0.0295	0.00085	0.396359	115	526.6	158.46	187.4	5.32	214.8	14.07	223.9	23.29	**187.4**

74322_76	0.05202	0.00223	0.01945	0.00209	0.32093	0.01354	0.04474	0.00089	0.471504	100	286.3	95.04	282.2	5.5	282.6	10.41	389.4	41.4	**282.2**
74322_77	0.05636	0.00198	0.03874	0.00431	0.72049	0.02516	0.09272	0.00171	0.528129	96	465.7	75.94	571.6	10.1	551	14.85	768.3	83.87	**571.6**
74322_78	0.05854	0.00353	0.02635	0.00515	0.71082	0.04133	0.08806	0.00218	0.425767	100	550.2	126.53	544.1	12.9	545.2	24.53	525.7	101.45	**544.1**
74322_79	0.05109	0.00535	0.00495	0.0008	0.10053	0.01008	0.01427	0.00051	0.356436	107	245	224.21	91.3	3.21	97.3	9.3	99.8	16	**91.3**
74322_80	0.074	0.00406	0.04821	0.00784	1.44374	0.07595	0.1415	0.00346	0.464816	106	1041.5	106.99	853.1	19.53	907.3	31.56	951.7	151.09	**853.1**
74323_01	0.05927	0.00226	0.02197	0.00334	0.70726	0.02709	0.08653	0.00161	0.485768	102	577.1	80.87	535	9.56	543.1	16.11	439.2	65.97	**535**
74323_02	0.05138	0.00257	0.00778	0.00064	0.19448	0.00971	0.02746	0.00046	0.335516	103	257.8	110.89	174.6	2.89	180.4	8.25	156.6	12.89	**174.6**
74323_03	0.05098	0.01174	0.00526	0.00084	0.11459	0.02612	0.01631	0.00059	0.158698	106	240	458.67	104.3	3.71	110.2	23.79	106	16.86	**104.3**
74323_04	0.05237	0.00171	0.01124	0.00099	0.30482	0.0101	0.04222	0.00066	0.471789	101	301.8	72.77	266.6	4.05	270.2	7.86	225.8	19.75	**266.6**
74323_05	0.18965	0.00353	0.11086	0.00968	11.91712	0.24033	0.45586	0.00663	0.721183	88	2739.1	30.29	2421.2	29.35	2597.9	18.89	2125	176.15	**2739.1**
74323_06	0.06188	0.0089	0.00758	0.00084	0.2261	0.03223	0.02651	0.00067	0.177299	123	670	281.04	168.6	4.2	207	26.69	152.5	16.79	**168.6**
74323_07	0.07173	0.00249	0.04865	0.00567	1.66885	0.05706	0.1688	0.00283	0.490342	103	978.2	69.11	1005.5	15.62	996.7	21.71	960.1	109.19	**978.2**
74323_08	0.04816	0.01077	0.00502	0.00065	0.10397	0.0231	0.01566	0.00049	0.140832	100	107	457.6	100.2	3.09	100.4	21.24	101.1	13.06	**100.2**
74323_09	0.06225	0.00269	0.02621	0.00292	0.78761	0.03355	0.09179	0.0016	0.409207	104	682.6	89.75	566.1	9.46	589.8	19.06	522.9	57.55	**566.1**
74323_10	0.05651	0.00228	0.02508	0.00261	0.72198	0.02914	0.09269	0.00153	0.408973	97	471.6	87.79	571.4	9	551.8	17.18	500.6	51.37	**571.4**
74323_11	0.05153	0.00627	0.00857	0.00108	0.25251	0.03048	0.03555	0.00081	0.18876	102	264.5	257.52	225.2	5.03	228.6	24.71	172.4	21.57	**225.2**
74323_12	0.0713	0.00169	0.04031	0.00457	1.62202	0.03972	0.16504	0.00246	0.608685	99	965.9	47.64	984.7	13.59	978.8	15.38	798.7	88.79	**984.7**
74323_13	0.05875	0.00514	0.02135	0.00331	0.73172	0.06313	0.09038	0.00215	0.275724	100	557.8	180.21	557.8	12.71	557.6	37.02	427	65.54	**557.8**
74323_14	0.0603	0.00418	0.02633	0.00364	0.7704	0.05218	0.09269	0.00197	0.313795	102	614.2	142.99	571.4	11.65	580	29.93	525.2	71.6	**571.4**
74323_15	0.05033	0.02141	0.00354	0.00215	0.19529	0.08263	0.02815	0.00133	0.111665	101	210.2	768.3	178.9	8.31	181.1	70.19	71.4	43.4	**178.9**
74323_16	0.0424	0.01015	0.00717	0.00128	0.15377	0.03661	0.02631	0.00078	0.124522	87	0.1	309.14	167.4	4.91	145.2	32.22	144.3	25.73	**167.4**
74323_17	0.03736	0.00574	0.00767	0.00103	0.1301	0.0199	0.02526	0.00056	0.144937	77	0.1	0	160.8	3.52	124.2	17.88	154.4	20.66	**160.8**
74323_18	0.0617	0.00168	0.02885	0.00373	0.98514	0.02713	0.11582	0.00178	0.558065	99	663.7	57.18	706.4	10.26	696.2	13.88	574.8	73.26	**706.4**
74323_19	0.06161	0.00177	0.03264	0.00433	1.03604	0.02986	0.12198	0.0019	0.540445	97	660.4	60.44	741.9	10.9	721.9	14.89	649.1	84.69	**741.9**
74323_20	0.06114	0.00181	0.03203	0.00427	1.01483	0.03001	0.12038	0.00189	0.530927	97	644.2	62.4	732.7	10.88	711.3	15.12	637.2	83.69	**732.7**
74323_21	0.05709	0.00163	0.02672	0.00118	0.76862	0.02218	0.0977	0.00144	0.510761	96	494.5	62.18	600.9	8.48	579	12.73	533	23.21	**600.9**
74323_22	0.06016	0.00134	0.02735	0.00129	0.80477	0.01839	0.09709	0.00137	0.617499	100	609.2	47.3	597.4	8.03	599.5	10.35	545.4	25.37	**597.4**
74323_23	0.06032	0.00115	0.02738	0.00131	0.82172	0.01655	0.09884	0.00137	0.688198	100	615.3	40.51	607.6	8.05	609	9.22	546	25.7	**607.6**
74323_24	0.05944	0.00102	0.02802	0.00135	0.83998	0.01544	0.10257	0.00138	0.731948	98	583.2	36.92	629.4	8.09	619.1	8.52	558.6	26.56	**629.4**
74323_25	0.0585	0.00149	0.0254	0.00105	0.77104	0.02019	0.09564	0.00139	0.555029	99	548.7	54.79	588.8	8.18	580.4	11.58	507.1	20.79	**588.8**
74323_26	0.05152	0.00473	0.01016	0.00057	0.21946	0.02	0.03091	0.0006	0.212999	103	264	197.39	196.3	3.75	201.5	16.66	204.2	11.37	**196.3**
74323_27	0.05467	0.00446	0.00861	0.00053	0.22742	0.01839	0.03018	0.00057	0.233562	109	398.9	173.03	191.7	3.57	208.1	15.21	173.3	10.66	**191.7**
74323_28	0.02787	0.01518	0.00734	0.00065	0.06342	0.03448	0.01651	0.00055	0.061274	59	0.1	0	105.6	3.49	62.4	32.93	147.7	13.03	**105.6**

74323_29	0.04418	0.00299	0.00455	0.00023	0.09393	0.00633	0.01543	0.00027	0.259656	92	0.1	57.25	98.7	1.69	91.2	5.87	91.8	4.57	**98.7**
74323_30	0.0475	0.00177	0.00416	0.00017	0.09856	0.00369	0.01506	0.00023	0.407922	99	73.5	86.99	96.4	1.45	95.4	3.41	83.8	3.52	**96.4**
74323_31	0.04727	0.00355	0.0042	0.00188	0.09685	0.00707	0.01486	0.00036	0.331867	99	62.6	170.17	95.1	2.31	93.9	6.55	84.8	37.85	**95.1**
74323_32	0.05093	0.0044	0.00416	0.00188	0.10521	0.00887	0.01498	0.00038	0.300888	106	237.8	187.63	95.9	2.42	101.6	8.15	84	37.78	**95.9**
74323_33	0.06152	0.00443	0.0277	0.01258	0.85195	0.05947	0.10044	0.00246	0.350869	101	657.6	147.23	617	14.39	625.7	32.61	552.3	247.49	**617**
74323_34	0.06202	0.00457	0.02804	0.01289	0.84389	0.06021	0.09869	0.00247	0.350785	102	674.9	150.2	606.7	14.47	621.3	33.16	559	253.44	**606.7**
74323_35	0.06229	0.00453	0.02749	0.01279	0.85458	0.06028	0.09951	0.00245	0.349043	103	684	148.11	611.5	14.35	627.2	33	548.2	251.63	**611.5**
74323_36	0.06196	0.00512	0.02581	0.01275	0.72777	0.0583	0.08519	0.00228	0.334096	105	672.7	167.51	527	13.57	555.2	34.26	515	251.31	**527**
74323_37	0.05804	0.00433	0.02474	0.01173	0.6895	0.04983	0.08617	0.00217	0.348455	100	530.7	156.03	532.9	12.88	532.5	29.95	493.9	231.31	**532.9**
74323_38	0.05619	0.00482	0.02464	0.01227	0.66716	0.05535	0.08612	0.00237	0.331709	97	459	180.42	532.6	14.06	519	33.71	491.9	242.14	**532.6**
74323_39	0.08943	0.02264	0.00887	0.00477	0.34621	0.08638	0.02808	0.0013	0.185555	169	1413.4	419.93	178.5	8.17	301.9	65.16	178.4	95.58	**178.5**
74323_40	0.05768	0.00478	0.02696	0.01322	0.72309	0.05804	0.09093	0.00241	0.330198	98	517.2	172.44	561	14.26	552.5	34.2	537.6	260.25	**561**
74323_41	0.05901	0.00456	0.02681	0.01342	0.69543	0.05197	0.08547	0.00221	0.346003	101	567.6	159.86	528.7	13.12	536.1	31.12	534.7	264.24	**528.7**
74323_42	0.19015	0.01422	0.11326	0.05682	9.66124	0.69904	0.36851	0.00933	0.349916	74	2743.4	117.99	2022.4	43.97	2403	66.58	2168.7	1031.68	**2743.4**
74323_43	0.05394	0.00287	0.00726	0.00037	0.16143	0.00844	0.02171	0.00044	0.387645	110	368.2	115.17	138.5	2.76	152	7.38	146.3	7.34	**138.5**
74323_44	0.05171	0.001	0.01496	0.00066	0.31821	0.0065	0.04464	0.00062	0.679936	100	272.4	43.72	281.5	3.84	280.5	5	300.2	13.22	**281.5**
74323_45	0.06275	0.00104	0.03568	0.00173	0.80809	0.01448	0.09341	0.00127	0.758755	104	699.7	34.96	575.7	7.49	601.4	8.13	708.7	33.79	**575.7**
74323_46	0.0592	0.0011	0.02903	0.00144	0.68672	0.01337	0.08414	0.00115	0.702011	102	574.4	39.76	520.8	6.86	530.8	8.05	578.5	28.24	**520.8**
74323_47	0.04389	0.00338	0.00563	0.0004	0.09979	0.00754	0.01649	0.00034	0.272881	92	0.1	61.94	105.4	2.15	96.6	6.96	113.4	8.08	**105.4**
74323_48	0.05939	0.00082	0.03247	0.00146	0.77511	0.01238	0.09467	0.00129	0.853139	100	581.4	29.81	583.1	7.59	582.7	7.08	645.9	28.59	**583.1**
74323_50	0.06692	0.00317	0.0059	0.00051	0.12849	0.00588	0.01393	0.00026	0.407863	138	835.3	95.74	89.2	1.67	122.7	5.29	118.8	10.16	**89.2**
74323_51	0.05221	0.00106	0.01609	0.00088	0.35566	0.0077	0.04941	0.00072	0.673073	99	294.7	45.77	310.9	4.44	309	5.77	322.7	17.55	**310.9**
74323_52	0.05676	0.00119	0.02836	0.00183	0.73825	0.01585	0.09434	0.00131	0.64677	97	481.5	45.95	581.2	7.7	561.4	9.26	565.3	35.89	**581.2**
74323_53	0.05883	0.00144	0.0305	0.00232	0.75461	0.01905	0.09304	0.00145	0.617342	100	560.6	52.49	573.5	8.53	570.9	11.02	607.2	45.52	**573.5**
74323_54	0.0711	0.00467	0.02812	0.00233	0.87583	0.05637	0.08935	0.00192	0.333871	116	960.2	128.8	551.7	11.39	638.7	30.52	560.6	45.76	**551.7**
74323_55	0.05557	0.00128	0.01528	0.0012	0.36721	0.00869	0.04793	0.00071	0.625959	105	434.8	50.17	301.8	4.34	317.6	6.46	306.5	23.83	**301.8**
74323_56	0.05969	0.00147	0.03136	0.00289	0.82063	0.02046	0.09971	0.00149	0.599362	99	592.9	51.88	612.7	8.72	608.4	11.41	624.2	56.59	**612.7**
74323_57	0.05477	0.0031	0.00887	0.00082	0.19794	0.01101	0.02621	0.0005	0.342965	110	402.7	121.63	166.8	3.16	183.4	9.33	178.4	16.38	**166.8**
74323_58	0.07647	0.00148	0.05323	0.00405	1.55061	0.03205	0.14708	0.00214	0.703938	107	1107.4	38.28	884.6	12.05	950.7	12.76	1048.3	77.78	**884.6**
74323_59	0.04863	0.00133	0.00587	0.00047	0.11593	0.00323	0.01729	0.00027	0.560483	101	130.2	63.2	110.5	1.7	111.4	2.94	118.4	9.41	**110.5**
74323_60	0.15105	0.00301	0.06327	0.00512	4.33552	0.09167	0.20818	0.00307	0.69745	52	2357.9	33.67	1219.1	16.39	1700.1	17.45	1240.1	97.36	**2357.9**
74323_61	0.13793	0.00304	0.05761	0.00518	3.38864	0.07817	0.1782	0.00272	0.661678	48	2201.4	37.84	1057.1	14.87	1501.8	18.09	1132.1	99.03	**2201.4**
74323_62	0.05051	0.0013	0.01058	0.00088	0.22837	0.00603	0.0328	0.00051	0.588868	100	218.5	58.55	208	3.15	208.9	4.98	212.7	17.52	**208**

74323_63	0.05888	0.00128	0.02663	0.00228	0.69306	0.01584	0.08537	0.00128	0.656025	101	562.8	46.74	528.1	7.63	534.6	9.5	531.3	44.88	**528.1**
74323_64	0.0588	0.00128	0.03129	0.0028	0.77853	0.01772	0.09603	0.00144	0.658821	99	559.7	46.64	591.1	8.44	584.6	10.12	622.8	54.97	**591.1**
74323_65	0.05495	0.00368	0.01322	0.00146	0.28089	0.01847	0.03707	0.00076	0.311789	107	410.3	143.18	234.7	4.74	251.4	14.64	265.4	29.2	**234.7**
74323_66	0.06046	0.00195	0.02801	0.00322	0.74814	0.02405	0.08975	0.00152	0.526838	102	620.2	68	554	9	567.1	13.97	558.3	63.22	**554**
74323_68	0.05158	0.004	0.00497	0.00069	0.12291	0.00937	0.01728	0.00038	0.288461	107	266.9	168.5	110.5	2.38	117.7	8.48	100.2	13.94	**110.5**
74323_69	0.0584	0.00186	0.02535	0.00302	0.66679	0.02121	0.08282	0.0014	0.531424	101	544.7	68.08	512.9	8.34	518.8	12.92	506	59.45	**512.9**
74323_70	0.05801	0.00199	0.03129	0.00456	0.76493	0.02592	0.09563	0.00164	0.5061	98	529.9	73.82	588.8	9.64	576.9	14.91	622.8	89.44	**588.8**
74323_71	0.05197	0.00263	0.01393	0.00254	0.29808	0.01465	0.0416	0.00086	0.42063	101	284.1	111.65	262.8	5.35	264.9	11.46	279.6	50.63	**262.8**
74323_72	0.08814	0.00264	0.06882	0.00841	2.85354	0.08593	0.23482	0.00392	0.554358	98	1385.5	56.43	1359.7	20.46	1369.7	22.64	1345.3	159.13	**1385.5**
74323_73	0.05917	0.00239	0.02719	0.0034	0.75998	0.03024	0.09316	0.0017	0.458606	100	573.4	85.36	574.2	10.03	574	17.45	542.3	66.91	**574.2**
74323_75	0.06024	0.00249	0.03289	0.0054	0.8223	0.03325	0.099	0.00185	0.462142	100	612.4	86.9	608.6	10.85	609.3	18.53	654.1	105.75	**608.6**
74323_76	0.06076	0.00251	0.03335	0.00538	0.85773	0.03468	0.1024	0.00191	0.461323	100	630.6	86.59	628.4	11.19	628.9	18.95	663.2	105.31	**628.4**
74324_01	0.05087	0.01059	0.00816	0.00185	0.18872	0.03894	0.0269	0.00085	0.15314	103	234.9	420.43	171.1	5.35	175.5	33.26	164.2	37.01	**171.1**
74324_02	0.06111	0.00552	0.03824	0.00852	0.87078	0.07783	0.1033	0.00215	0.232862	100	643.2	183.26	633.7	12.55	636	42.24	758.5	165.83	**633.7**
74324_03	0.05313	0.00464	0.01419	0.00317	0.35333	0.03036	0.04822	0.00105	0.25342	101	334.2	186.45	303.6	6.46	307.2	22.78	284.8	63.19	**303.6**
74324_04	0.05398	0.00752	0.01279	0.00298	0.36731	0.05048	0.04933	0.00139	0.20503	102	369.9	286.79	310.4	8.53	317.7	37.49	256.9	59.38	**310.4**
74324_05	0.05912	0.00418	0.02664	0.00622	0.7722	0.05396	0.09469	0.00181	0.273547	100	571.5	146.92	583.2	10.64	581	30.91	531.4	122.44	**583.2**
74324_06	0.05935	0.00318	0.02569	0.00611	0.7848	0.04139	0.09586	0.0017	0.33626	100	580	112.18	590.1	10.03	588.2	23.55	512.7	120.45	**590.1**
74324_07	0.0474	0.01253	0.01153	0.00295	0.24754	0.06474	0.03786	0.00162	0.163609	94	68.9	532.38	239.5	10.05	224.6	52.69	231.7	59.04	**239.5**
74324_08	0.0586	0.00645	0.02102	0.00544	0.71447	0.07774	0.08838	0.00206	0.214216	100	552.4	223.8	545.9	12.22	547.4	46.04	420.5	107.77	**545.9**
74324_09	0.05864	0.00374	0.02471	0.00643	0.76054	0.0477	0.09401	0.00183	0.310371	99	553.8	133.48	579.2	10.8	574.3	27.51	493.3	126.83	**579.2**
74324_10	0.05316	0.0126	0.01276	0.00358	0.30681	0.07219	0.04183	0.00135	0.137163	103	335.7	463.07	264.2	8.38	271.7	56.09	256.2	71.47	**264.2**
74324_11	0.05757	0.00418	0.02293	0.00626	0.71048	0.05081	0.08945	0.00176	0.275128	99	513.2	152.21	552.3	10.39	545	30.16	458.3	123.72	**552.3**
74324_12	0.06086	0.00598	0.03883	0.03337	0.84017	0.08068	0.10007	0.00268	0.27889	101	634.4	198.46	614.8	15.72	619.2	44.52	770	649.27	**614.8**
74324_13	0.06904	0.01239	0.07263	0.06062	1.83484	0.32276	0.19274	0.00806	0.237729	126	900	331.8	1136.2	43.54	1058	115.6	1417.2	1142.38	**1136.2**
74324_14	0.04104	0.01504	0.0126	0.01029	0.189	0.0688	0.03341	0.00151	0.124158	83	0.1	455.22	211.9	9.45	175.8	58.75	253	205.37	**211.9**
74324_15	0.06198	0.00674	0.03186	0.02508	0.74082	0.07854	0.08676	0.00245	0.26636	105	673.4	216.96	536.3	14.54	562.9	45.81	633.9	491.32	**536.3**
74324_16	0.0563	0.00584	0.03401	0.02611	0.7581	0.07642	0.09777	0.00268	0.271925	95	463.6	215.3	601.3	15.73	572.9	44.14	676	510.34	**601.3**
74324_17	0.05949	0.00605	0.03428	0.02572	0.88098	0.08696	0.10757	0.00292	0.275003	97	585.2	206.66	658.6	16.99	641.5	46.94	681.2	502.72	**658.6**
74324_18	0.06596	0.01133	0.00732	0.00537	0.19304	0.03261	0.02127	0.0007	0.194817	132	805	323.65	135.7	4.42	179.2	27.75	147.3	107.8	**135.7**
74324_19	0.06628	0.01425	0.03743	0.02727	0.91746	0.19465	0.10063	0.00368	0.172367	107	815.2	394.82	618.1	21.55	661	103.1	742.8	531.32	**618.1**
74324_20	0.07398	0.01156	0.05527	0.03899	2.00744	0.30589	0.19734	0.00717	0.238441	112	1041	286.69	1161	38.63	1118	103.3	1087.3	746.89	**1041**
74324_21	0.05549	0.00653	0.02901	0.02009	0.73703	0.08386	0.09664	0.00293	0.266466	94	431.6	243.25	594.7	17.23	560.7	49.02	577.9	394.7	**594.7**

74324_22	0.0607	0.00699	0.02585	0.01758	0.81033	0.09	0.09717	0.00286	0.265004	101	628.6	230.43	597.8	16.79	602.6	50.48	515.8	346.41	**597.8**
74324_23	0.05679	0.00773	0.02404	0.02025	0.68899	0.09135	0.08792	0.00304	0.26079	98	482.6	276.11	543.2	17.99	532.2	54.92	480.2	399.75	**543.2**
74324_24	0.16962	0.02126	0.0984	0.08529	9.39997	1.14509	0.40157	0.01317	0.269223	85	2553.9	195.88	2176.2	60.56	2377.8	111.8	1897	1569.51	**2553.9**
74324_25	0.04719	0.01264	0.0094	0.00845	0.21093	0.05591	0.03239	0.00134	0.156078	95	58.4	539.11	205.5	8.38	194.3	46.88	189.2	169.2	**205.5**
74324_26	0.04618	0.01867	0.00579	0.00538	0.10505	0.04211	0.01648	0.00089	0.134724	96	7.1	762.37	105.4	5.64	101.4	38.69	116.8	108.05	**105.4**
74324_27	0.06166	0.00981	0.02857	0.02709	0.78237	0.12135	0.09192	0.00344	0.24128	104	662.5	308.4	566.9	20.33	586.8	69.13	569.4	532.27	**566.9**
74324_28	0.05934	0.01203	0.02327	0.02302	0.75493	0.14962	0.09216	0.00417	0.228302	100	579.6	388.4	568.3	24.6	571.1	86.57	464.9	454.78	**568.3**
74324_29	0.08258	0.01102	0.01071	0.0108	0.60524	0.07825	0.05309	0.00185	0.269527	144	1259.4	240.84	333.5	11.31	480.6	49.5	215.2	215.92	**333.5**
74324_30	0.06671	0.00905	0.03983	0.04146	1.17804	0.15482	0.12793	0.00449	0.267059	102	828.6	260.1	776	25.67	790.4	72.18	789.4	805.83	**776**
74324_31	0.05491	0.01576	0.00905	0.00982	0.11819	0.03345	0.01559	0.00076	0.172247	114	408.6	539.46	99.7	4.84	113.4	30.37	182	196.77	**99.7**
74324_32	0.05506	0.00769	0.02628	0.0292	0.62645	0.08466	0.0824	0.00295	0.264913	97	414.7	285.18	510.4	17.58	493.9	52.85	524.3	574.99	**510.4**
74324_33	0.01957	0.02704	0.00756	0.00885	0.04167	0.05753	0.01542	0.001	0.046973	42	0.1	29.25	98.7	6.35	41.5	56.08	152.2	177.53	**98.7**
74324_34	0.05297	0.00792	0.01361	0.01186	0.34261	0.05018	0.04686	0.00174	0.253522	101	327.4	308.01	295.2	10.74	299.1	37.95	273.3	236.55	**295.2**
74324_35	0.03918	0.00775	0.00576	0.005	0.10055	0.01962	0.01858	0.00072	0.198596	82	0.1	45.18	118.7	4.58	97.3	18.1	116	100.43	**118.7**
74324_36	0.21099	0.02957	0.10079	0.08757	9.25657	1.26853	0.3176	0.01189	0.273181	61	2913.1	210.54	1778	58.17	2363.7	125.6	1940.9	1607.94	**2913.1**
74324_37	0.05355	0.01143	0.02567	0.02235	0.69969	0.14729	0.09454	0.00399	0.200489	92	352.2	421.54	582.4	23.51	538.6	87.99	512.4	440.4	**582.4**
74324_38	0.07983	0.02865	0.0033	0.00315	0.1744	0.06188	0.0158	0.00093	0.165891	161	1192.8	581.17	101.1	5.89	163.2	53.5	66.6	63.49	**101.1**
74324_39	0.06964	0.01446	0.00571	0.00511	0.16746	0.03419	0.01739	0.00078	0.219688	141	917.7	377.06	111.1	4.92	157.2	29.73	115.1	102.68	**111.1**
74324_40	0.03948	0.00856	0.00474	0.00415	0.09113	0.01954	0.01668	0.00067	0.187334	83	0.1	101.5	106.7	4.24	88.6	18.19	95.5	83.58	**106.7**
74324_41	0.06255	0.00954	0.03664	0.03207	1.02534	0.15334	0.11845	0.00454	0.256291	99	693	295.09	721.6	26.16	716.6	76.87	727.3	625.26	**721.6**
74324_42	0.05515	0.00912	0.02471	0.02166	0.66764	0.10854	0.08744	0.00344	0.241992	96	418.1	332.42	540.4	20.37	519.3	66.09	493.3	427.17	**540.4**
74324_43	0.05998	0.00907	0.03086	0.02705	0.79024	0.11736	0.09513	0.0036	0.254814	101	602.7	297.37	585.8	21.2	591.3	66.56	614.2	530.38	**585.8**
74324_44	0.0537	0.02005	0.00544	0.00484	0.11902	0.04402	0.016	0.00091	0.153777	112	358.2	676.25	102.3	5.79	114.2	39.95	109.7	97.3	**102.3**
74324_45	0.05685	0.0097	0.01829	0.01634	0.73022	0.12256	0.09267	0.00375	0.2411	97	485	338.66	571.3	22.09	556.7	71.93	366.2	324.41	**571.3**
74324_46	0.0614	0.00621	0.03021	0.00538	0.89566	0.08898	0.10574	0.00268	0.255121	100	653.1	203.26	648	15.62	649.4	47.66	601.6	105.58	**648**
74324_47	0.05284	0.01075	0.01064	0.00203	0.29246	0.05907	0.04012	0.00116	0.143152	103	321.7	406.11	253.6	7.19	260.5	46.41	213.9	40.61	**253.6**
74324_48	0.04217	0.01985	0.00565	0.00121	0.11635	0.05454	0.02	0.0009	0.095998	88	0.1	674.72	127.6	5.72	111.8	49.6	113.9	24.35	**127.6**
74324_49	0.05452	0.01376	0.01471	0.00303	0.32548	0.0812	0.04328	0.00183	0.169485	105	392.5	484.56	273.1	11.34	286.1	62.2	295.2	60.34	**273.1**
74324_50	0.05269	0.00563	0.01176	0.00212	0.31856	0.03371	0.04383	0.00094	0.20267	102	315.6	225.61	276.5	5.82	280.8	25.96	236.3	42.31	**276.5**
74324_51	0.05082	0.02116	0.01701	0.00387	0.30099	0.12465	0.04293	0.00196	0.110244	99	232.9	752.5	271	12.1	267.2	97.28	340.8	76.87	**271**
74324_52	0.13724	0.00458	0.09747	0.01757	6.87356	0.22883	0.36311	0.00595	0.492207	91	2192.7	56.83	1996.9	28.12	2095.3	29.51	1879.8	323.66	**2192.7**
74324_53	0.04736	0.00841	0.01014	0.00204	0.21906	0.0385	0.03354	0.00103	0.174734	95	66.9	376.19	212.6	6.44	201.1	32.07	204	40.9	**212.6**
74324_54	0.05203	0.00881	0.00894	0.00187	0.26405	0.04431	0.0368	0.00102	0.165172	102	286.7	346.79	233	6.34	237.9	35.59	180	37.46	**233**

74324_55	0.04811	0.0144	0.00511	0.00133	0.11581	0.0344	0.01746	0.00072	0.138828	100	104.5	587.09	111.6	4.56	111.3	31.3	102.9	26.76	**111.6**
74324_56	0.07552	0.0034	0.04735	0.01018	1.69904	0.07562	0.16314	0.00292	0.402151	103	1082.5	87.8	974.2	16.19	1008.2	28.45	935.1	196.37	**974.2**
74324_57	0.05092	0.01211	0.01002	0.00245	0.25531	0.06019	0.03636	0.00129	0.150491	100	237.1	471.93	230.2	8.01	230.9	48.68	201.6	48.97	**230.2**
74324_58	0.04918	0.00472	0.01358	0.00317	0.30922	0.02931	0.0456	0.001	0.231359	95	156.3	210.13	287.4	6.19	273.6	22.73	272.6	63.29	**287.4**
74324_59	0.06636	0.00266	0.03905	0.00915	1.22319	0.04897	0.13369	0.0022	0.411043	100	817.6	81.5	808.9	12.53	811.2	22.36	774.2	177.92	**808.9**
74324_60	0.05581	0.00346	0.01738	0.00426	0.47354	0.02892	0.06154	0.00125	0.332591	102	444.4	132.69	385	7.57	393.6	19.93	348.3	84.6	**385**
74324_61	0.07426	0.00234	0.04953	0.00375	1.5159	0.04628	0.14806	0.00245	0.542008	105	1048.5	62.21	890.1	13.74	936.8	18.68	977.1	72.23	**890.1**
74324_62	0.06169	0.00208	0.03262	0.0028	0.74163	0.02425	0.08719	0.00145	0.508601	105	663.4	70.6	538.9	8.58	563.4	14.14	648.8	54.87	**538.9**
74324_63	0.06069	0.00162	0.03469	0.00312	0.83275	0.02184	0.09953	0.00151	0.578475	101	628.1	56.39	611.6	8.83	615.1	12.1	689.2	60.88	**611.6**
74324_64	0.06117	0.00212	0.03052	0.00315	0.71926	0.02416	0.08528	0.00145	0.506186	104	645.2	72.64	527.6	8.6	550.2	14.27	607.7	61.7	**527.6**
74324_65	0.05199	0.00306	0.01912	0.00217	0.38069	0.02156	0.0531	0.00118	0.392383	98	285.1	129.11	333.5	7.22	327.5	15.86	382.8	43.1	**333.5**
74324_66	0.06173	0.00232	0.03306	0.00396	0.80372	0.02938	0.09443	0.00169	0.489587	103	664.8	78.42	581.7	9.97	598.9	16.54	657.4	77.47	**581.7**
74324_67	0.05382	0.00358	0.00958	0.00129	0.19269	0.01235	0.02597	0.00064	0.384503	108	363.3	143.27	165.3	4.01	178.9	10.51	192.6	25.86	**165.3**
74324_68	0.10333	0.00381	0.0828	0.01194	3.39821	0.12308	0.23852	0.00446	0.516265	82	1684.8	66.49	1379	23.23	1504	28.41	1607.8	222.95	**1684.8**
74324_69	0.0708	0.00295	0.05275	0.00831	1.55012	0.06375	0.1588	0.00313	0.479269	100	951.5	83.13	950.1	17.41	950.5	25.38	1038.9	159.5	**950.1**
74324_70	0.0635	0.00344	0.03328	0.0057	0.82521	0.04363	0.09425	0.00216	0.433463	105	725.1	110.78	580.6	12.71	610.9	24.27	661.8	111.49	**580.6**
74324_71	0.1131	0.00587	0.11104	0.02449	5.45258	0.27724	0.34965	0.00778	0.437615	104	1849.7	91.06	1932.9	37.16	1893.2	43.63	2128.3	445.49	**1849.7**
74324_72	0.0591	0.00394	0.03015	0.00684	0.71008	0.04567	0.08713	0.00227	0.405074	101	570.9	138.64	538.5	13.45	544.8	27.12	600.4	134.24	**538.5**
74324_73	0.54235	0.03895	0.10102	0.02354	4.16363	0.2577	0.05568	0.00234	0.679007	477	4360.7	101.28	349.3	14.31	1666.9	50.67	1945.1	432.13	**349.3**
74324_74	0.0519	0.00314	0.01692	0.00401	0.32839	0.01915	0.04589	0.0011	0.411051	100	280.9	132.63	289.2	6.77	288.3	14.63	339.1	79.61	**289.2**
74324_75	0.06329	0.00365	0.03819	0.00925	0.97635	0.05423	0.11187	0.00261	0.420042	101	718.1	118.01	683.6	15.14	691.7	27.86	757.4	180.16	**683.6**
74324_76	0.07158	0.00598	0.00722	0.00182	0.15862	0.0126	0.01607	0.0005	0.391689	145	973.9	161.64	102.8	3.15	149.5	11.04	145.4	36.59	**102.8**
74324_77	0.05852	0.0036	0.03403	0.00859	0.74086	0.04353	0.09182	0.00222	0.411494	99	549.3	129.06	566.3	13.13	562.9	25.39	676.3	167.9	**566.3**
74324_78	0.06991	0.00467	0.05213	0.0136	1.44138	0.09147	0.14953	0.00392	0.413102	101	925.8	131.3	898.3	21.96	906.3	38.04	1027	261.18	**898.3**
74324_79	0.05775	0.0038	0.02992	0.00789	0.66269	0.04131	0.08322	0.0021	0.404806	100	520.1	138.49	515.3	12.52	516.3	25.23	595.8	154.85	**515.3**
74324_80	0.10799	0.00694	0.0977	0.02636	4.29598	0.25987	0.28854	0.00735	0.421102	93	1765.7	113.06	1634.2	36.75	1692.6	49.82	1884.1	485.42	**1765.7**
74325_01	0.07103	0.00129	0.05137	0.00307	1.47851	0.02709	0.15105	0.00187	0.675672	102	958	36.71	906.9	10.47	921.6	11.1	1012.5	59.05	**906.9**
74325_02	0.05419	0.00207	0.00505	0.00028	0.10509	0.00393	0.01407	0.00022	0.418117	113	379	83.12	90.1	1.41	101.5	3.62	101.8	5.6	**90.1**
74325_03	0.05886	0.00161	0.02587	0.00138	0.7331	0.01997	0.09037	0.00132	0.53621	100	562	58.56	557.7	7.82	558.4	11.7	516.3	27.25	**557.7**
74325_04	0.09628	0.0016	0.0683	0.0036	3.05453	0.0532	0.23014	0.00299	0.745954	86	1553	30.86	1335.2	15.68	1421.4	13.32	1335.3	68.04	**1553.3**
74325_05	0.09019	0.00422	0.01881	0.00145	0.58764	0.02631	0.04728	0.00099	0.467679	158	1430	86.82	297.8	6.09	469.4	16.83	376.7	28.8	**297.8**
74325_06	0.08678	0.0024	0.0526	0.00405	2.49998	0.06938	0.20897	0.00343	0.591442	90	1356	52.38	1223.3	18.31	1272	20.13	1036.2	77.73	**1355.6**
74325_07	0.0592	0.00152	0.02474	0.00149	0.69268	0.01777	0.08487	0.00122	0.560339	102	574	54.72	525.1	7.26	534.4	10.66	494	29.32	**525.1**

74325_08	0.0749	0.00198	0.0356	0.00295	1.47391	0.0398	0.14272	0.00228	0.591613	107	1066	52.35	860	12.85	919.7	16.34	707.1	57.62	**860**
74325_09	0.05361	0.00138	0.01567	0.00105	0.39143	0.01013	0.05294	0.00076	0.554721	101	355	57.07	332.6	4.66	335.4	7.39	314.3	20.95	**332.6**
74325_10	0.10567	0.00196	0.08115	0.00538	4.4598	0.08705	0.30606	0.00418	0.699707	100	1726	33.63	1721.3	20.64	1723.5	16.19	1577	100.53	**1726**
74325_11	0.06019	0.00134	0.02527	0.00176	0.7899	0.01812	0.09517	0.00136	0.622949	101	610	47.39	586	8	591.1	10.28	504.5	34.71	**586**
74325_12	0.05452	0.00302	0.01086	0.00111	0.34429	0.01863	0.0458	0.00097	0.391397	104	393	119.4	288.7	6	300.4	14.07	218.3	22.11	**288.7**
74325_13	0.05287	0.00202	0.01365	0.00176	0.33756	0.01257	0.04632	0.0008	0.463807	101	323	84.71	291.9	4.91	295.3	9.54	274	35.05	**291.9**
74325_14	0.05973	0.00253	0.01149	0.00174	0.15852	0.0065	0.01926	0.00035	0.443182	121	594	89.27	123	2.21	149.4	5.7	231	34.85	**123**
74325_15	0.08046	0.0061	0.00561	0.00078	0.17978	0.01308	0.01621	0.00042	0.356123	162	1208	142.33	103.7	2.68	167.9	11.26	113.2	15.76	**103.7**
74325_16	0.04998	0.00219	0.00564	0.00085	0.13274	0.00564	0.01927	0.00035	0.427473	103	194	98.84	123	2.22	126.6	5.06	113.7	17.13	**123**
74325_17	0.10671	0.00497	0.07737	0.01369	3.1642	0.14232	0.21515	0.00445	0.45985	72	1744	83.03	1256.2	23.6	1448.5	34.7	1506.3	256.91	**1744**
74325_18	0.05385	0.00201	0.02	0.00292	0.50821	0.01852	0.06848	0.00118	0.472847	98	365	81.78	427	7.12	417.2	12.47	400.3	57.85	**427**
74325_20	0.06111	0.00346	0.02704	0.00578	0.7423	0.04048	0.08814	0.00195	0.405696	104	643	117.38	544.5	11.58	563.7	23.59	539.3	113.79	**544.5**
74325_21	0.10822	0.00724	0.09062	0.02482	4.47704	0.28836	0.30011	0.00811	0.419562	96	1770	117.4	1691.8	40.23	1726.7	53.46	1753.3	459.89	**1769.6**
74325_22	0.05027	0.00418	0.01366	0.00405	0.3141	0.02516	0.04531	0.0014	0.385737	97	208	182.2	285.7	8.66	277.4	19.44	274.2	80.72	**285.7**
74325_23	0.07194	0.0044	0.00734	0.00125	0.19121	0.0113	0.01928	0.00044	0.386169	144	984	119.64	123.1	2.75	177.7	9.63	147.9	25.05	**123.1**
74325_24	0.05107	0.00269	0.00809	0.00142	0.17507	0.009	0.02487	0.0005	0.391078	103	244	117.02	158.4	3.16	163.8	7.77	162.9	28.52	**158.4**
74325_25	0.06525	0.00465	0.02369	0.00724	0.76363	0.05221	0.0849	0.00229	0.394509	110	782	143.15	525.3	13.62	576.1	30.06	473.3	142.86	**525.3**
74325_26	0.09726	0.008	0.06423	0.02012	2.73574	0.21505	0.20403	0.00643	0.400915	76	1572	146.63	1196.9	34.41	1338.2	58.45	1258.2	382.08	**1572.3**
74325_27	0.06544	0.00481	0.02541	0.00733	0.7786	0.05499	0.08631	0.00238	0.390433	110	789	147.21	533.7	14.12	584.7	31.39	507.1	144.41	**533.7**
74325_28	0.05876	0.00466	0.00959	0.00292	0.27204	0.02066	0.03358	0.00098	0.38428	115	558	164.02	212.9	6.12	244.3	16.49	192.8	58.53	**212.9**
74325_29	0.05637	0.00439	0.01422	0.00413	0.40515	0.03026	0.05213	0.00148	0.38012	105	466	164.63	327.6	9.09	345.4	21.86	285.3	82.35	**327.6**
74325_30	0.06376	0.00404	0.02722	0.00703	0.78938	0.0481	0.0898	0.00218	0.398402	107	734	128.77	554.4	12.88	590.8	27.3	542.9	138.42	**554.4**
74325_31	0.092	0.00718	0.0805	0.02442	2.14001	0.15969	0.16873	0.00492	0.390761	68	1467	141.55	1005.1	27.13	1161.8	51.64	1564.8	456.78	**1467.3**
74325_32	0.08976	0.01202	0.04678	0.02484	2.19582	0.28002	0.17745	0.00819	0.361923	74	1420	236.43	1053	44.84	1179.7	88.97	924.1	479.55	**1420.4**
74325_33	0.08548	0.00747	0.00759	0.00221	0.24919	0.02083	0.02115	0.00066	0.373315	167	1327	160.4	134.9	4.15	225.9	16.93	152.9	44.3	**134.9**
74325_34	0.0792	0.00596	0.05221	0.01519	1.91246	0.13811	0.17516	0.00487	0.385	88	1177	142.08	1040.5	26.73	1085.4	48.15	1028.6	291.84	**1177**
74325_36	0.07294	0.0059	0.02772	0.0083	0.97013	0.07493	0.09647	0.00283	0.379812	116	1012	155.77	593.7	16.62	688.5	38.62	552.7	163.26	**593.7**
74325_38	0.06063	0.00758	0.03093	0.01632	0.83631	0.10016	0.10013	0.00439	0.366078	100	626	248.9	615.2	25.72	617.1	55.38	615.8	319.88	**615.2**
74325_39	0.12022	0.01293	0.00938	0.00354	0.32474	0.03314	0.01961	0.00079	0.39476	228	1960	180.46	125.2	4.98	285.5	25.4	188.6	70.83	**125.2**
74325_40	0.05281	0.00421	0.01597	0.00463	0.36559	0.02811	0.05022	0.00139	0.359974	100	321	171.03	315.9	8.51	316.4	20.9	320.3	92.14	**315.9**
74325_42	0.05736	0.00469	0.01647	0.00568	0.3562	0.02795	0.04506	0.00135	0.381816	109	505	170.76	284.1	8.31	309.4	20.93	330.3	112.91	**284.1**
74325_43	0.05049	0.00396	0.01148	0.0038	0.26202	0.01972	0.03766	0.00109	0.384569	99	218	171.91	238.3	6.75	236.3	15.87	230.8	75.85	**238.3**
74325_44	0.08204	0.01087	0.05276	0.02724	2.21913	0.28072	0.19644	0.00941	0.378677	93	1246	239.36	1156.1	50.72	1187.1	88.55	1039.3	523.02	**1246.4**

74325_46	0.06477	0.00645	0.0183	0.00751	0.40463	0.03855	0.04533	0.00164	0.379745	121	767	196.83	285.8	10.13	345	27.86	366.6	148.99	**285.8**
74325_47	0.05509	0.00723	0.00677	0.00373	0.14785	0.01845	0.01948	0.00089	0.366122	113	416	269.34	124.4	5.6	140	16.32	136.3	74.79	**124.4**
74325_48	0.04878	0.00478	0.00531	0.00175	0.10442	0.00988	0.01553	0.00048	0.32666	102	138	215.1	99.3	3.05	100.8	9.08	106.9	35.24	**99.3**
74325_49	0.0699	0.00654	0.03145	0.01243	1.30404	0.11678	0.13535	0.00466	0.384459	104	926	181.17	818.3	26.48	847.5	51.46	626	243.62	**818.3**
74325_51	0.05988	0.00672	0.03092	0.01561	0.78015	0.08272	0.09447	0.00367	0.366387	101	599	225.95	581.9	21.64	585.6	47.19	615.5	306.04	**581.9**
74325_52	0.06248	0.00687	0.02753	0.01335	0.7869	0.08208	0.09134	0.00354	0.371556	105	691	218.67	563.5	20.93	589.4	46.64	548.9	262.57	**563.5**
74325_53	0.05522	0.00511	0.01318	0.00548	0.32021	0.0282	0.04205	0.00137	0.369948	106	421	194.4	265.6	8.49	282.1	21.69	264.6	109.39	**265.6**
74325_54	0.07186	0.01001	0.05425	0.03352	1.67468	0.22227	0.16899	0.00822	0.36649	102	982	260.35	1006.6	45.33	999	84.38	1067.8	642.58	**982.1**
74325_55	0.05399	0.00707	0.00798	0.00333	0.17098	0.02166	0.02297	0.00087	0.298982	109	371	270.83	146.4	5.48	160.3	18.79	160.6	66.82	**146.4**
74325_56	0.05958	0.00564	0.00586	0.00234	0.14735	0.01334	0.01794	0.00059	0.363265	122	589	193.02	114.6	3.71	139.6	11.81	118.2	47.04	**114.6**
74325_57	0.05192	0.00497	0.00649	0.0026	0.13881	0.01277	0.01939	0.00063	0.353177	107	282	204.96	123.8	3.98	132	11.38	130.8	52.17	**123.8**
74325_58	0.1182	0.01077	0.09978	0.04297	4.91377	0.42891	0.30149	0.00988	0.375433	88	1929	154.8	1698.7	48.92	1804.6	73.64	1922.3	789.78	**1929.2**
74325_60	0.07192	0.01349	0.0481	0.03964	1.4984	0.26757	0.15107	0.00968	0.358829	103	984	341.05	907	54.23	929.7	108.8	949.6	764.45	**907**
74325_61	0.09942	0.01216	0.00727	0.00365	0.22534	0.02624	0.01644	0.00072	0.376102	196	1613	211.99	105.1	4.58	206.3	21.74	146.4	73.23	**105.1**
74325_62	0.08318	0.01143	0.01288	0.0072	0.26416	0.03456	0.02304	0.00111	0.368242	162	1273	246.88	146.8	7.01	238	27.76	258.8	143.71	**146.8**
74325_63	0.08966	0.01662	0.03625	0.02918	1.19503	0.21063	0.09666	0.00612	0.359222	134	1418	318.27	594.8	35.97	798.3	97.43	719.6	569.19	**594.8**
74325_64	0.10739	0.00941	0.09051	0.03892	4.91831	0.4158	0.33218	0.01058	0.376742	105	1756	152.3	1848.9	51.19	1805.4	71.34	1751.3	721.41	**1755.6**
74325_65	0.06752	0.01016	0.01565	0.01041	0.40334	0.05869	0.04332	0.00235	0.372809	126	854	284.9	273.4	14.52	344.1	42.47	313.8	207.1	**273.4**
74325_66	0.05958	0.00965	0.01605	0.0113	0.35455	0.0539	0.04317	0.00234	0.356552	113	589	317.24	272.5	14.48	308.1	40.4	321.8	224.87	**272.5**
74325_67	0.04962	0.00994	0.0156	0.01261	0.32667	0.06261	0.04776	0.00327	0.357231	95	177	410.48	300.8	20.13	287	47.92	313	250.92	**300.8**
74325_68	0.07276	0.00814	0.02923	0.0148	0.95214	0.1009	0.09496	0.00375	0.372649	116	1007	211.62	584.8	22.07	679.2	52.48	582.4	290.65	**584.8**
74325_69	0.06589	0.00786	0.00658	0.00333	0.16533	0.01877	0.01821	0.00074	0.357939	134	803	231.84	116.3	4.71	155.4	16.35	132.6	66.92	**116.3**
74325_70	0.06049	0.00793	0.02801	0.01616	0.76542	0.09518	0.09186	0.00421	0.368561	102	621	260.18	566.6	24.84	577.1	54.74	558.4	317.74	**566.6**
74325_71	0.104	0.02389	0.10239	0.10086	5.42242	1.16287	0.37953	0.02983	0.366496	122	1697	372.48	2074.1	139.39	1888.4	183.9	1970.2	1849.27	**1696.8**
74325_72	0.05027	0.00605	0.00599	0.00309	0.13264	0.01521	0.01915	0.00079	0.359752	103	207	256.86	122.3	4.97	126.5	13.64	120.8	62.13	**122.3**
74325_73	0.06164	0.00682	0.03508	0.0179	0.84705	0.08912	0.09974	0.0039	0.371646	102	662	220.82	612.9	22.86	623	48.99	696.9	349.56	**612.9**
74325_74	0.10818	0.01582	0.09507	0.06298	5.02652	0.69915	0.33716	0.01714	0.365487	106	1769	245.69	1873	82.65	1823.8	117.8	1835.7	1162.44	**1768.9**
74325_76	0.05306	0.00683	0.01451	0.00793	0.33544	0.04111	0.04593	0.00208	0.369517	101	331	268.2	289.5	12.81	293.7	31.26	291.1	157.94	**289.5**
74325_77	0.07976	0.0085	0.06252	0.0308	2.41377	0.24519	0.21965	0.00833	0.373342	107	1191	197.06	1280	44.02	1246.7	72.93	1225.8	585.91	**1191**
74325_78	0.06551	0.00697	0.04095	0.02013	1.24022	0.12576	0.13746	0.00521	0.373781	99	791	208.62	830.3	29.52	819	57	811.1	390.81	**830.3**
74325_79	0.05163	0.00589	0.01266	0.00648	0.29232	0.03181	0.0411	0.00165	0.368924	100	269	242.08	259.6	10.22	260.4	24.99	254.3	129.32	**259.6**
74325_80	0.07632	0.00851	0.05489	0.02759	1.88247	0.20017	0.17918	0.00712	0.373697	96	1103	208.11	1062.5	38.95	1074.9	70.51	1080.1	528.64	**1103.4**
74326_01	0.08337	0.00225	0.02696	0.0133	2.48386	0.0675	0.21609	0.0036	0.613043	100	1277.7	51.95	1261.2	19.08	1267.3	19.67	537.7	261.81	**1277.7**

74326_02	0.20297	0.00393	0.14688	0.01334	14.45227	0.29365	0.51642	0.00832	0.792914	104	2850.2	31.2	2684	35.36	2779.9	19.3	2770	235.16	**2850.2**
74326_03	0.04839	0.00616	0.00811	0.00073	0.1551	0.01902	0.02325	0.0009	0.315661	99	118.2	275.66	148.2	5.67	146.4	16.72	163.2	14.61	**148.2**
74326_04	0.17628	0.00464	0.15241	0.00715	12.66359	0.33077	0.52103	0.00989	0.726715	98	2618.1	43.15	2703.6	41.9	2655	24.58	2867.3	125.44	**2618.1**
74326_05	0.05368	0.00646	0.01027	0.00118	0.27138	0.03125	0.03667	0.00145	0.343388	105	357.5	251.24	232.1	9.01	243.8	24.96	206.6	23.52	**232.1**
74326_06	0.05477	0.00166	0.02248	0.00116	0.51458	0.01558	0.06814	0.00109	0.528336	99	402.9	65.8	424.9	6.58	421.5	10.44	449.4	23.03	**424.9**
74326_07	0.06272	0.00303	0.0385	0.00289	0.88949	0.04147	0.10286	0.00214	0.446246	102	698.6	99.55	631.2	12.5	646.1	22.28	763.5	56.2	**631.2**
74326_08	0.05262	0.00271	0.01526	0.00094	0.33231	0.01658	0.04581	0.00093	0.406894	101	312.3	112.93	288.7	5.75	291.3	12.64	306.1	18.75	**288.7**
74326_09	0.17772	0.00519	0.12477	0.00793	8.74701	0.24606	0.35696	0.00695	0.692124	117	2631.7	47.7	1967.7	33.02	2312	25.63	2376.5	142.44	**2631.7**
74326_10	0.10886	0.00193	0.08592	0.0048	4.22041	0.07943	0.28118	0.00391	0.73886	105	1780.4	31.97	1597.3	19.65	1678	15.45	1666.1	89.36	**1780.4**
74326_11	0.05236	0.00531	0.00426	0.00046	0.10999	0.0107	0.01524	0.0005	0.337252	109	301	215.84	97.5	3.18	106	9.78	85.9	9.18	**97.5**
74326_12	0.05991	0.00199	0.02683	0.00177	0.705	0.02304	0.08535	0.00142	0.509086	103	600.2	70.49	528	8.41	541.8	13.72	535.1	34.78	**528**
74326_13	0.05112	0.00571	0.00564	0.00058	0.11731	0.01259	0.01665	0.00058	0.324581	106	246	238.23	106.4	3.69	112.6	11.44	113.8	11.66	**106.4**
74326_14	0.05901	0.00167	0.02546	0.00167	0.67022	0.01882	0.08237	0.00127	0.549076	102	567.6	60.6	510.3	7.56	520.8	11.44	508.1	32.92	**510.3**
74326_15	0.04141	0.00932	0.00286	0.00065	0.08102	0.01776	0.01419	0.00077	0.247547	87	0.1	228.56	90.8	4.87	79.1	16.68	57.8	13.06	**90.8**
74326_16	0.07934	0.00321	0.06066	0.0089	2.09258	0.08212	0.19128	0.00359	0.478253	102	1180.7	77.99	1128.3	19.44	1146.4	26.96	1190.3	169.53	**1180.7**
74326_17	0.05541	0.00316	0.01163	0.00177	0.27351	0.01503	0.0358	0.0008	0.40665	108	428.7	122.75	226.7	4.98	245.5	11.99	233.7	35.39	**226.7**
74326_18	0.06205	0.00515	0.01245	0.00209	0.33094	0.02619	0.03868	0.00117	0.38222	119	675.8	168.04	244.7	7.24	290.3	19.98	250.2	41.68	**244.7**
74326_19	0.06262	0.00306	0.04254	0.00672	1.02947	0.04879	0.11924	0.00249	0.440616	99	695.3	100.98	726.2	14.33	718.7	24.41	842.1	130.28	**726.2**
74326_20	0.05111	0.00288	0.01603	0.00259	0.30038	0.01638	0.04262	0.00094	0.404456	99	245.9	124.63	269.1	5.81	266.7	12.79	321.3	51.61	**269.1**
74326_21	0.15763	0.00716	0.065	0.01085	4.05079	0.17707	0.18638	0.00407	0.499563	149	2430.4	75.04	1101.7	22.11	1644.5	35.6	1272.9	205.86	**2430.4**
74326_22	0.05729	0.00318	0.03152	0.00552	0.6555	0.03528	0.08299	0.00186	0.41642	100	502.1	118.25	513.9	11.09	511.9	21.64	627.2	108.18	**513.9**
74326_23	0.06215	0.00322	0.03596	0.00629	0.83494	0.04208	0.09744	0.00212	0.431696	103	679.3	107.01	599.4	12.45	616.3	23.28	714.1	122.81	**599.4**
74326_24	0.05941	0.00274	0.04137	0.00729	0.8692	0.03932	0.10612	0.00215	0.447865	98	582	97.05	650.2	12.51	635.1	21.36	819.3	141.52	**650.2**
74326_25	0.07371	0.0032	0.05017	0.00883	1.51349	0.0649	0.14893	0.00293	0.458797	105	1033.4	85.35	895	16.46	935.8	26.22	989.5	170	**895**
74326_26	0.06248	0.00344	0.02927	0.00538	0.78009	0.04193	0.09055	0.00207	0.425306	105	690.6	113.16	558.8	12.21	585.5	23.92	583.1	105.7	**558.8**
74326_27	0.05634	0.00286	0.03067	0.00551	0.70577	0.03515	0.09086	0.00194	0.428713	97	465	109.42	560.6	11.49	542.2	20.92	610.5	108.02	**560.6**
74326_28	0.07381	0.00439	0.05013	0.01026	1.42446	0.08235	0.13998	0.00349	0.431267	106	1036.3	115.7	844.5	19.72	899.2	34.49	988.6	197.45	**844.5**
74326_29	0.05553	0.0036	0.00794	0.00153	0.18966	0.012	0.02477	0.00062	0.395604	112	433.5	138.71	157.7	3.87	176.3	10.24	159.8	30.66	**157.7**
74326_30	0.05885	0.00334	0.01837	0.0036	0.40708	0.02269	0.05017	0.00117	0.418396	110	561.5	119.12	315.6	7.16	346.8	16.37	368	71.51	**315.6**
74326_31	0.04734	0.0033	0.00435	0.00043	0.09999	0.00674	0.01532	0.00037	0.697472	99	65.9	158.53	98	2.37	96.8	6.22	87.7	8.58	**98**
74326_32	0.06052	0.00169	0.03021	0.00184	0.79195	0.02238	0.09492	0.00155	0.592254	101	622.2	59.06	584.6	9.1	592.3	12.68	601.6	36.18	**584.6**
74326_33	0.06346	0.00725	0.00529	0.00057	0.12898	0.01397	0.01474	0.0006	0.358294	131	723.5	225.35	94.4	3.79	123.2	12.56	106.7	11.46	**94.4**
74326_34	0.05364	0.00213	0.01919	0.00133	0.42283	0.01654	0.05718	0.00105	0.577845	100	355.8	87.07	358.5	6.39	358.1	11.8	384.2	26.47	**358.5**

74326_35	0.04842	0.00311	0.0103	0.00074	0.2081	0.01294	0.03118	0.00072	0.37582	97	119.7	144.59	197.9	4.52	192	10.88	207	14.83	**197.9**
74326_36	0.05367	0.00527	0.00898	0.00083	0.18701	0.01763	0.02527	0.00083	0.469435	108	357.2	207.77	160.9	5.19	174.1	15.08	180.6	16.7	**160.9**
74326_37	0.05123	0.00903	0.00302	0.00056	0.09725	0.01648	0.01377	0.00071	0.371359	107	251.1	361.8	88.2	4.54	94.2	15.25	61	11.38	**88.2**
74326_38	0.05382	0.00235	0.0159	0.00121	0.35664	0.01522	0.04806	0.00092	0.348406	102	363.5	95.23	302.6	5.67	309.7	11.39	318.9	23.99	**302.6**
74326_39	0.0516	0.00222	0.0137	0.0011	0.29572	0.01245	0.04157	0.00078	0.304268	100	267.8	95.51	262.5	4.86	263	9.75	274.9	21.91	**262.5**
74326_40	0.05245	0.00356	0.0139	0.00131	0.30243	0.01982	0.04183	0.00104	0.448559	102	304.9	147.48	264.2	6.43	268.3	15.45	279	26.05	**264.2**
74326_41	0.053	0.00194	0.01358	0.00112	0.27886	0.01006	0.03817	0.00067	0.445683	103	328.5	80.84	241.5	4.18	249.8	7.99	272.6	22.27	**241.5**
74326_42	0.05961	0.0022	0.02986	0.00257	0.75339	0.02742	0.09168	0.00165	0.379373	101	589.3	78.13	565.5	9.77	570.2	15.88	594.8	50.39	**565.5**
74326_43	0.05406	0.00201	0.01331	0.00124	0.28594	0.01048	0.03837	0.00068	0.486565	105	373.5	81.43	242.7	4.25	255.4	8.28	267.3	24.69	**242.7**
74326_44	0.06166	0.00266	0.03268	0.00303	0.90336	0.03804	0.10627	0.0021	0.494495	100	662.3	89.99	651.1	12.24	653.5	20.29	649.9	59.35	**651.1**
74326_45	0.05778	0.00227	0.02556	0.00283	0.64737	0.02495	0.08127	0.00151	0.483538	101	521.3	84.21	503.7	8.99	506.9	15.38	510.2	55.68	**503.7**
74326_46	0.06775	0.00275	0.04575	0.00716	1.18781	0.04751	0.12716	0.00245	0.481701	103	861	82.09	771.7	14.01	794.9	22.05	904.1	138.4	**771.7**
74326_47	0.05335	0.00482	0.01371	0.00232	0.26748	0.02317	0.03637	0.00114	0.361849	105	343.5	191.9	230.3	7.12	240.7	18.56	275.2	46.35	**230.3**
74326_48	0.05364	0.00563	0.00797	0.00133	0.16185	0.01627	0.02188	0.00077	0.350081	109	356	221.24	139.6	4.88	152.3	14.22	160.4	26.67	**139.6**
74326_49	0.0922	0.00415	0.03968	0.0063	1.53949	0.06715	0.12112	0.00254	0.480783	128	1471.4	83.29	737	14.63	946.3	26.85	786.5	122.57	**737**
74326_50	0.06002	0.00242	0.03218	0.00535	0.71944	0.02847	0.08695	0.00164	0.47663	102	604.3	85.03	537.5	9.75	550.3	16.81	640.1	104.74	**537.5**
74326_51	0.17521	0.00786	0.14415	0.02581	10.7344	0.46284	0.44439	0.01027	0.535986	105	2608.1	72.79	2370.3	45.81	2500.4	40.05	2721.8	455.99	**2608.1**
74326_52	0.05655	0.00412	0.00609	0.00107	0.13214	0.00923	0.01695	0.00045	0.38008	116	473.2	154.17	108.4	2.85	126	8.28	122.7	21.4	**108.4**
74326_53	0.06159	0.0032	0.03207	0.00552	0.76827	0.03851	0.09048	0.00198	0.436569	104	659.9	107.68	558.4	11.69	578.8	22.11	638	108.07	**558.4**
74326_54	0.06549	0.00481	0.02859	0.00511	0.74553	0.05215	0.08258	0.00235	0.406821	111	790.1	146.9	511.5	14	565.6	30.34	569.8	100.4	**511.5**
74326_55	0.06028	0.00257	0.02563	0.00554	0.71348	0.02942	0.08585	0.00165	0.466104	103	613.8	89.42	530.9	9.82	546.8	17.44	511.5	109.16	**530.9**
74326_56	0.11978	0.00513	0.10249	0.01906	4.75236	0.19604	0.28778	0.00572	0.481837	109	1953	74.56	1630.4	28.64	1776.5	34.6	1972.1	349.47	**1953**
74326_57	0.05708	0.00326	0.03426	0.0067	0.63978	0.03502	0.08131	0.00186	0.417911	100	493.9	121.76	503.9	11.11	502.2	21.68	680.9	130.91	**503.9**
74326_58	0.0628	0.00307	0.03426	0.00663	0.75833	0.03551	0.08758	0.00183	0.446225	106	701.6	100.72	541.2	10.83	573	20.5	680.9	129.63	**541.2**
74326_59	0.06454	0.00308	0.03739	0.00744	0.86308	0.03942	0.09699	0.00199	0.449222	106	759.5	97.57	596.8	11.72	631.8	21.49	742	144.98	**596.8**
74326_60	0.05108	0.00242	0.01786	0.00366	0.31929	0.01449	0.04533	0.00091	0.442357	98	244.6	105.6	285.8	5.62	281.4	11.15	357.7	72.68	**285.8**
74326_61	0.10577	0.00297	0.09291	0.00576	4.25188	0.11957	0.29158	0.00523	0.637827	102	1727.8	50.68	1649.4	26.09	1684.1	23.12	1795.7	106.43	**1727.8**
74326_62	0.04837	0.00374	0.00795	0.00068	0.17023	0.01269	0.02553	0.00068	0.3573	98	117.5	172.61	162.5	4.27	159.6	11.01	160.1	13.68	**162.5**
74326_63	0.09411	0.00401	0.04106	0.00324	2.10708	0.08613	0.1624	0.00356	0.536279	119	1510.4	78.37	970.1	19.76	1151.1	28.15	813.4	62.88	**970.1**
74326_64	0.06381	0.0017	0.03593	0.00257	0.78794	0.0213	0.08956	0.00145	0.598918	107	735.5	55.29	552.9	8.56	590	12.1	713.4	50.09	**552.9**
74326_65	0.1449	0.00382	0.10886	0.00806	6.90759	0.18242	0.34578	0.00612	0.670202	110	2286.6	44.63	1914.4	29.29	2099.6	23.42	2088.6	146.92	**2286.6**
74326_66	0.06537	0.00143	0.03653	0.00278	1.01112	0.02315	0.11219	0.00171	0.665723	104	786.4	45.24	685.4	9.9	709.4	11.69	725.1	54.24	**685.4**
74326_67	0.05151	0.00231	0.02113	0.00187	0.42094	0.01843	0.05928	0.00115	0.443082	96	263.6	99.53	371.2	6.99	356.7	13.17	422.6	36.98	**371.2**

74326_68	0.06534	0.0024	0.03226	0.00288	0.88964	0.03204	0.09877	0.00181	0.508833	106	785.1	75.19	607.2	10.63	646.2	17.22	641.7	56.44	**607.2**
74326_69	0.06639	0.00347	0.03135	0.00295	0.84767	0.0426	0.09261	0.00209	0.449061	109	818.7	105.47	571	12.34	623.4	23.41	623.9	57.86	**571**
74326_70	0.07498	0.00256	0.04463	0.00454	1.40619	0.04717	0.13603	0.00245	0.53692	108	1068	67.11	822.2	13.91	891.6	19.91	882.5	87.92	**822.2**
74326_71	0.05198	0.00333	0.01289	0.00108	0.27496	0.01709	0.03838	0.00086	0.360513	102	284.4	139.99	242.8	5.33	246.7	13.61	258.9	21.59	**242.8**
74326_72	0.06797	0.00166	0.03831	0.00325	1.18162	0.02942	0.12612	0.00192	0.611438	103	867.8	49.95	765.7	10.97	792.1	13.7	759.8	63.27	**765.7**
74326_73	0.0547	0.00311	0.01401	0.00134	0.32286	0.01777	0.04282	0.00093	0.394605	105	400.1	122.33	270.3	5.73	284.1	13.64	281.3	26.65	**270.3**
74326_74	0.05341	0.00302	0.00499	0.0005	0.10685	0.00584	0.01451	0.00031	0.390891	111	346.2	122.27	92.9	1.96	103.1	5.36	100.7	9.99	**92.9**
74326_75	0.1541	0.00368	0.10799	0.01017	8.02677	0.19479	0.37793	0.00567	0.618224	108	2391.9	40.08	2066.6	26.51	2234	21.91	2072.7	185.44	**2391.9**
74326_76	0.0586	0.00281	0.01675	0.00174	0.39311	0.0182	0.04867	0.00098	0.434918	110	552.3	101.29	306.4	6.01	336.6	13.26	335.8	34.58	**306.4**
74326_77	0.12542	0.00339	0.09448	0.00991	5.77009	0.15535	0.33377	0.0052	0.578665	105	2034.8	47	1856.7	25.11	1941.9	23.3	1824.8	182.93	**2034.8**
74326_78	0.05341	0.00379	0.01314	0.00166	0.28413	0.01943	0.0386	0.00097	0.367476	104	346	152.74	244.1	6	253.9	15.36	263.9	33.02	**244.1**
74326_79	0.06614	0.00213	0.04011	0.00469	1.21085	0.03827	0.13281	0.00219	0.521729	100	810.9	66.08	803.9	12.45	805.6	17.58	794.8	91.21	**803.9**
74326_80	0.05839	0.01298	0.00376	0.00062	0.12711	0.02726	0.01579	0.00096	0.283493	120	544.5	423.65	101	6.12	121.5	24.56	75.8	12.51	**101**

74317

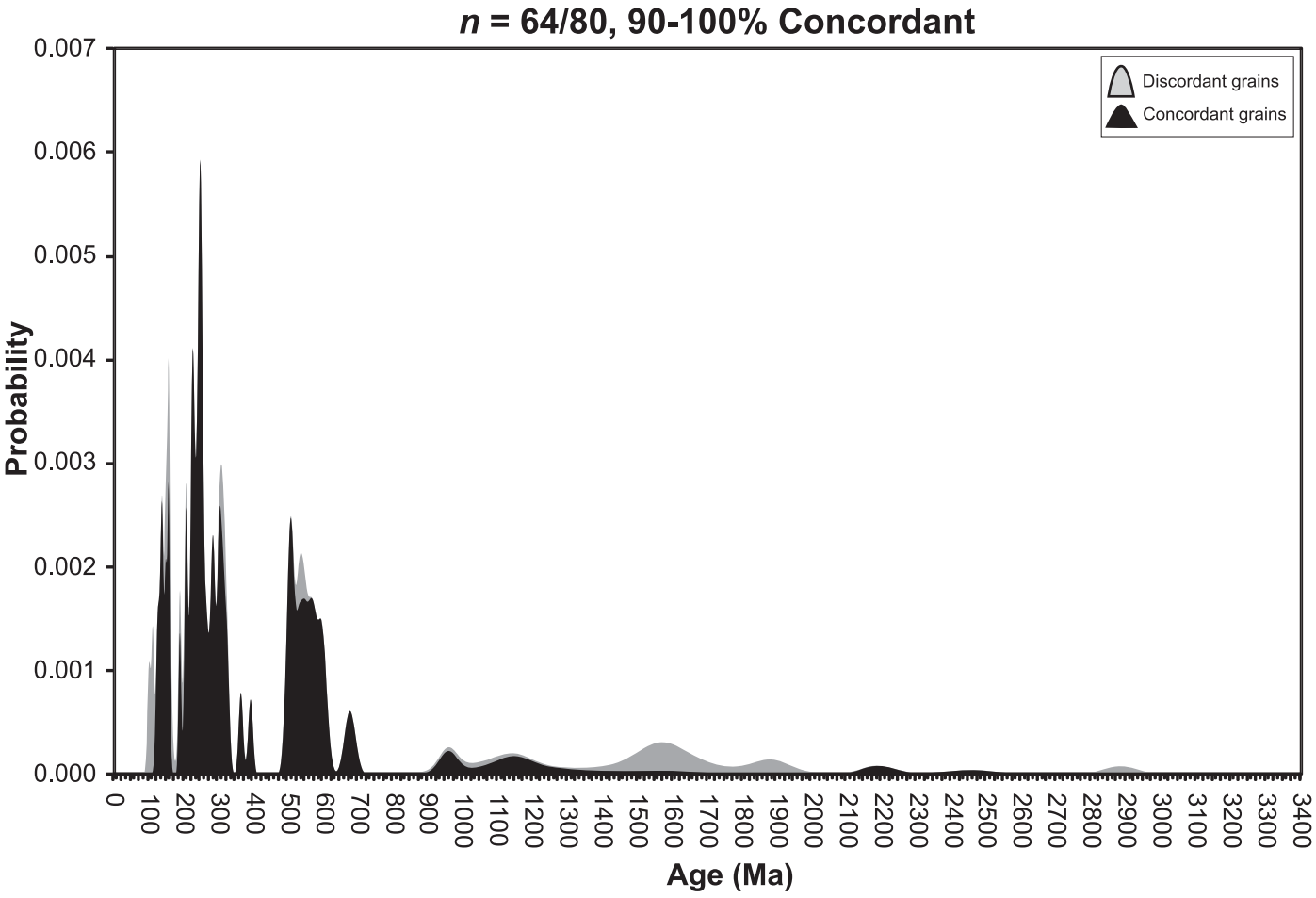
n = 64/80, 90-100% Concordant
Discordant grains
Concordant grains
Probability
0.007
0.006
0.005
0.004
0.003
0.002
0.001
0.000
0 100 200 300 400 500 600 700 800 900 1000 1100 1200 1300 1400 1500 1600 1700 1800 1900 2000 2100 2200 2300 2400 2500 2600 2700 2800 2900 3000 3100 3200 3300 3400
Age (Ma)

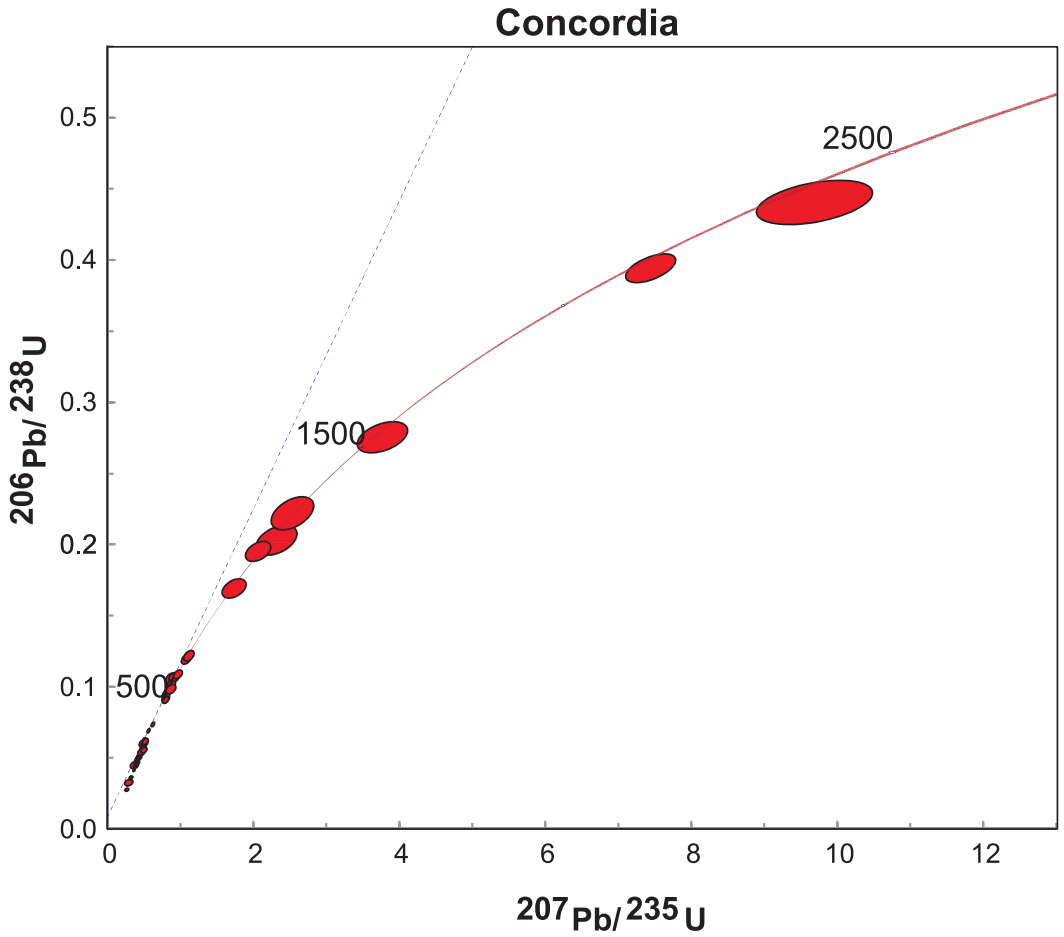
Concordia
2500
1500
500
0.5
0.4
0.3
0.2
0.1
0.0
0 2 4 6 8 10 12
206Pb/238U
207Pb/235U

74318

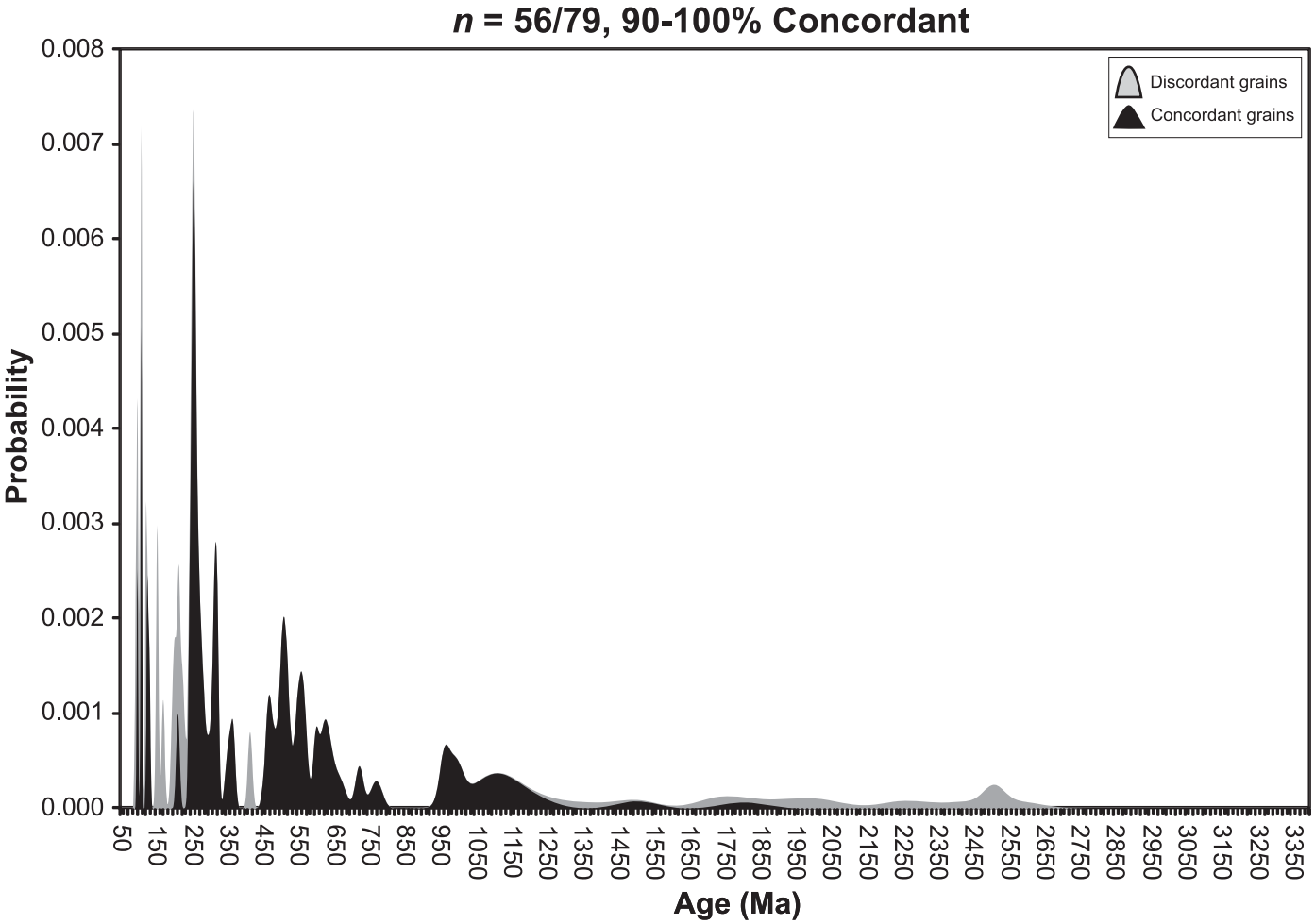
n = 56/79, 90-100% Concordant
Discordant grains
Concordant grains
Probability
0.008
0.007
0.006
0.005
0.004
0.003
0.002
0.001
0.000
50 150 250 350 450 550 650 750 850 950 1050 1150 1250 1350 1450 1550 1650 1750 1850 1950 2050 2150 2250 2350 2450 2550 2650 2750 2850 2950 3050 3150 3250 3350
Age (Ma)

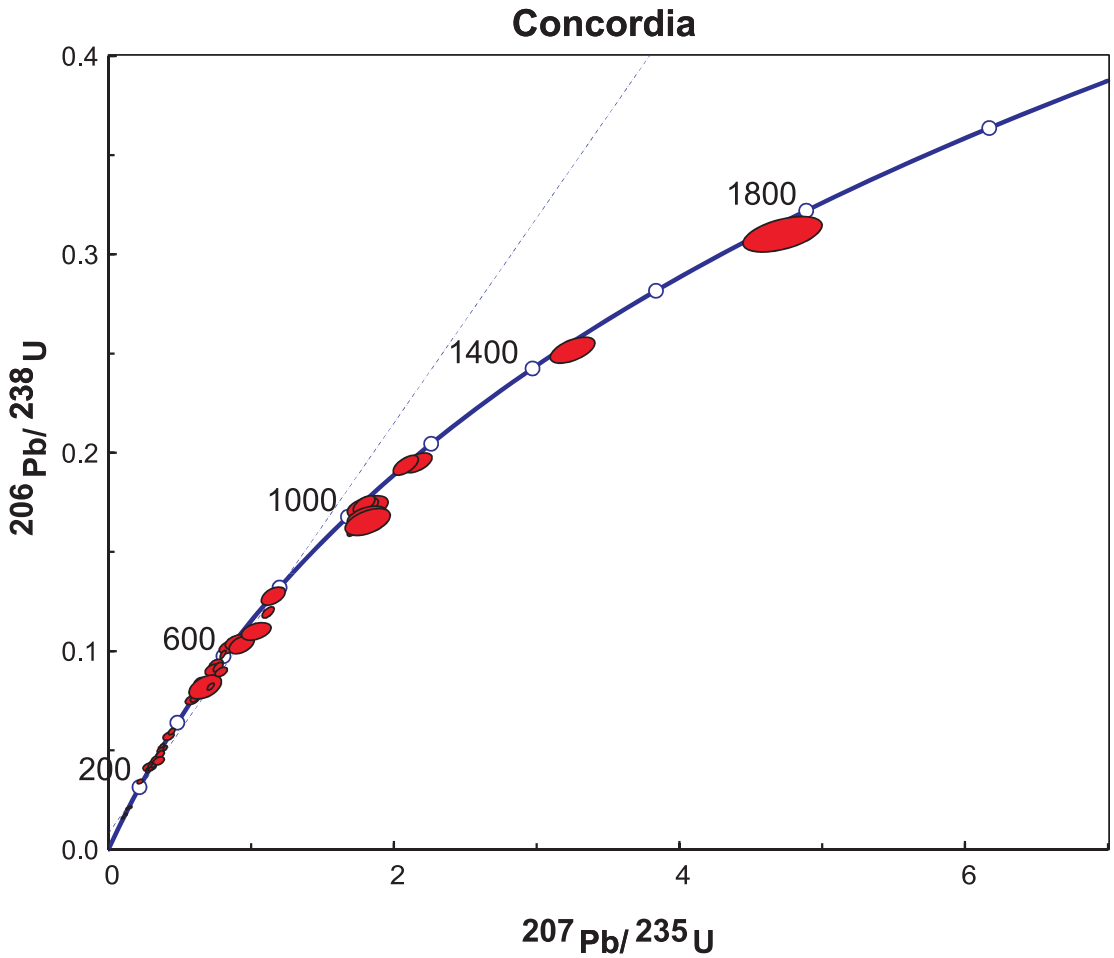
Concordia
0.4
0.3
0.2
0.1
0.0
206 Pb/ 238 U
1800
1400
1000
600
200
0
2
4
6
207 Pb/ 235 U

74319

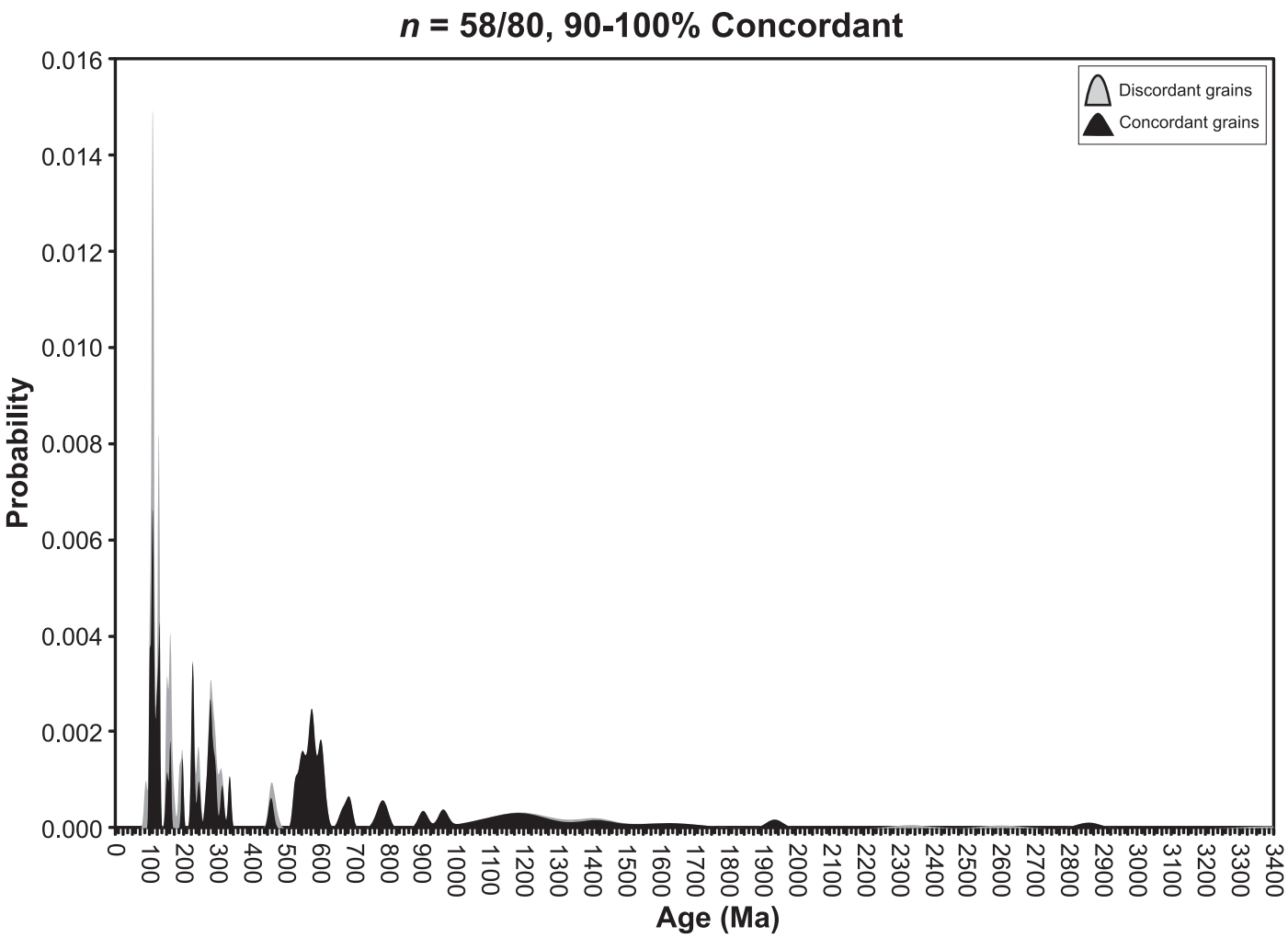
n = 58/80, 90-100% Concordant
Discordant grains
Concordant grains
Probability
0.016
0.014
0.012
0.010
0.008
0.006
0.004
0.002
0.000
0 100 200 300 400 500 600 700 800 900 1000 1100 1200 1300 1400 1500 1600 1700 1800 1900 2000 2100 2200 2300 2400 2500 2600 2700 2800 2900 3000 3100 3200 3300 3400
Age (Ma)

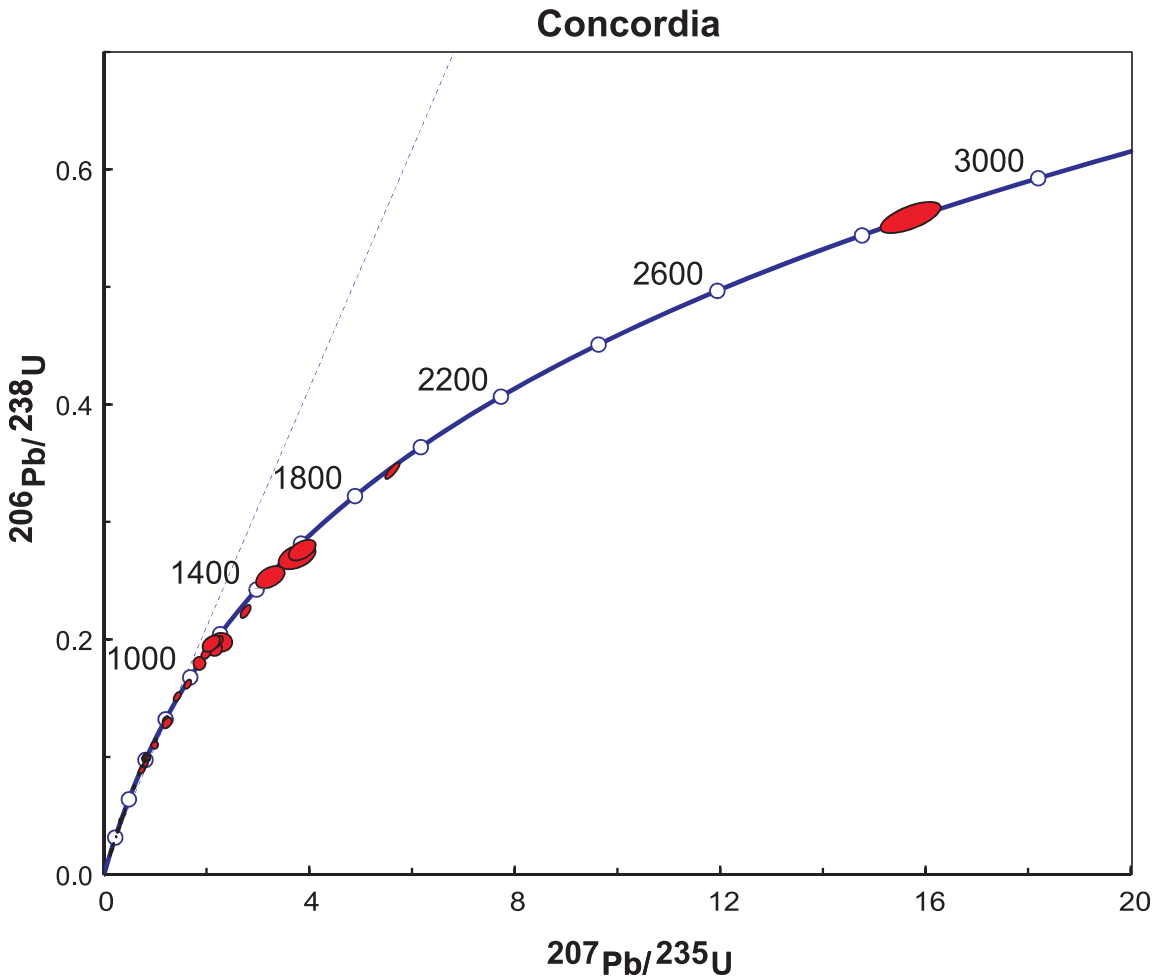
Concordia
206Pb/238U
0.6
0.4
0.2
0.0
0 4 8 12 16 20
207Pb/235U
3000
2600
2200
1800
1400
1000

74320

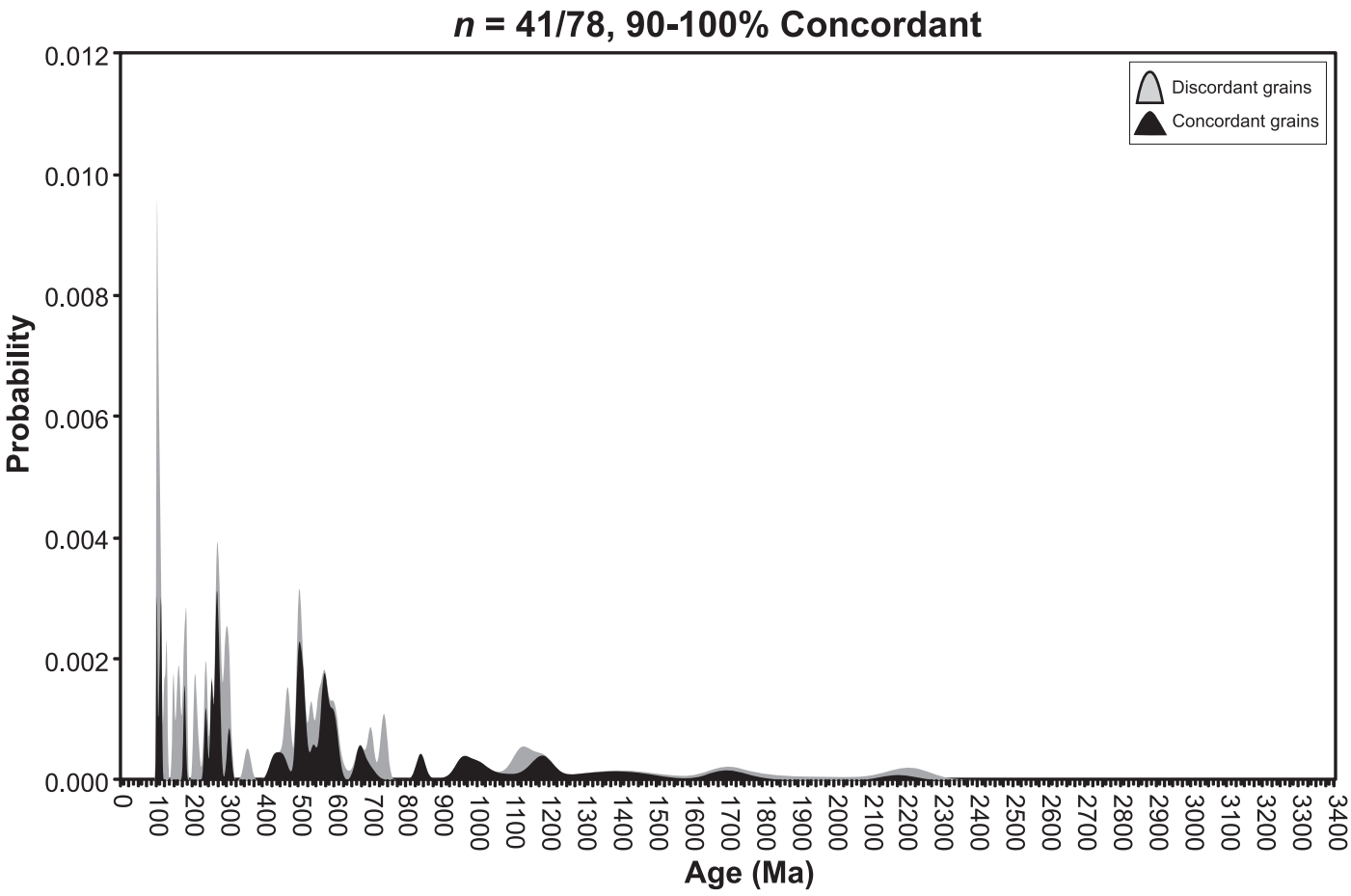
n = 41/78, 90-100% Concordant
Discordant grains
Concordant grains
Probability
0.012
0.010
0.008
0.006
0.004
0.002
0.000
0 100 200 300 400 500 600 700 800 900 1000 1100 1200 1300 1400 1500 1600 1700 1800 1900 2000 2100 2200 2300 2400 2500 2600 2700 2800 2900 3000 3100 3200 3300 3400
Age (Ma)

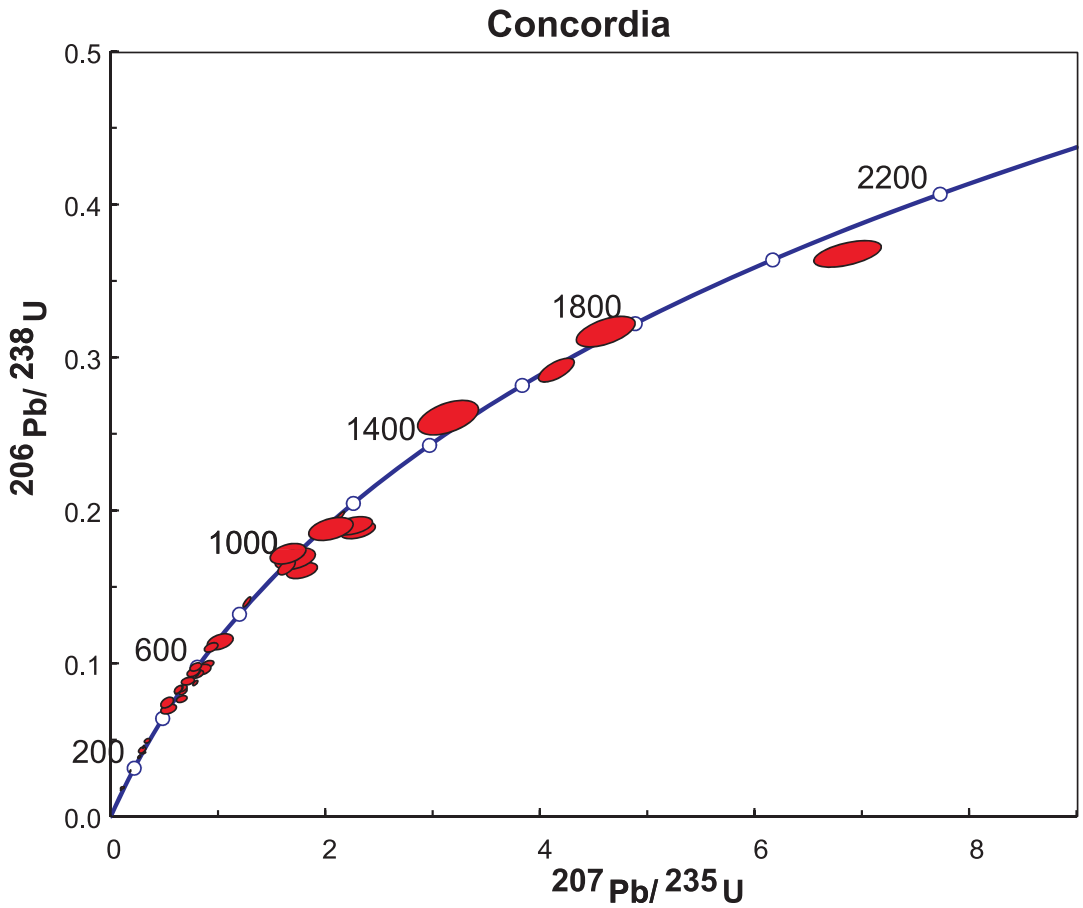
Concordia
0.5
0.4
0.3
0.2
0.1
0.0
206Pb/238U
2200
1800
1400
1000
600
200
0
2
4
6
8
207Pb/235U

74321

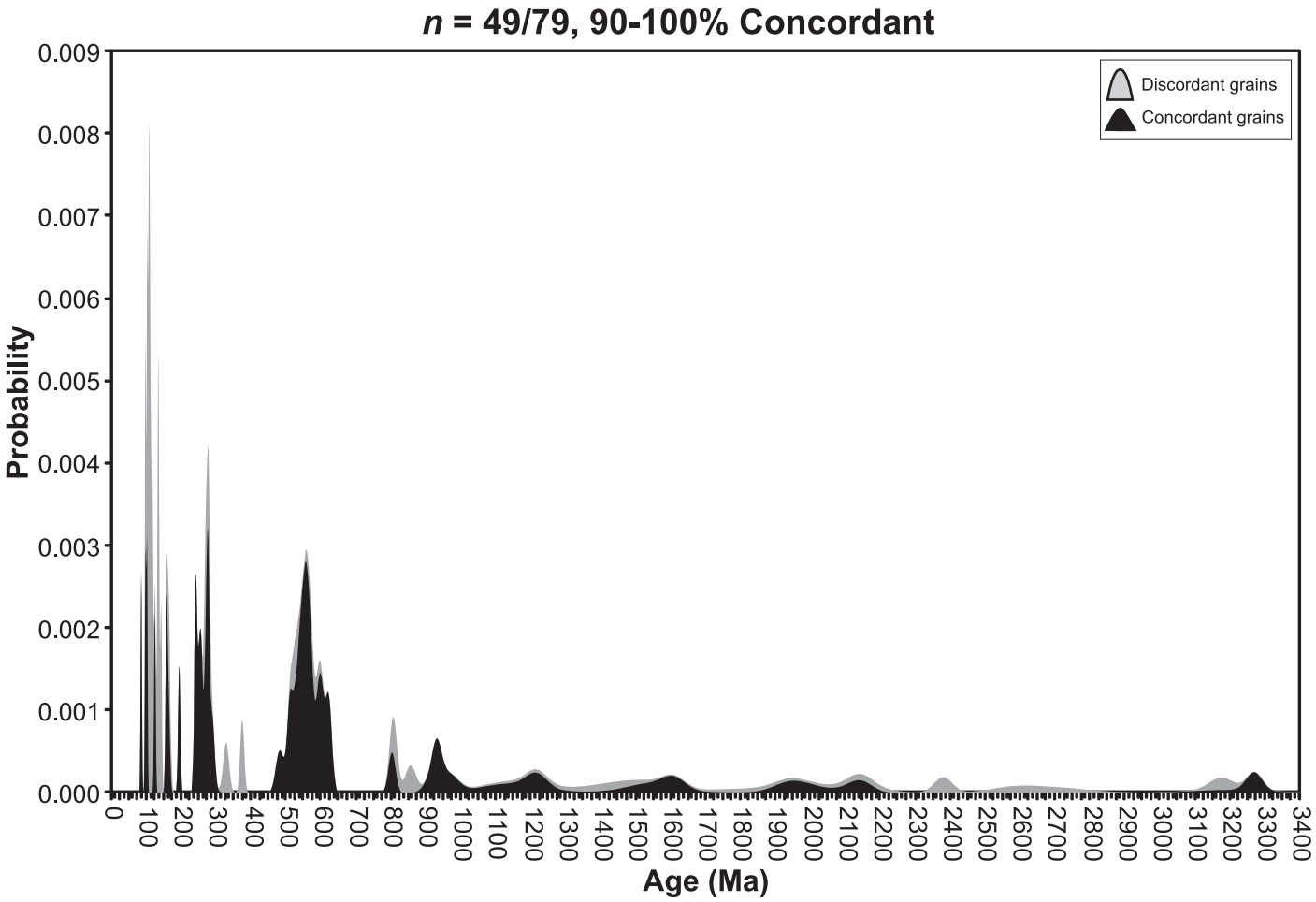
n = 49/79, 90-100% Concordant
Discordant grains
Concordant grains
Probability
0.009
0.008
0.007
0.006
0.005
0.004
0.003
0.002
0.001
0.000
0 100 200 300 400 500 600 700 800 900 1000 1100 1200 1300 1400 1500 1600 1700 1800 1900 2000 2100 2200 2300 2400 2500 2600 2700 2800 2900 3000 3100 3200 3300 3400
Age (Ma)

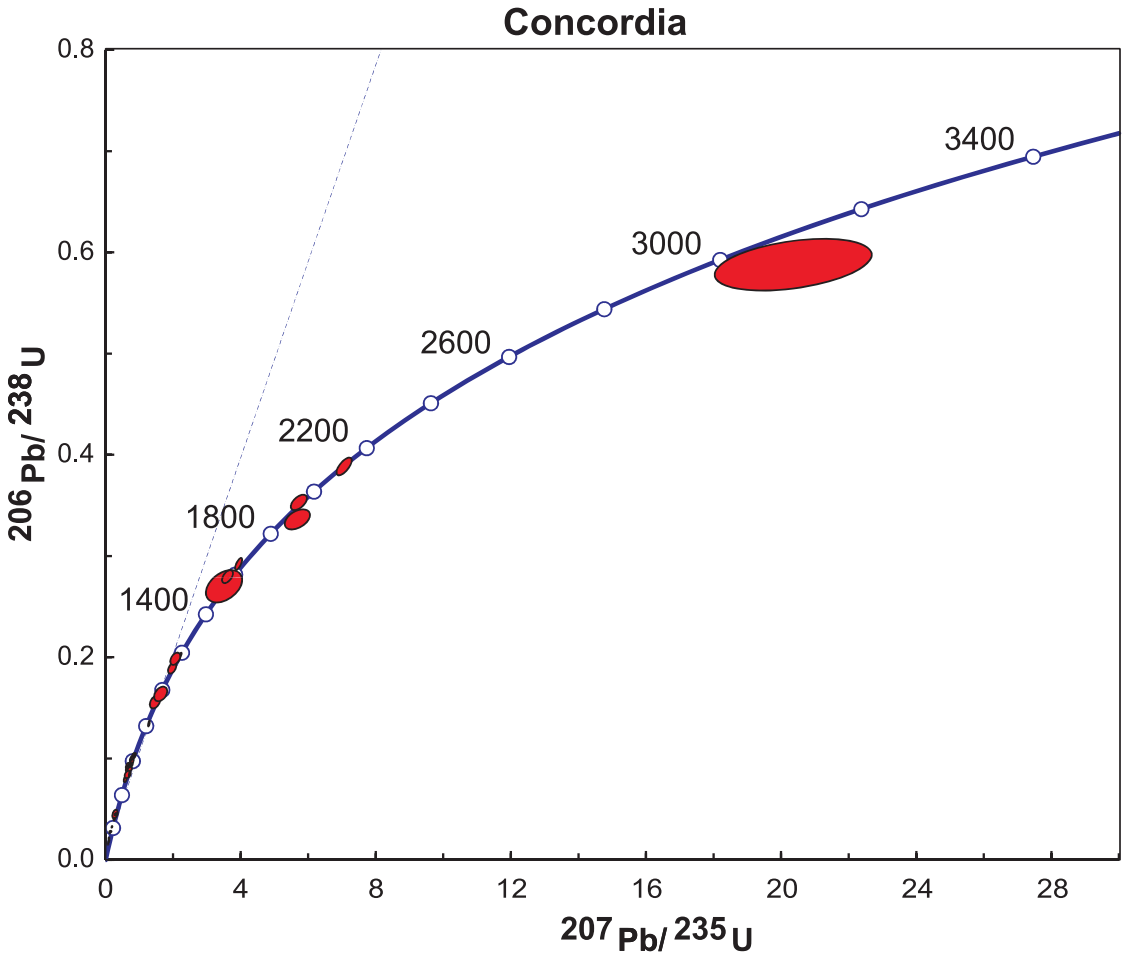
Concordia
0.8
0.6
0.4
0.2
0.0
206 Pb/ 238 U
0 4 8 12 16 20 24 28
207 Pb/ 235 U
3400
3000
2600
2200
1800
1400

74322

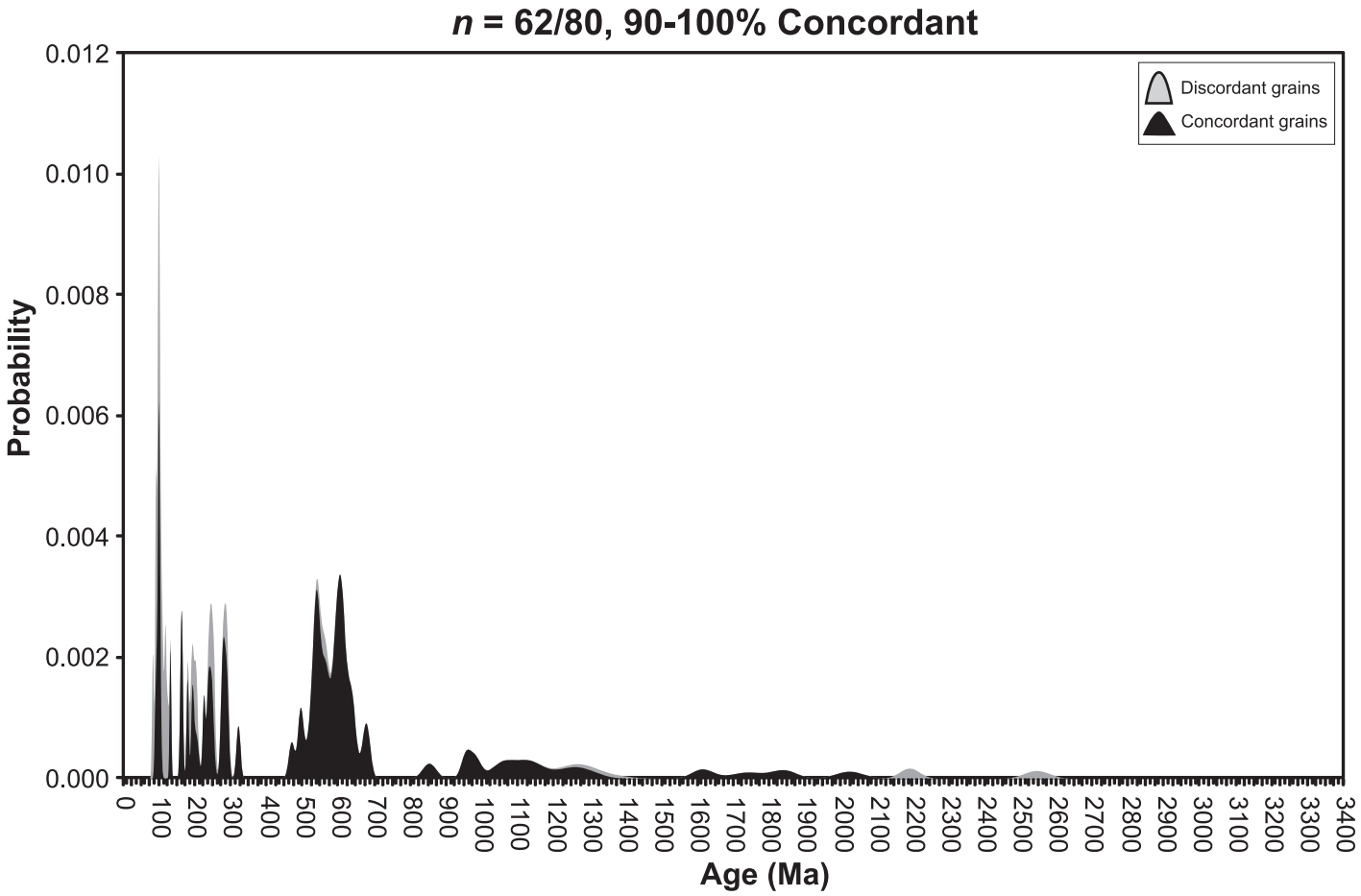
n = 62/80, 90-100% Concordant
Discordant grains
Concordant grains
Probability
0.012
0.010
0.008
0.006
0.004
0.002
0.000
0 100 200 300 400 500 600 700 800 900 1000 1100 1200 1300 1400 1500 1600 1700 1800 1900 2000 2100 2200 2300 2400 2500 2600 2700 2800 2900 3000 3100 3200 3300 3400
Age (Ma)

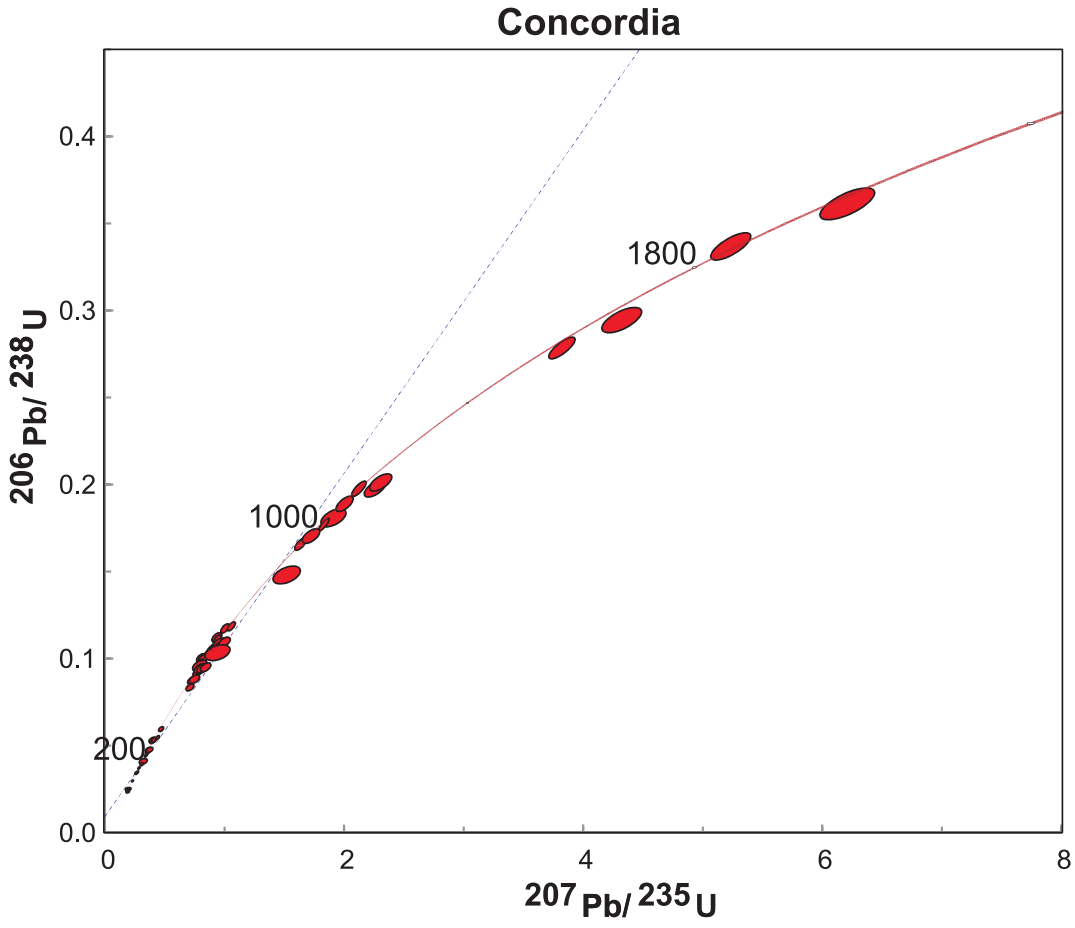
Concordia
206 Pb/ 238 U
0.4
0.3
0.2
0.1
0.0
1800
1000
200
0 2 4 6 8
207 Pb/ 235 U

74323

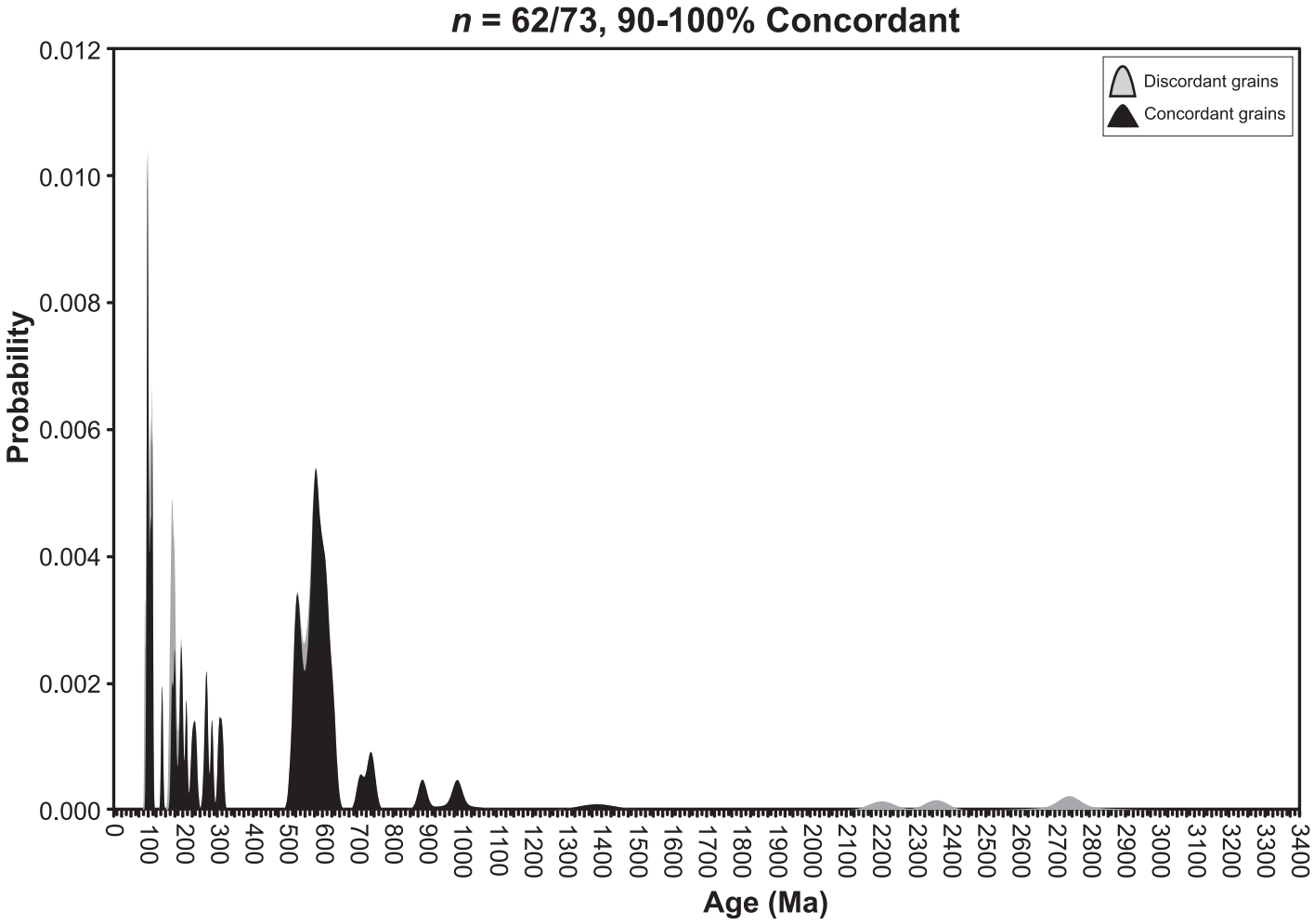
n = 62/73, 90-100% Concordant
Discordant grains
Concordant grains
Probability
0.012
0.010
0.008
0.006
0.004
0.002
0.000
0 100 200 300 400 500 600 700 800 900 1000 1100 1200 1300 1400 1500 1600 1700 1800 1900 2000 2100 2200 2300 2400 2500 2600 2700 2800 2900 3000 3100 3200 3300 3400
Age (Ma)

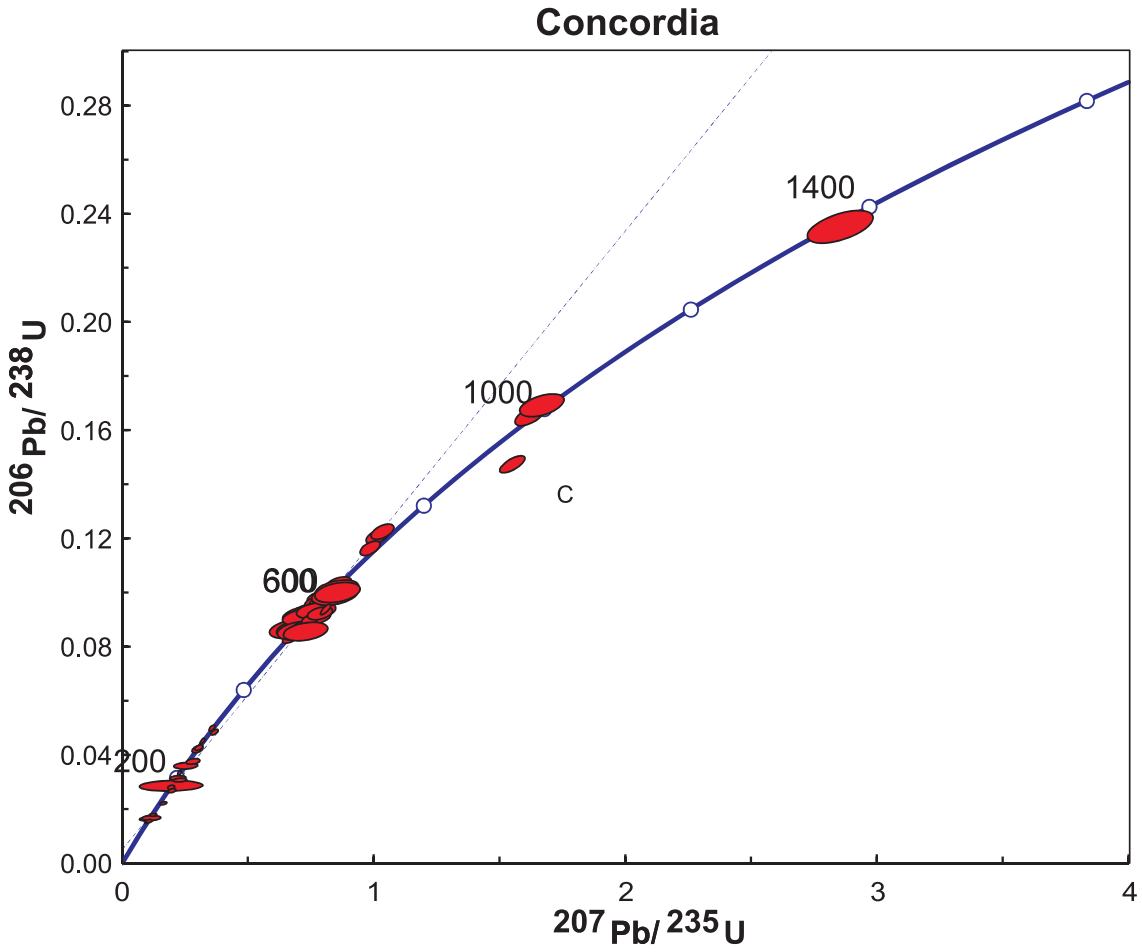
Concordia
206Pb/238U
0.28
0.24
0.20
0.16
0.12
0.08
0.04
0.00
0 1 2 3 4
207Pb/235U
1400
1000
600
200
C

74324

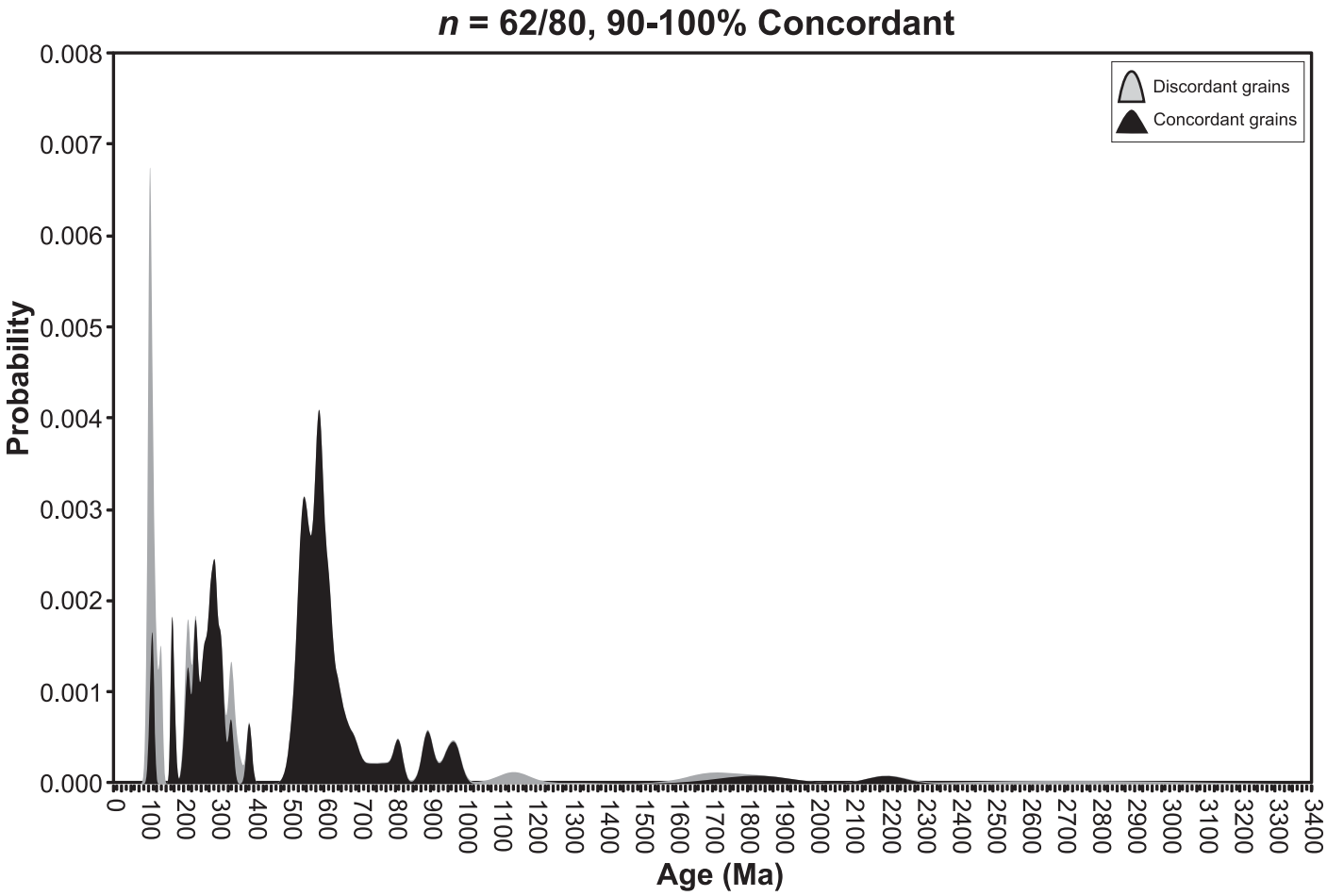
n = 62/80, 90-100% Concordant
Discordant grains
Concordant grains
Probability
0.008
0.007
0.006
0.005
0.004
0.003
0.002
0.001
0.000
0 100 200 300 400 500 600 700 800 900 1000 1100 1200 1300 1400 1500 1600 1700 1800 1900 2000 2100 2200 2300 2400 2500 2600 2700 2800 2900 3000 3100 3200 3300 3400
Age (Ma)

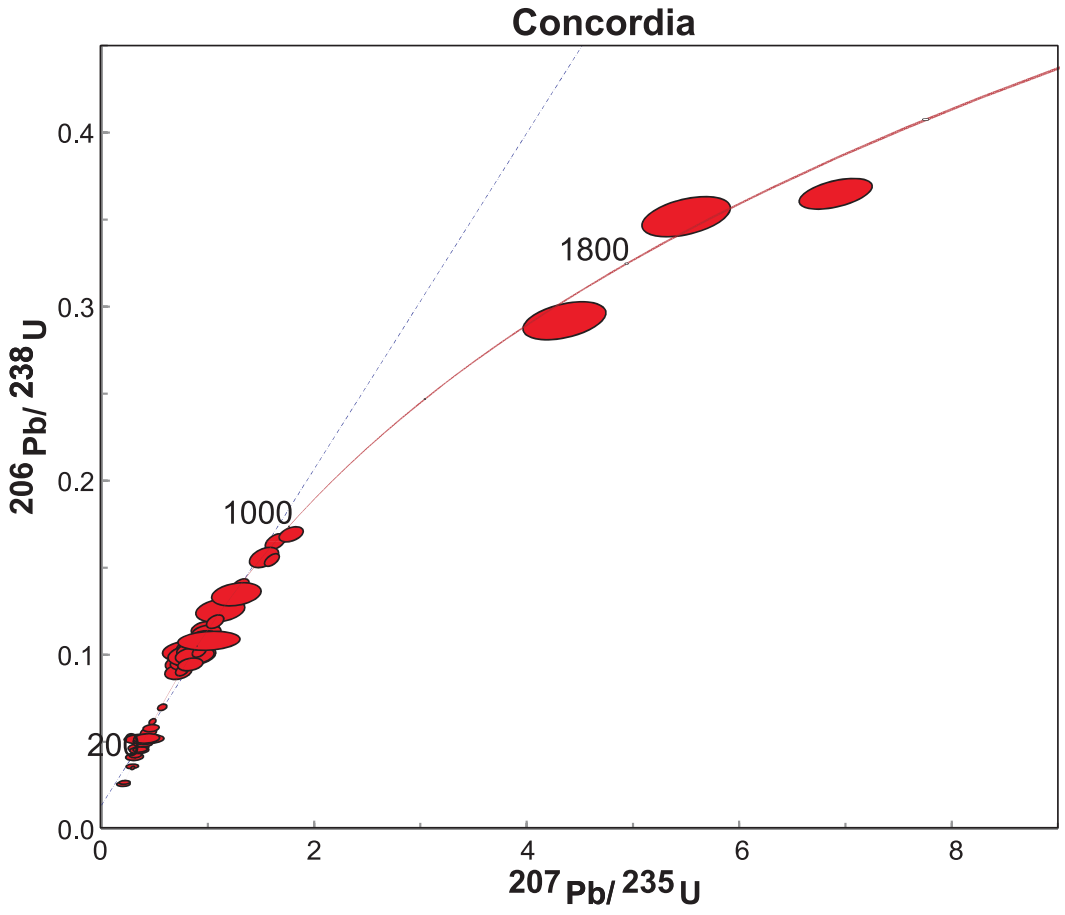
Concordia
1800
1000
206 Pb/ 238 U
207 Pb/ 235 U
0.0
0.1
0.2
0.3
0.4
0
2
4
6
8

74325

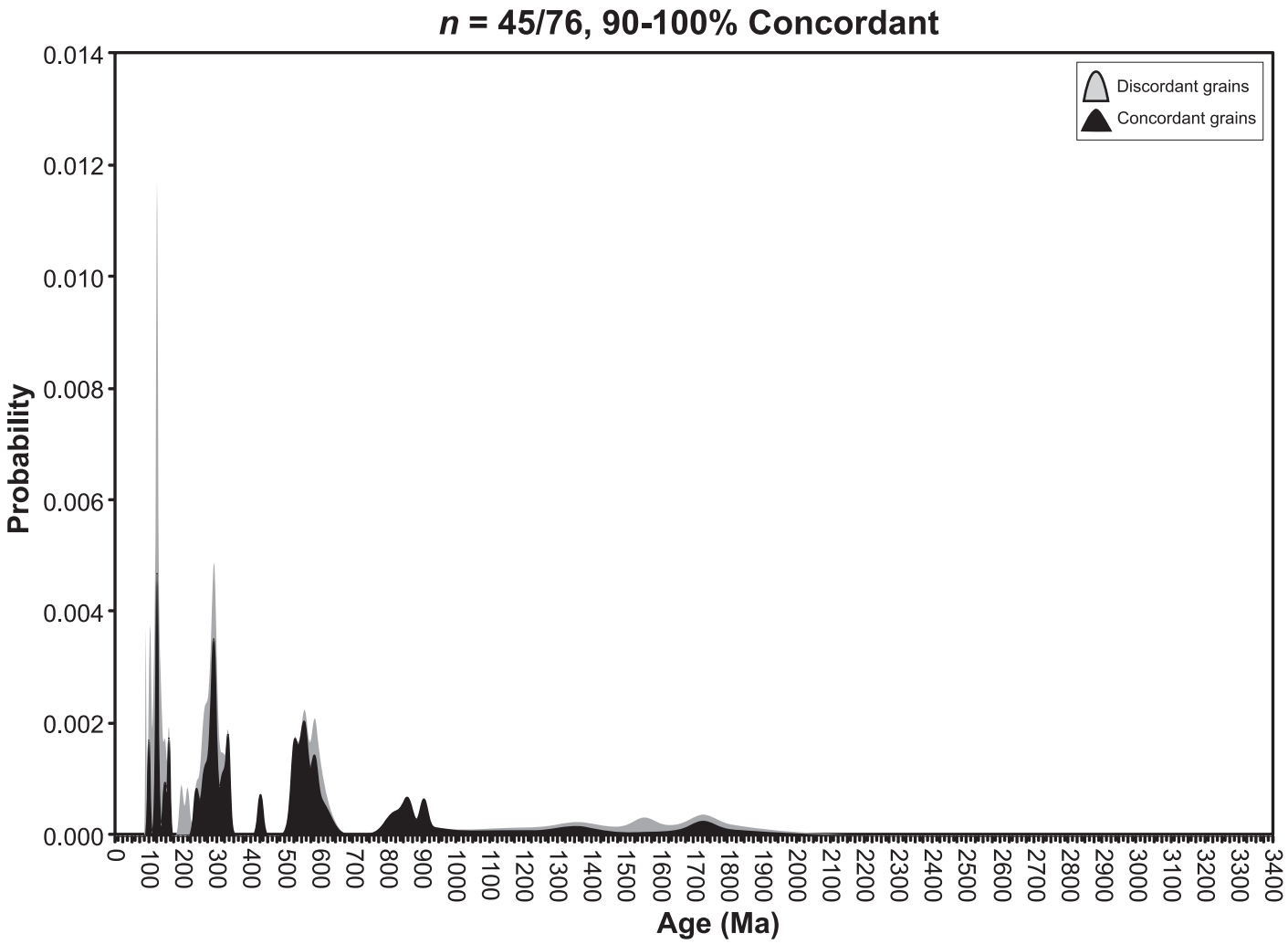
n = 45/76, 90-100% Concordant
Discordant grains
Concordant grains
Probability
0.014
0.012
0.010
0.008
0.006
0.004
0.002
0.000
0 100 200 300 400 500 600 700 800 900 1000 1100 1200 1300 1400 1500 1600 1700 1800 1900 2000 2100 2200 2300 2400 2500 2600 2700 2800 2900 3000 3100 3200 3300 3400
Age (Ma)

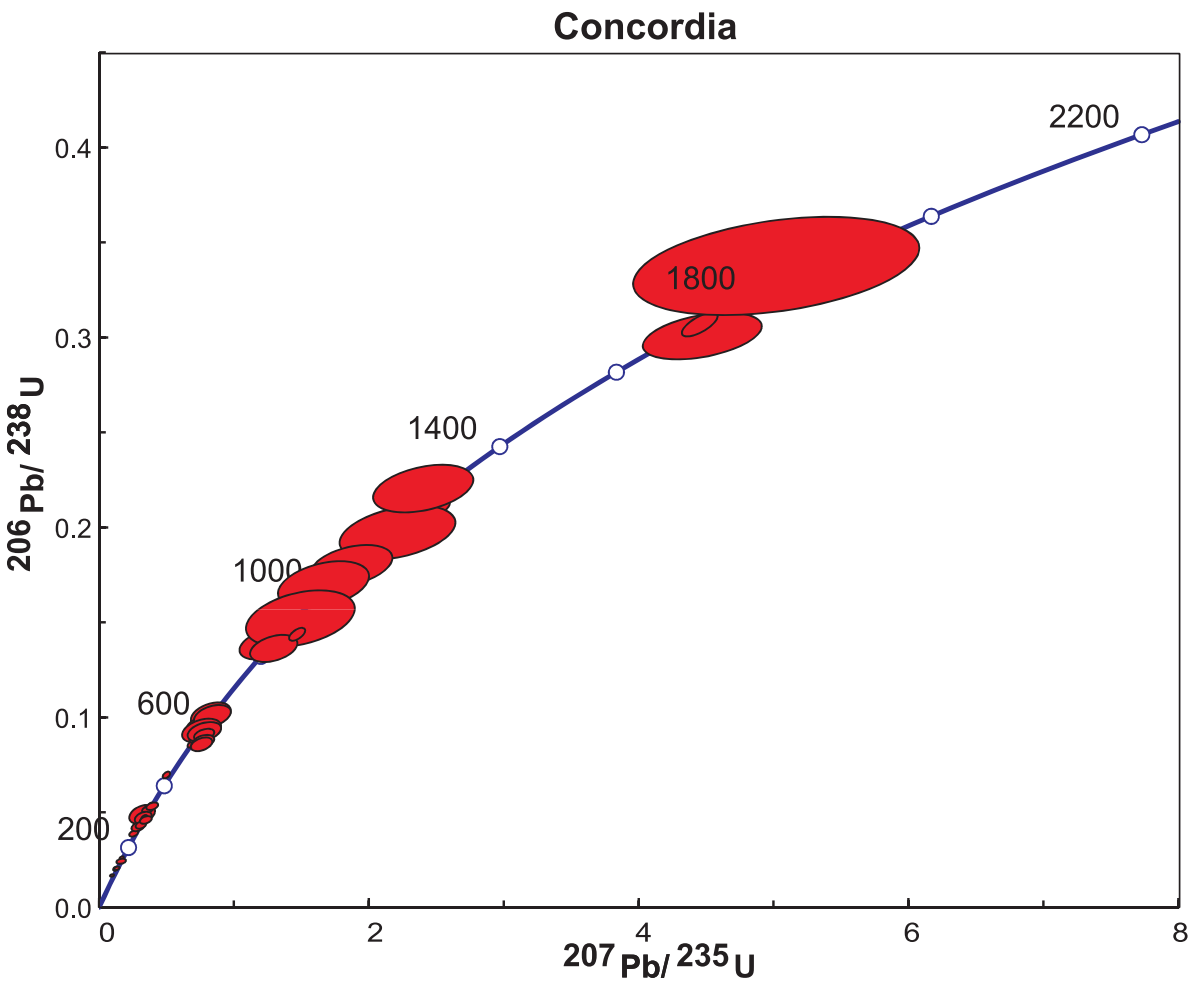
Concordia
2200
1800
1400
1000
600
200
0.4
0.3
0.2
0.1
0.0
0
2
4
6
8
206 Pb/ 238 U
207 Pb/ 235 U

74326

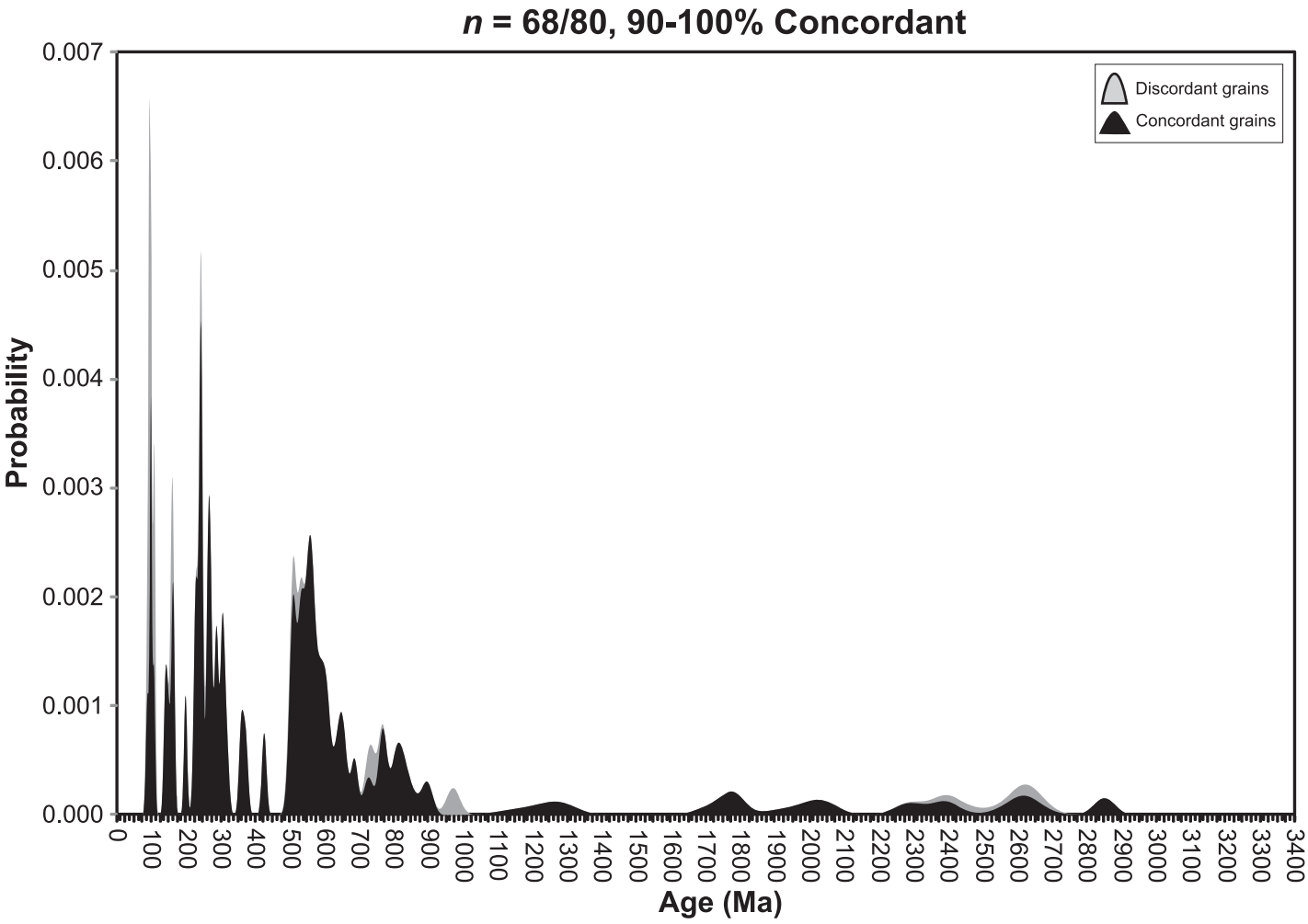
n = 68/80, 90-100% Concordant
Discordant grains
Concordant grains
Probability
0.007
0.006
0.005
0.004
0.003
0.002
0.001
0.000
0 100 200 300 400 500 600 700 800 900 1000 1100 1200 1300 1400 1500 1600 1700 1800 1900 2000 2100 2200 2300 2400 2500 2600 2700 2800 2900 3000 3100 3200 3300 3400
Age (Ma)

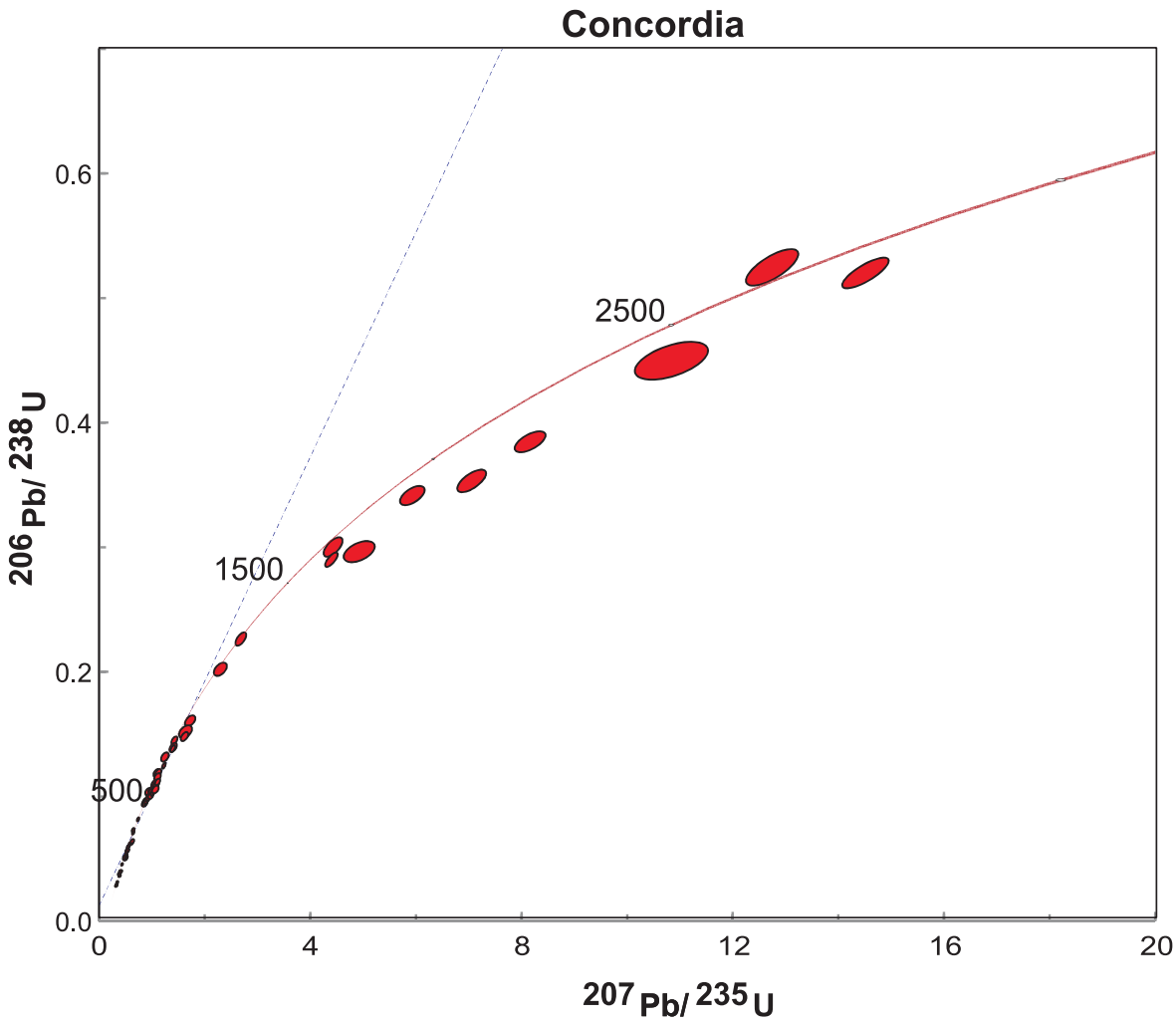
Concordia
0.6
0.4
0.2
0.0
2500
1500
500
0
4
8
12
16
20
206 Pb/ 238 U
207 Pb/ 235 U

Supplementary Data

LA-ICP-MS Methodology

Analytical procedures: LA–ICP–MS U–Pb zircon Geochronology

U–Pb geochronology was conducted using the Laser Ablation Inductively Coupled Plasma Mass Spectrometer (LA–ICP–MS) at Adelaide Microscopy, University of Adelaide. Samples for zircon geochronology were crushed using a jaw crusher, placed in a tungsten carbide mill for 3–5 seconds and sieved using 75 μm and 425 μm mesh, retaining a size fraction between 75–425 μm. Zircon grains were subsequently separated using traditional panning techniques, followed by removal of magnetic mineral grains from the heavier mineral fraction using conventional and neodymium magnets. Approximately 80 zircon grains per sample were randomly handpicked and mounted in epoxy resin. Mounted zircon grains were ground down to approximately half their width.

Epoxy mounts were imaged using a Phillips XL20 SEM with attached Gatan cathodoluminescence (CL) detector at Adelaide Microscopy to determine internal chemical zonation of zircon. A beam accelerating voltage of 12 kV was used, combined with a spot size of 7 when zircon mounts were imaged using CL detector.

U–Pb analysis of zircon was undertaken using an Agilent 7500cs ICPMS with a New Wave 213 nm Nd-YAG laser in a helium ablation atmosphere, following similar methods and operating procedures outlined by Payne et al. (2008; 2010). A laser spot size of 30 μm and repetition rate of 5 Hz was used for zircon analyses. A 40 second gas blank was initially measured followed by 60 seconds of zircon sample ablation. The laser was fired for 10 seconds with the shutter closed seconds prior to ablation in order to allow for beam and crystal stabilisation.

The real-time correction program Glitter version 4.0 (Griffin et al., 2008) was used to correct zircon data. Mass bias and fractionation were corrected for zircon analyses using the GEMOC standard GJ-1 (TIMS normalisation data: 207Pb/206Pb = 608.3 Ma, 206Pb/238U = 600.7 Ma and 207Pb/235U = 602.2 Ma, Jackson et al., 2004). An uncertainty of 1% was assigned to the age of the GJ-1 zircon standard for sample age error calculations to avoid inaccurate age reporting.

Over the duration of this study the reported average normalised ages for GJ-1 are 609.1 ± 6.0 Ma, 600.5 ± 1.4 Ma and 602.6 ± 1.3 Ma for the 207Pb/206Pb, 206Pb/238U and 207Pb/235U ratios. The ages used for provenance determination are 206Pb/238U ages for grains less than 1000 Ma, and 207Pb/206Pb ages for grains older than 1000 Ma. This cut-off is placed due to the well-known effect of a reduction in precision of 207Pb/206Pb ages in younger zircons (e.g. Ireland et al., 1998; Collins et al., 2007).

An internal standard, the Plesovice zircon standard (ID TIMS U-Pb 206Pb/238U age = 337.13 ± 0.37 Ma; Sláma et al., 2008) was used to assess accuracy before and during the analysis of unknowns. Average Plesovice ages obtained during this study were 207Pb/235U = 340.7 ± 2.1 Ma, 207Pb/206Pb = 342 ± 11 Ma and 206Pb/238U = 340.6 ± 2.3 Ma.

Conventional concordia, weighted averages, and probability density distribution plots were generated using Isoplot vers. 4.11 (Ludwig, 2003). Due to the inability of the LA-ICP-MS to measure common Pb, correction for the unknowns was carried out

using the 'CommPbcorr' macro in Microsoft Excel (Andersen, 2002). In most samples, negligible (<0.5% 206Pb) common Pb was inferred in the analyses when the 3D concordia method was employed by 'CommPbcorr'.

References

Andersen, T. 2002. Correction of common lead in U–Pb analyses that do not report Pb-204. *Chemical Geology*, **192** (1/2), 59-79.

Collins, A.S., Santosh, M., Braun, I. & Clark, C. 2007. Age and sedimentary provenance of the Southern Granulites, South India: U–Th–Pb SHRIMP secondary ion mass spectrometry. *Precambrian Research*, **155** (1/2), 125-138.

Griffin, W.L., Powell, W.J., Pearson, N.J., & O'Reilly, S.Y. 2008. GLITTER: data reduction software for laser ablation ICP-MS. *In:* Sylvester, P., (ed) *Laser Ablation ICP-MS in the Earth Sciences: Current Practices and Outstanding Issues, Mineralogical Association of Canada. Short Course Series,* **40**, 308-311.

Ireland, T.R., Flottmann, T., Fanning, C.M., Gibson, G.M. & Preiss, W.V. 1998. Development of the early Paleozoic Pacific margin of Gondwana from detrital-zircon ages across the Delamerian orogen. *Geology*, **26** (3), 243-246.

Jackson, S.E., Pearson, N.J., Griffin, W.L., & Belousova, E.A. 2004. The application of laser ablation-inductively coupled plasma-mass spectrometry to in-situ U/Pb zircon geochronology. *Chemical Geology*, **211**, 47-69.

Ludwig, K.R. 2003. User's Manual for Isoplot 3.00. *Berkeley Geochronological Center, Special Publication,* **4**, 71.

Payne, J.L., Ferris, G., Barovich, K.M., & Hand, M. 2010. Pitfalls of classifying ancient magmatic suites with tectonic discrimination diagrams: An example from the Paleoproterozoic Tunkillia Suite, southern Australia. *Precambrian Research*, **177**, 227-240.

Payne, J.L., Hand, M., Barovich, K.M., & Wade, B.P. 2008. Temporal constraints on the timing of high-grade metamorphism in the northern Gawler Craton; implications for assembly of the Australian Proterozoic. *Australian Journal of Earth Sciences*, **55**, 623-640.

Sláma, J., Kosler, J., Condon, D.J., Crowley, J.L., Gerdes, A., Hanchar, J.M., Horstwood, M.S.A., Morris, G.A., Nasdala, L., Norberg, N., Schaltegger, U., Schoene, B., Tubrett, M.N., & Whitehouse, M.J. 2008. Plesovice zircon – A new natural reference material for U-Pb and Hf isotopic microanalysis. *Chemical Geology*, **249**, 1-35.

Supplementary Data

Zircon Fission Track Data

GC743-17 Zircon
Counted by: PFG

Gnarly Knots-1 1825-1950m

Slide ref	Current grain no	N_s	N_i	N_a	ρ_s	ρ_i	RATIO	U (ppm)	F.T. AGE (Ma)	
G1098-5	2	260	70	40	1.033E+07	2.781E+06	3.714	91.8	257.8 ±	35.2
G1098-5	3	287	93	40	1.140E+07	3.695E+06	3.086	121.9	214.9 ±	26.1
G1098-5	6	294	50	40	1.168E+07	1.986E+06	5.880	65.6	403.5 ±	62.4
G1098-5	7	509	76	30	2.696E+07	4.026E+06	6.697	132.9	457.6 ±	57.2
G1098-5	9	121	104	50	3.846E+06	3.305E+06	1.163	109.1	81.9 ±	11.1
G1098-5	10	187	64	21	1.415E+07	4.843E+06	2.922	159.8	203.6 ±	29.8
G1098-5	11	149	48	20	1.184E+07	3.814E+06	3.104	125.9	216.1 ±	36.2
G1098-5	13	229	85	40	9.097E+06	3.377E+06	2.694	111.5	188.0 ±	24.2
G1098-5	16	272	125	40	1.081E+07	4.966E+06	2.176	163.9	152.3 ±	16.8
G1098-5	18	360	196	50	1.144E+07	6.229E+06	1.837	205.6	128.8 ±	11.8
G1098-5	22	393	68	40	1.561E+07	2.701E+06	5.779	89.2	396.8 ±	52.8
G1098-5	23	233	144	40	9.256E+06	5.721E+06	1.618	188.8	113.6 ±	12.3
G1098-5	24	227	97	50	7.214E+06	3.083E+06	2.340	101.8	163.6 ±	20.2
G1098-5	25	465	75	40	1.847E+07	2.980E+06	6.200	98.3	424.7 ±	53.7
G1098-5	31	272	80	40	1.081E+07	3.178E+06	3.400	104.9	236.4 ±	30.5
G1098-5	32	188	40	30	9.958E+06	2.119E+06	4.700	69.9	324.5 ±	57.0
G1098-5	33	158	24	30	8.369E+06	1.271E+06	6.583	42.0	450.1 ±	99.1
		4604	1439		1.141E+07	3.567E+06		117.7		

Area of basic unit = 6.293E-07 cm^{-2}
χ^2 = 289.301 with 16 degrees of freedom
P(χ^2) = 0.0%
Age Dispersion = 49.140%

Ns / Ni = 3.199 ± 0.097
Mean Ratio = 3.759 ± 0.447

Ages calculated using a zeta of 87.7 ± 0.8 for U3 glass
ρ_D = 1.615E+06cm^{-2} ND = 2478
ρ_D interpolated between top of can; ρ_D = 1.644E+06cm^{-2} ND = 1293
bottom of can; ρ_D = 1.506E+06cm^{-2} ND = 1185

POOLED AGE = 222.7 ± 8.3 Ma
CENTRAL AGE = 216.9 ± 27.1 Ma

A:

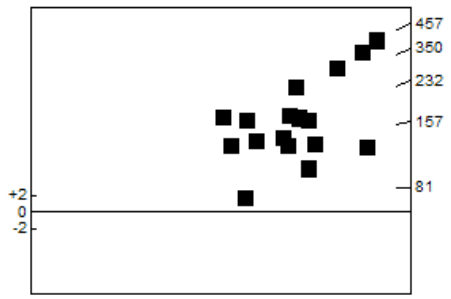

GC743-18 Zircon
Counted by: PFG

Gnarly Knots-1 2500-2600m

Slide ref	Current grain no	N_s	N_i	N_a	ρ_s	ρ_i	RATIO	U (ppm)	F.T. AGE (Ma)	
G1098-6	1	98	43	12	1.298E+07	5.694E+06	2.279	188.8	158.7 ±	29.2
G1098-6	4	162	76	20	1.287E+07	6.038E+06	2.132	200.2	148.5 ±	20.9
G1098-6	5	111	58	9	1.960E+07	1.024E+07	1.914	339.5	133.5 ±	21.8
G1098-6	6	92	98	38	3.847E+06	4.098E+06	0.939	135.9	65.8 ±	9.7
G1098-6	7	162	111	50	5.149E+06	3.528E+06	1.459	117.0	102.1 ±	12.8
G1098-6	8	73	28	25	4.640E+06	1.780E+06	2.607	59.0	181.2 ±	40.5
G1098-6	10	145	37	20	1.152E+07	2.940E+06	3.919	97.5	270.5 ±	50.2
G1098-6	11	117	80	28	6.640E+06	4.540E+06	1.462	150.5	102.3 ±	15.0
G1098-6	16	264	192	50	8.390E+06	6.102E+06	1.375	202.3	96.2 ±	9.4
G1098-6	23	225	54	40	8.939E+06	2.145E+06	4.167	71.1	287.2 ±	44.0
G1098-6	24	163	40	20	1.295E+07	3.178E+06	4.075	105.4	281.0 ±	50.0
G1098-6	28	165	93	40	6.555E+06	3.695E+06	1.774	122.5	123.9 ±	16.3
G1098-6	29	116	104	60	3.072E+06	2.754E+06	1.115	91.3	78.2 ±	10.7
G1098-6	31	212	133	80	4.211E+06	2.642E+06	1.594	87.6	111.4 ±	12.6
G1098-6	33	108	45	24	7.151E+06	2.980E+06	2.400	98.8	167.0 ±	29.9
G1098-6	38	555	304	100	8.819E+06	4.831E+06	1.826	160.2	127.4 ±	9.5
G1098-6	39	100	165	40	3.973E+06	6.555E+06	0.606	217.3	42.6 ±	5.5
G1098-6	44	90	47	25	5.721E+06	2.987E+06	1.915	99.0	133.6 ±	24.2
G1098-6	49	217	55	20	1.724E+07	4.370E+06	3.945	144.9	272.3 ±	41.5
G1098-6	56	203	54	20	1.613E+07	4.290E+06	3.759	142.3	259.7 ±	40.2
		3378	1817		7.445E+06	4.005E+06		132.8		

Area of basic unit = 6.293E-07 cm^{-2}
χ^2 = 266.059 with 19 degrees of freedom
P(χ^2) = 0.0%
Age Dispersion = 48.024%

Ns / Ni = 1.859 ± 0.054
Mean Ratio = 2.263 ± 0.251

Ages calculated using a zeta of 87.7 ± 0.8 for U3 glass
ρ_D = 1.608E+06cm^{-2} ND = 2478
ρ_D interpolated between top of can; ρ_D = 1.644E+06cm^{-2} ND = 1293
bottom of can; ρ_D = 1.506E+06cm^{-2} ND = 1185

POOLED AGE = 129.7 ± 4.7 Ma
CENTRAL AGE = 134.1 ± 15.3 Ma

A:

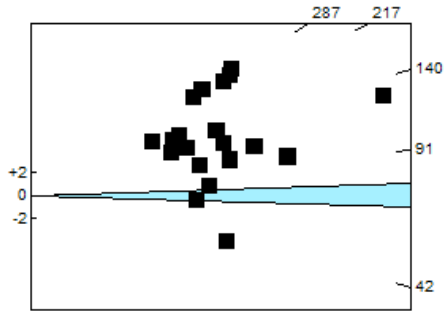

GC743-19 Zircon
Counted by: PFG

Gnarly Knots-1 2890-2990m

Slide ref	Current grain no	N_s	N_i	N_a	ρ_s	ρ_i	RATIO	U (ppm)	F.T. AGE (Ma)	
G1098-7	1	183	101	40	7.270E+06	4.012E+06	1.812	133.6	125.9 ±	15.9
G1098-7	4	272	53	40	1.081E+07	2.106E+06	5.132	70.1	350.4 ±	53.2
G1098-7	6	143	58	20	1.136E+07	4.608E+06	2.466	153.5	170.7 ±	26.8
G1098-7	10	188	40	20	1.494E+07	3.178E+06	4.700	105.8	321.7 ±	56.5
G1098-7	11	142	51	20	1.128E+07	4.052E+06	2.784	135.0	192.5 ±	31.7
G1098-7	13	97	69	40	3.853E+06	2.741E+06	1.406	91.3	97.9 ±	15.6
G1098-7	15	173	80	40	6.873E+06	3.178E+06	2.162	105.8	150.0 ±	20.5
G1098-7	16	103	76	25	6.547E+06	4.831E+06	1.355	160.9	94.4 ±	14.4
G1098-7	17	208	137	50	6.611E+06	4.354E+06	1.518	145.0	105.7 ±	11.9
G1098-7	19	104	85	50	3.305E+06	2.701E+06	1.224	90.0	85.3 ±	12.6
G1098-7	21	139	26	20	1.104E+07	2.066E+06	5.346	68.8	364.7 ±	78.3
G1098-7	26	98	66	25	6.229E+06	4.195E+06	1.485	139.7	103.4 ±	16.6
G1098-7	27	303	100	50	9.630E+06	3.178E+06	3.030	105.8	209.2 ±	24.6
G1098-7	38	126	24	25	8.009E+06	1.526E+06	5.250	50.8	358.3 ±	80.2
G1098-7	43	161	90	50	5.117E+06	2.860E+06	1.789	95.3	124.3 ±	16.6
G1098-7	44	167	96	50	5.307E+06	3.051E+06	1.740	101.6	120.9 ±	15.7
G1098-7	45	197	207	100	3.130E+06	3.289E+06	0.952	109.6	66.4 ±	6.8
G1098-7	47	214	200	50	6.801E+06	6.356E+06	1.070	211.7	74.7 ±	7.5
G1098-7	48	248	192	80	4.926E+06	3.814E+06	1.292	127.0	90.0 ±	8.9
G1098-7	59	141	124	50	4.481E+06	3.941E+06	1.137	131.3	79.3 ±	9.9
		3407	1875		6.407E+06	3.526E+06		117.4		

Area of basic unit = 6.293E-07 cm^{-2}
χ^2 = 289.086 with 19 degrees of freedom
P(χ^2) = 0.0%
Age Dispersion = 47.803%

Ns / Ni = 1.817 ± 0.052
Mean Ratio = 2.382 ± 0.337

Ages calculated using a zeta of 87.7 ± 0.8 for U3 glass
ρ_D = 1.600E+06cm^{-2} ND = 2478
ρ_D interpolated between top of can; ρ_D = 1.644E+06cm^{-2} ND = 1293
bottom of can; ρ_D = 1.506E+06cm^{-2} ND = 1185

POOLED AGE = 126.3 ± 4.6 Ma
CENTRAL AGE = 133.1 ± 15.1 Ma

A:

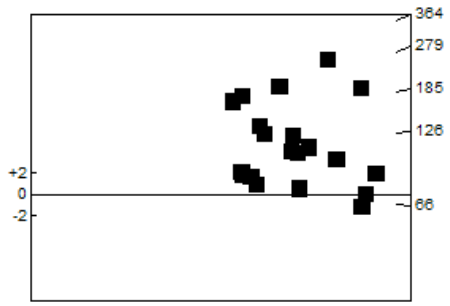

GC743-20 Zircon
Counted by: PFG

Gnarly Knots-1 3400-3500m

Slide ref	Current grain no	N_s	N_i	N_a	ρ_s	ρ_i	RATIO	U (ppm)	F.T. AGE (Ma)	
G1098-8	1	83	82	16	8.243E+06	8.144E+06	1.012	272.5	70.3 ±	11.1
G1098-8	3	115	34	15	1.218E+07	3.602E+06	3.382	120.5	232.1 ±	45.6
G1098-8	4	174	63	20	1.382E+07	5.006E+06	2.762	167.5	190.1 ±	28.3
G1098-8	5	90	71	16	8.939E+06	7.051E+06	1.268	235.9	88.0 ±	14.1
G1098-8	10	118	60	25	7.500E+06	3.814E+06	1.967	127.6	135.9 ±	21.8
G1098-8	11	251	120	40	9.971E+06	4.767E+06	2.092	159.5	144.5 ±	16.3
G1098-8	12	85	49	24	5.628E+06	3.244E+06	1.735	108.5	120.1 ±	21.7
G1098-8	18	146	28	25	9.280E+06	1.780E+06	5.214	59.5	354.3 ±	73.5
G1098-8	20	71	93	24	4.701E+06	6.158E+06	0.763	206.0	53.1 ±	8.5
G1098-8	27	63	43	20	5.006E+06	3.416E+06	1.465	114.3	101.5 ±	20.2
G1098-8	28	102	69	28	5.789E+06	3.916E+06	1.478	131.0	102.5 ±	16.1
G1098-8	36	145	151	18	1.280E+07	1.333E+07	0.960	446.0	66.7 ±	7.9
G1098-8	38	101	19	25	6.420E+06	1.208E+06	5.316	40.4	361.1 ±	90.6
G1098-8	39	40	42	25	2.543E+06	2.670E+06	0.952	89.3	66.2 ±	14.7
G1098-8	40	89	36	20	7.071E+06	2.860E+06	2.472	95.7	170.4 ±	33.9
G1098-8	47	78	53	25	4.958E+06	3.369E+06	1.472	112.7	102.0 ±	18.3
G1098-8	48	118	17	15	1.250E+07	1.801E+06	6.941	60.3	467.5 ±	121.7
G1098-8	50	131	48	50	4.163E+06	1.526E+06	2.729	51.0	187.9 ±	32.0
G1098-8	53	94	17	15	9.958E+06	1.801E+06	5.529	60.3	375.2 ±	99.2
G1098-8	58	77	44	24	5.098E+06	2.913E+06	1.750	97.5	121.1 ±	23.0
		2171	1139		7.340E+06	3.851E+06		128.8		

Area of basic unit = 6.293E-07 cm^{-2}
χ^2 = 226.367 with 19 degrees of freedom
P(χ^2) = 0.0%
Age Dispersion = 54.637%

Ns / Ni = 1.906 ± 0.070
Mean Ratio = 2.563 ± 0.402

Ages calculated using a zeta of 87.7 ± 0.8 for U3 glass
ρ_D = 1.593E+06cm^{-2} ND = 2478
ρ_D interpolated between top of can; ρ_D = 1.644E+06cm^{-2} ND = 1293
bottom of can; ρ_D = 1.506E+06cm^{-2} ND = 1185

POOLED AGE = 131.8 ± 5.6 Ma
CENTRAL AGE = 134.7 ± 17.5 Ma

A:

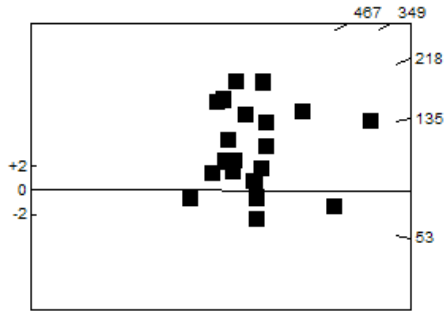

GC743-21 Zircon
Counted by: PFG

Gnarly Knots-1 3800-3900m

Slide ref	Current grain no	N_s	N_i	N_a	ρ_s	ρ_i	RATIO	U (ppm)	F.T. AGE (Ma)	
G1098-9	1	223	53	25	1.417E+07	3.369E+06	4.208	113.2	286.2 ±	44.2
G1098-9	3	258	38	50	8.200E+06	1.208E+06	6.789	40.6	455.7 ±	79.8
G1098-9	4	110	55	25	6.992E+06	3.496E+06	2.000	117.5	137.6 ±	22.9
G1098-9	14	63	31	20	5.006E+06	2.463E+06	2.032	82.8	139.8 ±	30.8
G1098-9	15	81	28	21	6.129E+06	2.119E+06	2.893	71.2	198.1 ±	43.6
G1098-9	22	95	37	9	1.677E+07	6.533E+06	2.568	219.6	176.1 ±	34.4
G1098-9	23	159	33	20	1.263E+07	2.622E+06	4.818	88.1	326.7 ±	62.9
G1098-9	24	180	98	20	1.430E+07	7.786E+06	1.837	261.7	126.5 ±	16.1
G1098-9	25	147	59	30	7.786E+06	3.125E+06	2.492	105.0	171.0 ±	26.6
G1098-9	28	85	62	20	6.754E+06	4.926E+06	1.371	165.6	94.6 ±	15.9
G1098-9	30	113	114	100	1.796E+06	1.812E+06	0.991	60.9	68.6 ±	9.2
G1098-9	31	119	36	25	7.564E+06	2.288E+06	3.306	76.9	225.9 ±	43.3
G1098-9	34	223	68	20	1.772E+07	5.403E+06	3.279	181.6	224.1 ±	31.4
G1098-9	36	103	18	20	8.184E+06	1.430E+06	5.722	48.1	386.1 ±	99.0
G1098-9	38	109	31	20	8.660E+06	2.463E+06	3.516	82.8	240.0 ±	49.1
G1098-9	40	257	41	20	2.042E+07	3.258E+06	6.268	109.5	421.8 ±	71.5
G1098-9	47	106	63	18	9.358E+06	5.562E+06	1.683	186.9	116.0 ±	18.6
G1098-9	50	197	144	20	1.565E+07	1.144E+07	1.368	384.5	94.4 ±	10.6
G1098-9	57	154	67	20	1.224E+07	5.323E+06	2.299	178.9	157.9 ±	23.4
G1098-9	66	78	76	40	3.099E+06	3.019E+06	1.026	101.5	71.0 ±	11.5
		2860	1152		8.370E+06	3.371E+06		113.3		

Area of basic unit = 6.293E-07 cm^{-2}
χ^2 = 256.280 with 19 degrees of freedom
P(χ^2) = 0.0%
Age Dispersion = 51.244%

Ns / Ni = 2.483 ± 0.087
Mean Ratio = 3.023 ± 0.387

Ages calculated using a zeta of 87.7 ± 0.8 for U3 glass
ρ_D = 1.586E+06cm^{-2} ND = 2478
ρ_D interpolated between top of can; ρ_D = 1.644E+06cm^{-2} ND = 1293
bottom of can; ρ_D = 1.506E+06cm^{-2} ND = 1185

POOLED AGE = 170.4 ± 7.0 Ma
CENTRAL AGE = 167.4 ± 20.4 Ma

A:

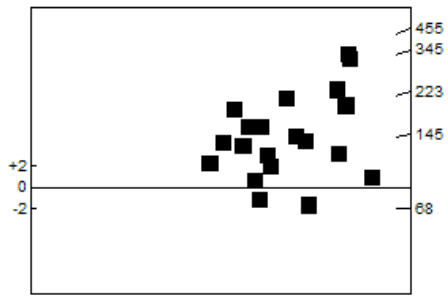

GC743-22 Zircon
Counted by: PFG

Gnarly Knots-1 4000-4110m

Slide ref	Current grain no	N_s	N_i	N_a	ρ_s	ρ_i	RATIO	U (ppm)	F.T. AGE (Ma)	
G1098-1	5	134	47	25	8.517E+06	2.987E+06	2.851	100.9	194.4 ±	33.2
G1098-1	6	160	62	24	1.059E+07	4.105E+06	2.581	138.6	176.2 ±	26.6
G1098-1	8	117	102	16	1.162E+07	1.013E+07	1.147	342.0	78.9 ±	10.8
G1098-1	10	145	93	25	9.217E+06	5.911E+06	1.559	199.6	107.0 ±	14.4
G1098-1	16	118	144	36	5.209E+06	6.356E+06	0.819	214.6	56.5 ±	7.1
G1098-1	18	72	55	15	7.628E+06	5.827E+06	1.309	196.7	90.0 ±	16.2
G1098-1	19	93	47	12	1.232E+07	6.224E+06	1.979	210.1	135.5 ±	24.4
G1098-1	27	175	222	30	9.270E+06	1.176E+07	0.788	397.0	54.3 ±	5.6
G1098-1	28	192	48	16	1.907E+07	4.767E+06	4.000	161.0	271.1 ±	44.2
G1098-1	32	227	69	20	1.804E+07	5.482E+06	3.290	185.1	223.8 ±	31.2
G1098-1	33	118	99	50	3.750E+06	3.146E+06	1.192	106.2	82.0 ±	11.3
G1098-1	38	121	107	30	6.409E+06	5.668E+06	1.131	191.4	77.8 ±	10.5
G1098-1	39	321	99	40	1.275E+07	3.933E+06	3.242	132.8	220.6 ±	25.8
G1098-1	42	98	71	16	9.733E+06	7.051E+06	1.380	238.1	94.8 ±	14.9
G1098-1	44	133	53	40	5.284E+06	2.106E+06	2.509	71.1	171.4 ±	28.1
G1098-1	45	74	24	25	4.704E+06	1.526E+06	3.083	51.5	210.0 ±	49.5
G1098-1	46	63	17	15	6.674E+06	1.801E+06	3.706	60.8	251.6 ±	69.0
G1098-1	55	189	60	25	1.201E+07	3.814E+06	3.150	128.8	214.5 ±	32.1
G1098-1	57	363	114	40	1.442E+07	4.529E+06	3.184	152.9	216.7 ±	23.8
G1098-1	63	102	85	40	4.052E+06	3.377E+06	1.200	114.0	82.5 ±	12.3
		3015	1618		8.872E+06	4.761E+06		160.8		

Area of basic unit = 6.293E-07 cm^{-2}
χ^2 = 309.550 with 19 degrees of freedom
P(χ^2) = 0.0%
Age Dispersion = 49.262%

Ns / Ni = 1.863 ± 0.057
Mean Ratio = 2.205 ± 0.236

Ages calculated using a zeta of 87.7 ± 0.8 for U3 glass
ρ_D = 1.579E+06cm^{-2} ND = 2478
ρ_D interpolated between top of can; ρ_D = 1.644E+06cm^{-2} ND = 1293
bottom of can; ρ_D = 1.506E+06cm^{-2} ND = 1185

POOLED AGE = 127.7 ± 4.8 Ma
CENTRAL AGE = 127.8 ± 15.0 Ma

A:

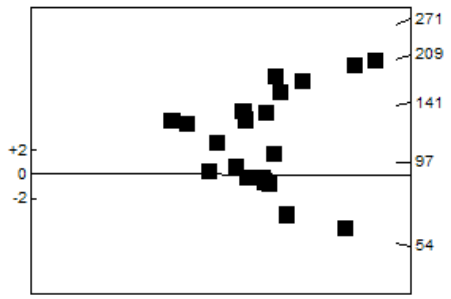

GC743-23 Zircon
Counted by: PFG

Gnarly Knots-1 4200-4300m

Slide ref	Current grain no	N_s	N_i	N_a	ρ_s	ρ_i	RATIO	U (ppm)	F.T. AGE (Ma)	
G1098-1	1	119	107	30	6.303E+06	5.668E+06	1.112	192.2	76.2 ±	10.3
G1098-1	4	123	47	20	9.773E+06	3.734E+06	2.617	126.7	177.9 ±	30.8
G1098-1	8	145	66	25	9.217E+06	4.195E+06	2.197	142.3	149.6 ±	22.5
G1098-1	9	130	82	40	5.164E+06	3.258E+06	1.585	110.5	108.3 ±	15.5
G1098-1	11	152	33	25	9.662E+06	2.098E+06	4.606	71.1	309.8 ±	59.9
G1098-1	12	155	126	50	4.926E+06	4.004E+06	1.230	135.8	84.2 ±	10.3
G1098-1	14	448	109	40	1.780E+07	4.330E+06	4.110	146.9	277.2 ±	30.2
G1098-1	16	99	75	16	9.832E+06	7.449E+06	1.320	252.6	90.3 ±	14.0
G1098-1	23	74	71	15	7.839E+06	7.522E+06	1.042	255.1	71.4 ±	12.0
G1098-1	38	276	121	40	1.096E+07	4.807E+06	2.281	163.0	155.3 ±	17.3
G1098-1	42	299	48	25	1.901E+07	3.051E+06	6.229	103.5	415.6 ±	65.3
G1098-1	50	140	142	50	4.449E+06	4.513E+06	0.986	153.1	67.6 ±	8.2
G1098-1	55	89	74	20	7.071E+06	5.880E+06	1.203	199.4	82.3 ±	13.1
G1098-1	62	81	13	25	5.149E+06	8.263E+05	6.231	28.0	415.7 ±	124.5
G1098-1	64	138	20	20	1.096E+07	1.589E+06	6.900	53.9	458.8 ±	110.2
G1098-1	69	124	96	15	1.314E+07	1.017E+07	1.292	344.9	88.4 ±	12.2
G1098-1	73	239	98	50	7.596E+06	3.115E+06	2.439	105.6	165.9 ±	20.2
G1098-1	74	196	41	20	1.557E+07	3.258E+06	4.780	110.5	321.3 ±	55.6
G1098-1	75	254	52	25	1.614E+07	3.305E+06	4.885	112.1	328.1 ±	50.5
G1098-1	76	66	21	15	6.992E+06	2.225E+06	3.143	75.5	213.0 ±	53.6
		3347	1442		9.397E+06	4.048E+06		137.3		

Area of basic unit = 6.293E-07 cm^{-2}
χ^2 = 365.717 with 19 degrees of freedom
P(χ^2) = 0.0%
Age Dispersion = 59.217%

Ns / Ni = 2.321 ± 0.073
Mean Ratio = 3.009 ± 0.441

Ages calculated using a zeta of 87.7 ± 0.8 for U3 glass
ρ_D = 1.571E+06cm^{-2} ND = 2478
ρ_D interpolated between top of can; ρ_D = 1.644E+06cm^{-2} ND = 1293
bottom of can; ρ_D = 1.506E+06cm^{-2} ND = 1185

POOLED AGE = 158.0 ± 6.1 Ma
CENTRAL AGE = 152.4 ± 21.1 Ma

A:

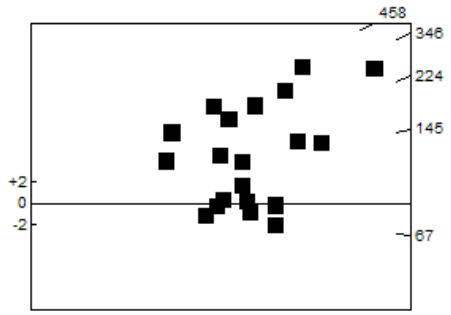

GC743-24 Zircon
Counted by: PFG

Gnarly Knots-1 4350-4450m

Slide ref	Current grain no	N_s	N_i	N_a	ρ_s	ρ_i	RATIO	U (ppm)	F.T. AGE (Ma)	
G1098-1	2	176	100	50	5.594E+06	3.178E+06	1.760	108.3	119.6 ±	15.2
G1098-1	8	125	104	30	6.621E+06	5.509E+06	1.202	187.7	81.9 ±	11.0
G1098-1	11	207	40	25	1.316E+07	2.543E+06	5.175	86.6	345.5 ±	60.2
G1098-1	13	273	34	20	2.169E+07	2.701E+06	8.029	92.0	528.5 ±	96.8
G1098-1	17	69	15	20	5.482E+06	1.192E+06	4.600	40.6	308.0 ±	88.0
G1098-1	18	215	83	40	8.541E+06	3.297E+06	2.590	112.4	175.3 ±	23.0
G1098-1	19	237	27	36	1.046E+07	1.192E+06	8.778	40.6	575.6 ±	117.6
G1098-1	24	161	33	25	1.023E+07	2.098E+06	4.879	71.5	326.2 ±	62.8
G1098-1	26	130	28	20	1.033E+07	2.225E+06	4.643	75.8	310.8 ±	65.1
G1098-1	32	223	96	40	8.859E+06	3.814E+06	2.323	129.9	157.4 ±	19.5
G1098-1	36	209	74	30	1.107E+07	3.920E+06	2.824	133.6	190.9 ±	26.2
G1098-1	38	98	54	25	6.229E+06	3.432E+06	1.815	117.0	123.3 ±	21.1
G1098-1	43	109	114	50	3.464E+06	3.623E+06	0.956	123.5	65.3 ±	8.9
G1098-1	44	83	74	50	2.638E+06	2.352E+06	1.122	80.1	76.5 ±	12.3
G1098-1	45	180	35	25	1.144E+07	2.225E+06	5.143	75.8	343.4 ±	63.9
G1098-1	50	211	51	20	1.676E+07	4.052E+06	4.137	138.1	277.7 ±	43.8
G1098-1	51	179	128	40	7.111E+06	5.085E+06	1.398	173.3	95.2 ±	11.2
G1098-1	53	180	101	40	7.151E+06	4.012E+06	1.782	136.7	121.1 ±	15.3
G1098-1	56	114	79	36	5.032E+06	3.487E+06	1.443	118.8	98.2 ±	14.5
G1098-1	70	137	99	50	4.354E+06	3.146E+06	1.384	107.2	94.2 ±	12.6
		3316	1369		7.841E+06	3.237E+06		110.3		

Area of basic unit = 6.293E-07 cm^{-2}
χ^2 = 350.776 with 19 degrees of freedom
P(χ^2) = 0.0%
Age Dispersion = 59.229%

Ns / Ni = 2.422 ± 0.078
Mean Ratio = 3.299 ± 0.513

Ages calculated using a zeta of 87.7 ± 0.8 for U3 glass
ρ_D = 1.564E+06cm^{-2} ND = 2478
ρ_D interpolated between top of can; ρ_D = 1.644E+06cm^{-2} ND = 1293
bottom of can; ρ_D = 1.506E+06cm^{-2} ND = 1185

POOLED AGE = 164.0 ± 6.4 Ma
CENTRAL AGE = 163.3 ± 22.6 Ma

A:

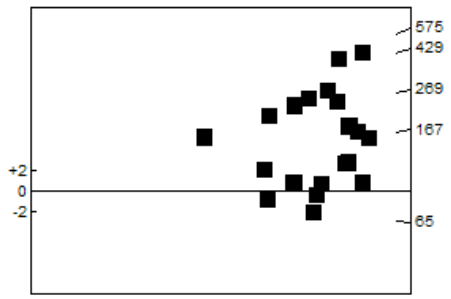

GC743-25 Zircon
Counted by: PFG

Gnarly Knots-1 4500-4600m

Slide ref	Current grain no	N_s	N_i	N_a	ρ_s	ρ_i	RATIO	U (ppm)	F.T. AGE (Ma)	
G1098-1	3	215	187	40	8.541E+06	7.429E+06	1.150	254.3	78.0 ±	8.0
G1098-1	4	93	50	20	7.389E+06	3.973E+06	1.860	136.0	125.8 ±	22.2
G1098-1	7	256	93	30	1.356E+07	4.926E+06	2.753	168.6	185.3 ±	22.8
G1098-1	11	173	108	25	1.100E+07	6.865E+06	1.602	235.0	108.4 ±	13.5
G1098-1	12	96	58	20	7.628E+06	4.608E+06	1.655	157.8	112.0 ±	18.8
G1098-1	15	72	72	60	1.907E+06	1.907E+06	1.000	65.3	67.9 ±	11.4
G1098-1	25	137	39	16	1.361E+07	3.873E+06	3.513	132.6	235.5 ±	43.1
G1098-1	32	196	39	25	1.246E+07	2.479E+06	5.026	84.9	334.3 ±	59.1
G1098-1	41	132	18	20	1.049E+07	1.430E+06	7.333	49.0	482.2 ±	121.6
G1098-1	44	87	55	25	5.530E+06	3.496E+06	1.582	119.7	107.1 ±	18.6
G1098-1	45	118	89	36	5.209E+06	3.929E+06	1.326	134.5	89.9 ±	12.8
G1098-1	46	165	38	30	8.740E+06	2.013E+06	4.342	68.9	289.8 ±	52.5
G1098-1	49	251	150	50	7.977E+06	4.767E+06	1.673	163.2	113.2 ±	12.0
G1098-1	54	199	48	20	1.581E+07	3.814E+06	4.146	130.6	277.0 ±	45.0
G1098-1	55	321	102	30	1.700E+07	5.403E+06	3.147	185.0	211.4 ±	24.5
G1098-1	56	285	184	50	9.058E+06	5.848E+06	1.549	200.2	104.9 ±	10.2
G1098-1	58	38	31	20	3.019E+06	2.463E+06	1.226	84.3	83.2 ±	20.2
G1098-1	59	169	61	16	1.678E+07	6.058E+06	2.770	207.4	186.4 ±	28.1
G1098-1	63	154	52	25	9.789E+06	3.305E+06	2.962	113.1	199.1 ±	32.2
G1098-1	66	140	94	30	7.416E+06	4.979E+06	1.489	170.4	100.9 ±	13.6
		3297	1568		8.910E+06	4.238E+06		145.1		

Area of basic unit = 6.293E-07 cm^{-2}
χ^2 = 230.770 with 19 degrees of freedom
P(χ^2) = 0.0%
Age Dispersion = 46.879%

Ns / Ni = 2.103 ± 0.065
Mean Ratio = 2.605 ± 0.362

Ages calculated using a zeta of 87.7 ± 0.8 for U3 glass
ρ_D = 1.557E+06cm^{-2} ND = 2478
ρ_D interpolated between top of can; ρ_D = 1.644E+06cm^{-2} ND = 1293
bottom of can; ρ_D = 1.506E+06cm^{-2} ND = 1185

POOLED AGE = 142.0 ± 5.4 Ma
CENTRAL AGE = 143.2 ± 16.1 Ma

A:

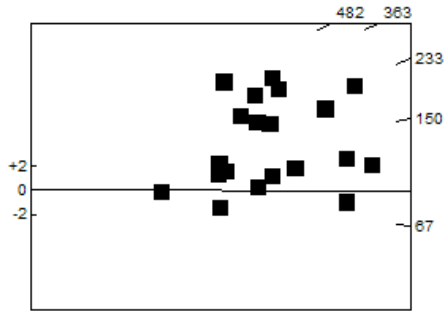

GC743-26 Zircon
Counted by: PFG

Gnarly Knots-1 4625-4725m

Slide ref	Current grain no	N_s	N_i	N_a	ρ_s	ρ_i	RATIO	U (ppm)	F.T. AGE (Ma)	
G1098-1	1	268	171	40	1.065E+07	6.793E+06	1.567	233.6	105.6 ±	10.6
G1098-1	3	149	48	25	9.471E+06	3.051E+06	3.104	104.9	207.6 ±	34.8
G1098-1	7	55	47	25	3.496E+06	2.987E+06	1.170	102.7	79.0 ±	15.8
G1098-1	8	276	124	50	8.772E+06	3.941E+06	2.226	135.5	149.5 ±	16.5
G1098-1	9	190	116	40	7.548E+06	4.608E+06	1.638	158.5	110.4 ±	13.2
G1098-1	11	129	90	20	1.025E+07	7.151E+06	1.433	245.9	96.7 ±	13.4
G1098-1	20	315	52	40	1.251E+07	2.066E+06	6.058	71.0	399.1 ±	60.4
G1098-1	28	126	58	25	8.009E+06	3.687E+06	2.172	126.8	146.0 ±	23.4
G1098-1	29	251	74	40	9.971E+06	2.940E+06	3.392	101.1	226.5 ±	30.4
G1098-1	33	265	76	25	1.684E+07	4.831E+06	3.487	166.1	232.7 ±	30.7
G1098-1	35	82	82	40	3.258E+06	3.258E+06	1.000	112.0	67.6 ±	10.7
G1098-1	36	134	73	36	5.915E+06	3.222E+06	1.836	110.8	123.6 ±	18.2
G1098-1	37	142	63	28	8.059E+06	3.575E+06	2.254	123.0	151.4 ±	23.2
G1098-1	46	174	120	40	6.912E+06	4.767E+06	1.450	164.0	97.8 ±	11.8
G1098-1	51	101	26	12	1.337E+07	3.443E+06	3.885	118.4	258.7 ±	57.2
G1098-1	65	135	65	50	4.290E+06	2.066E+06	2.077	71.0	139.6 ±	21.3
G1098-1	72	336	150	40	1.335E+07	5.959E+06	2.240	204.9	150.5 ±	15.1
G1098-1	73	202	73	50	6.420E+06	2.320E+06	2.767	79.8	185.4 ±	25.6
G1098-1	80	337	83	50	1.071E+07	2.638E+06	4.060	90.7	270.2 ±	33.6
G1098-1	82	193	47	40	7.667E+06	1.867E+06	4.106	64.2	273.2 ±	44.8
		3860	1638		8.567E+06	3.635E+06		125.0		

Area of basic unit = 6.293E-07 cm^{-2}
χ^2 = 208.487 with 19 degrees of freedom
P(χ^2) = 0.0%
Age Dispersion = 41.434%

Ns / Ni = 2.357 ± 0.069
Mean Ratio = 2.596 ± 0.283

Ages calculated using a zeta of 87.7 ± 0.8 for U3 glass
ρ_D = 1.550E+06cm^{-2} ND = 2478
ρ_D interpolated between top of can; ρ_D = 1.644E+06cm^{-2} ND = 1293
bottom of can; ρ_D = 1.506E+06cm^{-2} ND = 1185

POOLED AGE = 158.2 ± 5.8 Ma
CENTRAL AGE = 151.6 ± 15.2 Ma

A:

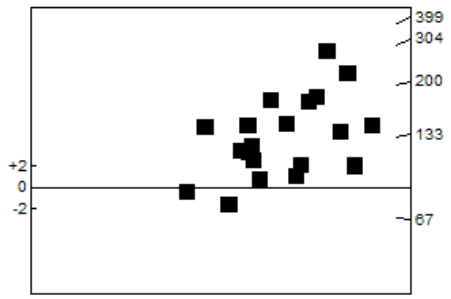

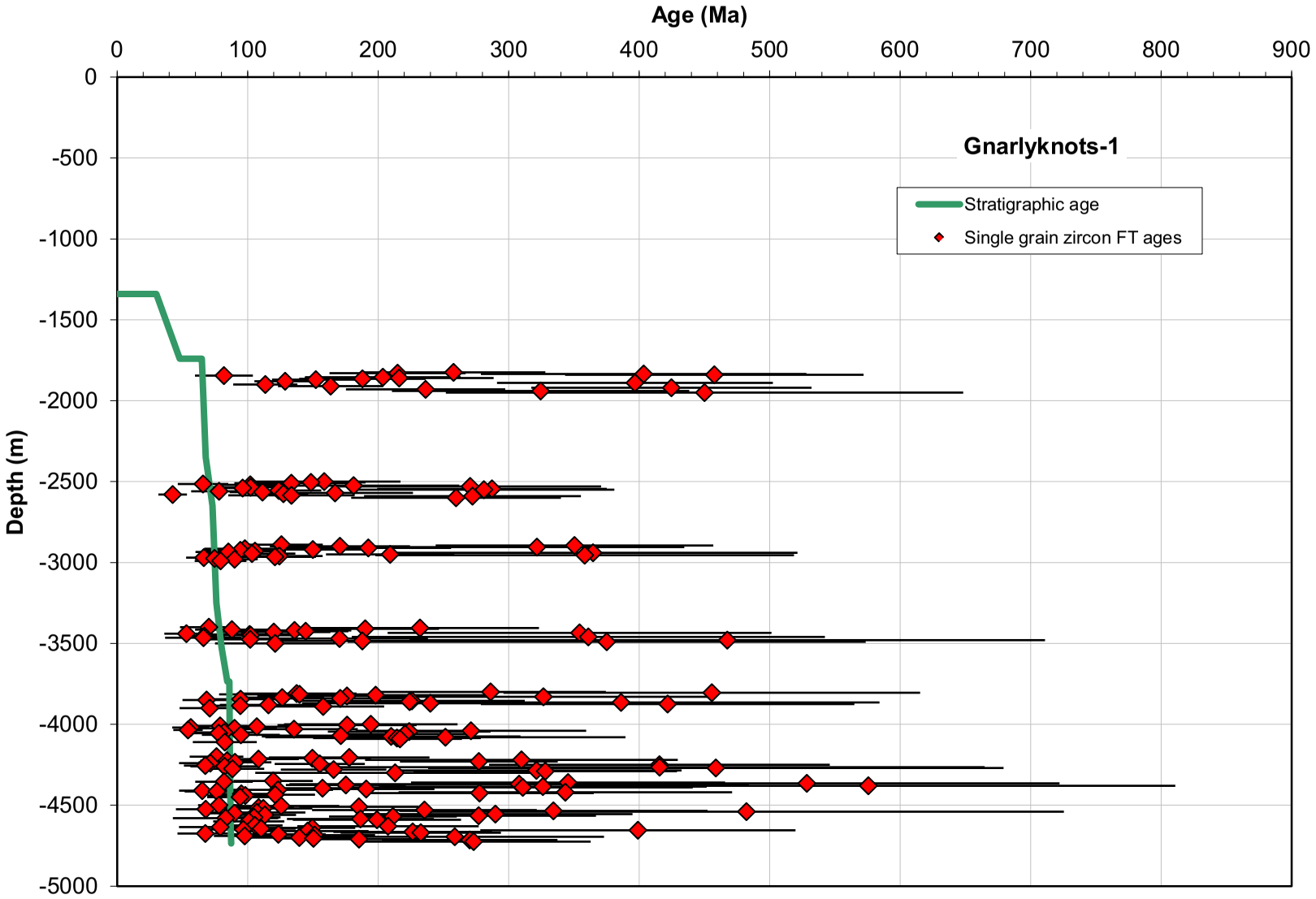
Age (Ma)
0
100
200
300
400
500
600
700
800
900
Depth (m)
0
-500
-1000
-1500
-2000
-2500
-3000
-3500
-4000
-4500
-5000
Gnarlyknots-1
Stratigraphic age
Single grain zircon FT ages

Supplementary Data

Well and Sample Information

Well	Sample #	Depth (m)	Strat. Age	Formation Name
Gnarlyknots-1A	74317	1825-1950	Maastrichtian	Potoroo Fm.
Gnarlyknots-1A	74318	2500-2600	Campanian-Maastrichtian	Potoroo Fm.
Gnarlyknots-1A	74319	2890-2990	Campanian	Potoroo Fm.
Gnarlyknots-1A	74320	3400-3500	Santonian	Potoroo Fm.
Gnarlyknots-1A	74321	3800-3900	Santonian	Potoroo-Wigunda Fms.
Gnarlyknots-1A	74322	4000-4110	Santonian	Potoroo-Wigunda Fms.
Gnarlyknots-1A	74323	4200-4300	Santonian	Potoroo-Wigunda Fms.
Gnarlyknots-1A	74324	4350-4450	Coniacian	Potoroo-Wigunda Fms.
Gnarlyknots-1A	74325	4500-4600	Coniacian	Potoroo-Wigunda Fms.
Gnarlyknots-1A	74326	4625-4725	Coniacian-Turonian	Potoroo-Wigunda Fms.

Coordinates - Gnarlyknots-1A

LAT	LONG	
34° 17' 39.06" S	131° 23' 03.01" E	WGS 84
EASTING	NORTHING	
719 434.2 m	6 202 651.4 m	UTM Zone 52

4.5 Paper 5

MacDonald, J.D., Holford, S., and King, R., (*in press*): Structure and Prospectivity of the Ceduna Delta—Deepwater Fold-Thrust Belt Systems, Bight Basin, Australia, *in*: Rosen, N.C., (ed) 2012. New understanding of the petroleum systems of the continental margins of the world. *GCSSEPM Foundation Bob F. Perkins Research Conference, v 32.*

MacDonald, J.D., Holford, S. & King, R. (2012) Structure and Prospectivity of the Ceduna Delta—Deepwater Fold-Thrust Belt Systems, Bight Basin, Australia, *in*: Rosen, N.C., (ed) 2012. New understanding of the petroleum systems of the continental margins of the world.
GCSSEPM Foundation Bob F. Perkins Research Conference, v 32, pp. 779-816

5. Thesis Conclusions

This thesis presented a new and innovative methodology for predicting basal pore fluid pressure in the deepwater Niger Delta toe using the Critical Taper Wedge (CTW) model. By designing a new multi-scale measurement workflow for seabed dip (α), detachment dip (β) and wedge thickness (H) we are now able to take hundreds of measurements on a single 2D seismic line to obtain the input parameters for the CTW equation, predicting small scale changes in basal pore fluid pressure. From this we have produced the first map of basal pore fluid pressure for any DDWFTB system worldwide; using the data-rich Niger Delta example we have related it to the observed structural geometry. By understanding the relationship between detachment parameters (thickness, geometry, lithology) and their control on structural geometry in the Niger Delta, a robust interpretation of the Ceduna Delta systems was now tenable.

Previously considered a stacked delta system, the two DDWFTB systems in the Ceduna Sub-basin are now considered separate systems based on the geometry of delta toe provinces and regional detachments. New seismic reflection data has imaged the geographically restricted area where the two delta toes overlap, resulting in an increased understanding of the structural variation between these systems. This has furthered our understanding of the Ceduna Delta structural geometry and allowed for further explanation of the interaction between its two systems in terms of sediment routing, fault control and fault reactivation potential.

The geomechanical fault reactivation model presented in this thesis was coupled with the previous understanding of the in-situ stress tensor in the Ceduna Sub-basin to determine fault reactivation potential using a 3D model based on 3D seismic data. The use of this methodology was the first such study in the Ceduna Sub-basin and resulted in illustrating the present-day fault reactivation potential in the delta top of both DDWFTBs. Orientation of present day delta top

synthetic and antithetic extensional faults is favorable for moderate to high fault reactivation potential for areas dipping 40-70^{o}, while thrust faults are thought to be at low reactivation risk. Evidence on 2D seismic reflection data shows seabed offset throughout the Cenozoic, supporting the geomechanical modelling predictions.

The most significant finding in this thesis involves the origin of the Ceduna Delta systems, based on an extensive thermochronological and geochronological study from onshore and offshore wells, and an extensive literature review. The results clearly indicate the younger Santonian-Maastrichtian delta system was a product of extensive Late Cretaceous exhumation of the proximal South Australian southern margin, through progressive erosion of Permian to Early Cretaceous sediments and underlying Proterozoic-Archean basement. This result challenges the previous postulation that the system was a product of a large and far travelled river system originating in the Australian Eastern Highlands (2000 km away) and has significant implications for reservoir quality in the Ceduna DDWFTBs and the Cretaceous palaeogeography of the Australian Continent.

Hydrocarbon prospectivity of the basin is discussed and new trap geometries are mapped on the delta-top demonstrating four-way closure on the listric grown faults in the Hammerhead supersequence. In addition, the absence of significant Cenozoic burial is viewed as a potential risk in the basin as any hydrocarbons must have been generated in the late Cretaceous and remain in situ ever since. Given the moderate to high risk of fault reactivation in the basin this may present a significant risk for exploration.

6. Appendix

6.1 MacDonald, J.D., Backé, G., King, R. and Hillis, R.R., (2011): The Hammerhead Delta—Deepwater Fold-Thrust Belt, Bight Basin, Australia: 2D Geomechanical and Kinematic Reconstructions. *The Australian Petroleum Production and Exploration Association Extended Abstracts Volume*.

6.2 Unpublished Comment on *"Interactions between continental breakup dynamics and large-scale delta system evolution: Insights from the Cretaceous Ceduna delta system, Bight Basin, Southern Australian margin"* by N. Espurt, J-P. Callot, J. Totterdell, H. Struckmeyer and R. Vially.

THE HAMMERHEAD DELTA—DEEPWATER FOLD-THRUST BELT, BIGHT BASIN, AUSTRALIA: 2D GEOMECHANICAL AND KINEMATIC RECONSTRUCTIONS

[1]MACDONALD, J.D., [1]BACKÉ, G., [2]KING, R.C. AND [3]HILLIS, R.R.

[1]Centre for Tectonics, Resources and Exploration (TRaX), Australian School of Petroleum, University of Adelaide, North Terrace, Adelaide, SA, 5005
[2] Centre for Tectonics, Resources and Exploration (TRaX), School of Earth and Environmental Sciences, University of Adelaide, North Terrace, SA, 5005
[3] Deep Exploration Technologies Cooperative Research Centre, University of Adelaide, North Terrace, SA, 5005

Author Correspondence: jmacdonald@asp.adelaide.edu.au

INTRODUCTION

The Bight Basin extends for over 3,000 km along the south coast of Australia between Port Lincoln (South Australia) and Cape Leeuwin (Western Australia; Fig. 1a). Only 12 exploration wells have been drilled to date in the Bight Basin, two of which were drilled in the Ceduna Sub-basin. The Ceduna Sub-basin, defined by the broad bathymetric Ceduna Terrace (Fig. 1b), covers an area of approximately 90,000 km^2 with water depths ranging from 200 m to more than 5,000 m (Fig. 1a).

The thickness of Middle Jurassic to Cenozoic sedimentary rocks in the Ceduna Sub-basin exceeds 12 km (Struckmeyer et al, 2001; Krassay and Totterdell, 2003). The Ceduna Sub-basin contains two spatially and temporally separate Cretaceous delta—deepwater fold- thrust belt (DDWFTB) systems: 1) the late Albian-Santonian White Pointer DDWFTB, and; 2) the late Santonian-Maastrichtian Hammerhead DDWFTB. These systems detach above the mud-rich Blue Whale and Tiger supersequences, respectively (Fig. 2a).

Previous work completed by Geoscience Australia (in 1999–2008) and Woodside (including drilling of the most recent well, Gnarlyknots–1; Fig. 1a) resulted in an improved understanding of the hydrocarbon prospectivity of the Bight Basin, particularly the Ceduna Sub-basin. For a detailed insight into the Bight Basin, the author would like to refer the reader to this work which focused on the sequence stratigraphy, tectonics and petroleum systems of the Bight Basin to identify organic-rich supersequences, understand the regional maturity of these rocks, and identify suitable traps and seals for hydrocarbon accumulation (Blevin et al, 2000; Totterdell et al, 2000; Somerville, 2001; Ruble et al, 2001; Struckmeyer et al, 2001; Sayers et al, 2001; Struckmeyer et al, 2002; Krassay and Totterdell, 2003; Totterdell and Krassay, 2003; Totterdell and Bradshaw, 2004; King and Mee, 2004; Tapley et al, 2005; Totterdell et al, 2008).

Here, we present a brief introduction to the Ceduna Sub-basin delta systems, their regional structural style, and the results of the restoration of a two-dimensional (2D) geological cross section across the Hammerhead DDWFTB (Fig. 1c; line 199-07), using kinematic and geomechanical techniques. We demonstrate that the Hammerhead DDWFTB is a near-balanced system. The absence of significant excess extension that is commonly observed in other DDWFTB systems (such as the Niger Delta; Morley and Guerin, 1996) is attributed to shut off of sediment supply in the late Maastrichtian, with a possible loss of extension to the underlying Cenomanian growth faults of the Albian-Cenomanian White Pointer DDWFTB system.

STRUCTURAL STYLE OF THE CEDUNA SUB-BASIN DDWFTB SYSTEMS

The Ceduna Sub-basin contains two Cretaceous DDWFTBs: the late Albian-Cenomanian White Pointer and the Late Santonian-Maastrichtian Hammerhead. The geometry of the Ceduna DDWFTBs was first recognized by Boeuf and Doust (1975) and Fraser and Tilbury (1979) and have since been investigated by several authors including Totterdell and Krassay (2003), Totterdell and Bradshaw (2004), Espurt et al (2009), King and Backé (2010) and MacDonald et al (2010).

The Ceduna Sub-basin provides a unique opportunity to study two separate progradational DDWFTB systems that are independent in size, shape and structural geometry (MacDonald et al., 2010). Both DDWFTBs exhibit well-developed gravity-driven deformation structures, making them analogous to other delta systems around the world (Totterdell and Krassay, 2003; MacDonald et al., 2010). Here we focus on the structural interpretation of the Hammerhead DDWFTB, based on newly acquired 2D BightSPAN seismic data and an existing public domain 2D seismic dataset. Both 2D seismic datasets were interpreted in the time domain while seismic line 199-07 was depth converted for the kinematic and geomechanical restorations (Fig. 2c, 3), using a simplified velocity model.

In this study, we present two representative 2D seismic lines that demonstrate the regional variation in the structural style of the Late Cretaceous DDWFTB systems (Figs 2a, b).

Seismic line Bi 300 (Fig. 1b, 2a) images the western side of the Ceduna Sub-basin and illustrates a linked system of extension and shortening within the Cenomanian White Pointer DDWFTB. This linked system is overlain by the Tiger supersequence (Turonian-Santonian) and the Hammerhead supersequence (Campanian-Maastrichtian). In the western Ceduna Sub-basin the Hammerhead supersequence did not develop into a DDWFTB system (MacDonald et al., 2010). In the eastern Ceduna Sub-basin, seismic line Bi 500 (Fig. 2b) illustrates a linked system of extension and shortening within the Hammerhead supersequence, forming a DDWFTB system. In this section, the Cenomanian White Pointer supersequence is purely an extensional system that is lacking a down dip deepwater fold-thrust belt (Espurt et al., 2010; MacDonald et al., 2010). Therefore, it cannot be classified as a linked DDWFTB system at this location.

Examination of additional regional 2D seismic data indicates that the White Pointer and Hammerhead DDWFTBs prograded in slightly different directions based on the positions of their

deepwater fold-thrust belts (Fig. 1b). Overlap occurs between the lobes on the delta top (Fig. 1b; yellow dashed line) due to proximity to the source and the deeper Mulgara Fault System shared at this location in the White Pointer supersequence (MacDonald et al, 2010). Linkage between the White Pointer, Tiger and Hammerhead supersequences on the delta top is achieved via the Mulgara Fault System, whereby selective faults were reactivated as the Hammerhead supersequence prograded over the existing White Pointer system (MacDonald et al., in review).

GEOMECHANICAL VS. KINEMATIC RESTORATION

Two methods were utilized for the restoration of the Hammerhead DDWFTB in the Ceduna Sub-basin, a kinematic line-length technique and a geomechanical code. Each of these techniques was applied to the same 2D seismic line (199-07; Fig. 2c) to compare the restoration of such a linked system of extension and shortening.

Kinematic Restoration

The kinematic restoration was completed using Midland Valley Explorations 2D MOVE© software. Kinematic restoration is a classical technique that is based on geometric and kinematic analysis of observed structures in nature (Griffiths et al. 2002). The section is balanced by applying flexural slip to accommodate the deformation caused by slip along and infinite number of bedding planes, without taking into account the variations in rock behavior between different rock types (Maerten and Maerten, 2006).

Geomechanical Restoration

The geomechanical restoration was completed by King and Backé (2010) using Dynel 2D© geomechanical code (Maerten and Maerten, 2006). Dynel 2D is a Finite Element Model (FEM) code which combine geomechanics and stochastic techniques, whereby the fundamental laws that govern rock deformation and linear-elastic theory are obeyed and the necessary kinematic constraints are built into the code (Maerten and Maerten, 2006). A significant benefit of the code is that it allows for the investigation of the simultaneous mechanical interaction between extension and shortening in a linked system, such as a DDWFTB.

2D RESTORATION OF THE HAMMERHEAD DDWFTB

The two methods described above were applied to the depth converted seismic line 199-07 (Fig. 2c) to restore the Hammerhead DDWFTB and investigate the different parameter controlling the geometry of the system.

Kinematic Restoration

Kinematic restoration tool allow to restore deformation sequentially, one structure at a time, using a specific algorithm for each type of deformation. Thus, for a naturally linked-system such as a DDWFTB, it is necessary to split the section into an extensional province and a compressional, before summing the overall amount of net negative or net positive extension or shortening.

Seismic line 199-07 was split roughly in the center of the section (center pin line, Fig. 2c, d), where we interpreted that there was no structural thickening and assumed no interbed shear, at

least at seismic resolution. This allowed us to split the section into a purely extensional delta top (NNE side; Fig. 2c, d) and a compressional delta toe (SSW side; Fig. 2c, d).

A unique marker bed, interpreted through the entire length of the model, is necessary to successfully restore a section using kinematic technique (Fig. 2c, d; yellow line). This is a potential limitation of the technique, particularly when the quality of the seismic resolution below the extensional growth faults is degraded as a consequence of the presence of mobile shale and compaction processes having reduced the continuity of the original bedding.

Thus, we were forced to choose a continuous line higher up in the Hammerhead stratigraphy for both the delta top and delta toe, having them meet at the center pin line where we assumed no interbed shear.

The restoration was completed for each deformation domain using a simple shear algorithm, by sequentially restoring each fault and joining the segments to restore the bed length to its pre-faulting stage. This line (red; Fig. 2d) is then unfolded using the flexural slip algorithm to a target line (red; Fig. 2d), which was chosen based on the regional elevation of the "continuous bed" in the footwall of each fault corresponding to the interpreted level of the stratigraphy before faulting. We finally compared the amount of excess line length in the shortened component (delta toe) to the amount of missing line length in the extension component (delta top) to determine if the system is balanced. The result demonstrates that there is < 1% excess extension in the system, indicating a near perfect balance in the system (Fig. 2d; red line).

Geomechanical Restoration

The geomechanical restoration of the Hammerhead DDWFTB was completed by King and Backé (2010) using the Dynel 2D geomechanical code (Fig. 3). For this restoration, the seismic line was divided up into 5 units based on age and rheology (Fig. 3a). The surfaces between the units were locked for the restoration, to concentrate the deformation along the faults, which were allowed to slide in the model. The geological model was then meshed using triangular elements, and the different units were assigned different rock properties. These were derived from available well data from Potoroo – 1 and Gnarlyknots – 1A wells. The model was assigned a target line of 4°, corresponding to the idealized shape of a submarine slope (Porebski and Steel, 2003; Fig. 3a). The model was run in 5 iterations to restore each unit sequentially to the target line and each of the units was allowed to extend or contract laterally. After each iteration the line lengths were measured and input into the equation for extension:

$$e = (L_1-L_0)/L_0$$

where L_0 is the initial length and L_1 is the deformed length (King and Backé, 2010). The result from the calculation indicated a 2.4% excess of extension in the Hammerhead DDWFTB system (King and Backé, 2010).

COMPARISON OF RESULTS AND CONCLUSIONS

The geomechanical modeling resulted in an excess extension of 2.4% for the Hammerhead DDWFTB, indicating that the system is nearly balanced when taking into account the potential

error in the depth conversion, interpretation and modelling. The kinematic restoration indicated an excess extension of < 1%, closer still to being a balanced system, in agreement with the results of a similar restoration by Espurt et al (2010) for the same seismic line, 199-07. These results indicate that even though two different restoration techniques were used, the system is almost balanced, with only 1-2% percent difference between the extension and compression in the system.

Most physical models of actively deforming DDWFTB systems indicate they are balanced systems (Mandl and Crans, 1981; McClay et al., 1998; 2003). However, there is evidence suggesting that whole systems are commonly imbalanced, often resulting in an excess of extension up to 20% (Morley and Guerin, 1996; King et al. 2010). This excess of extension may be attributed to sub-seismic deformation in the more ductile down-dip delta toe that is not measurable due to seismic resolution, thus resulting in a very conservative shortening estimate (Strachan and Alsop, 2006). In the case of the Hammerhead DDWFTB, it may also be attributed to the sudden shut off of sediment supply resulting in a restricted system that did not suffer extensive progradation, thus limiting its size and fault development (King and Backé, 2010). In addition, it is possible that underlying Cenomanian growth faults from the White Pointer DDWFTB were reactivated, accommodating some of the (excess) extension, thus inhibiting the Hammerhead system from developing a more complexly faulted delta top (Fig. 2a, b; linked extensional faults).

ACKNOWLEDGEMENTS

The authors would like to thank the Australian Research Council and the University of Adelaide for their financial support of this study. The authors would also like to thank IGEOSS, Ion Geophysical and Midland Valley for the data and software used in this study.

REFERENCES

BOUEF, M.G., AND DOUST, H., 1975—Structure and development of the southern margin of Australia. APEA Journal, 15, 33-43.

BLEVIN, J.E., TOTTERDELL, J.M., LOGAN, G.A., KENNARD, J.M., STRUCKMEYER, H.I.M. AND COLWELL, J.B., 2000— Hydrocarbon prospectivity of the Bight Basin—petroleum systems analysis in a frontier basin, In: 2nd Sprigg Symposium – Frontier Basins, Frontier Ideas, Adelaide, June 29-30th, 2000. Geological Society of Australia, Abstracts 60, 24–29.

ESPURT, N., CALLOT, J.-P., TOTTERDELL, J., STRUCKMEYER, H., AND VIALLY, R., 2009—Interactions between continental breakup dynamics and large-scale delta system evolution: Insights from the Cretaceous Ceduna delta system, Bight basin, Southern Australia margin. Tectonics, 28, TC6002, doi:10.1029/2009TC002447, 2009.

FRASER, A.R. AND TILBURY, L.A., 1979—Structure and stratigraphy of the Ceduna Terrace region, Great Australian Bight. The APEA Journal, 19, 53–65.

GRIFFITHS, P., JONES, S., SALTER, N., SCHAEFER, F., OSFIELD, R. AND REISER, H., 2002—A new technique for 3-D flexural-slip restoration. Journal of Structural Geology 24, 773–782.

KING, R.C. AND BACKÉ, G., (2010)—A balanced 2D structural model of Hammerhead Delta—Deepwater Fold-Thrust Belt, Bight Basin, Australia. Australian Journal of Earth Sciences.

KING, R.C., BACKÉ, G., MORLEY, C.K., HILLIS, R.R. & TINGAY M.R.P., 2010—Balancing deformation in NW Borneo: Quantifying plate-scale vs. gravitational tectonics in a Delta and Deepwater Fold-Thrust Belt Systems. Marine and Petroleum Geology, 27, 238-246.

KING, S.J. AND MEE, B.C., 2004—The seismic stratigraphy and petroleum potential of the Late Cretaceous Ceduna Delta, Ceduna Sub-basin, Great Australian Bight. *In*: Boult, P.J., Johns, D.R. and Lang, S.C. (Eds), Eastern Australasian Basins Symposium II. Petroleum Exploration Society of Australia, Special Publication, 63–73.

KRASSAY, A.A. AND TOTTERDELL, J.M., 2003—Seismic stratigraphy of a large, Cretaceous shelf-margin delta complex, offshore southern Australia. American Association of Petroleum Geologists Bulletin, 87(6), 935–963.

MACDONALD, J.D., BACKÉ, G., KING, R., HOLFORD, S.P., AND HILLIS, R.R., (*in review*)—Geomechanical Modelling of Fault Reactivation in the Ceduna Sub-basin, Bight Basin, Australia. In: Sibson, R., Butler, R, and Healy, D., eds. Faulting, Fracturing and Igneous Intrusion in the Earth's crust, xx-xx. The Geological Society, London, Special Publication xxx.

MACDONALD, J.D., KING, R., HILLIS, R.R., & BACKÉ, G., 2010—Structural style of the White Pointer and Hammerhead delta—deepwater fold-thrust belts, Bight Basin, Australia. The Australian Petroleum Production and Exploration Association Journal, 50, 487-510.

MAERTEN, L. AND MAERTEN, F., 2006—Chronologic modelling of faulted and fractured reservoirs using geomechanically based restoration: Technique and industry applications. American Association of Petroleum Geologists Bulletin 90, 1201–1226.

MANDL, G. AND CRANS, W., 1981—Gravitational gliding in deltas. In: McClay K. R. & Price N. J. eds. Mechanics of thrusts and nappes, 41–54. The Geological Society, London, Special Publication 9.

MCCLAY, K., T. DOOLEY, AND G. ZAMORA., 2003—Analogue models of delta systems above ductile substrates, In: Van Rensbergen, P., Hillis, R.R.., Maltman, A.J. and Morley, C.K. (Eds), Subsurface sediment mobilization, Geological Society, London, Special Publications, 216, 411–428.

MCCLAY, K.R., DOOLEY, T. AND LEWIS, G. 1998—Analog modelling of progradational delta systems. Geology, 26, 9, 771-774.

MORLEY, C.K. AND GUERIN, G., 1996—Comparison of gravity-driven deformation styles and behaviour associated with mobile shales and salt. Tectonics, 15, 1154-1170.

PORÉBSKI, S. J. AND STEEL R. J., 2003—Shelf margin deltas: Their stratigraphic significance and relation to deepwater sands. Earth Science Reviews 62, 283–326.

RUBLE, T.E., LOGAN, G.A., BLEVIN, J.E., STRUCKMEYER, H.I.M., LIU, K., AHMED, M., EADINGTON, P.J. AND QUEZADA, R.A., 2001—Geochemistry and charge history of a palaeo-oil column: Jerboa-1, Eyre Sub-basin, Great Australian Bight. In: Hill, K.C. and Bernecker, T. (eds), Eastern Australasian Basins Symposium. A Refocused Energy Perspective for the Future. Petroleum Exploration Society of Australia, Special Publication, 521-530.

SAYERS, J., SYMONDS, P., DIREEN, N.G., AND BERNARDEL, G., 2001—Nature of the continent-ocean transition on the non-volcanic rifted margin of the central Great Australian Bight, in R. C. L. Wilson, R. B. Whitmarsh, B. Taylor, and N. Froitzheim, eds., Non-volcanic rifting of continental margins: a comparison of evidence from land and sea: Geological Society (London) Special Publication, 187, p. 51–76.

SOMERVILLE, R., 2001—The Ceduna Sub-basin – a snapshot of prospectivity. The APPEA Journal, 41, 321–346.

STRACHAN, L.J. AND ALSOP, G.I., 2006—Slump folds as estimators of palaeoslope: a case study from the Fisherstreet Slump of County Clare, Ireland, Basin Research 18, 451–470.

STRUCKMEYER, H.I.M., TOTTERDELL, J.M., BLEVIN, J.E., LOGAN, G.A., BOREHAM, C.J., DEIGHTON, I., KRASSAY, A.A. AND BRADSHAW, M.T., 2001—Character, maturity and distribution of potential Cretaceous oil source rocks in the Ceduna Sub-basin, Bight Basin, Great Australian Bight. In: Hill, K.C. and Bernecker, T. (Eds), Eastern Australasian Basin Symposium, a refocused energy perspective for the future. Petroleum Exploration Society of Australia, Special Publication, 543–552.

STRUCKMEYER, H.I.M., WILLIAMS, A.K., COWLEY, R., TOTTERDELL, J.M., LAWRENCE, G. AND O'BRIEN, G.W., 2002—Evaluation of hydrocarbon seepage in the Great Australian Bight. The APPEA Journal , 42, 371-385.

TAPLEY, D., MEE, B.C., KING, S.J., DAVIS, R.C. AND LEISCHNER, K.R., 2005—Petroleum potential of the Ceduna Sub-basin: impact of Gnarlyknots-1A. The APPEA Journal, 45, 365–380.

TOTTERDELL, J.M., BLEVIN, J.E., STRUCKMEYER, H.I.M., BRADSHAW, B.E., COLWELL, J.B. AND KENNARD, J.M., 2000—A new sequence framework for the Great Australian Bight: starting with a clean slate. The APPEA Journal, 40, 95–117.

TOTTERDELL, J.M. AND KRASSAY, A.A., 2003—The role of shale deformation and growth faulting in the Late Cretaceous evolution of the Bight Basin, offshore southern Australia. In: Van Rensbergen, P., Hillis, R.R.., Maltman, A.J. and Morley, C.K. (Eds), Subsurface sediment mobilisation. Geological Society of London, Special Publications 216, 429–442.

TOTTERDELL, J.M. AND BRADSHAW, B.E., 2004—The structural framework and tectonic evolution of the Bight Basin. In: Boult, P.J., Johns, D.R. & Lang, S.C. (Eds), Eastern Australasian Basins Symposium II. Petroleum Exploration Society of Australia, Special Publication, 41-61.

TOTTERDELL, J.M., STRUCKMEYER, H.I.M., BOREHAM, C.J., MITCHELL, C.H., MONTEIL, E., AND BRADSHAW, B.E., 2008—Mid–Late Cretaceous organic-rich rocks from the eastern Bight Basin: implications for prospectivity. PESA Eastern Australasian Basins Symposium III, 137-158.

FIGURE CAPTIONS

Figure 1: Location map (a) showing the position of the Ceduna Sub-basin in the Bight Basin on the southern Australian margin (from Totterdell and Bradshaw, 2004). Location map (b) showing the broad bathymetry of the Ceduna Terrace, outline of delta lobes and overlap zone (yellow dashed line) with approximate progradation direction, location of delta—deepwater fold-thrust belts (DDWFTBs), well locations and location of seismic surveys used in this study.

Figure 2: Seismic line Bi 300 (a) showing sequence stratigraphic framework for the western Ceduna Sub-basin including the White Pointer DDWFTB (blue) with extensional (delta top) and shortening (delta toe) provinces. Seismic line Bi 500 from the eastern Ceduna Sub-basin (b) demonstrating growth of deeper White Pointer DDWFTB extensional faults upward into the Hammerhead DDWFTB nearest the margin. Outboard of this, extensional, listric growth faults of the Hammerhead DDWFTB detach above Turonian-Santonian strata and are linked down dip to a deepwater fold-thrust belt (delta toe). The White Pointer Supersequence images well-developed extensional faults but is missing a linked down dip delta toe. Seismic line 199-07 (c) is shown in the undeformed state (line trace) with yellow line representing continuous reflector used for kinematic line length restoration while red line demonstrates restored continuous reflector after restoration with simple shear algorithm. Final restored state (d) demonstrates continuous reflector (red line) which has been restored to a target line using the flexural slip algorithm with approximately equal amounts of extension and shortening in the system indicating a near-balance.

Figure 3: Present-day structural model (a) of the Hammerhead Delta–Deepwater Fold-Thrust Belt, Bight Basin, Australia. The five steps of restoration (b–f) of the Hammerhead Delta–Deepwater Fold-Thrust Belt demonstrating the subsequent undeformed line lengths (L01, L02, L03, L04, L05). L01 is the deformed present-day line length (after King and Backé, 2010).


a)
120
130
140
30
40
WESTERN AUSTRALIA
SOUTH AUSTRALIA
Madura Shelf
Gawler Craton
Potoroo 1
Polda Basin
Cape Leeuwin
Eyre Sub-basin
Gnarlyknots 1A
Port Lincoln
BIGHT BASIN
Bremer Sub-basin
Ceduna Sub-basin
Duntroon Sub-basin
Denmark Sub-basin
Recherche Sub-basin
Kangaroo Island
Couedic Shelf
Otway Basin
0
500 km
23/OA/1506

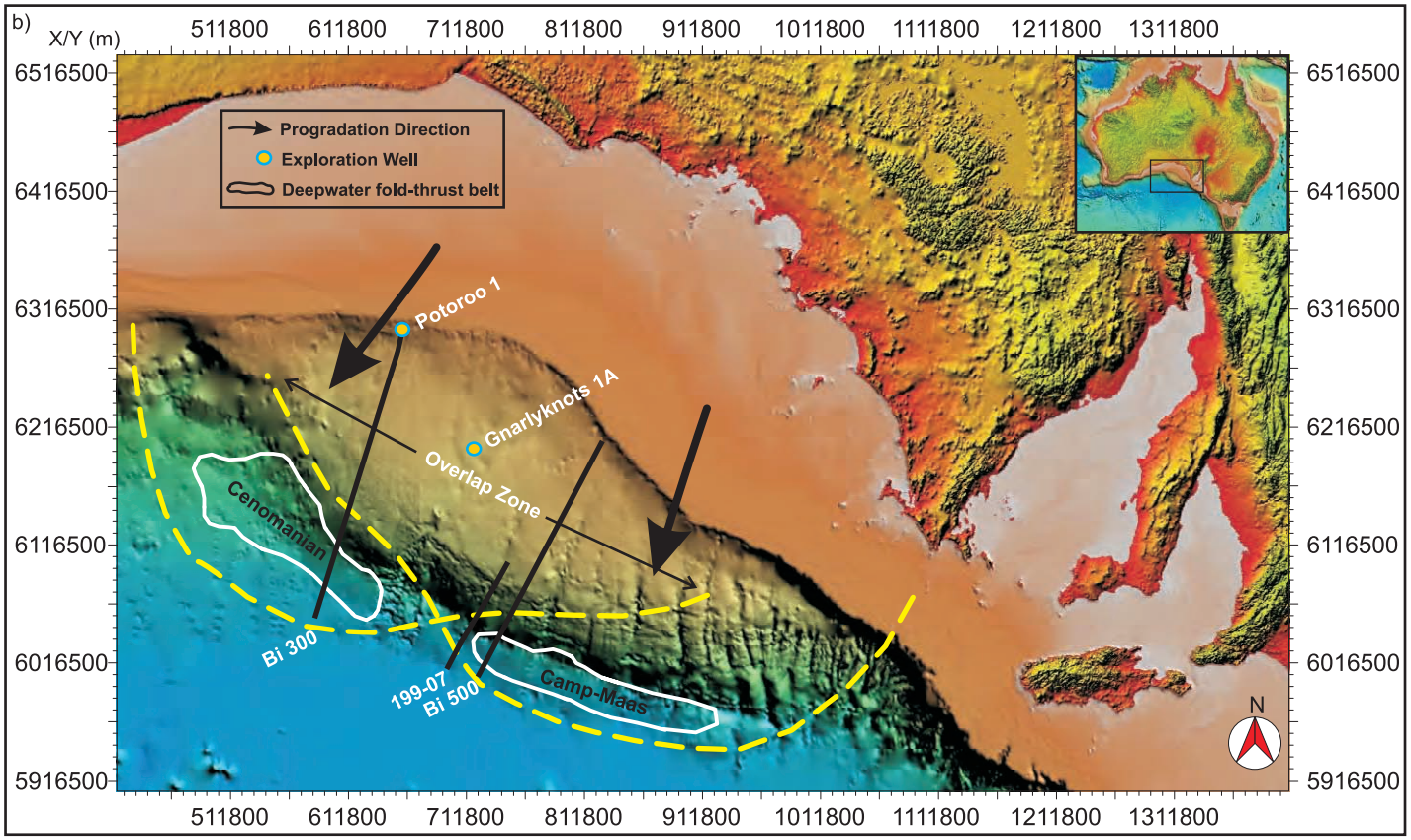
b)
X/Y (m)
511800
611800
711800
811800
911800
1011800
1111800
1211800
1311800
6516500
6416500
6316500
6216500
6116500
6016500
5916500
Progradation Direction
Exploration Well
Deepwater fold-thrust belt
Potoroo 1
Gnarlyknots 1A
Overlap Zone
Cenomanian
Bi 300
199-07
Bi 500
Camp-Maas
N

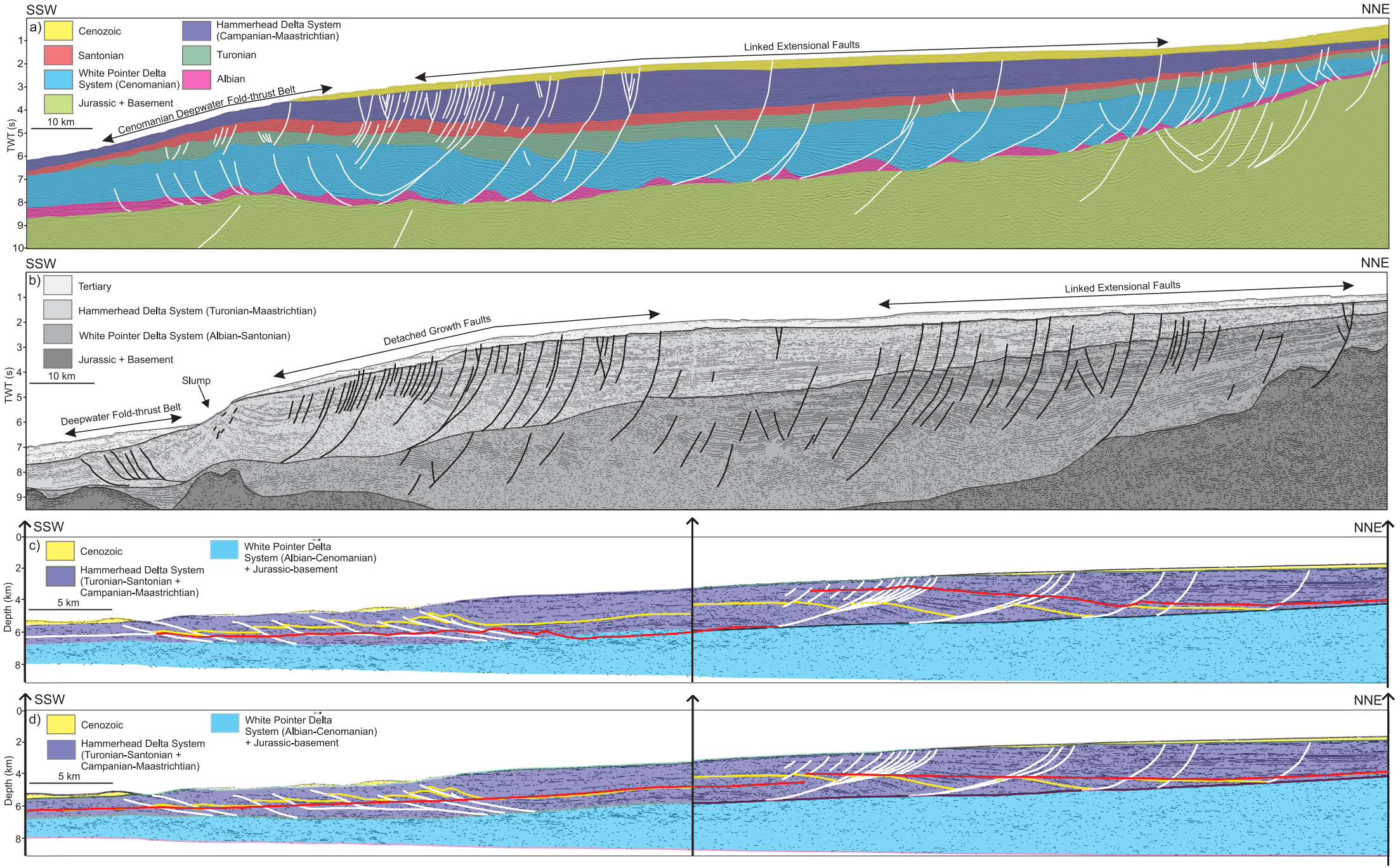
SSW
NNE
a)
Cenozoic
Santonian
White Pointer Delta System (Cenomanian)
Jurassic + Basement
Hammerhead Delta System (Campanian-Maastrichtian)
Turonian
Albian
10 km
TWT (s)
Cenomanian Deepwater Fold-thrust Belt
Linked Extensional Faults
b)
Tertiary
Hammerhead Delta System (Turonian-Maastrichtian)
White Pointer Delta System (Albian-Santonian)
Jurassic + Basement
10 km
TWT (s)
Slump
Deepwater Fold-thrust Belt
Detached Growth Faults
Linked Extensional Faults
c)
Cenozoic
Hammerhead Delta System (Turonian-Santonian + Campanian-Maastrichtian)
White Pointer Delta System (Albian-Cenomanian) + Jurassic-basement
5 km
Depth (km)
d)
Cenozoic
Hammerhead Delta System (Turonian-Santonian + Campanian-Maastrichtian)
White Pointer Delta System (Albian-Cenomanian) + Jurassic-basement
5 km
Depth (km)

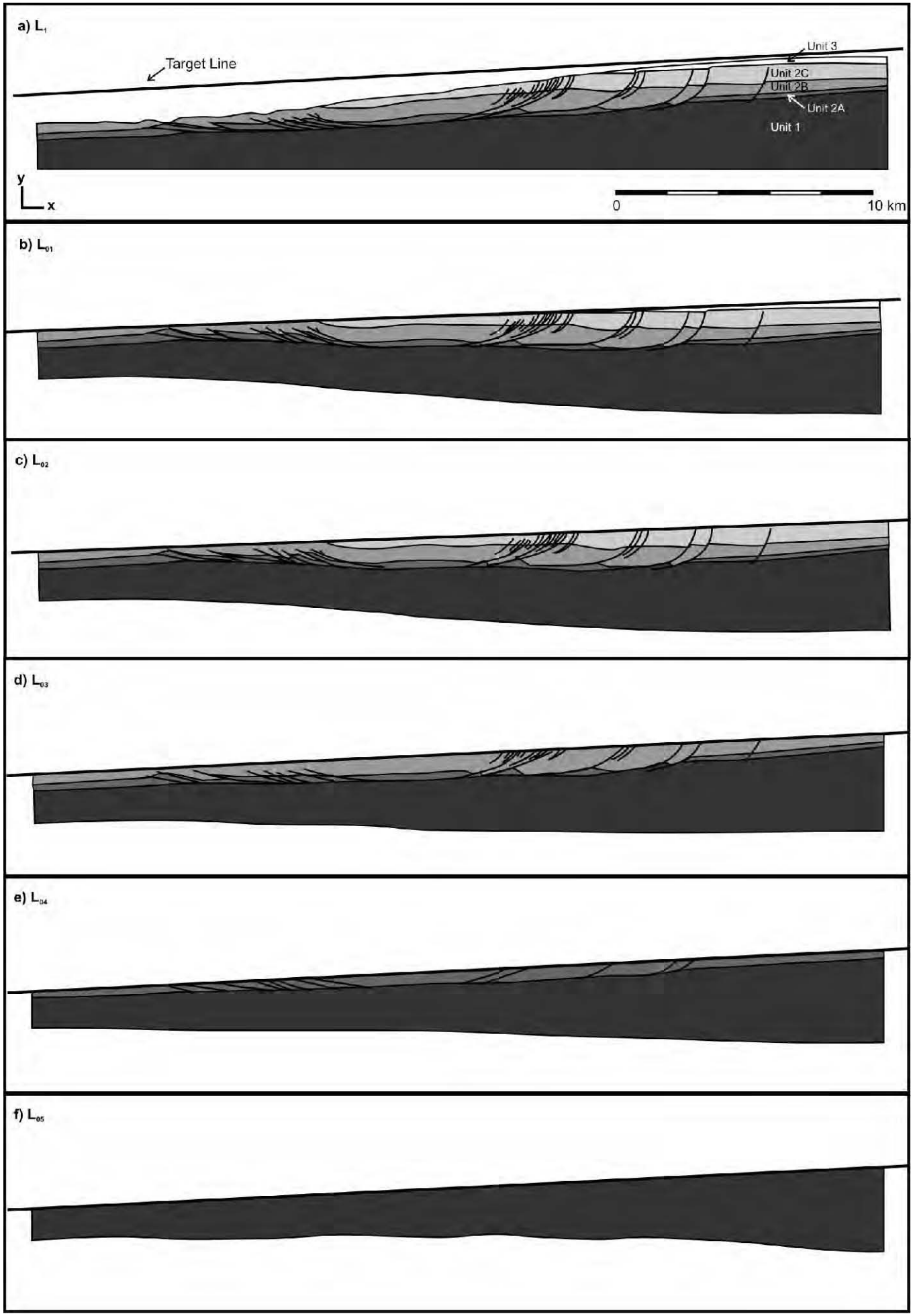
a) L1
Target Line
Unit 3
Unit 2C
Unit 2B
Unit 2A
Unit 1
y
x
0
10 km
b) L01
c) L02
d) L03
e) L04
f) L05

Comment on "Interactions between continental breakup dynamics and large-scale delta system evolution: Insights from the Cretaceous Ceduna delta system, Bight Basin, Southern Australian margin" by N Espurt, J-P Callot, J Totterdell, H Struckmeyer and R Vially

J. MacDonald[1], R. King[2], G. Backé[1] and R. Hillis[3]
[1] Australian School of Petroleum, University of Adelaide, SA 5005, Australia
[2] School of Earth and Environmental Sciences, The University of Adelaide, SA, 5005, Australia
[3] Deep Exploration Technologies Cooperative Research Centre, Mawson Building, University of Adelaide, SA 5005, Australia

1. Introduction

Espurt et al. [2009] interpret two seismic transects (including six seismic reflection lines) to resolve the geometry of the Bight Basin, the kinematic evolution of the White Pointer and Hammerhead delta systems and their role in the continental breakup dynamics of the southern Australian margin. However, the structural geometry of the delta systems has been oversimplified in their interpretations.

There are three major issues that arise in this paper: [1] the authors present regional interpretations on the structural style of the White Pointer and Hammerhead delta—deepwater fold-thrust belts (DDWFTBs) and the geometry of the Bight Basin using only two seismic transects and only one of these for reconstructions, [2] the authors interpret that the deepwater fold-thrust belt or delta-toe provinces of the White Pointer and Hammerhead delta systems are vertically stacked, and [3] the authors estimation of thick-skinned crustal stretching rates include thin-skinned deltaic extension, a result of gravitational collapse.

In this comment we demonstrate that regional mapping of both DDWFTBs indicates two independent systems that do not have vertically stacked deepwater fold-thrust belts, and that both systems demonstrate well-developed extensional provinces (delta-top) and compressional provinces (delta-toe). Finally, we explain why the Espurt et al. [2009] estimates for crustal stretching are unreliable based on the misinterpretation of the White Pointer DDWFTB and the models that they used to achieve this result.

2. Ceduna Sub-basin Delta—Deepwater Fold-Thrust Belts

A chronostratigraphic framework was proposed for the Bight Basin by Totterdell et al. (2000) which grouped the existing lithostratigraphic formations into 10 basin-scale Supersequences. Of the 10 supersequences, two are deltaic systems that exhibit gravity-driven deformation, the Cenomanian White Pointer Supersequence and the Santonian-Maastrichtian Hammerhead Supersequence. However, Espurt et al. [2009] describe the Cenomanian White Pointer delta system to include an additional two Supersequences: "The lower, Late Albian-Santonian White Pointer delta system is formed by the Blue Whale Supersequence, the strongly progradational White Pointer Supersequence and the progradational to aggradational Tiger Supersequence". This statement indicates that the delta system is composed of a pro-delta mud (Blue Whale Supersequence), a delta system (White Pointer Supersequence) a major unconformity and a later marine mud (Tiger Supersequence). Grouping of these unrelated Supersequences into one system is a major oversimplification, as only one of the three Supersequences (the White Pointer Supersequence) is actually deltaic.

Delta—deepwater fold-thrust belts typically form at continental margins where rapid progradation of deltaic sediments over salt or water prone mud results in gravitational collapse (Morley, 2003). These systems display a broad segregation of the delta into extensional and compressional provinces, whereby margin-parallel gravitational extensional stresses on the delta top drive down-dip, margin-normal, compressional stresses in the deepwater fold-thrust belt (Yassir & Zerwer, 1997; Corredor et al., 2005; King et al., 2009; MacDonald et al., 2010).

Our structural interpretation of 2D seismic data provided by Geoscience Australia, which include the two seismic transects (six seismic lines) from Espurt et al. [2009], enabled us to map the extent of both the White Pointer and Hammerhead deepwater fold-thrust belts within the Ceduna Sub-basin (Fig. 1a). Our structural analysis indicates that both the White Pointer and Hammerhead Supersequences contain well-developed DDWFTB systems that display excellent examples of linked extension and compression. We further demonstrate that the two systems are independent in both extent and areal geometry (Fig. 1a); with the deepwater fold-thrust belts being spatially and temporally separated by a basement high (Fig. 1a).

Espurt et al., state that for the Ceduna Sub-basin DDWFTB systems "the White Pointer delta system is characterized by only rare compressional features accommodating less than 2 kilometres of shortening" even though they present section A-A' and suggest a ~15 kilometre zone of compressional structures across the delta-toe in this section (Espurt et al. [2009]; Fig. 6). Espurt et al., also state that of the two seismic transects they present, transect B-B' best represents the geometry of the White Pointer and Hammerhead DDWFTBs, however, we demonstrate that transect B-B' has been subjected to over-interpretation (Fig. 1b). From our interpretations of the same transect, the White Pointer deepwater fold-thrust belt is not evident. Seismic

reflections beneath the Hammerhead deepwater fold-thrust belt, where we might expect to see the White Pointer Supersequence, are chaotic (Fig. 1b).

From the available seismic data in the Ceduna Sub-basin, there is no evidence that the White Pointer and Hammerhead deepwater fold-thrust belts are stacked. To be clear, the chronostratigraphic White Pointer and Hammerhead Supersequences are present throughout the Bight Basin; however, not everywhere do they possess the gravity-driven compressional structures that are needed to classify them as part of the DDWFTBs (MacDonald et al., 2010). We do acknowledge there may be some stacking of extensional structures nearest the paleo-shoreline; however, these systems prograded in different seaward directions, e.g. the White Pointer prograded to the southwest while the Hammerhead prograded to the south-southwest (Fig. 1a). The available seismic data demonstrate there is a minimum of ~60 km between the outermost edge of the compressional provinces of each system (MacDonald et al., 2010; Fig. 1a). For example, faults in the White Pointer deepwater fold-thrust belt strike approximately 308-128° while those of the Hammerhead strike 290-110°.

While seismic lines in the northwest Ceduna Sub-basin clearly display the White Pointer DDWFTB and those to the southeast display the Hammerhead DDWFTB, one seismic line, S65r 065-15, passing through the centre of the sub-basin does not demonstrate any compressional deformation (Fig. 1c). The White Pointer deepwater fold-thrust belt is only present in the northwest of the Ceduna Sub-basin, while the Hammerhead deepwater fold-thrust belt is only observed in the southeast (Fig. 1a). These two deepwater fold-thrust belts are separated in the Ceduna Sub-basin by a ~1.5 s basement high, clearly demonstrated on the two-way-time to basement grid interpreted from the available seismic reflection data (Fig. 1a). We propose that the basement high may have influenced the location of the depocentres for the White Pointer and Hammerhead DDWFTBs, which resulted in two separate systems; that demonstrate different locations, extents, ages, lithologies, internal structural geometries and detachment levels (Fig. 1a). Figure 2a demonstrates the extensive deepwater fold-thrust belt of the White Pointer DDWFTB in the western Ceduna Sub-basin.

Having been provided access to Geoscience Australia's 2D seismic database, we were able to complete a regional map (Fig. 1a) of the White Pointer and Hammerhead deepwater fold-thrust belts. We recognize that the authors may not have been provided the entire dataset, which may have lead to this over-interpretation. However, neglecting to map the extent of both DDWFTB systems resulted in the authors having based majority of their interpretations for an entire region on a single, poorly imaged seismic transect.

3. Regional Tectonics and Stretching Calculations

Espurt et al.'s basis for many of their conclusions revolve around the absence of a well-developed White Pointer deepwater fold-thrust belt in the eastern Ceduna Sub-basin. Three possible scenarios are presented for the absence of this deepwater fold-thrust belt, the third of which is chosen as the basis for the author's calculation of horizontal stretching of the crust. This third scenario, and major conclusion of the paper, suggests that part of the "missing compression" in this thin-skinned White Pointer system was accounted for by "tectonic coupling" of the displacement from the D1detachment, immediately beneath the White Pointer, to the deeper D0 detachment, at the moho. Thus, a deepwater fold-thrust belt did not form because compressional stresses were accommodated by D0.

When the authors address the relationship between the overlying, thin-skinned deltaic wedge and the extension in the crust, they state that the White Pointer delta system accommodated crustal extension. We feel the term "accommodated" is not suitable, as a gravitationally deformed thin-skinned tectonic system that slides or spreads above a detachment would not accommodate stress from the underlying extensional regime. There are a number of examples using in-situ stress data from producing DDWFTBs that demonstrate stresses are not transmitted from the underlying crust across thick undercompacted detachments into overlying deltaic sediments e.g. the Nile Delta (Tingay et al., 2010) and the Gulf of Mexico (Yale, 2003).

The authors do not properly differentiate between crustal-scale normal faults that are linked to crustal stretching events and detach at the proposed D0 detachment and deltaic growth faults that sole out along the shallower D1 detachment. The paper fails to explain exactly how the displacement for each fault set was calculated and does not properly address: 1) the isolated nature of a delta system above detachment and 2) the out-of-plane stress, three-dimensional nature of the system. For example the authors neglect the possibility that this transect lacks a fold-thrust belt due to along strike transfer of strain, resulting in a well-developed deepwater fold-thrust belt in the west; such as is imaged in Figure 2a. On the thick-skinned side, it is also possible that if such a D0 detachment exists, out-of-plane stress from the Potoroo Fault System farther along the margin may have localized strain in this area resulting in the formation of the exhumed mantle; thus, requiring little influence from the delta system above.

The authors neglect to consider the much simpler solution for the absence of a deepwater fold-thrust belt; that the seaward dipping detachment D1 (prior to exhumation of the subcontinental mantle; i.e. State 2: 93.5 Ma on Espurt et al. [2009] Fig.11) may have initiated a gravity-sliding scenario on the eastern flank of the White Pointer DDWFTB resulting in a system of pure extension. Formation of a deepwater fold-thrust belt would not be necessary if the slope angle was constant and long enough to accommodate the extending sediment

e.g. the Nile Delta (Tingay et al., 2010) and offshore Angola (Fort et al., 2004). The White Pointer deepwater fold-thrust belt is well developed in the western Ceduna Sub-basin possibly due to its position in the direction of maximum progradation and thus, sediment input resulting in the maximum development of overpressure along the detachment D1 (Fig. 1a, 2b).

Espurt et al., suggest that the exhumation of the mantle resulted in the cessation of gravity sliding in the White Pointer DDWFTB. However, due to decreasing sediment supply (Veevers et al., 1991; Totterdell et al., 2000) gravity sliding would have been waning by the end of the Cenomanian. The decreasing sediment supply resulted in loss of gravitational potential and reduced regeneration of overpressure in the Blue Whale Supersequence causing slowed deformation rates and eventually cessation (Morley and Guerin, 1996; Morley et al., 2003). We would certainly not rule out the possibility of the crust accommodating (via the Potoroo Fault System) some of the sedimentary loading of the margin; however, it is unlikely that the crust accommodated any more sediment along transect B-B' than it did to the west where the White Pointer deepwater fold-thrust belt is well developed and the Potoroo Fault System is also in place (Fig. 2b; Totterdell et al., 2000; Krassay and Totterdell, 2003).

The stretching calculations in the paper correspond to periods of margin evolution and yet, are founded, in part, on the structural geometry of the White Pointer DDWFTB (an isolated system of extension and compression above D1). We feel that the model-driven nature of this paper, and mis-interpretations of the White Pointer delta discredit the estimated stretching values that are presented. The presence of an extensive deepwater fold-thrust belt that balances up-dip extension in the west shows that regionally this is a complex system that likely involves out-of-plane transfer of stress (not uncommon in DDWFTB systems e.g. Niger Delta; Briggs et al., 2006). The authors have attempted to calculate the stretching of the crust on a plate margin using one seismic transect without fully understanding the regional framework of the Ceduna Sub-basin (e.g. the distribution of the Potoroo Fault System) and isolated nature of the White Pointer DDWFTB.

4. Summary

- The authors present two seismic transects for the Ceduna Sub-basin, of which transect B-B' is used for restorations, to explain the structural geometry of the White Pointer DDWFTB when it is not well represented in this transect: we demonstrate that transect B-B' is not a "representative" section through the White Pointer DDWFTB and therefore does not provide a realistic result.
- The Espurt et al. [2009] paper presents a regional structural interpretation for the White Pointer and Hammerhead DDWFTBs indicating that they are vertically stacked systems in their entirety: we demonstrate that at least the deepwater fold-thrust belts are not stacked
- The paper suggests stress is transmitted from the crust at detachment D0 to the White Pointer DDWFTB through the shallower D1 detachment: we propose alternative scenarios for the undeveloped deepwater fold-thrust belt and how it is unlikely that stress is transmitted through thin-skinned detachment D1.
- Estimations of stretching in the crust are presented in the paper and rely heavily on interaction with the overlying White Pointer DDWFTB: we demonstrate that the author's model-driven interpretations are the basis for these estimates and are therefore, unlikely to be truly representative.

5. References

Briggs, W.1., S.E., R.J. Davies, J.A. Cartwright, and R. Morgan (2006), Multiple detachment levels and their control on fold styles in the compressional domain of the deepwater west Niger Delta. *Basin Res*., 18, 435-50. doi:10.1111/j.1365-2117.2006.00300.x.

Corredor, F., J. H. Shaw, and F. Bilotti (2005), Structural styles in the deep-water fold and thrust belts of the Niger Delta, *AAPG Bull*., 89, 753-780.

Espurt, N., J.-P. Callot, J. Totterdell, H. Struckmeyer, and R. Vially (2009), Interactions between continental breakup dynamics and large-scale delta system evolution: Insights from the Cretaceous Ceduna delta system, Bight basin, Southern Australia margin. *Tectonics*, 28, TC6002, doi: 10.1029/2 009TC002447.

Fort, X., J-P. Brun, and F. Chauvel (2004), Salt tectonics on the Angolan margin, synsedimentary deformation processes. *AAPG Bull.*, 88 (11), 1523–1544.

King, R.C., R.R. Hillis, and M.R.P. Tingay (2009), Present-day stress and neotectonic provinces of the Baram Delta and deepwater fold-thrust belt. *J. Geol. Soc. Lon.*, 166, 197-200.

Krassay, A.A., and J.M. Totterdell (2003), Seismic stratigraphy of a large, Cretaceous shelf margin delta complex, offshore southern Australia. *AAPG Bull*., 87(6), 935-963.

MacDonald, J.D., R. King, R.R. Hillis, and G. Backé (2010), Structural style of the White Pointer and Hammerhead Delta—Deepwater Fold-Thrust Belts, Bight Basin, Australia. *APPEA J.*, v 50, xxx-xxx.

Morley, C.K. and G. Guerin (1996), Comparison of gravity-driven deformation styles and behaviour associated with mobile shales and salt. *Tectonics*, 15, 1154-1170.

Morley, C.K. (2003), Mobile shale related deformation in large deltas developed on passive and active margins. In *Subsurface Sediment Mobilization* edited by P. van Rensbergen, R.R. Hillis, A.J. Maltman, and C.K. Morley. *Geol. Soc. Lon. Spec. Publ.*, 216, 335-357.

Rowan, M.G., F.J. Peel, and B.C. Vendeville (2004), Gravity-driven fold belts on passive margins. In *Thrust Tectonics and Hydrocarbon Systems* edited by K.R. McClay. *AAPG Mem.*, 82, 157-182.

Tingay, M., P. Bentham, A.D. Feyter, and A. Kellner (2010), Present-day stress field rotations associated with evaporites in the offshore Nile Delta. *Geol. Soc. Am. Bull.*

Totterdell, J.M., J.E. Blevin, H.I.M. Struckmeyer, B.E. Bradshaw, J.B. Colwell, and J.M. Kennard (2000), A new sequence framework for the Great Australian Bight: starting with a clean slate. *APPEA J.*, 40, 95-117.

Veevers, J.J., C.McA. Powell, and S.R. Roots (1991), Review of seafloor spreading around Australia. I. Synthesis of the patterns of spreading. *Aust. J. Earth Sci.*, 38 (4), 373-89.

Yale, D.P. (2003), Fault and stress magnitude controls on variations in the orientation of in situ stress. In *Fracture and In-situ Stress Characterization of Hydrocarbon Reservoirs* edited by M. Ameen. *Geol. Soc. Lon. Spec. Pub*., 209, 55-64.

Yassir, N.A. and Zerwer, A. (1997), Stress regimes in the Gulf Coast, offshore Louisiana: data from well-bore breakout analysis. *AAPG Bull*., 81, 293-307.

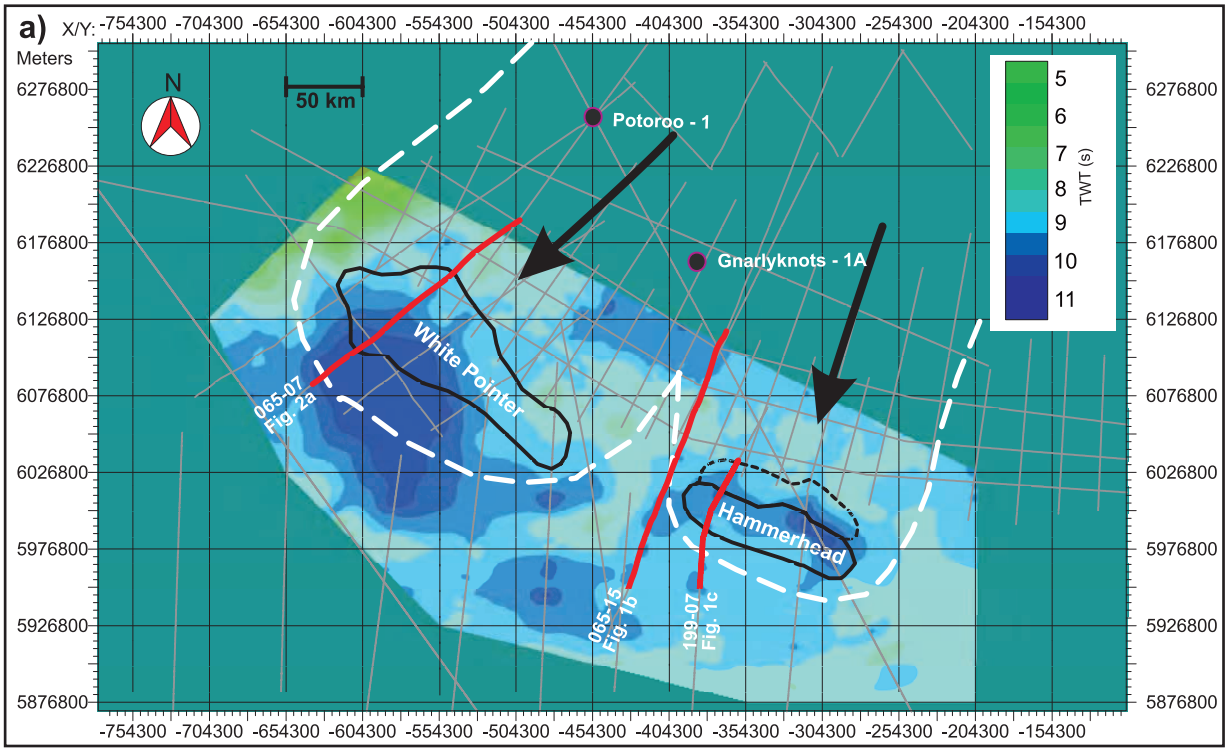

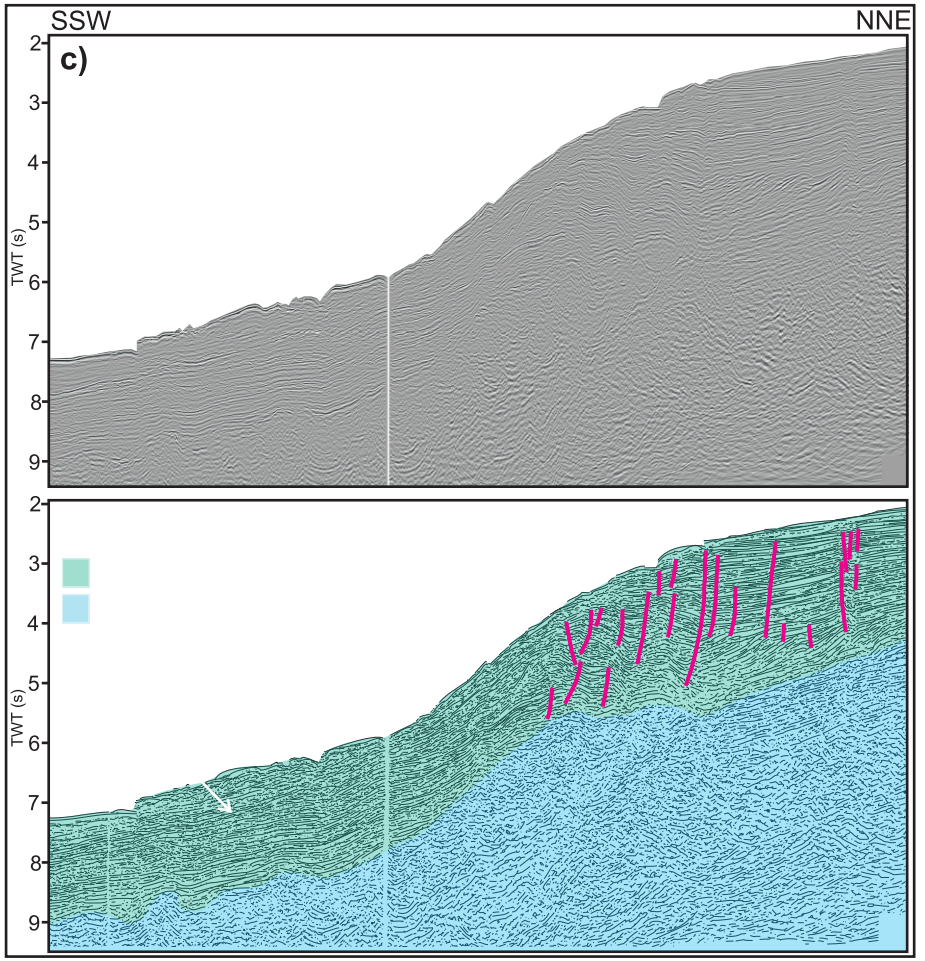

Figure 1: Location of Ceduna Sub-basin Cenomanian White Pointer and Campanian-Maastrichtian Hammerhead DDWFTBs (a) showing two-way-time to basement isopach map with ~ 1.5 s basement high between the DWFTBs. White dashed line represents delta lobes and arrows show direction of progradation. Seismic line 199-07 below (b) displays well developed Hammerhead DWFTB with chaotic reflections below where Espurt et al. [2009] interpreted a White Pointer DWFTB. Seismic line 065-15 (c) indicates an absence of compressional structures in the White Pointer or Hammerhead Supersequences, demonstrating that the DWFTBs are not stacked in the Ceduna Sub-basin (MacDonald et al., 2010).

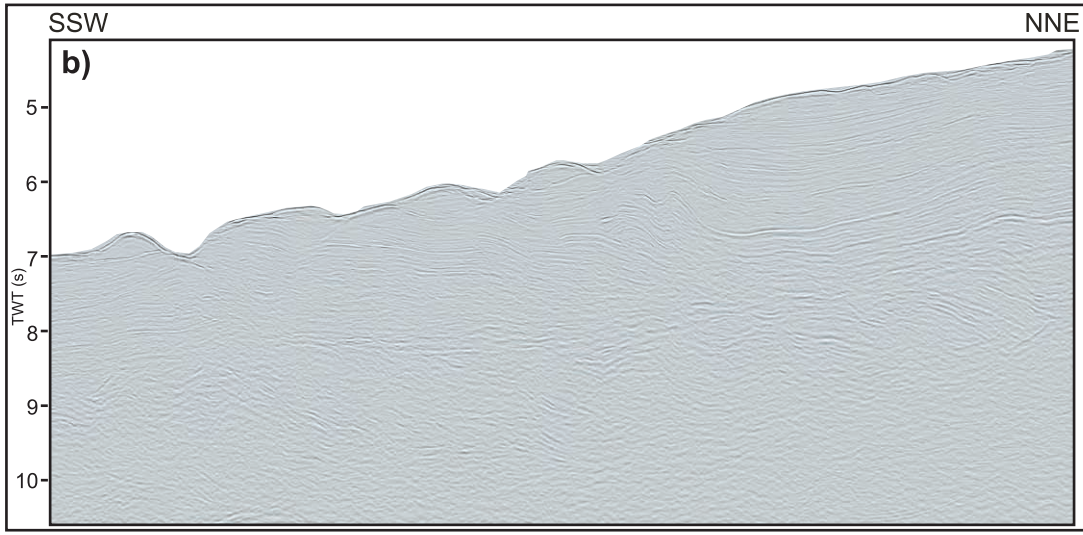

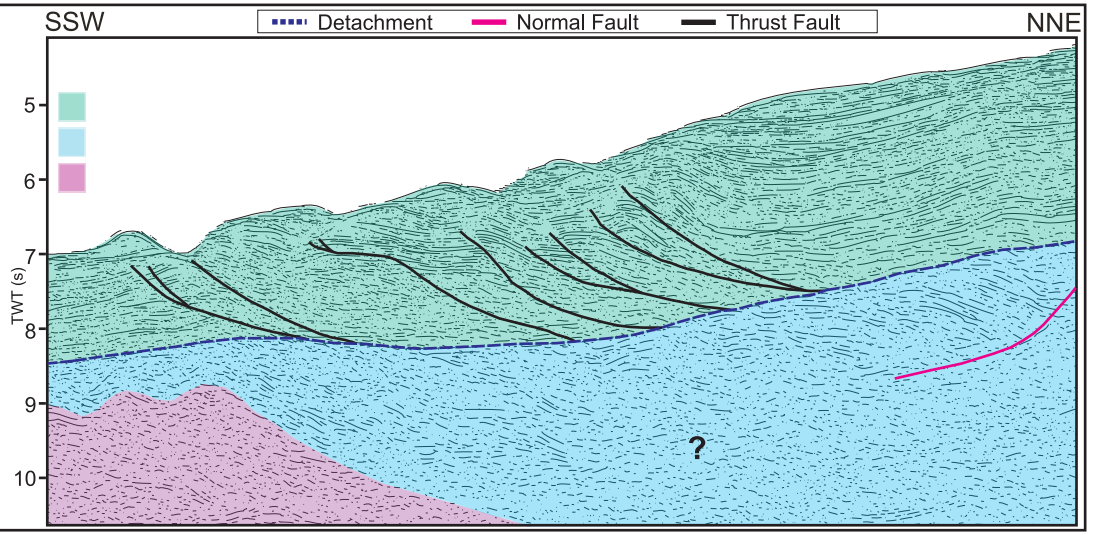

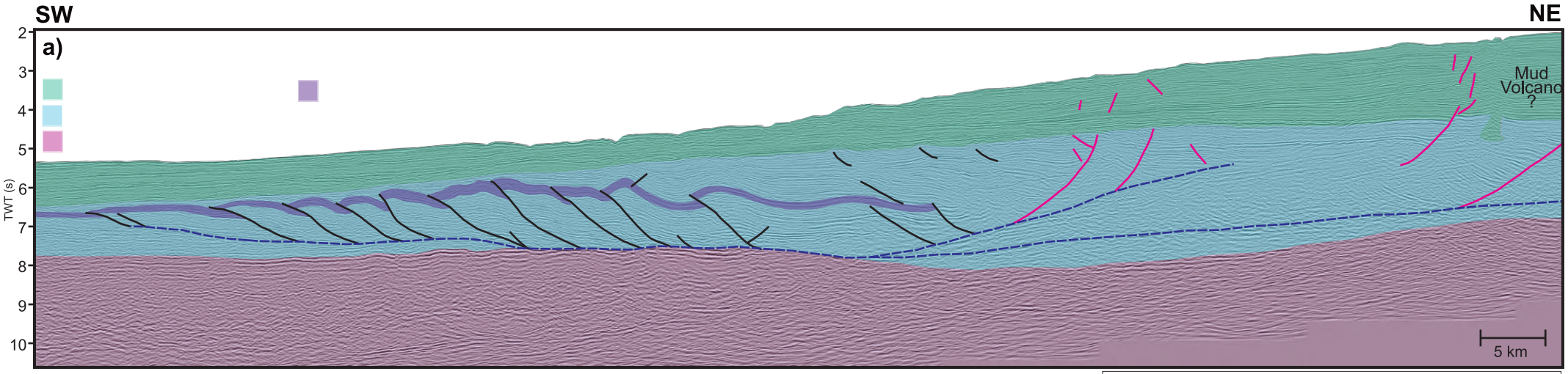

Figure 2a:Seismic line 065-07p from the northwestern Ceduna Sub-basin showing the well developed DWFTB in the Cenomanian White Pointer DDWFTB. Compressional province is > 80 km in width and characterized by an imbricate fault system linked to extension in the NE on the delta-top.

Figure 2b: Schematic cross section from the northwestern Ceduna Sub-basin showing the well developed White Pointer DDWFTB and the position of the Potoroo Fault System; Bw = Albian Blue Whale Supersequence, Wp = Cenomanian White pointer Supersequence, Ti = Turonian-Santonian Tiger Supersequence and Hh = Campanian-Maastrichtian Hammerhead Supersequence (after Krassay and Totterdell, 2003).